Synthesis of Graphene and h-BN by Chemical Vapor Deposition and their Transfer Process

by

YONG CHEOL SHIN

B. S., Seoul National University, Korea, 2006
M. S., Seoul National University, Korea, 2008
S.M., Massachusetts Institute of Technology, MA, United States, 2011

Submitted to the Department of Materials Science and Engineering
in Partial Fulfillment of the Requirements of the Degree of

DOCTOR OF PHILOSOPHY

at the

MASSACHUSETTS INSTITUTE OF TECHNOLOGY

February, 2015

Author Signature redacted
Department of Materials Science and Engineering
November 21, 2014

Certified by Signature redacted
Jing Kong
Department of Computer Science and Electrical Engineering
Thesis Supervisor

Accepted by Signature redacted
Donald R. Sadoway
Department of Materials Science and Engineering
Chair, Departmental Committee on Graduate Students

Synthesis of Graphene and h-BN by Chemical Vapor Deposition and their Transfer Process

by

YONG CHEOL SHIN

Submitted to the Department of Materials Science and Engineering on November 21, 2014
in Partial Fulfillment of the Requirements for
the Degree of Doctor of Philosophy in Materials Science and Engineering

ABSTRACT

Since graphene was discovered as an existing form by isolating from graphite in 2004, intense research and developments have been devoted to exploring this unique material; eventually, they pioneered a research field of 2-D materials including hexagonal boron nitride (h-BN) and transitional metal dichalcogenide (TMDC). In particular, the excellent material properties of graphene fascinated engineering fields to use it as a device component of applications such as RF-device or photodetector. Among various synthesis methods, metal-catalyzed chemical vapor deposition (CVD) has been the main process of 2-D materials because of their high film quality, scalability, and low production cost. In this thesis, I address challenging issues yet to be solved by separating the CVD process into two parts: synthesis and transfer. First, in the synthesis part, Cu-mediated CVD processes will be mainly discussed. Throughout an in-depth understanding of the growth mechanisms, I demonstrate a process to increase the domain size of graphene in sub-mm scale; and present a novel atmospheric CVD process to obtain a pristine monolayer graphene through an understating of a role of hydrogen. Besides, a method to evaluate the domain size is presented through a moderate oxidation. With the knowledge accumulated in this part, the thesis scope is extended to the growth of h-BN and to the use of Pt as a new growth substrate for both 2-D materials to gain better quality. In the transfer of 2-D materials, it is highly required to preserve the original quality of 2-D materials when transferred onto a target substrate. In this respect, I analyze the effect of various steps in the poly(methyl methacrylate) (PMMA)-supported wet transfer on graphene samples. Afterwards, a transfer process is proposed to result in a clean graphene surface and to suppress hole-doping in graphene. In addition, by selecting a new supporting polymer, I demonstrate a route to transfer 2-D materials that allows reducing the density of wrinkles and enabling a conformal coating on uneven target substrates. The addressed questionings and proposed solutions in this thesis will provide criteria in the preparation of other 2-D materials beyond graphene and h-BN prepared by CVD processes.

Thesis Supervisor: Jing Kong
Title: ITT Career Development Associate Professor of Electrical Engineering

Acknowledgement

It was a great journey to complete my PhD at MIT which I have dreamed from the moment I received an admission letter from Prof. Gradecak in 2008. Looking back on the times I spent here at MIT, I realized that this work cannot be completed without people who helped and stimulated me. I would like express my sincere gratitude through this space.

First of all, I would like to thank Prof. Kong for her support, inspiration, and guidance. Not to mention her insightful and encouraging comments on my research, she has been a strong support that I could count on whenever I was tumbling down in my PhD course. Together with being as a student of Jing, I believe I was truly blessed by having an opportunity to learn from Prof. Dresselhaus. It was a great honor for me to watch her passion to research close at hand. They serve as a model who I would like to follow after. I appreciate also the committee members of my thesis, Prof. Gradecak as the thesis reader and Prof. Schuh for their helpful discussion and comments.

It is great to have colleagues and friends who I would like to express my deep gratitude. I thank the NMELab and the MGM group colleagues. Please understand me that I cannot call over the names one after another, but it was a pleasure indeed to work together with all of them. In particular, I thank Wenjing, Jin-Yong, Daniel, Albert, Joaquin, and Alan. I am also grateful to my collaborators, Patrick, Xu, Lili, Paulo, and Alex. In particular, I have to remark the exceptional cooperation and friendship with Roman, Han, and Ahmad. I am also thankful to my friends who have been another stem to support my PhD life. Thank you indeed for your support, Gyuweon (and Hee-Sun) and Jae Jin. I believe this one sentence will be enough for them to understand my deep gratitude. I thank Sehoon, Kyoo Chul, and other KGMSE members and KGSA '08 members who went through together by caring for each other. I thank my seniors, Jihoon, Seung Woo, and Jin Young for their warm-hearted advices. And, I thank So-woong and Hyejin for encouraging me as always.

Finally, I would like to express my deepest gratitude to my family for their unconditional support, patience, trust, and encouragement. I wish them all the happiness and hope to return their favors in any ways.

This work was supported by ONR/AFOR Joint Graphene Approaches to Terahertz Electronics Multidisciplinary University Initiative and NSF Science and Technology Center for Integrated Quantum Materials.

Table of Contents

List of Figures

List of Tables

Glossary

AFM: atomic force microscopy

APCVD: atmospheric chemical vapor deposition

BLG: bilayer graphene

CPD: contact potential difference

CVD: chemical vapor deposition

CVD-G: graphene synthesized by CVD process

DI water: deionized water

EBSD: electron-backscattered diffraction

Exf-G: graphene prepared by mechanical exfoliation

FET: field effect transistor

FLG: few-layer graphene

h-BN: hexagonal boron nitride

HMDS: hexamethyldisilazane

HOPG: highly ordered pyrolytic graphite

I_D-I_{BKG}: The subtraction of background intensity from D band in the Raman spectroscopy of graphene

I_D/I_G : D band to G band intensity ratio in the Raman spectroscopy of graphene

I_{2D}/I_G: 2D band to G band intensity ratio in the Raman spectroscopy of graphene

IPA: isopropyl alcohol

I-V: current–voltage

LPCVD: low pressure chemical vapor deposition

min: minute

mRCA cleaning: modified RCA cleaning

NCG: nanocrystalline graphite

OBG: optical band gap

OM: optical microscopy

PDMS: polydimethylsiloxane

PMMA: poly(methyl methacrylate)

MLG: monolayer graphene

rms: root mean square

RT: room temperature

SAM: self-assembled monolayer

sccm: standard cubic centimeter per minute

SEM: scanning electron microscopy

SKPM: scanning Kelvin probe microscopy

TEC: thermal expansion coefficient

TEM: tunneling electron microscopy

ω_{2D}: The 2D-band peak position in the Raman spectroscopy of graphene

ω_G: The G-band peak position in the Raman spectroscopy of graphene

XRD: X-ray diffraction

Chapter 1. Introduction

1.1 Background

Graphene, an atomic plane composed of hexagonally arranged sp^2-hybridized carbon atoms, has been highly investigated in both physics and engineering fields for its attractive materials properties and feasibility for applications in the established manufacturing process. The simple and straightforward isolation of monolayer graphene (MLG) in 2004 from a highly ordered pyrolytic graphite (HOPG) bulk sample, using the so-called *a scotch tape method*, was worth noting here, since this work in 2004 enabled the experimental preparation and characterization of graphene [1]. The observation of the unique properties of graphene, such as the anomalous integer quantum Hall effect [2, 3], led to intensive research on graphene for physicists not just as a successor of carbon nanotubes (CNT), but as a pioneering material in the two-dimensional (2-D) materials family. Besides, it was fascinating that the electrical and electronic properties of graphene can be modulated by opening up a band gap through a structural modification on the edges of a graphene ribbon [4] or on ordered bilayer graphene (BLG) [5].

On the other hand, together with the demonstrated ultrahigh carrier mobility (>200,000 $cm^2 V^{-1} s^{-1}$) [6], the promising thermal [7], mechanical [8], and optical properties [9] have significantly drawn industrial attention to using graphene as a device component for practical applications. Different from CNTs, the 2-D morphological features of graphene have also been beneficial for ease in processing. This industrial demand for graphene has promoted the development of routes to *produce* graphene in large size, for which the mechanical exfoliation method fails. Based on established processes like thin film deposition, various methods have been attempted with two approaches: top-down exfoliation from graphite and bottom-up synthesis with a carbonaceous precursor. Among those, the chemical vapor deposition (CVD) process [10, 11] has been remarked as the most promising graphene production method because of the relatively high sample quality, low production cost, and scalability. Consequently, various electronic and optoelectronic graphene applications taking advantage of the CVD process, for example, RF-devices [12], sensors [13], photodetectors [14], photovoltaics [15], displays [16], etc. have been developed both under

laboratory settings and at the industry level aimed at manufacturing [16]. Nonetheless, when graphene synthesized by CVD (CVD-G) is compared to the mechanically exfoliated graphene (Exf-G), the quality of CVD-G is still far inferior, due to its poly-crystallinity and the present need for a transfer process. For this reason, many efforts have been devoted to improving the quality of CVD-G to make its quality closer to that of the Exf-G, which requires an in-depth understanding of the graphene growth and transfer.

As stated earlier, the emergence of graphene also created a material category, the 2-D materials family, including materials such as hexagonal boron nitride (h-BN) [17] or molybdenum disulfide (MoS_2) [18]. In general, the 2-D materials denote mono- to few-atomic layered materials, each of which has unique properties, distinct from its bulk form. For example, monolayer MoS_2 has a direct band gap of 1.8 eV while bulk MoS_2 has an indirect band gap of 1.29 eV [19]. Together with graphene, these 2-D materials are now being heavily studied with an eye toward not only improving existing applications, but also for creating a new structure that consists of various combinations of the layered materials. In this respect, for the last decade the development of synthesis, characterization, and device fabrication processes for graphene has acted as a platform for research on other 2-D materials. For example, both h-BN [20] and MoS_2 [21] can also be prepared by mechanical exfoliation methods. Due to the same limitations to scale up as for graphene, CVD-based processes, inspired by graphene growth, are now being widely investigated in both h-BN [22] and MoS_2 [23].

This thesis focuses mainly on the synthesis process of graphene by CVD and its transfer process. I discuss the challenges of CVD-G that degrade its material quality in this preparation process. Attempts to tackle such challenges follow. Furthermore, with the knowledge accumulated from developing this graphene preparation process, I explore the synthesis of another 2-D material, h-BN by the CVD approach. Meanwhile, I start by reviewing basic backgrounds needed to understand the technical content of this thesis.

1.2 Electronic structure of graphene and properties

Graphene consists of sp^2 hybridized carbon atoms in a hexagonally arranged lattice with two atoms per unit cell. Figure 1.1(a) and (b) show the arrangement of atoms with basis vectors for the unit cell of graphene in real space and in reciprocal space, respectively [24]. The inter-carbon spacing is 1.412 Å in plane and the calculated densities of graphene are 3.812×10^{15} atoms cm^{-2} and 7.604×10^{-8} g cm^{-2}. For its hexagonal arrangement, the lattice parameter of graphene in real space, a, is, $a = |\vec{a}_1| = |\vec{a}_2| = \sqrt{3}\times1.412 = 2.45$ Å while the lattice parameter in reciprocal space, b, is, $b = |\vec{b}_1| = |\vec{b}_2| = \frac{4\pi}{\sqrt{3}a}$. The carbon atom has four valence electrons. As a 2-D structure, namely, MLG has three valence electrons which form a sp^2 hybrid configuration that contributes covalent σ bonds between carbon atoms in plane. 1 TPa of Young's modulus [8] stronger than steel is arising from these strong σ bonds. On the other hand, the fourth valence electron is configured to form a half-filled $2p_z$ orbital, elongated in the perpendicular direction to the carbon lattice plane. The electronic structure by a simple tight binding calculation shows that neighboring two $2p_z$ orbitals in a unit cell gives rise to two energy bands, which are the fully-occupied π valance band and the fully-unoccupied π* conduction band [25]. These π bands account for the carrier transport in graphene, thereby behaving as a semi-metal. For the ***E(k)*** dispersion relation shown in Fig. 1.1(c) [25], the π bands touch each other at the K and K' points, corresponding to the six corners of the hexagonal Brillouin zone. The K and K' points in the Brillouin zone are arising from inequivalent carbon atoms that lead to the zero-band gap. For h-BN where boron and nitrogen are alternatively arranged instead of identical carbon atoms in graphene, the energy dispersion gives rise to the direct band gap of 6.07 eV (indirect: 4.64 eV) [17]. Near the K point where the π bands intersect, graphene exhibits a linear dispersion relation, described as,

$$E = \hbar v_f |k|, \qquad \text{(Eq. 1.1)}$$

where v_f is the Fermi velocity (approx.. 1×10^8 cm s^{-1}) [26]. Regarding 2-D space, the corresponding density of states, ***g(E)***, can be expressed as,

$$g(E) = \frac{2E}{\pi(\hbar v_f)^2}. \quad \text{(Eq. 1.2)}$$

Therefore, because of this linear relationship, the effective mass of both the electron and hole is zero near at the K and K' points. Thus, electron and hole near the Dirac points are *massless*, behaving like photons. In other words, the transport of electrons in graphene is expected to be at the Fermi velocity (~1/300 of the speed of light). Together with the low optical phonon scattering, this linear dispersion relation provides an ultrahigh carrier mobility (>200,000 $cm^2 V^{-1} s^{-1}$) [6] and allows ballistic transport on a μm length scale at room temperature (RT) [27].

1.3 Graphene synthesis methods

As stated earlier, the route of graphene preparation can be divided into either top-down or bottom up approaches. Top-down methods take advantage of the weak interlayer bonding, which is Van der Waals bonding. By mechanically peeling a layer off from the bulk graphite or by intercalating a guest material between graphene layers, MLG can be separated. The bottom-up approach involves chemical reactions. Starting from a carbonaceous precursor no matter what is gaseous, solid, or even liquid, the synthesis method attempts to form a *very* thin crystalline carbon as the final product through diverse chemical manipulations. Certainly, the control of the process parameters should be crucial to determine the quality of the synthesized graphene. In this chapter, representative graphene synthesis methods for different purposes will be reviewed.

1.3.1 Mechanical exfoliation

Mechanical exfoliation by cleaving bulk layered material is the most straightforward method to obtain a monolayer 2-D material. By applying a sufficient force perpendicular to the plane directions, such that the weak Van der Waals forces between sheets can be overcome, and then repeating this process over and over again, eventually a single atomic layer can be isolated and placed onto a substrate for

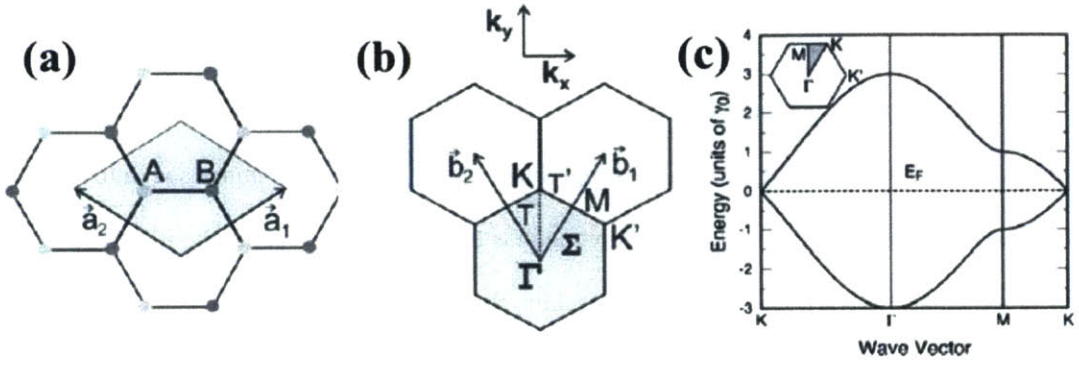

Figure 1.1 (a) The real space unit cell of graphene, showing inequivalent carbon atoms A and B and the basis vectors, $\vec{a}_1$ and $\vec{a}_2$. (b) The reciprocal space unit cell of graphene, showing the first Brillouin zone with high symmetry points, *Γ*, *K*, and *M*, and the basis vectors, $\vec{b}_1$ and $\vec{b}_2$. Reprinted permission from [24] . ©2011 Taylor & Francis. (c) ***E(k)*** dispersion relation of MLG. Reprinted permission from [25]. ©2011 Royal Society of Chemistry.

characterization [1-3]. Novoselov *et al.* used an adhesive tape to peel off graphene layers [1]. They first prepared square HOPG mesas with 20 μm to 2 mm in length and then attached them to photoresist. Using the adhesive tape, graphite sheets were peeled off from the photoresist, still leaving mono- to few-layered graphene. These layers were finally brought onto a Si substrate by releasing the photoresist from the tape by an acetone treatment. This method is highly remarkable, since not only was the graphene one atomic layer and μm-sized, but the preparation technique also opened up a simple strategy for preparing other 2-D mono-atomic layers, such as h-BN and MoS_2. This preparation technique in its simplicity has proven very effective for many groups around the world and has enabled the wide spread dissemination of these materials nowadays.

1.3.2 Chemical exfoliation

To address scalability issues, chemical exfoliation techniques were later developed to create

dispersions of layered compounds in solution that can then be deposited over very large areas [28]. Chemical synthesis of graphene starts from graphite, just like the mechanical exfoliation method. The general process is to take advantage of the intercalation of different chemical elements between graphite layers that can weaken van der Waals bonding. First, when graphite is immersed into concentrated sulfuric and nitric acid, graphite intercalation compounds (GIC) form, expanding the interspacing distance between graphite layers [29]. Subsequently, graphite sheets can be exfoliated by applying mechanical energy to the GIC's with an ultrasonicator [30, 31]. To obtain single-layer graphene from graphite using this process, graphite oxide (GO) is used as a GIC. Hummer and Offeman synthesized a GO with sulfuric acid, sodium nitrate, and potassium permanganate [32]. This GO was well dispersed in water owing to the electrostatic repulsion by intercalated hydroxyl and ether groups. After the deposition of the dispersed GO onto a nonspecific substrate, a reduction process was followed, resulting in graphene sheets. Although there are a number of methods to prepare graphene by this chemical exfoliation technique, the general process follows in the same way as described above. The main advantage of this technique is that the production of graphene can be easily scaled up with low cost. However, there is a challenge to using this chemically derived graphene in electric applications because its electric properties are degraded due to the defects created during the oxidation and reduction processes. This drawback of creating defects, on the other hand, can be useful for functionalizing graphene where the defects act as active sites to facilitate reactions with other materials [33, 34].

1.3.3 Epitaxial growth on SiC

A route toward wafer-scale graphene synthesis is the large-area, epitaxial growth of graphene on single crystalline SiC. As the graphene is directly prepared on this wide band gap semiconductor material, it is ideally compatible with industrial semiconductor processes. A number of different polymorphs of SiC, either 6H-SiC with AB stacking or 4H-SiC with ABC stacking, can be used for this type of epitaxial graphene growth. Both of these hexagonal forms of SiC have two different topmost layers along the c-

axis, Si-face SiC and C-face SiC, which affect the morphology and quality of the resulting graphene differently [35].

Van Bommel *et al.* first developed the graphene synthesis through high-temperature annealing of SiC [36]. They found that thin graphite layers formed after heating SiC between 1000 °C and 1500 °C in ultrahigh vacuum (UHV) below 10^{-10} Torr. The synthesis process involves three steps [37, 38]: the desorption of Si atoms from the SiC surface at high temperatures, subsequent surface reconstruction to a C-rich surface, and the formation of a conformal graphene layer initiated from islands at step edges. The critical step in the synthesis process is to control the desorption rate of Si from the SiC surface. A single crystalline graphite layer is typically observed on the Si-face SiC, while in contrast, the C-face SiC shows a polycrystalline graphite layer with various in-plane orientations with respect to the lattice underneath.

Epitaxial graphene growth on top of SiC has advantages in electronic applications by directly preparing high quality graphene on a semiconductor material on the wafer scale. In spite of this merit and high compatibility with present Si-based process, there are some obstacles to industrialize this technique for graphene production. First, in terms of production cost, this process is expensive. Not only is the price of a single crystalline SiC wafer quite expensive, but also only specific versions of SiC, 4H-SiC(0001) or 6H-SiC (0001), are suitable for graphene growth [39-41]. To address these problems, much work has been done on growing graphene on thin films of SiC deposited on top of Si substrates as a cheaper alternative [42, 43]. Furthermore, the epitaxial process usually requires either UHV or a very high process temperature (>1000 °C), which are not suitable for back-end processes. Graphene grown on 6H-SiC (0001) is shown in Figure 1.2(a).

1.3.4 Chemical vapor deposition (CVD)

CVD has been widely used in the microelectronics industry as a thin film deposition method because this process can take advantage of low production cost, good film quality, scalability, and good step coverage on a substrate with a complex structure. The deposition is achieved through the adsorption

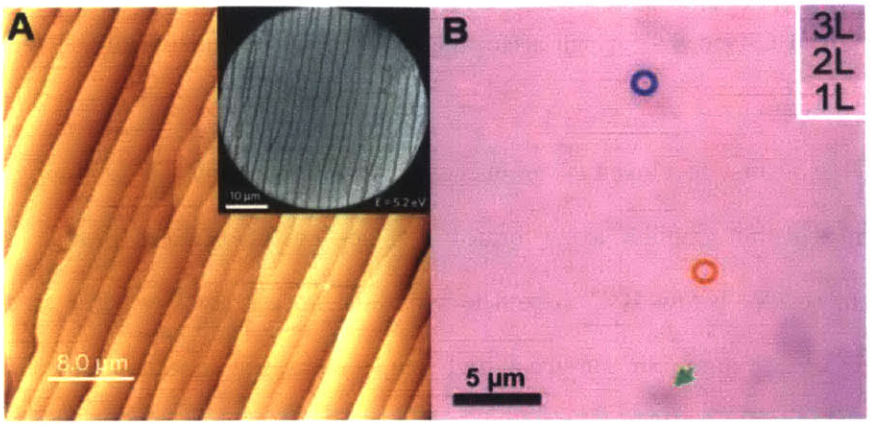

Figure 1.2 (a) Atomic force microscope (AFM) height image of graphene on 6H-SiC (0001) obtained by annealing in Ar (900 mbar at 1650 °C). The inset is the corresponding low electron energy microscopy (LEEM) image that reveals the terrace region covered with graphene up to 1 μm. Reprinted permission from [40]. ©2009 Nature Publishing Group. (b) Optical microscope image of transferred graphene on SiO_2/Si substrate after growing on a Cu foil by CVD. Although few layer formed locally, more than 95% of the area was covered by MLG. Reprinted permission from [11]. ©2009 American Association for the Advancement of Science.

of a vapor phase precursor on a substrate, the pyrolysis of this precursor, a phase transformation to a condensed phase occurring through nucleation and growth.

The synthesis of carbon materials has also exploited the CVD process. In the 1960s, graphitic thin film was already prepared on a transition metal substrate through the pyrolysis of carbon precursors, such as methane, ethylene, and acetylene [44, 45]. The metal substrate played a catalytic role to promote the decomposition of hydrocarbon sources. It may not be surprising that the current CVD system to synthesize graphene does not significantly deviate from this graphitic thin film deposition process. As well as the synthesis of the sp^3-carbon material, diamond, sp^2-carbon nanomaterials have been obtained by CVD with transition metal substrate. For example, CNTs are mostly synthesized by CVD using Ni, Co, or Fe nanoparticles [3, 4]. By adjusting the process parameters, such as the size of metal nanoparticles,

CNTs with controlled height, diameter, and the number of walls can be prepared in large quantity [46, 47]. These materials have a chemical structure with partially filled d-orbitals, which lower the activation energy for the formation of carbonaceous species [48, 49].

Based on these historical approaches, the synthesis of a new form of sp^2-carbon nanomaterial, graphene, was also attempted through the CVD process using transition metal substrates, although the synthesis of single layer graphite was already realized earlier in the 1960s [50]. In terms of the process development of graphene synthesis, the predominantly studied parameter was the choice of a substrate material because it turned out the growth mechanism of graphene appeared to be dependent to the type of material. With respect to the relative carbon solubility in the substrate at a typical growth temperature as high as 1000 °C where hydrocarbon precursor can be decomposed, graphene could form through either segregated carbon atoms diffusing out from the bulk substrate upon cooling or the deposition of carbon species on the surface of the substrate. Particularly, the discovery of Cu with negligible carbon solubility as a substrate material for graphene growth is remarkable. While mono- to few-layer graphene (FLG) could be obtained on a polycrystalline Ni thin film by an atmospheric CVD (APCVD) process [10, 51], Li *et al.* developed a process of MLG growth over a bulk Cu foil by low pressure CVD (LPCVD) as shown in Fig. 1.2(b) [11]. Since this process was carried out as a self-limiting manner, uniform MLG could be obtained over the substrate in large size. This opened up a route so that graphene could become industrially applicable beyond only theoretical interest. Since then, efforts have been made toward the synthesis of graphene with improved quality and the development of an optimized transfer process of this graphene from the metal substrate onto a target substrate, maintaining the properties achieved when it was grown.

There are, however, integration challenges for CVD-G. First, since metal substrates are used as a catalyst, post-transfer processes are necessary for many applications. Both dry and wet transfer methods can cause deterioration of the properties of the as-prepared graphene. For dry transfer [52], mechanical stresses induced during the transfer process scan break graphene flakes, while for wet transfers using

polymers [53], residues are left on the graphene surface. Although the direct graphene growth on an insulator, similar to epitaxial graphene, is currently still being optimized [54], the quality of the resulting graphene is still behind the graphene prepared by the Cu-mediated CVD method. In addition, interesting results for graphene grown on Pt have suggested that graphene can be repeatedly transferred off of the Pt substrate without the need for chemical etching through the hydrogen gas bubbling approach [55].

1.3.5 Properties comparison with respect to the synthesis method

Carrier mobility, μ, and carrier concentration, n, can be appropriate figures of merit to assess the quality of graphene prepared by various methods. Table 1-1 shows the corresponding values for μ and n with respect to the synthesis method and underlying substrate, as adapted from Hsu *et al.* [56]. Although those values can also be sensitive to device fabrication process, the range of values in terms of their order of magnitudes still remains valid.

Table 1.1 Carrier mobility and concentration with respect to the synthesis method and the device substrate. Adapted from [56].

Method-substrate	**Mobility [$cm^2 V^{-1} s^{-1}$]**	**Carrier concentration [cm^{-2}]**
SiC-C face [57]	500-5,000	10^{13}-10^{14}
SiC-Si face [57]	100-5,000	10^{11}-10^{13}
SiC-Si face, hydrogenated [58]	2,000-20,000	10^{13}
Exf-G-SiO_2 [20]	2,000-20,000	~10^{12}
Exf-G-suspended [6]	200,000	~2×10^{11}
Exf-G-h-BN [20]	60,000-80,000	5×10^{12}
CVD-G-SiO_2 [59]	1,200-24,000	4-20×10^{11}
CVD-G-h-BN [59]	1,000-70,000	10^{11}-10^{12}

1.4 Transfer of graphene

When graphene is prepared by a metal-mediated CVD process, the use of graphene on a metal substrate is limited, except for application as an anti-corrosive layer [60, 61]. Therefore, more often the transfer of graphene from the metal substrate onto suitable substrates is required, such as transfer to dielectrics for electronic applications. In order to obtain high-quality graphene material, not only is it important to optimize the graphene growth, but the transfer process is also critical to avoid deterioration of the graphene quality during transfer. Because most transfer processes are carried out with a wet etchant, surface tension of the etchant (or water) could cause graphene layer ripping or breaking. Furthermore, it has been shown that the protective layer (most often poly(methyl methacrylate) (PMMA) is used) or the etchant (*e.g.* acids or $FeCl_3$) can leave residues (*e.g.* FeO_x) on graphene. Otherwise, the transfer process (*e.g.* exposure to etchant or annealing) causes doping in graphene. For all these reasons, particular care and various strategies have been proposed to improve the transfer process. Other aspects of consideration for improving the graphene transfer process include how to make the process capable of scaling up, and integratable with the graphene synthesis process. Prior to my work, there have been some initial developments in this area, such as development of a roll-to-roll process for graphene transfer [16].

1.4.1 Choice of the supporting layer

In the graphene transfer, polymers have been found to be very suitable for as a supporting layer for both handling convenience and selective removability at the end of the transfer process. Up to now, the most commonly used supporting material has been the e-beam lithography resist, PMMA [62], which was also used in the transfer of CNTs [63]. In addition, polydimethylsiloxane (PDMS), which has been used in soft lithography [64] has also been applied to graphene transfer.

The PDMS-supported transfer process takes advantage of the robustness and good adhesion to graphene, an example of which is given in Figure 1.3(a) [51]. Because both PDMS and graphene are hydrophobic, the floating PDMS/graphene stack can be easily placed onto a target substrate when the

underlying metal is etched. The advantage of this PDMS-supported transfer is the compatibility with soft lithography. By exploiting a pre-patterned PDMS mold in the transfer process, the patterned graphene can be stamped on a target substrate [65]. Another advantage is that the mold can be reused. However, for MLG on Cu foils, it has been found from our experiments that when using a PDMS layer, having a complete film transferred without any breaks or tears is quite challenging. Therefore, PDMS might be more suitable for multilayer graphene transfer. In addition, in order to let the PDMS adhere well to the as-grown graphene on Cu foils, the PDMS should not be hard-baked, and conversely this tends to leave residues on graphene. Nevertheless, the PMMA-supported transfer is a very useful alternative method, offering the capability of direct patterning, particularly for applications involving soft-lithography.

The PMMA-supported method is the most widely used transfer process at present for graphene prepared by CVD [10]. PMMA has a good adhesion to graphene that gives rise to a conformal coating on graphene. In addition, PMMA is also suitable for a supporting layer that can be easily removed by either acetone and/or annealing without damaging the underlying graphene. The PMMA-supported transfer is in general similar to the PDMS-supported transfer, as shown in Fig. 1.3(b) [66]. However, in order to preserve the original properties of the as-grown graphene during the transfer, various parameters and more process steps should be considered than those that are simply described in the figure. This topic will be discussed in more detail in Chapter 4.

Apart from these polymers, an evaporated Au thin film can be used as a supporting material [67] when the target substrate is incompatible with PMMA. In contrast to most polymer supporting materials, this non-polymer can be advantageous, especially when it does not leave a residue on the graphene surface. It appears that the quality of the resulting graphene (as reflected from the performance of the devices) was reasonably good. Nevertheless, systematic studies should be carried out to compare this type of transfer, with the PMMA transfer regarding damage to the graphene by evaporation or resulting from the residue issue. Obviously, the cost is a lot more than using PMMA for the transfer.

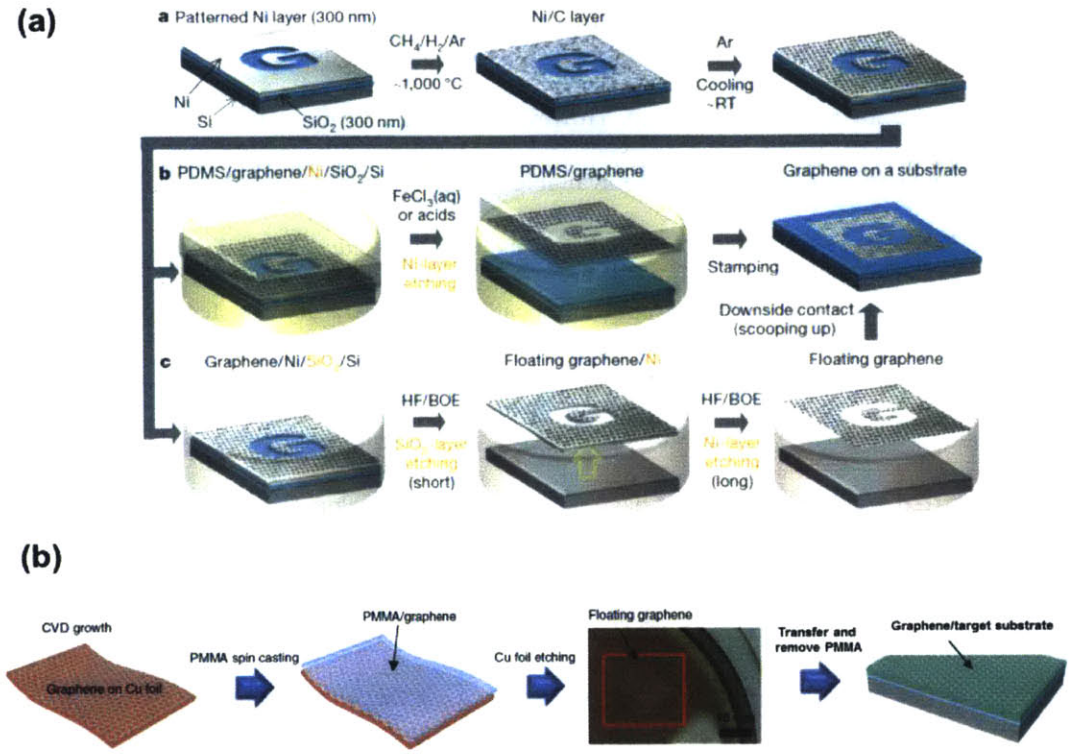

Figure 1.3 (a) PDMS-supported wet transfer process of graphene grown a Ni thin film. Reprinted with permission from [51]. ©2009 Nature Publishing Group. (b) Typical PMMA-supported wet transfer process of graphene grown on a Cu foil. Adapted with permission from [66]. ©2013 Nature Publishing Group.

1.4.2 Non-destructive exfoliation transfer process

One practical requirement is that the production cost of the graphene synthesis by CVD cannot be excessively high. Presently, MLG with a carrier mobility showing three orders of magnitude can be prepared with a CVD system that simply consists of a stationary thermal furnace, a mechanical pump, gas flow lines for CH_4 and H_2 and a metal substrate, such as a Ni thin film or a Cu foil. However, the post-transfer process can increase the cost significantly because in most of the present working procedures, the metal substrate is wasted by etching, *i.e.* it is treated as a consumable. Moreover, the disposal of the chemical etchants containing the metal wastes creates additional cost and is environmentally hazardous

by itself.

For these reasons, the most favorable strategy is an elimination of the transfer process by directly growing graphene on an arbitrary substrate. However, it is still challenging, on one hand, to obtain graphene with comparable quality to the one available by the established metal-mediated CVD process. Consequently, efforts have been made to develop a transfer process not requiring the etching of the metal substrate and allowing its reuse to grow graphene repeatedly. Firstly, a dry transfer process could enable the mechanical exfoliation of graphene from the metal substrate [52, 68]. The approach is straightforward, but it is still challenging to apply a force homogenously over the graphene on a growth substrate. For that reason, the transferred graphene is prone to have physical damage, such as due to cracks or holes.

A remarkable transfer process without sacrificing the metal substrate is to electrochemically exfoliate the graphene by generating gas bubbles (*e.g.* H_2) in between the graphene and the metal substrate [55, 69]. This bubbling transfer process was already demonstrated through an experiment preparing graphene with a mm-size domain grown on a Pt foil [55]. The bubble transfer process of the past work is illustrated in Figure 1.4. After PMMA is spun on such a graphene/Pt foil stack, an electrochemical cell is constructed that consists of a PMMA/graphene/Pt foil as a cathode, another Pt foil as an anode and 1 M NaOH as an electrolyte. When 1 A of constant current was maintained across the electrodes, H_2 bubbles started to be generated on the surface of the Pt as a result of the water reduction reaction; and these bubbles separated the PMMA/graphene layer from the Pt substrate. Although Pt is not an inexpensive material, by exploiting this transfer process, the Pt substrate can be repeatedly used to prepare graphene. Therefore, the bubble transfer process is expected to be available soon as a low-cost alternative to the established chemical etching-based transfer process.

1.5 Raman spectroscopy

Raman spectroscopy is one of the tools used to characterize 2-D materials. This characterization technique can be carried out in-situ, non-destructively, in atmospheric ambient on graphene at RT. Since

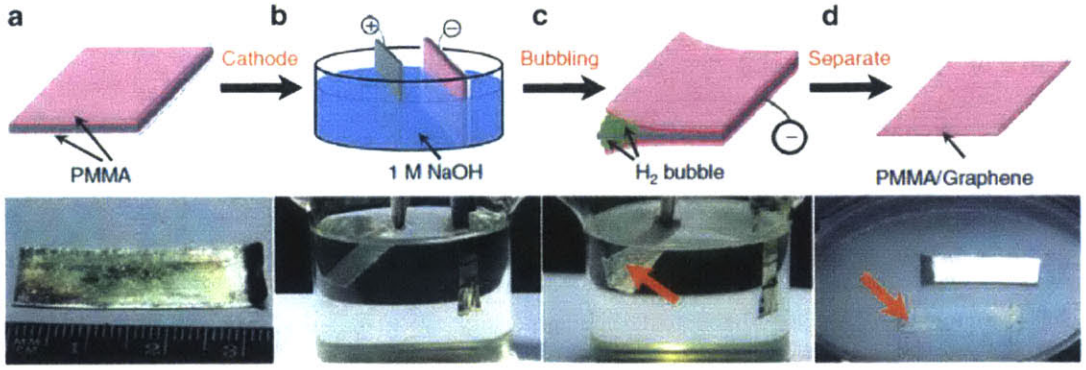

Figure 1.4 Schematic illustration of the bubble transfer process of graphene grown on a Pt foil (top) and the corresponding photographic images in each step (bottom), respectively. Reprinted permission from [55]. ©2012 Nature Publishing Group. (a) spin-coating of PMMA on graphene grown on a Pt foil, (b) electrochemical cell constructed to take off PMMA/graphene from the Pt foil with another Pt foil as an anode, (c) the generation of H_2 bubbles at graphene/Pt interfaces by a negative bias voltage, and (d) a separated PMMA/graphene stack floating on an electrolyte.

the discussion of the physics of Raman spectroscopy of the 2-D materials [24] is beyond the scope of this thesis, the analysis of the Raman spectra will be briefly described. Figure 1.5(a) is a typical Raman spectrum of both MLG and graphite [24]. For MLG, the intensity of the symmetry allowed 2D (or G′) band is strong through a fully resonance scattering process, where both the absorption and emission processes between electrons and phonons are resonant, which results in a usually high 2D to G intensity ratio, (I_{2D}/I_G). This ratio, thus, can be indicative of the number of graphene layers because that is decreasing by the addition of layers. However, such estimation is not guaranteed to provide a reliable metric because the I_{2D}/I_G is also influenced by the doping effect and by various sources of disorder. Instead of I_{2D}/I_G, the shape of the 2D band can reveal the number of layers. By addition of a graphene layer, the possible resonance process is increased by four such that the 2D band becomes the superposition of four sub-2D bands, which increases the bandwidth. This change in line shape allows for distinguishing between MLG and AB-stacked BLG. Finally, the D-band which is negligible in Fig. 1.5(a)

is also considered in the analysis of such types of spectra. D-band generally appears at 1345 cm^{-1} and is an indicative of symmetry-breaking disorder in graphene. This disorder from point defects in graphene can be created by impurities like nitrogen, interaction with dangling bonds of substrate, or domain boundaries in CVD-G.

In this thesis, Raman spectroscopy is used as one of main characterization methods to evaluate the quality of graphene. While the D-band to G-band intensity ratio (I_D/I_G) is indicated as an index of the defectiveness of graphene, the positions of G-band peak (ω_G), position of 2D-band peak (ω_{2D}), and the I_{2D}/I_G, are characterized as metrics that are sensitive to the doping of graphene caused by charged impurities based on the established experimental correlations [70-72].

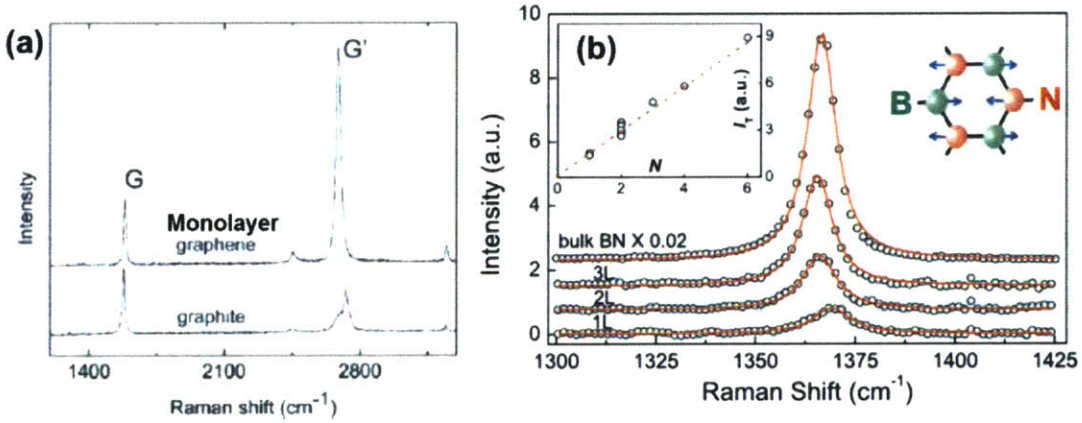

Figure 1.5 (a) Raman spectrum of MLG and graphite (λ_{laser}: 514 nm). Reprinted permission from [24]. ©2011 Taylor & Francis. (b) Raman spectrum of mono-, bi-, tri-layered, and bulk h-BN, highlighted around 1365 cm^{-1} for the E_{2g} phonon mode (λ_{laser}: 514 nm). The E_{2g} peak intensity with respect to the number of h-BN layers is shown in the inset. Reprinted permission from [73]. © 2011 WILEY-VCH Verlag GmbH & Co. KGaA, Weinheim

Apart from graphene, h-BN can also be characterized with Raman spectroscopy. As shown in Fig. 1.5(b), a weak but significant peak is found in the h-BN Raman spectra around 1365 cm^{-1} arising from its

B-N vibrational mode (E_{2g} phonon mode) [73]. Like the graphene Raman spectra, the E_{2g} peak has a relation to the number of h-BN layers in terms of its position and intensity, illustrated in the figure. Thus, in this thesis, the characterization of h-BN with Raman spectroscopy is mainly used to confirm the number of h-BN layers.

1.6 Thesis outline

The objective of this thesis is to provide the process developments of 2-D materials, graphene and h-BN, grown by metal-catalyzed CVD processes. The scope of the works is limited to the preparation from synthesis to transfer onto a target substrate. This preparation process is considered in detail for determining the baseline properties of specific device applications using 2-D materials.

For this preparation, I separate the discussion and presentation into two parts: synthesis and transfer. I then address current issues for each part emphasizing the aspects of the materials preparation that make the quality of the CVD-materials inferior to mechanically exfoliated ones with presently applicable technology. Afterwards, I develop processes to tackle the issues and eventually to improve the quality, through in-depth understating of the underlying mechanisms. First, in the synthesis part, Cu-mediated graphene growth is mainly explored. This process not only is the most widely studied process currently in the 2-D materials field, but also serves as groundwork for either the use of another growth substrate or the growth of other types of 2-D materials. In this part, I aim to understand the fundamental growth mechanisms, thereby developing new growth processes and a characterization method. With the knowledge accumulated in this part, I extend the study to the use of Pt as a new growth substrate and to the growth of h-BN.

The second part is the transfer of 2-D materials, which is necessary in most cases for carrying out the desired applications at present. In this thesis research, I aim to devise a transfer process to preserve the original quality of the 2-D materials on the growth substrate when transferred onto a target substrate. The study is carried out two ways: the investigation of the established PMMA-supported wet transfer method

and the choice of a supporting layer instead of PMMA. The development of these processes throughout has been further characterized by evaluating the electrical properties on a device scale to justify and evaluate the effectiveness of our synthesis and transfer methodologies.

This thesis consists of an introduction chapter (Chapter 1) followed by four main chapters with nine individual projects as follows:

In Chapter 2, graphene synthesis by CVD process is investigated. I analyze the effects of various process parameters on the graphene morphology. Through this analysis, I address challenges in the Cu-mediated CVD process, the most well-known growth process to synthesize monolayer graphene. Firstly, I introduce the domain boundary of graphene as one of the defects that degrades the properties of graphene. To reduce the density of the domain boundaries of graphene, it is desired to increase the domain size. I adopt a Cu enclosure system to obtain a sub-mm sized single crystalline graphene domain and report its far better electrical properties on a device scale.

Next, I attempt to synthesize a monolayer graphene by an atmospheric CVD (APCVD). With the APCVD process, it is generally known to be hard to obtain a continuous monolayer graphene. I remark here that hydrogen is one of the parameters that determine the growth kinetics in APCVD. I study the effect of the introduction of hydrogen on each growth step. I report a novel APCVD process resulting in a pristine monolayer of graphene.

Furthermore, I report a simple method to characterize the domain size of graphene. As the domain boundaries are atomically imperfective sites, it is challenging to directly observe through microscopes. I assume the nucleation sites would be relatively susceptible to a chemical reaction. By a mild oxidation, morphological changes are found in each domain center, namely, at the nucleation sites. The average distance between nucleation sites is consistent with the average domain size, in agreement with Raman spectroscopy measurements.

Finally, as a new growth metal substrate (Pt), the graphene growth on a Pt foil is explored. The recyclability of the Pt substrate can potentially reduce the production cost of graphene together with the development of an environmentally friendly electrochemical transfer process. The Pt-mediated graphene growth was known to be a challenging process to synthesize a monolayer graphene because Pt has greater carbon solubility than Cu that contributes to form multilayer graphene by precipitation upon cooling. By adjusting the growth temperature, I am able to gain a monolayer graphene using the LPCVD and to explain the growth mechanism. Afterwards, I confirm on a device scale that better electrical properties are achieved for graphene grown on a Pt foil than those obtained from growth on a Cu foil.

In Chapter 3, h-BN synthesis by the CVD process is investigated based on the study on the graphene synthesis process in Chapter 2. The wide band gap material h-BN is one of the promising 2-D materials because of its highly insulating electrical properties, ultra-flatness, and non-existing dangling bonds on the surface. Nevertheless, in terms of the synthesis, the metal-catalyzed CVD process still remained to be improved for using synthesized h-BN in device component. I report the developments of the h-BN growth process by CVD using a Cu foil and a Pt foil as growth substrates, aiming for gaining better material quality.

Firstly, I investigate the Cu-mediated h-BN synthesis process by monitoring the morphology of the h-BN with respect to the process parameters. Various characterizations are presented to verify the number of h-BN layers and to assess the quality of the resulting materials. Afterwards, I discuss the challenges of this synthesis process. Next, by using a Pt foil, I report a far better quality that I could achieve for monolayer h-BN; I confirm that the growth process turns out to be self-limiting with a wide process window. I suggest the suitability of the h-BN by Pt as a viable device component by presenting evidence for excellent electrical property of graphene devices fabricated on the type of h-BN that I was able to produce.

Besides, by taking advantage of the compatibility of the h-BN growth set up with a graphene growth system, I demonstrate how h-BN/graphene hybrid structure can be synthesized in a single flow process.

In Chapter 4, the graphene transfer process from its growth substrate onto a target substrate is investigated. 2-D materials grown on a metal foil usually have a limit for their application; thus, transfer onto a suitable substrate is required. I explore polymer-supported wet graphene transfer process.

Firstly, in the PMMA-supported transfer, after understating the effect of various parameters involved in each transfer step, I propose an optimized transfer process to result in a clean graphene surface and to suppress hole-doping in graphene. I justify the developed transfer method through the feasible electrical properties of graphene samples. Next, I attempt to use a new polymer, ethylene-vinyl acetate (EVA), as a supporting transfer material. Using two extreme process designs, I provide the evidence of effectiveness of the EVA-supported transfer by showing a mitigated graphene texture in one case and a conformal coating on a target substrate with uneven surface topography in the other case.

In Chapter 5, I summarize the works performed in this thesis. I also suggest relevant future studies to facilitate the preparation of 2-D materials.

References

[1] Novoselov KS, Geim AK, Morozov SV, Jiang D, Zhang Y, Dubonos SV, et al. Electric Field Effect in Atomically Thin Carbon Films. Science. 2004;306(5696):666-9.

[2] Zhang YB, Tan YW, Stormer HL, Kim P. Experimental observation of the quantum Hall effect and Berry's phase in graphene. Nature. 2005;438(7065):201-4.

[3] Novoselov KS, Geim AK, Morozov SV, Jiang D, Katsnelson MI, Grigorieva IV, et al. Two-dimensional gas of massless Dirac fermions in graphene. Nature. 2005;438(7065):197-200.

[4] Han MY, Oezyilmaz B, Zhang Y, Kim P. Energy band-gap engineering of graphene nanoribbons. Physical Review Letters. 2007;98(20).

[5] Zhang Y, Tang T-T, Girit C, Hao Z, Martin MC, Zettl A, et al. Direct observation of a widely tunable bandgap in bilayer graphene. Nature. 2009;459(7248):820-3.

[6] Bolotin KI, Sikes KJ, Jiang Z, Klima M, Fudenberg G, Hone J, et al. Ultrahigh electron mobility in suspended graphene. Solid State Communications. 2008;146(9-10):351-5.

[7] Balandin AA, Ghosh S, Bao W, Calizo I, Teweldebrhan D, Miao F, et al. Superior thermal conductivity of single-layer graphene. Nano Letters. 2008;8(3):902-7.

[8] Lee C, Wei X, Kysar JW, Hone J. Measurement of the elastic properties and intrinsic strength of monolayer graphene. Science. 2008;321(5887):385-8.

[9] Nair RR, Blake P, Grigorenko AN, Novoselov KS, Booth TJ, Stauber T, et al. Fine structure constant defines visual transparency of graphene. Science. 2008;320(5881):1308-.

[10] Reina A, Jia X, Ho J, Nezich D, Son H, Bulovic V, et al. Large Area, Few-Layer Graphene Films on Arbitrary Substrates by Chemical Vapor Deposition. Nano Letters. 2009;9(1):30-5.

[11] Li X, Cai W, An J, Kim S, Nah J, Yang D, et al. Large-Area Synthesis of High-Quality and Uniform Graphene Films on Copper Foils. Science. 2009;324(5932):1312-4.

[12] Lin Y-M, Valdes-Garcia A, Han S-J, Farmer DB, Meric I, Sun Y, et al. Wafer-Scale Graphene Integrated Circuit. Science. 2011;332(6035):1294-7.

[13] Kwak YH, Choi DS, Kim YN, Kim H, Yoon DH, Ahn S-S, et al. Flexible glucose sensor using CVD-grown graphene-based field effect transistor. Biosensors & Bioelectronics. 2012;37(1):82-7.

[14] Herring PK, Hsu AL, Gabor NM, Shin YC, Kong J, Palacios T, et al. Photoresponse of an Electrically Tunable Ambipolar Graphene Infrared Thermocouple. Nano Letters. 2014;14(2):901-7.

[15] Park H, Chang S, Zhou X, Kong J, Palacios T, Gradecak S. Flexible Graphene Electrode-Based Organic Photovoltaics with Record-High Efficiency. Nano Letters. 2014;14(9):5148-54.

[16] Bae S, Kim H, Lee Y, Xu X, Park J-S, Zheng Y, et al. Roll-to-roll production of 30-inch graphene films for transparent electrodes. Nature Nanotechnology. 2010;5(8):574-8.

[17] Topsakal M, Aktuerk E, Ciraci S. First-principles study of two- and one-dimensional honeycomb structures of boron nitride. Physical Review B. 2009;79(11).

[18] Helveg S, Lauritsen JV, Laegsgaard E, Stensgaard I, Norskov JK, Clausen BS, et al. Atomic-scale structure of single-layer MoS2 nanoclusters. Physical Review Letters. 2000;84(5):951-4.

[19] Mak KF, Lee C, Hone J, Shan J, Heinz TF. Atomically Thin MoS2: A New Direct-Gap Semiconductor. Physical Review Letters. 2010;105(13).

[20] Dean CR, Young AF, Meric I, Lee C, Wang L, Sorgenfrei S, et al. Boron nitride substrates for high-quality graphene electronics. Nature Nanotechnology. 2010;5(10):722-6.

[21] Splendiani A, Sun L, Zhang Y, Li T, Kim J, Chim C-Y, et al. Emerging Photoluminescence in Monolayer MoS2. Nano Letters. 2010;10(4):1271-5.

[22] Song L, Ci L, Lu H, Sorokin PB, Jin C, Ni J, et al. Large Scale Growth and Characterization of Atomic Hexagonal Boron Nitride Layers. Nano Letters. 2010;10(8):3209-15.

[23] Lee Y-H, Zhang X-Q, Zhang W, Chang M-T, Lin C-T, Chang K-D, et al. Synthesis of Large-Area MoS2 Atomic Layers with Chemical Vapor Deposition. Advanced Materials. 2012;24(17):2320-5.

[24] Saito R, Hofmann M, Dresselhaus G, Jorio A, Dresselhaus MS. Raman spectroscopy of graphene and carbon nanotubes. Advances in Physics. 2011;60(3):413-550.
[25] Yao J, Sun Y, Yang M, Duan Y. Chemistry, physics and biology of graphene-based nanomaterials: new horizons for sensing, imaging and medicine. Journal of Materials Chemistry. 2012;22(29):14313-29.
[26] Wallace PR. THE BAND THEORY OF GRAPHITE. Physical Review. 1947;71(9):622-34.
[27] Mayorov AS, Gorbachev RV, Morozov SV, Britnell L, Jalil R, Ponomarenko LA, et al. Micrometer-Scale Ballistic Transport in Encapsulated Graphene at Room Temperature. Nano Letters. 2011;11(6):2396-9.
[28] Hernandez Y, Nicolosi V, Lotya M, Blighe FM, Sun Z, De S, et al. High-yield production of graphene by liquid-phase exfoliation of graphite. Nature Nanotechnology. 2008;3(9):563-8.
[29] Dresselhaus MS, Dresselhaus G. INTERCALATION COMPOUNDS OF GRAPHITE. Advances in Physics. 1981;30(2):139-326.
[30] Chung DDL. EXFOLIATION OF GRAPHITE. Journal of Materials Science. 1987;22(12):4190-8.
[31] Chen GH, Wu DJ, Weng WU, Wu CL. Exfoliation of graphite flake and its nanocomposites. Carbon. 2003;41(3):619-21.
[32] Hummers WS, Offeman RE. PREPARATION OF GRAPHITIC OXIDE. Journal of the American Chemical Society. 1958;80(6):1339-.
[33] Subrahmanyam KS, Ghosh A, Gomathi A, Govindaraj A, Rao CNR. Covalent and Noncovalent Functionalization and Solubilization of Graphene. Nanoscience and Nanotechnology Letters. 2009;1(1):28-31.
[34] Lomeda JR, Doyle CD, Kosynkin DV, Hwang W-F, Tour JM. Diazonium Functionalization of Surfactant-Wrapped Chemically Converted Graphene Sheets. Journal of the American Chemical Society. 2008;130(48):16201-6.
[35] Hass J, Varchon F, Millan-Otoya JE, Sprinkle M, Sharma N, De Heer WA, et al. Why multilayer graphene on 4H-SiC(000(1)over-bar) behaves like a single sheet of graphene. Physical Review Letters. 2008;100(12).
[36] Vanbommel AJ, Crombeen JE, Vantooren A. LEED AND AUGER-ELECTRON OBSERVATIONS OF SIC (0001) SURFACE. Surface Science. 1975;48(2):463-72.
[37] Robinson J, Weng X, Trumbull K, Cavalero R, Wetherington M, Frantz E, et al. Nucleation of Epitaxial Graphene on SiC(0001). Acs Nano. 2010;4(1):153-8.
[38] Bolen ML, Harrison SE, Biedermann LB, Capano MA. Graphene formation mechanisms on 4H-SiC(0001). Physical Review B. 2009;80(11).
[39] de Heer WA, Berger C, Ruan M, Sprinkle M, Li X, Hu Y, et al. Large area and structured epitaxial graphene produced by confinement controlled sublimation of silicon carbide. Proceedings of the National Academy of Sciences of the United States of America. 2011;108(41):16900-5.
[40] Emtsev KV, Bostwick A, Horn K, Jobst J, Kellogg GL, Ley L, et al. Towards wafer-size graphene layers by atmospheric pressure graphitization of silicon carbide. Nature Materials. 2009;8(3):203-7.
[41] Virojanadara C, Syvaejarvi M, Yakimova R, Johansson LI, Zakharov AA, Balasubramanian T. Homogeneous large-area graphene layer growth on 6H-SiC(0001). Physical Review B. 2008;78(24).
[42] Aristov VY, Urbanik G, Kummer K, Vyalikh DV, Molodtsova OV, Preobrajenski AB, et al. Graphene Synthesis on Cubic SiC/Si Wafers. Perspectives for Mass Production of Graphene-Based Electronic Devices. Nano Letters. 2010;10(3):992-5.
[43] Kang H-C, Karasawa H, Miyamoto Y, Handa H, Fukidome H, Suemitsu T, et al. Epitaxial graphene top-gate FETs on silicon substrates. Solid-State Electronics. 2010;54(10):1071-5.
[44] Karu AE, Beer M. PYROLYTIC FORMATION OF HIGHLY CRYSTALLINE GRAPHITE FILMS. Journal of Applied Physics. 1966;37(5):2179-&.

[45] Presland AE, Walker PL. GROWTH OF SINGLE-CRYSTAL GRAPHITE BY PYROLYSIS OF ACETYLENE OVER METALS. Carbon. 1969;7(1):1-&.
[46] Ren ZF, Huang ZP, Xu JW, Wang JH, Bush P, Siegal MP, et al. Synthesis of large arrays of well-aligned carbon nanotubes on glass. Science. 1998;282(5391):1105-7.
[47] Li WZ, Xie SS, Qian LX, Chang BH, Zou BS, Zhou WY, et al. Large-scale synthesis of aligned carbon nanotubes. Science. 1996;274(5293):1701-3.
[48] Aizawa T, Souda R, Otani S, Ishizawa Y, Oshima C. ANOMALOUS BOND OF MONOLAYER GRAPHITE ON TRANSITION-METAL CARBIDE SURFACES. Physical Review Letters. 1990;64(7):768-71.
[49] Gamo Y, Nagashima A, Wakabayashi M, Terai M, Oshima C. Atomic structure of monolayer graphite formed on Ni(111). Surface Science. 1997;374(1-3):61-4.
[50] May JW. PLATINUM SURFACE LEED RINGS. Surface Science. 1969;17(1):267-&.
[51] Kim KS, Zhao Y, Jang H, Lee SY, Kim JM, Kim KS, et al. Large-scale pattern growth of graphene films for stretchable transparent electrodes. Nature. 2009;457(7230):706-10.
[52] Caldwell JD, Anderson TJ, Culbertson JC, Jernigan GG, Hobart KD, Kub FJ, et al. Technique for the Dry Transfer of Epitaxial Graphene onto Arbitrary Substrates. Acs Nano. 2010;4(2):1108-14.
[53] Kim K-S, Lee H-J, Lee C, Lee S-K, Jang H, Ahn J-H, et al. Chemical Vapor Deposition-Grown Graphene: The Thinnest Solid Lubricant. Acs Nano. 2011;5(6):5107-14.
[54] Ismach A, Druzgalski C, Penwell S, Schwartzberg A, Zheng M, Javey A, et al. Direct Chemical Vapor Deposition of Graphene on Dielectric Surfaces. Nano Letters. 2010;10(5):1542-8.
[55] Gao L, Ren W, Xu H, Jin L, Wang Z, Ma T, et al. Repeated growth and bubbling transfer of graphene with millimetre-size single-crystal grains using platinum. Nature Communications. 2012;3.
[56] Hsu A, Wang H, Shin YC, Mailly B, Zhang X, Yu L, et al. Large-Area 2-D Electronics: Materials, Technology, and Devices. Proceedings of the Ieee. 2013;101(7):1638-52.
[57] Tedesco JL, VanMil BL, Myers-Ward RL, McCrate JM, Kitt SA, Campbell PM, et al. Hall effect mobility of epitaxial graphene grown on silicon carbide. Applied Physics Letters. 2009;95(12).
[58] Robinson JA, Hollander M, LaBella M, III, Trumbull KA, Cavalero R, Snyder DW. Epitaxial Graphene Transistors: Enhancing Performance via Hydrogen Intercalation. Nano Letters. 2011;11(9):3875-80.
[59] Petrone N, Dean CR, Meric I, van der Zande AM, Huang PY, Wang L, et al. Chemical Vapor Deposition-Derived Graphene with Electrical Performance of Exfoliated Graphene. Nano Letters. 2012;12(6):2751-6.
[60] Yu Q, Jauregui LA, Wu W, Colby R, Tian J, Su Z, et al. Control and characterization of individual grains and grain boundaries in graphene grown by chemical vapour deposition. Nature Materials. 2011;10(6):443-9.
[61] Prasai D, Tuberquia JC, Harl RR, Jennings GK, Bolotin KI. Graphene: Corrosion-Inhibiting Coating. Acs Nano. 2012;6(2):1102-8.
[62] Hatzakis M. ELECTRON RESISTS FOR MICROCIRCUIT AND MASK PRODUCTION. Journal of the Electrochemical Society. 1969;116(7):1033-&.
[63] Jiao L, Fan B, Xian X, Wu Z, Zhang J, Liu Z. Creation of nanostructures with poly(methyl methacrylate)-mediated nanotransfer printing. Journal of the American Chemical Society. 2008;130(38):12612-+.
[64] Lee JN, Park C, Whitesides GM. Solvent compatibility of poly(dimethylsiloxane)-based microfluidic devices. Analytical Chemistry. 2003;75(23):6544-54.
[65] Kang SJ, Kim B, Kim KS, Zhao Y, Chen Z, Lee GH, et al. Inking Elastomeric Stamps with Micro-Patterned, Single Layer Graphene to Create High-Performance OFETs. Advanced Materials. 2011;23(31):3531-+.
[66] Kim Y, Lee J, Yeom MS, Shin JW, Kim H, Cui Y, et al. Strengthening effect of single-atomic-layer graphene in metal-graphene nanolayered composites. Nature Communications. 2013;4.

[67] Hsu C-L, Lin C-T, Huang J-H, Chu C-W, Wei K-H, Li L-J. Layer-by-Layer Graphene/TCNQ Stacked Films as Conducting Anodes for Organic Solar Cells. Acs Nano. 2012;6(6):5031-9.
[68] Unarunotai S, Murata Y, Chialvo CE, Kim H-s, MacLaren S, Mason N, et al. Transfer of graphene layers grown on SiC wafers to other substrates and their integration into field effect transistors. Applied Physics Letters. 2009;95(20).
[69] Wang Y, Zheng Y, Xu X, Dubuisson E, Bao Q, Lu J, et al. Electrochemical Delamination of CVD-Grown Graphene Film: Toward the Recyclable Use of Copper Catalyst. Acs Nano. 2011;5(12):9927-33.
[70] Ni ZH, Yu T, Luo ZQ, Wang YY, Liu L, Wong CP, et al. Probing Charged Impurities in Suspended Graphene Using Raman Spectroscopy. Acs Nano. 2009;3(3):569-74.
[71] Das A, Pisana S, Chakraborty B, Piscanec S, Saha SK, Waghmare UV, et al. Monitoring dopants by Raman scattering in an electrochemically top-gated graphene transistor. Nature Nanotechnology. 2008;3(4):210-5.
[72] Wang QH, Jin Z, Kim KK, Hilmer AJ, Paulus GLC, Shih C-J, et al. Understanding and controlling the substrate effect on graphene electron-transfer chemistry via reactivity imprint lithography. Nature Chemistry. 2012;4(9):724-32.
[73] Gorbachev RV, Riaz I, Nair RR, Jalil R, Britnell L, Belle BD, et al. Hunting for Monolayer Boron Nitride: Optical and Raman Signatures. Small. 2011;7(4):465-8.

Chapter 2. Synthesis of Graphene by CVD

2.1 Background

Graphene is a unique material by itself as a form of a monatomic layer. To understand how graphene forms, however, its synthesis process by CVD can be regarded as a deposition process of a *very* thin film through a simple pyrolysis of a hydrocarbon gas. This may allow us to model the graphene growth by CVD by adapting to the growth mechanism used in the thin-film deposition. In this manner, it can be understood how the process parameters affect the morphology of the resulting graphene. This helps in preparing graphene in large area with material properties closer to the theoretical values and those achieved in mechanically exfoliated graphene.

As can be seen in Figure 2.1, the graphene growth process by CVD typically consists of four steps: heating, annealing, growth and a cooling step. For MLG growth, a bulk Cu foil is commonly used as a catalyst substrate. First, in the heating step, the substrate temperature is ramped up to 1000 °C to facilitate the dissociation of the hydrocarbon precursor, such as CH_4. In the subsequent annealing step, the substrate removes a native oxide on the surface and develops larger grain sizes and sometimes smoother surfaces at the elevated temperature. Hydrocarbon gas is introduced into the chamber in the growth step, giving rise to the formation of graphene on the substrate surface. Finally, the supply of hydrocarbon gas is stopped and the chamber is cooled down to room temperature. For catalysts such as Ni that has a specific solubility of carbon at the growth temperature, the control of this cooling rate can influence the thickness of graphene [1]. Thus, adjustable process parameters can be the growth temperature, the flow rate of gases, the partial pressure of CH_4, the ambient pressure, and the cooling rate. Considering that the thin-film deposition by CVD is achieved by a phase transformation process, *i.e.* nucleation and growth, these process parameters can be associated with the process kinetics, determining the morphology of graphene.

In this chapter, the graphene growth by CVD will be studied mainly with a Cu foil as a growth substrate. This Cu-mediated graphene growth is widely known as a process to obtain a uniform MLG layer over the substrate, based on a self-limiting process. After reviewing the growth kinetics of graphene and the effect

of the process parameters on the graphene morphologies, an atmospheric CVD (APCVD) process to achieve a uniform MLG will be discussed. In the following, as a novel graphene growth substrate, a Pt-mediated graphene growth will be investigated. Finally, a technique to measure the domain size of a graphene sample will be introduced.

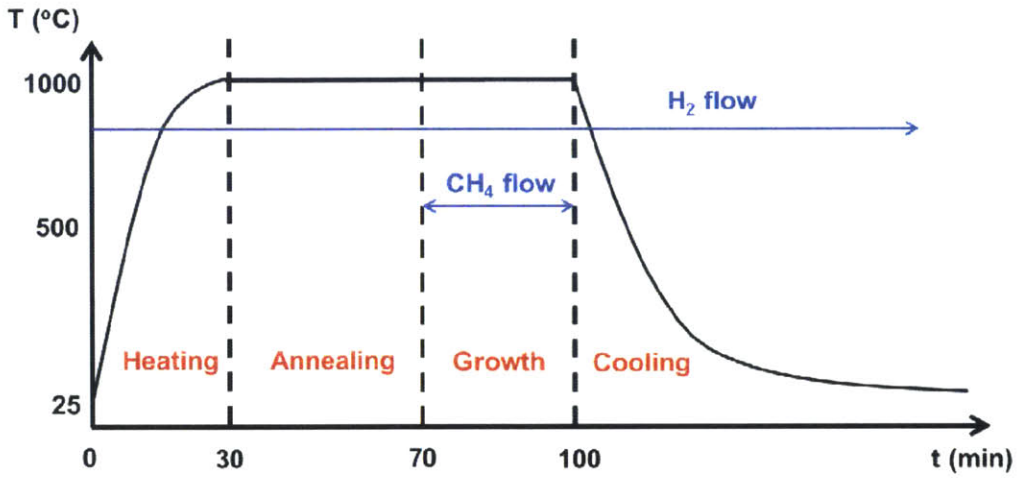

Figure 2.1 Typical schematic flow of the graphene growth process by CVD. The process consists of a heating, annealing, growth and cooling step. In the annealing step, the grain growth and the cleaning of the substrate are achieved. Hydrocarbon precursors are provided in the subsequent growth step.

2.2 The effect of process parameters

2.2.1 The kinetics of the graphene growth process with respect to the process parameters

When the graphene growth is assumed to be purely carried out by a surface reaction, ignoring the segregation of supersaturated carbon from the bulk substrate, either the mass-transport regime or the surface-reaction regime dominates the kinetics, depending on the competition of between the corresponding fluxes. As illustrated in Figure 2.2 [2], the growth step involves the following six sequential processes: (1) mass transport of gas-phase hydrocarbon molecules from the bulk region to the surface region; (2) adsorption of these molecules on the substrate surface; (3) decomposition of the

molecules into active hydrogen and carbon species; (4) surface diffusion of these active species, resulting in the formation of graphene islands; (5) desorption of active hydrogen species (H^*) and hydrogen gas molecules (H_2) and (6) mass transport of the gas species in (5) from the surface region to the bulk region. These processes can be divided into two kinetic regimes: the mass transport regime that involves the diffusion of gas species through the boundary layer region ((1) and (6)); and the surface reaction regime ((2)–(5)). Because these regimes have different reaction characteristics, if first-order reaction is simply assumed, the corresponding fluxes are given by,

$$F_{mass\ transport} = h_g(C_g - C_S) \qquad \text{(Eq. 2.1)}$$

$$F_{surface\ reaction} = K_s C_s, \qquad \text{(Eq. 2.2)}$$

where h_g is the mass transport coefficient, C_g and C_s the concentrations of hydrocarbon (CH_4 in this model) in the bulk region and in the surface region, respectively, and K_s is the surface reaction constant.

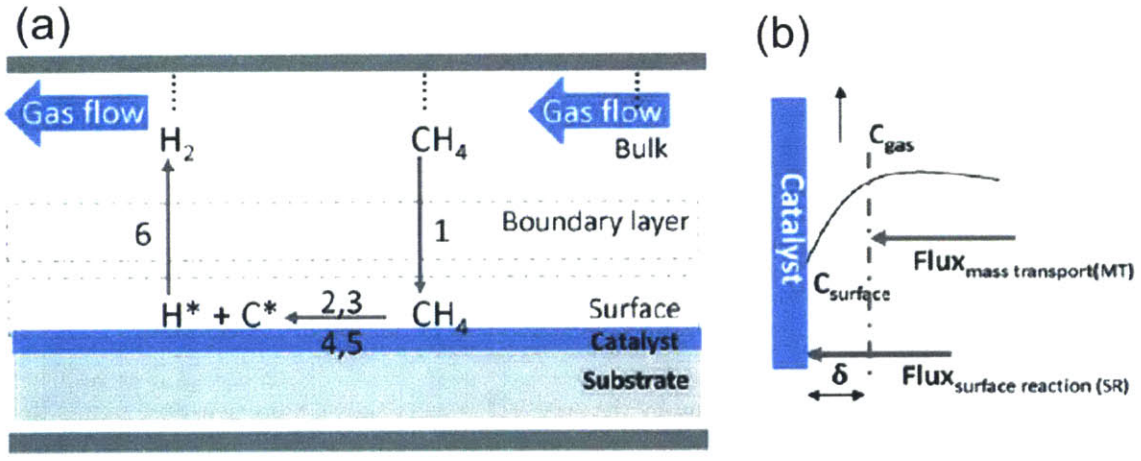

Figure 2.2 (a) Steps involved in a graphene growth on a substrate where the segregation of the supersaturated carbon atoms from the bulk region is not assumed. (b) Steady-state mass transport and surface reaction fluxes, where δ is the boundary layer thickness. Reprinted with permission from [2]. ©2010 American Chemical Society.

One can consider a steady state where both fluxes are equal to each other and the steady-state flux is then:

$$F_{mass\ transport} = F_{surface\ reaction} = F_{steady\ state} = \left[\frac{K_s h_g}{K_s + h_g}\right] C_s . \quad \text{(Eq. 2.3)}$$

Therefore, the kinetics of the graphene growth can be limited by the competition between K_s and h_g. In other words, when the surface reaction is fast ($K_s >> h_g$), the kinetics is dominated by mass transport of gas molecules through the boundary layer and vice versa. Since Eq. 2.1 is derived from Fick's first law describing the diffusion of mass, h_g can be expressed as,

$$h_g = \frac{D_g}{\delta}, \quad D_g \propto \frac{1}{P}, \quad \delta \propto \frac{1}{U}, \quad \text{(Eq. 2.4)}$$

where D_g is the diffusion coefficient of gas molecules, δ the thickness of boundary layer formed by a gas flow, P the ambient pressure and U the flow rate of gases. Together with the observation that K_s has an exponential relationship with the substrate temperature because all the surface reactions involving adsorption, decomposition, surface diffusion and desorption are thermally activated, these allow us to control the kinetics by adjusting the process parameters. For example, when the ambient pressure is low, D_g becomes higher than the case of the atmospheric process, leading to an increase in h_g. Consequently, surface reactions become the rate-limiting step, and the graphene growth process appears to be self-limiting. That is the reason why MLG is mostly achieved through the Cu-mediated LPCVD process, even with rough Cu foil surfaces, or varied flow rates or partial pressures of hydrocarbon are applied.

In contrast, the morphology of graphene by the APCVD process shows more sensitive trends to the process parameters. For APCVD, the process kinetics is usually in the mass transport-limited regime; the process is not self-limiting, and therefore it is challenging in this case to obtain uniform MLG. In this regime, the diffusion distance of the hydrocarbon gas molecule, or the boundary layer thickness, is an important factor. This means that the topography of the substrate surface will influence the morphology of graphene. Consequently, FLG or multilayer graphene with a preferred nucleation along the rolling lines

(*i.e.* straight striations on a Cu-foil surface given by the cold rolling process) is observed in the APCVD process [2, 3].

Currently, MLG by APCVD is achieved using two strategies: (1) changing the dominant kinetics into a surface reaction-limiting process, and (2) decreasing the concentration of the hydrocarbon feedstock, C_s [2, 3]. The former process will be discussed in the following sec. **2.2.3**. In the most cases, both strategies are applied at the same time by flowing highly diluted hydrocarbon gas with an excess of an inert carrier gas, such as argon. The increase in the flow rate by this carrier gas can reduce δ, thereby increasing h_g. The decrease in C_s also makes it harder to nucleate graphene on the substrate surface, leading to surface reaction-limiting kinetics. In addition, to exclude the effect of the topography of the substrate surface, pre-treatment of the substrate, such as by electropolishing [3] or chemomechanical polishing [4], can be applied before the CVD process in order to prepare a highly flat substrate surface.

2.2.2 The nucleation of graphene with respect to the process parameters

Due to its self-limiting nature of the LPCVD process, MLG can be obtained by the LPCVD process even when the process parameters are varied. However, the morphology of the graphene at its initial growth state shows a more sensitive dependency on these growth parameters, as reflected in the size of a graphene domain (which is a graphene island with the same in-plane crystallographic orientation). When atomic carbons are created on the substrate surface from the dissociation of hydrocarbon precursors, a few carbon atoms attach to each other and form a nucleus. A graphene cluster made by the coalescence of these nuclei keeps growing to form a graphene domain through an adatom diffusion of carbon atoms. As time elapses, these domains eventually meet and form a boundary. In contrast to the case of a typical thin-film growth, the domain boundary of as-grown graphene is assumed to be static even with further treatment, such as annealing. Since this domain boundary is an intrinsic defect that scatters carriers in electronic [5] and thermal transport [6], and degrades the mechanical strength [7] of the graphene, significant efforts were made to increase the domain size to become as large as possible. Achieving a

large domain size is directly associated with the decrease in the nucleation density. In this section, we discuss how process parameters are connected to the nucleation of graphene.

As shown in Figure 2.3 [8], the nucleation density of graphene flakes can be controlled by adjusting the process parameters. If an identical state of the substrate surface is assumed, these behaviors in the figure can be understood by applying a heterogeneous nucleation model to the graphene growth. Nucleation is a phase transformation process of supersaturated species at the expense of the addition of surface free energy by the phase transformation. For a heterogeneous nucleation process, the critical nucleus size (r^*) and the corresponding Gibbs free energy (ΔG^*) to achieve a critical nucleus size are given by [9],

$$r^* = -\frac{2\gamma_{AB}}{\Delta G_V}, \quad \Delta G^* = -\frac{16\pi}{3}\frac{\gamma_{AB}^3}{\Delta G_V^2}S(\theta), \qquad \text{(Eq. 2.5)}$$

where γ_{AB} is the surface-free energy of the phase A over the phase B (graphene over a substrate in this case), ΔG_V the change of the free energy by the phase transformation and $S(\theta)$ a shape factor of the substrate contributing to the additional promotion of the nucleation. Here, ΔG_V corresponds to the driving force of the nucleation and can be expressed as,

$$\Delta G_V \approx -RT\Omega_A^{-1}\alpha_{SS}, \ \alpha_{SS} = \frac{p_A^{act} - p_A^{eq}}{p_A^{eq}}, \qquad \text{(Eq. 2.6)}$$

where R is the gas constant, T the temperature, Ω_A the molar volume of the phase A, and α_{SS} the supersaturation defined by the difference of partial pressure of phase A (carbon in this case) between a given state (p_A^{act}) and the equilibrium state (p_A^{eq}).

The kinetics of the nucleation process should also be considered. The nucleation rate ($\dot{N}$) is given by the attachment rate of adatoms times the concentration of clusters with the critical nucleus size (C_r^*),

$$\dot{N} = \omega \exp\left(\frac{-\Delta G_m}{RT}\right) C_{r^*} = \omega \exp\left(\frac{-\Delta G_m}{RT}\right) C_0 \exp\left(\frac{-\Delta G^*}{RT}\right), \qquad \text{(Eq. 2.7)}$$

where ω is the vibration frequency of the atoms, ΔG_m the migration-free energy of an adatom, and C_0 the

total concentration of atoms. Fig. 2.3(b)–(d) show that a lower nucleation density or a larger domain size can be achieved by increasing the substrate temperature, decreasing the flow rate of the hydrocarbon gas (CH_4 in this case) and decreasing the partial pressure of the hydrocarbon gas, respectively. First, since this nucleation is a thermally-activated process, the increase in temperature can be expected to promote the nucleation, leading to a decrease in the domain size. However, this increase in domain size shown in Fig. 2.3(b) implies that the temperature appears to more actively contribute to the increase in desorption and evaporation of the decomposed carbon and hydrogen, thereby decreasing the nucleation density [10, 11]. The increase in the domain size by the decrease in the flow rate in Fig. 2.3(c) and the decrease in the

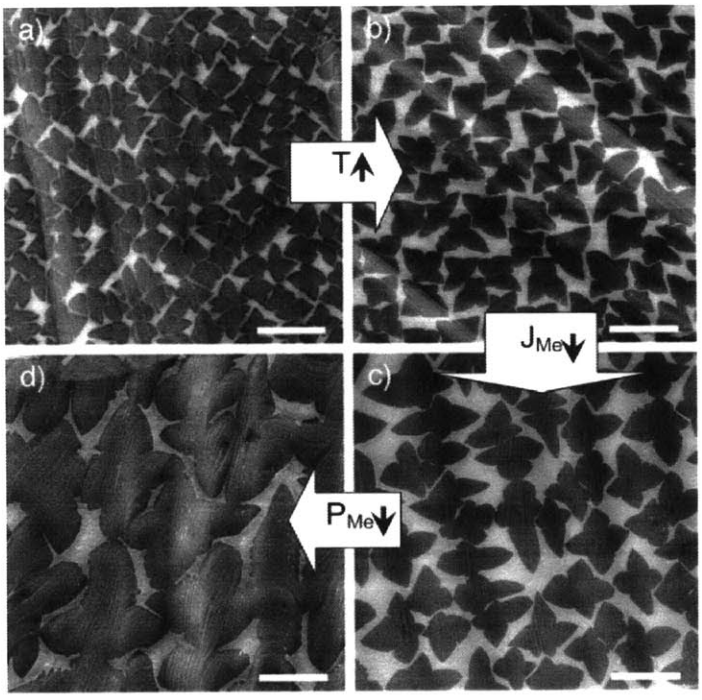

Figure 2.3 Scanning electron microscope (SEM) images of partially grown graphene flakes on a Cu foil with respect to different variations of the process parameters. The nucleation density obtained at a given condition (a) was decreased by (b) an increase in temperature (T), (c) a decrease in the flow rate of CH_4 (J_{Me}) and (d) a decrease in the partial pressure of CH_4 (P_{Me}). Scale bars are 10 μm. Reprinted with permission from [8]. ©2010 American Chemical Society.

partial pressure in Fig. 2.3(d) can be accounted for by the promoted adatom attachment through surface diffusion and the suppressed supersaturation, respectively. However, this strategy to have a large domain size by decreasing the supersaturation can fail to achieve a full coverage of graphene over a substrate.

Therefore, the growth step can be modified by a two-step process that aims at achieving a continuous graphene growth with a large domain size. In the first step, a low flow rate and a low partial pressure of hydrocarbon gas are provided at a high temperature in order to nucleate graphene islands with a low density. In the subsequent growth regime, by increasing both the partial pressure and the flow rate, gaps among domains are filled up and, finally, a continuous graphene layer with a full coverage over a substrate can be obtained. Since no further nucleation is expected as long as the temperature is fixed, the second regime only contributes to the growth of each domain by adatom attachment. This is an example showing how the quality of graphene can be controlled by adjusting the process parameters of CVD without any special additional treatment, thereby giving rise to the improvement in the material properties.

2.2.3 The role of hydrogen in the graphene growth

For a silicon thin-film deposition by the CVD process using silane (SiH_4) as a precursor, flowing hydrogen together with silane has an influence on the deposition rate of silicon by controlling the desorption rate of hydrogen decomposed from the silane [12]. This gives rise to a change in the dominant kinetics at a given growth temperature. For a graphene growth process by CVD, however, the role of hydrogen typically fed in all the steps is different to some extent. Hydrogen introduced in the heating and annealing step is related to the cleaning of the surface of the substrate. Since a Cu foil has a native oxide, hydrogen reduces this oxide in the heating and annealing step to expose the catalytic Cu surface. In the growth step, hydrogen also participates in the surface reaction beyond the role of a diluent gas for a hydrocarbon precursor. The effect of hydrogen on the graphene morphology is shown in Figure 2.4 [13]. Regardless of whether the ambient pressure was of the AP or LP type, a shape evolution of the graphene domain was observed with respect to the partial pressure of hydrogen in the growth step. Together with

this shape evolution, the graphene domain size also has a dependency on the partial pressure of hydrogen as shown in Fig. 2.4, and the maximum point for the grain size can be understood from the dual role of hydrogen in the surface reaction: *i.e.* as a catalyst to dehydrogenate hydrocarbon and as an etching reagent for carbon atoms.

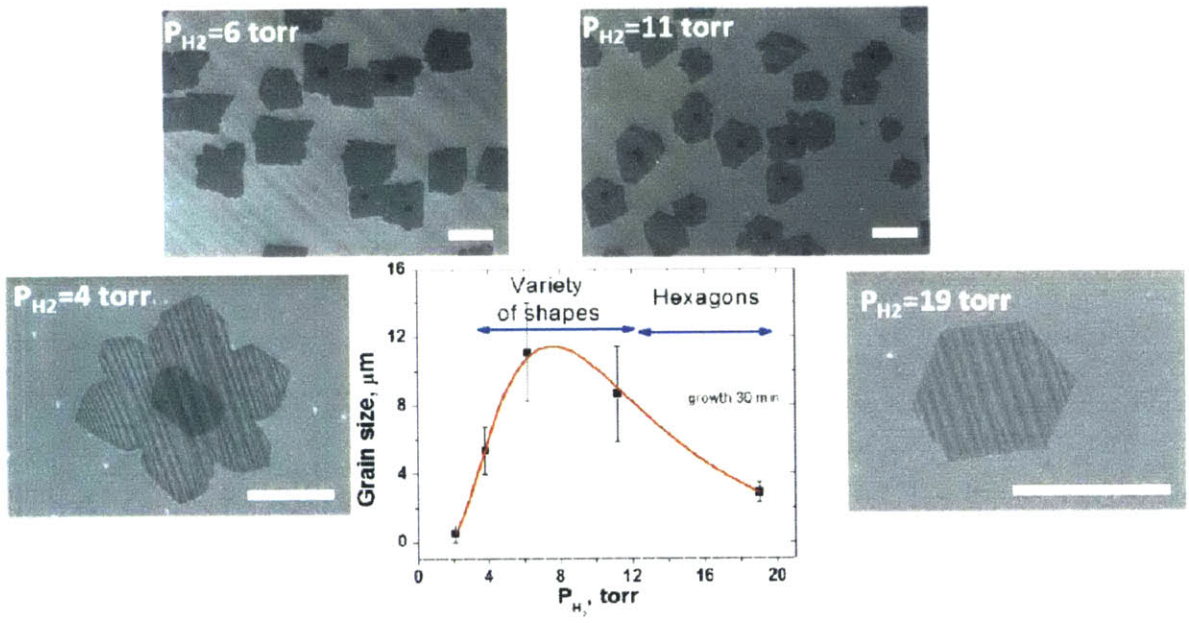

Figure 2.4 SEM images of partially grown graphene flakes with respect to various values of the partial pressure of hydrogen in a LPCVD graphene growth process. With the increase in the partial pressure of hydrogen, a maximum point of the domain size (grain size) of graphene was observed and a further increase in pressure led to the evolution of the domain shape to a hexagon. Reprinted with permission from [13]. ©2011 American Chemical Society.

A first-principle calculation of the graphene growth on a Cu substrate using CH_4 as a precursor indicates that the simple direct decomposition of hydrocarbon,

$$CH_4(g) \xrightarrow[Cu]{} C(s,\ graphene) + 2H_2(g) \tag{2-1}$$

is unlikely to happen, because this thermal decomposition is a thermodynamically unfavorable

endothermic process and the corresponding activation energy is also very high, even if Cu is employed as a catalyst [14].

Therefore, one should consider more complicated reactions, including stepwise dehydrogenating reactions of hydrocarbon and hydrogen-induced reactions. According to models [11, 13], hydrogen plays the role of a catalyst to dehydrogenate CH_4 and agglomerate one another as given by,

$$(CH_4)_{Cu} + H^*_{Cu} \Leftrightarrow (CH_3)_{Cu} + H_2 \tag{2.2}$$

$$(CH_3)_{Cu} + graphene \Leftrightarrow (graphene + C) + H_2 \tag{2.3}$$

Although the thermal dehydrogenation of CH_4 is unfavorable, the decomposed active hydrogen atom (H^*) can provide a relatively facile route for CH_4 dehydrogenation on the Cu surface, leading to the formation of an active hydrocarbon species. Since these active species, CH_x (x<4), are unstable, they are subsequently dimerized, forming stable graphene flakes. Numerical calculations [11] also predict that there is a threshold for the partial pressure of hydrogen (p_{H_2}) for the nucleation of graphene in the LPCVD process using Cu as a catalyst. However, the further increase in p_{H_2} can lead to a decrease in the growth rate of graphene. This effect is due to the etching reaction of carbonaceous materials by hydrogen expressed as,

$$H_{Cu} + graphene \Leftrightarrow (graphene - C) + (CH_x)_{Cu} \tag{2.4}$$

The model accounts for this speculation by correlating the p_{H_2} with the shape evolution of the graphene islands. When a sufficiently high p_{H_2} is applied, the shape of the graphene islands appears to be hexagonal. This was attributed to the equilibrium between the graphene growth and graphene etching, *i.e.* the dual role of hydrogen. Therefore, not only are other process parameters, such as the partial pressure of the hydrocarbon source, its flow rate, and the growth temperature, but also the p_{H_2} is one of the factors to determine the size of graphene domain and the coverage of graphene over a substrate.

The preparation of MLG in large area by CVD is not as challenging as one might expect. Without a

special treatment, uniform MLG over a substrate can be obtained by simply flowing CH_4 as a hydrocarbon precursor over a commercial Cu foil as a substrate at a high temperature of around 1000 °C. Due to its self-limiting growth characteristics, there is a fairly wide process parameter window to obtain MLG on Cu by LPCVD process. However, to achieve high quality CVD-G material with materials properties close to Exf-G requires careful tuning of the growth parameters and good understanding of the growth mechanism. Better understanding of the growth of graphene is also essential for predicting behaviors when one tries to modify the growth process, *e.g.* by the use of plasma to decrease the process temperature [15] or the introduction of different types of carbonaceous precursors beyond CH_4 [16, 17].

2.3 Synthesis of graphene on a Cu foil

2.3.1 Introduction

Cu is the most widely used catalyst material to grow uniform MLG in large area. Cu has a negligible carbon solubility [18], so that graphene formation *via* segregation of carbon from Cu substrate can be mostly neglected. At a typical graphene growth temperature around 1000 °C, the carbon solubility of Cu is remarkably as low as ~0.0006 at. % [18], while the carbon solubility in other metals, for example, Ni, Pd, Co, and Pt is comparable one another, as ~1.1 [19], 3.5 [20], 1.3 [20] and 0.7 [20] at. %, respectively. Figures 2.5 (a)-(b) show the binary phase diagram of carbon with Cu [18] and Pt [21], respectively.

It is also intriguing to correlate the surface state of the Cu substrate with the graphene morphology. A typically used Cu substrate is a polycrystalline foil with the purity of 99.8% or higher and with a thickness of 25 μm or thicker. A Cu thin film is generally not preferred because when the substrate is heated up to a temperature of around 1000 °C, dewetting in the film by surface diffusion takes place easily since the melting point (T_m) of Cu is 1085 °C. Since the graphene growth on a Cu substrate starts from a heterogeneous nucleation process, it is hypothesized that the microstructure of the Cu substrate, such as the crystallographic orientation or the grain size of Cu, could play a role in the graphene growth. The interaction between the graphene and the Cu substrate in terms of the crystallographic orientation has

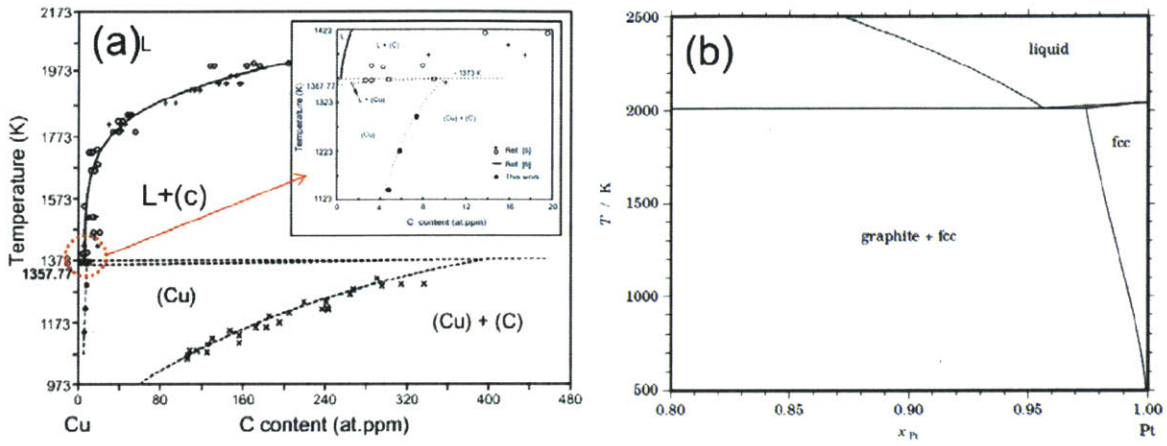

Figure 2.5 (a) The Cu-C phase diagram. Cu-rich region is highlighted as shown in the inset. Reprinted with permission from [18]. ©2004 Acta Materialia, (b) Pt-C phase diagram. Reprinted with permission from [21]. ©1969 Springer.

been studied by examining the shape of the graphene islands that are formed, as explained below.

The lobe shape of the graphene islands, typically observed in LPCVD and in an ultrahigh vacuum (UHV)-CVD process, was attributed to the discrepancy between the in-plane texture of the six fold graphene and the (100)-texture of a Cu foil prepared by the rolling process [22]. The shape evolution from the lobe shape to a hexagonal shape was also explained by the degree of the interaction between the graphene and the Cu substrate; the strong interaction in the LPCVD gives rise to a lobe-shaped graphene, whereas little interplay occurs with the Cu in the APCVD process, in which case, the mass transport of the precursors is more important and gives rise to a hexagonal shape [23, 24]. As well as the determination of graphene islands, an electron-backscattered diffraction (EBSD) analysis showed a close packed plane of Cu, *i.e.* a (111) plane led to preferentially form a uniform MLG with a high growth rate. Since Cu provides surface sites to CH_4 for decomposition, relatively denser carbon plane, (111) appears to more actively promote the nucleation and growth of graphene than other Cu planes [25].

Through examination of experimental results, it turns out that the grain boundary of Cu is generally not a preferred nucleation site for graphene growth, and in many cases, it was observed that the graphene

islands were growing across the grain boundary of Cu [26]. This observation contradicts the common expectation that normally the grain boundary serves as a location of nucleation sites. On the other hand, impurities segregated on the surface, or structural irregularities (along the rolling line) have been observed as more effective nucleation sites. It is thus important to minimize these active sites because the presence of such sites will contribute to both an increase in the nucleation sites density and smaller graphene domain sizes. Although it was reported that the graphene sample grown on a Cu foil with higher purity (99.9995%) showed better performance than graphene grown from a lower-purity (99.98%) Cu foil [27], nevertheless the high-purity Cu foils are costly. Rather, it is much easier to clean and prepare the Cu foil with chemical treatment, high temperature annealing and/or electrochemical or chemical–mechanical polishing before the CVD synthesis. Acetic acid has been used to remove copper oxides [28] on the foil surface. And a substantial improvement of the graphene morphology from multilayer to monolayer graphene has also been reported by using an electropolished Cu foil [3].

2.3.2 Toward the large domain size

2.3.2.1 Motivation

As stated earlier, one intrinsic defect in the graphene prepared by most CVD processes is the domain boundary created by the graphene growth. The domain boundary contributes to the inferior properties of CVD-G relative to Exf-G. As long as graphene is not epitaxially grown, the formation of domain boundaries in the CVD process is unavoidable, because as graphene nucleate on the substrate, they can be of different orientations and when they meet one another, they stitch up incommensurately due to their random in-plane orientation. Since these boundaries are basically atomic imperfections of carbons [29], the electric carriers responsible for in-plane electronic [5] and thermal transport [6] in the graphene layer can be scattered across the boundaries, thereby reducing carrier mobility. In addition, mechanical failure by in-plane tensile stress can also occur along the domain boundaries [7]. The carrier scattering effect by the domain boundary has already been experimentally observed in both indirect and direct ways. For a

continuous graphene sample with the different areal density of domain boundaries, the resulting carrier mobility across the in-plane graphene layer could be described as a function of an average domain size of the graphene when they were fabricated as field effect transistor (FET) devices. As expected, an improved carrier mobility value was observed in graphene with a larger domain size [30]. The direct observation of the impinging role of a domain boundary for electronic transport was provided in discontinuous graphene flakes [31].

As illustrated in Figure 2.6 [5], the resistivity obtained from four-point probe measurements showed a noticeable difference for transport occurring in the intra-domain as compared to the inter-domain region transport, depending on whether or not a domain boundary is involved in the conduction. While values of 2 kΩ $sq.^{-1}$ and 0.40 kΩ $sq.^{-1}$ were deduced for the resistivity from the current–voltage (*I-V*) characteristics in the intra-domain regions, higher resistivity values of 5 kΩ $sq.^{-1}$ were obtained in the inter-domain region, which confirmed the importance of scattering by domain boundaries for electronic transport. Therefore, in order to achieve high-mobility devices, we concluded that it is necessary to prepare graphene with a domain size as large as possible.

For the Cu-mediated graphene CVD process, the size of the graphene domains is directly connected to the nucleation density during the growth. In this respect, a number of efforts have been made to increase the domain size by modifying the process parameters [8, 13, 32-34]. Yan *et al.* [32] suggested criteria to adjust the parameters to achieve a mm-sized domain size in 11 growth conditions as presented in Table 2.1. Referring to E7 condition in Table 2.1, firstly the Cu surface should be clean and flat so that researchers can perform electopolishing on the Cu foil and can anneal it for a long time (7 hours) at high pressure (~2 atm) under a hydrogen ambient. Second, in the growth step, a high temperature as 1077 °C, and a low CH_4 to H_2 ratio of flow rate, such as 0.15 to70 sccm, respectively, contributed to the largest domain size. Further dilution of CH_4 failed to result in graphene nucleation, and this failure appears to be due to insufficient supersaturation. Furthermore, the change of the ambient pressure led to the shape evolution of the graphene domain from a square shape to a hexagonal shape.

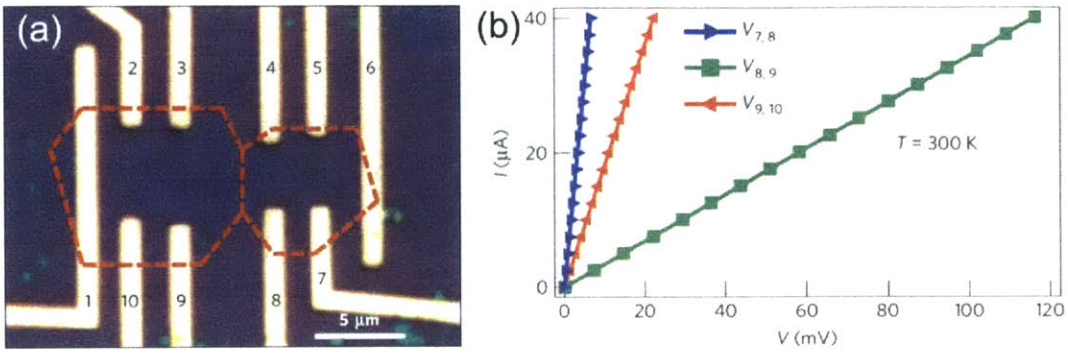

Figure 2.6 (a) Optical image of a device with multiple electrodes (1–10) contacting two graphene domains forming a boundary in between (indicated by dashed lines). (b) *I–V* curves measuring the inter-domain region (green) across the boundary and the intra-domain region (blue and red) inside a single domain. Reprinted with permission from [5]. ©2011 Nature Publishing Group.

Apart from the control of the process parameters, the modification of a Cu foil was also attempted. This approach involved several efforts, including one experiment where a Cu enclosure system was used [35] and the approach which used molten Cu at a growth temperature above the melting point of Cu (1085 °C) [36]. I took advantage of the former method because the process was amenable to the challenge and the resulting domain size was effectively as large as a sub-mm scale.

2.3.2.2 Sub-mm scale domain size of graphene *via* a Cu enclosure

After Li *et al.*'s method was tried [35], a Cu enclosure prepared by folding the foil was attempted as a graphene substrate, as presented in Figure 2.7(a). The experimental goal was to obtain a graphene sample with a domain size as large as possible, after the criteria provided in sec. 2.2.2.1, growths were performed at slightly high growth temperatures and with the low flow rate of CH_4/H_2 gases. In order that the Cu not to be evaporated at this high growth temperature, a thick Cu foil (127 μm, 99.9%, Alfa Aesar) was used. To make the Cu surface clean and flat, the foil was electropolished, at first with a 75% vol. % of phosphoric acid for 30 min by applying 2V. Then, the foil was folded with a plier into an enclosure.

Table 2.1 Eleven growth conditions (E1–E11) carried out in an experiment with different growth conditions

Sample	E1	E2	E3	E4	E5	E6	E7	E8	E9	E10	E11
Cu polishing	No	No	Yes	Yes	Yes	Yes	Yes	Yes	Yes	Yes	No
t_A(hr)	0.5	0.5	7	7	7	7	7	7	7	7	7
P_A (Torr)	8.2	8.2	1500	1500	1500	1500	1500	1500	1500	8.2	1500
U_{H2_A} (sccm)	500	500	500	500	500	500	500	500	500	500	500
T_{A-G} (°C)	1060	1060	1060	1060	1070	1075	1077	1077	1077	1077	1077
U_{CH4} (sccm)	5	0.15	0.15	0.15	0.15	0.15	0.15	0.3	0.3	0.15	0.15
t_G (min)	1	15	70	80	110	120	125	90	125	15	20
P_G (Torr)	8.2	8.2	8.2	108	108	108	108	108	108	108	108
U_{H2} (sccm)	500	70	70	70	70	70	70	150	200	70	70
Domain size (mm)	~0.015	~0.03	~0.3	~0.4	~1	~1.8	~2.3	~0.1	None	~0.1	~0.2
Domain shape	square	square	square	hexagon	hexagon	hexagon	hexagon	hexagon		hexagon	hexagon

t_A , P_A, U_{H2_A}, T_{A-G}, U_{CH4}, t_G, P_G, and U_{H2} denote the annealing time, total pressure in the annealing step, the flow rate of H_2 in the annealing step, the temperature in the annealing and growth step, the flow rate of CH_4 in the growth step, growth time, total pressure in the growth step, and the flow rate of H_2 in the growth step, respectively. E7 condition that resulted in the largest domain size provides an optimal condition with a clean Cu surface a high growth temperature and a low CH_4 concentration. The shape evolution appears to be attributed to the partial pressure of H_2 as discussed earlier. Adapted with permission Ref. [32]. ©2012 American Chemical Society.

As a result of the LPCVD process performed in this structure, sub-mm scaled single crystalline graphene domains could be obtained inside the Cu foil, over a range of process windows, as shown in Fig. 2.7(b)-(e). The morphology of the graphene grown on the outside surface of the enclosure was not significantly different from what is typically obtained in a LPCVD process, although the formation of FLG was observed to be more prequent. In fact, this aspect has provided an insight into developing a process to grow BLG [37].

On the other hand, a sub-mm scaled domain size on the inside the surface should then be extraordinary, while the one on a flat Cu foil with the same growth condition is producing a graphene sample of ~μm. According to Eq. 2.5, 2.6, and 2.7, the nucleation rate is sensitively related to the supersaturation, namely, the partial pressure of CH_4. The diffusion coefficient of C in Cu is reported to be 4.35×10^{-9} cm^2 s^{-1} at 920 °C [38], while the one of hydrogen in Cu is 2.0×10^{-4} cm^2 s^{-1}at 900 °C [39]. These data lead to an estimate of the diffusion length of carbon coming from the outside for one hour to be ~40 μm, which is less than the thickness of Cu by one order of magnitude. However, considering the Cu foil is poly-crystalline, it is reasonable that the origin of carbon formed inside the foil is through the foil by bulk diffusion.

The environment inside this pseudo seamless Cu pocket would be totally different from a flat Cu foil. For the discrepant diffusivity in Cu, the concentration of CH_4 inside is much lower than outside, by ~1000 times [37]. Thus, the nucleation rate becomes remarkably sluggish, so that only a few μm sized nuclei were sporadically found after 15 min of flow of CH_4 as indicated by arrows in Fig. 2.7(b). Note that typically it takes 10 min to complete the graphene growth with a full coverage over a flat Cu foil. Once nucleation happens, the nuclei deplete adjacent carbon species. Thereby the lowered carbon concentration only contributes to the growth of each domain without further nucleation. The low nucleation density inside the foil, therefore, favored the growth of large domains in a continued growth process, as shown in Fig. 2.7(c). We thus obtained a record graphene domain size up to 1 mm shown in the inset in Fig. 2.7(c). Besides, a dependency on the CH_4 flow rate was observed. As presented in Fig. 2.7(d)-(e), the increase of

CH_4 flow rate by twice increased the graphene growth rate, leading to full graphene coverage over the Cu. This behavior was consistent with the earlier two-step growth introduced in Fig. 2.3.

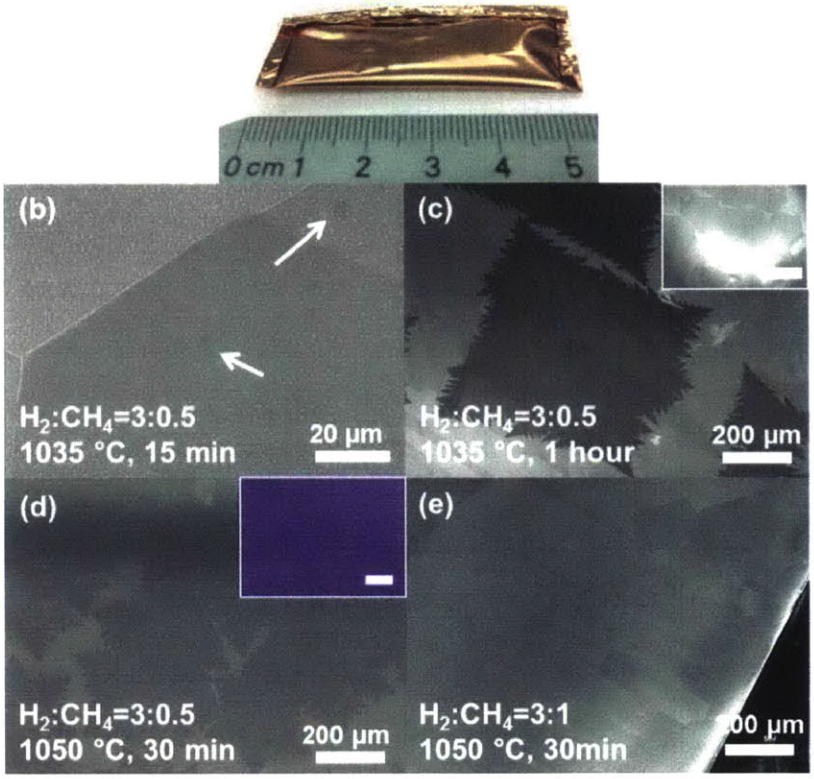

Figure 2.7 (a) Cu enclosure prepared by folding a foil. (b)-(e) SEM image of as-grown graphene on the inside of a Cu enclosure with respect to the growth conditions. Inset to (c) is a low magnification image of (c) (scale bar: 1 mm). Inset (d) is an optical microscope image of graphene (d) That was transferred onto a SiO_2/Si substrate (scale bar: 50 μm). Note that graphene fully covered over the Cu in (e).

- Device characteristics

A domain size of a few hundreds of μm is sufficiently large to fabricate a device without involving domain boundaries. Since it is of interest to compare the electric properties of a single crystalline graphene flake with a poly-crystalline graphene sheet, both of the graphene samples were transferred onto

a target substrate using a poly (methyl methacrylate) (PMMA)-supported wet transfer method [2]. The poly-crystalline graphene sheet was synthesized using a typical Cu-mediated LPCVD process (growth pressure: ~1.6 Torr). The target substrate was a thermally oxidized 300 nm-thick SiO_2 on a heavily p-doped Si. The detailed transfer process will be presented later in this thesis. As a result, intact graphene flakes were prepared on the substrate as shown in Fig. 2.7(d) inset. Subsequently, each graphene sample was patterned by electron beam (eBeam) lithography and metallized with an evaporated Ti/Pd/Au thin film through a lift-off process. Finally, graphene FET devices with the dimension of 10 μm by 20 μm were fabricated. The electrical properties were characterized with by applying back gate biases using a semiconductor parameter analyzer (Agilent 4155C) in an ambient air at room temperature. During the measurements, the source-drain bias (V_{DS}) was maintained at 100 mV. As figures of merit to assess the quality of graphene, The Hall mobility (μ_{Hall}) was extracted through Hall measurements in each graphene FET device where the current was set to 1 μA and the magnetic field of 4230 Gauss was applied. The electrical characterizations in this thesis work were performed with these fabrication and measurement processes, except the characterization in sec. **4.2.2.**

In graphene, there are multiple scattering mechanisms that limit the carrier mobility of graphene in transport. The overall mobility, μ, can be expressed via the Matthiessen's rule [40]:

$$\mu^{-1} = \mu_{CI}^{-1} + \mu_{LD}^{-1} + \mu_{EP}^{-1} \qquad \text{(Eq. 2.8)}$$

where μ_{CI}, μ_{LD}, and μ_{EP} denote the limitation of mobility by charged impurity, lattice disorder, and electron-hole scattering in graphene, respectively. The charged impurity scattering is related to the long-range ordered Coulombic interaction of graphene with polar substances residing either on graphene surface or the substrate surface underneath. This effect is carrier density-dependent and is verified by the shift of the Dirac point. The second scattering mechanism by lattice disorder is arising from the short range-ordered distortion of sp^2-carbn structure in graphene. This distortion is carrier density-independent and can be characterized through a notable increase in I_D/I_G. In particular, the domain boundary of CVD-G serves as a scattering center in this type of scattering mechanism. Finally, it is known that the electron-

phonon scattering mechanism becomes dominating when the other mechanisms are eliminated at lower temperatures than RT. In particular, phonons of a polar substrate like SiO_2 can produce local charge puddles that scatter charge transport in graphene.

Figure 2.8 shows the results of the electrical characterization. As expected, while the value of μ_{Hall}, 2401.3±273.4 $cm^2\ V^{-1}s^{-1}$ was obtained in the poly-crystalline continuous graphene samples, a far greater value of μ_{Hall}, 7414.1±928.8 $cm^2\ V^{-1}s^{-1}$ was gained in single crystalline graphene devices. In terms of the scattering mechanism, we can exclude the third scattering mechanism by the electron-phonon scattering because the transferred substrates were identical in this case as a SiO_2/Si substrate. Obviously, the single crystalline graphene device was free from the lattice disorder scattering by excluding the domain boundaries inside each device. Furthermore, considering the measurement was carried out in an ambient air, it should be taken into account that the polar adsorbates are likely to adhere on the domain boundaries of graphene. Since the domain boundaries are atomically imperfective sites, the poly-crystalline graphene sample can become more doped by this adsorption reaction than the single crystalline graphene sample.

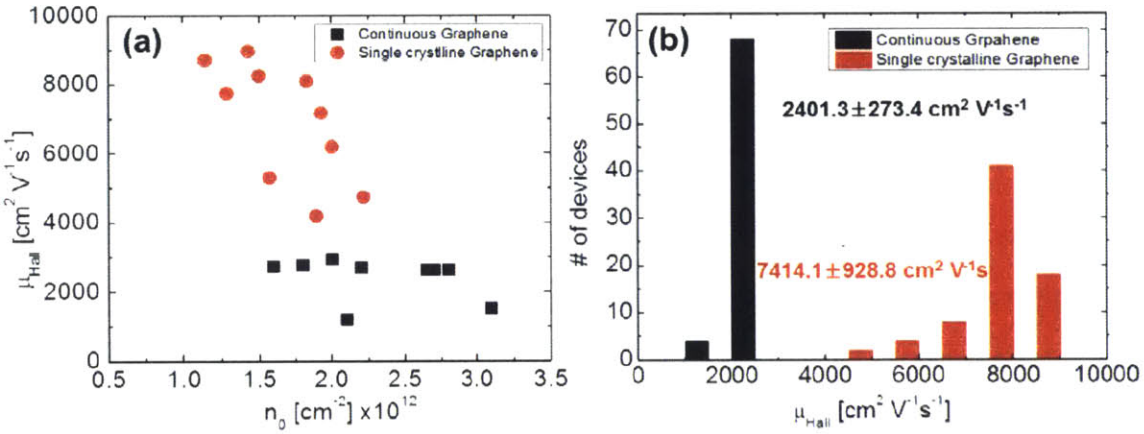

Figure 2.8 (a) Carrier density and the corresponding μ_{Hall} of 10 devices of each continuous graphene samples and single crystalline graphene flakes. (b) Entire μ_{Hall} of the fabricated FET devices of each continuous graphene samples and single crystalline graphene flakes. The average values of μ_{Hall} of each type of graphene FET devices are included.

The relatively wider distribution of carrier density in the poly-crystalline graphene sample, as indicated in Fig. 2.8(a), supports the scattering mechanism combined by both the charged impurity and the lattice disorder because the density of domain boundaries in the poly-crystalline graphene sample can be different from device to device. Hence, through the improvements of both the carrier scattering mechanisms, the increase of carrier mobility more than 300 % was resulted in the devices fabricated with a single crystalline, big domain graphene sample.

2.3.2.3 Conclusion

It has been desired to increase the domain size of graphene because the domain boundaries serve as scattering centers in carrier transport, thereby reducing the carrier mobility. In terms of the CVD process parameters, the criteria to increase the domain size were discussed. In the following, an experiment to obtain sub-mm sized single crystalline domains was attempted by using a Cu enclosure. The large graphene domain was only dissimilarly observed inside the enclosure. This was understood as arising from an extremely low CH_4 concentration inside. Remarkably, the carrier mobility obtained in this big graphene domain was about 3.1 times larger than in a continuous graphene sample that would contain domain boundaries. It is true that the Cu enclosure in this study is not practically suitable for manufacturing applications. Nonetheless, if this Cu enclosure is regarded as a virtual chamber surrounded by Cu walls, I believe that an analogous graphene growth system similar to the Cu enclosure could be developed beyond the demonstration level.

2.3.3 Hydrogen-excluded atmospheric chemical vapor deposition (APCVD)

2.3.3.1 Introduction

The Cu-mediated LPCVD process can produce MLG material without a special effort because the growth process is likely to be self-limiting. On the other hand, there have also been various attempts to synthesize graphene under atmospheric (AP) conditions as in general APCVD is easier and cheaper to

implement than LPCVD. MLG was only obtained when highly diluted CH_4 (ppm) gas was used for the growth [2, 3]. In this work, by investigating the graphene growth mechanism and the role of hydrogen in the APCVD process, it was found that when hydrogen is excluded in the growth process, the surface reaction becomes the rate-limiting step of the APCVD process, thereby leading to the preferred formation of MLG. Further investigations were carried out to elucidate this understanding. The quality of these MLG films was found to be better than the typical LPCVD grown MLG through electrical characterization and an etch pit density method.

2.3.3.2 Experimental

The general process of the graphene synthesis by the APCVD process followed the one in Fig. 2.1. A 25 μm-thick Cu foil (99.8%, Alfa Aesar) was used as a growth substrate and the graphene growth temperature was 1000 °C. Apart from a LPCVD process, the exhaust line was connected to an ambient air outlet. Besides, Ar gas was additionally supplied as an inert diluent. To investigate the effect of hydrogen in the growth process, four types of graphene samples were prepared depending on whether there was exposure to H_2 in each of the four steps: heating, annealing, growth, and cooling step. In the meantime, the flow rate of Ar was fixed during all the steps. The detailed composition of gases for sample preparation is given in Table 2.2. The four conditions are labeled as A1–A4, in which A1 corresponds to having H_2 in all steps (''H_2_In_All''), A2 corresponds to not having H_2 in the growth step, but having the other three steps (''H_2_NOTIn_Growth''), A3 corresponds to excluding H_2 in all the four steps (''H_2_Excluded''), whereas A4 corresponds to having H_2 only in the growth step but not the other steps (''H_2_ONLYIn_Growth''). After the synthesis finished, the samples were transferred onto either a 300 nm-thick SiO_2/Si substrate or to transparent boron silicate substrates for analysis with a PMMA-supported wet transfer process [2].

2.3.3.3 The morphology of graphene samples transferred on a SiO_2/Si substrate

Figure 2.9 shows the optical microscope (OM) images of four graphene samples (transferred on a SiO_2/Si substrate) prepared with a different H_2 feedstock as indicated in Table 2.2. It is remarkable that a coarse multilayer graphene was obtained when H_2 was flowed in all the synthesis steps (Fig. 2.9(a), the A1 condition in Table 2.2) while a pristine monolayer graphene was observed when H_2 was completely excluded from the process (Fig. 2.9(c), the A3 condition in Table 2.2). The equivalent number of layers was calculated by measuring the transmittance of the samples transferred onto a transparent boron silicate substrate. Since the specific transmittance of the sample by the A3 condition was 96.5% at 550 nm of the wavelength, a graphene monolayer was estimated to identify this sample. Although this value is a little lower than the theoretical value for a monolayer, 97.7% [41], this small discrepancy appears to be due to wrinkles formed upon the cooling step [42] or defects on the graphene such as some polymer residue remaining on this sample by the transfer process.

Table 2.2 Graphene samples prepared by the APCVD process with a different composition of gases.

H_2:CH_4:Ar (sccm)	Heating	Annealing	Growth	Cooling
A1: H_2_In_All	50:0:500	50:0:500	50:3:500	50:0:500
A2: H_2_NOTIn_Growth	50:0:500	50:0:500	0:3:500	50:0:500
A3: H_2_Excluded	0:0:500	0:0:500	0:3:500	0:0:500
A4: H_2_ONLYIn_Growth	0:0:500	0:0:500	50:3:500	0:0:500

On the other hand, the sample A1 has 85.9% of the transmittance at the same wavelength which corresponds to 5–6 eq. layers of graphene [42]. Both of the samples by the A2 and A4 conditions seemed to have a smaller numbers of graphene layers than the sample by the A1 condition; however, as depicted by Fig. 2.9(b) and (d), three samples were not monolayer graphene. The general trend could thus be divided into two aspects. First, in Fig. 2.9(a)-(b) where H_2 was fed in the heating and annealing steps, multilayer graphene formed aligned to the rolling line of the Cu foil. In contrast, in Fig. 2.9(c)-(d) where H_2 was excluded in both of the steps, such a directional arrangement of the multilayer graphene was not observed. The effect of hydrogen in the cooling step was also investigated by transposing the H_2 flow in

the cooling step with the conditions in Table 2.2; very interestingly, no noticeable deviation from Fig. 2.9 was observed under these conditions.

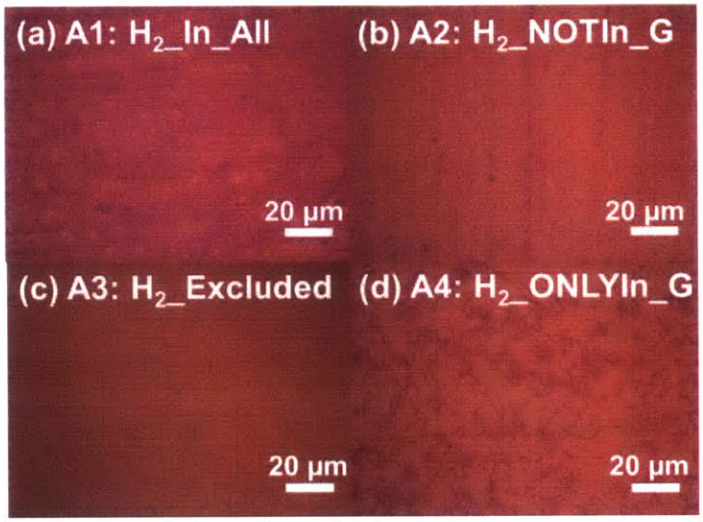

Figure 2.9 OM image of transferred graphene samples on a SiO_2/Si substrate. The compositions of flow gases for (a)–(d) are corresponding to A1–A4 in Table 2.2, respectively.

2.3.3.4 The morphology of Cu foils with different annealing treatments

Since these morphologies might be associated with the surface of a Cu foil underneath, we attempted to confirm how hydrogen assists morphological changes in the Cu surface. Cu foils were taken out of the reactor right after the annealing step (the two conditions studied here are: annealing with H_2 and Ar used in A1, A2, and annealing with Ar only used in A3, A4). A Cu foil annealed under LP was also separately prepared. The corresponding OM and atomic force microscope (AFM) height images are presented in Fig. 2.10(a–h), respectively.

As expected, the surface of an as-received Cu foil with rolling lines on the surface (Fig. 2.10(a) and (e)) was smoothened after annealing under LP (with Fig. 2.10(b) and (f), showing the rms roughness change from 9.4 nm to 0.83 nm). The aspect of the morphology change of the Cu surface after annealing under AP was more notable. While the formation of voids or hillocks aligned with the pattern was

observed in the H_2 and Ar annealing under AP (Fig. 2.10(c) and (g)), the Cu surface annealed with Ar only under AP (Fig. 2.10(d) and (h)) showed a flat surface with an rms roughness of 1.82 nm. (This slightly higher roughness than the one annealed under LP was attributed to the local faceting shown in the inset of Fig. 2.10(h)). The same bumpy topography in Fig. 2.10(c) and (g) also resulted in other annealing experiments carried out with a diluted H_2 concentration (0.1% in vol.) or in using forming gas (5% H_2 in N_2) under AP. This suggested that the roughening of the Cu surface should be related to the H_2 flowed in during the heating and annealing steps under AP.

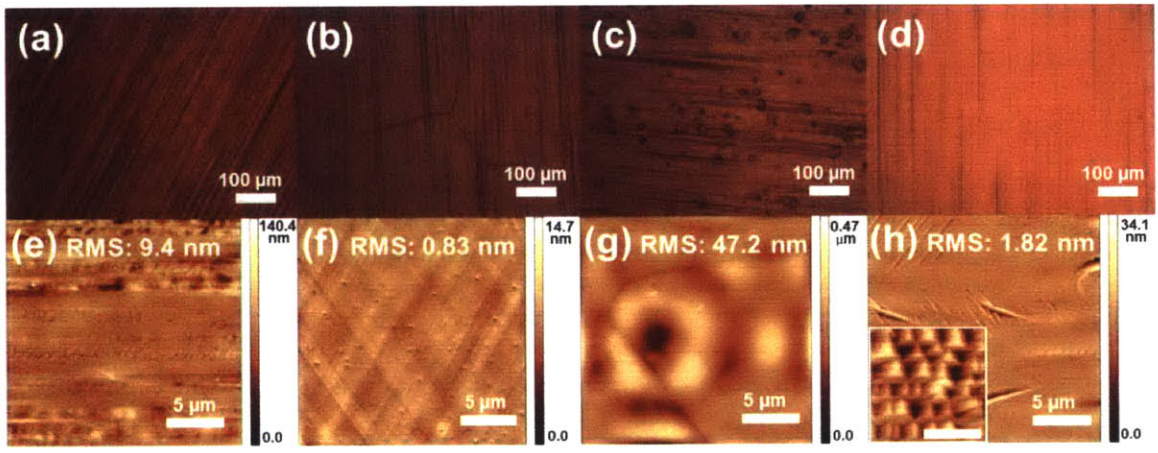

Figure 2.10 (a)–(d) OM image of Cu foils treated under different conditions. (a) as-received, (b) after annealing under LP with H_2 only, (c) after annealing under AP with H_2 and Ar, and (d) after annealing under AP with Ar only. (e)–(h) are the corresponding AFM height images of (a)–(d), respectively. The scale bar of inset (h) is 500 nm.

At this stage the mechanism of how H_2 under AP caused the Cu foil to be rougher in the annealing step is not completely clear, but there are two possible explanations: H_2 embrittlement by degassing [43] and surface diffusion. The H_2 embrittlement develops with Cu or Cu alloys during annealing with H_2. When the H_2 reacts with O_2 existing as a form of CuO_x, the resulting water vapor can have high vapor pressure at the sites where this reduction reaction happens since the vapor molecules cannot diffuse

through the metal. In the end, these sites are replaced by voids and cracks. The annealing condition of both A1 and A2 was within the reported H_2 embrittlement condition [43] In addition, although the Cu foil used in the experiment was 25 μm-thick, the roughening by the surface diffusion should also be considered because not only that the Cu was poly-crystalline, but the annealing temperature was close to the T_m of Cu, 1085 °C.

Finally, it should be noted that there was no change in crystallographic orientation of the Cu foil, regardless of the annealing condition. This Cu foil in all cases exhibited a preferred orientation along [100], confirmed by X-ray diffraction (XRD).

2.3.3.5 Self-limiting growth characteristics of the hydrogen excluded APCVD process

There was no noticeable change in topography of the foil shown in Fig. 2.10 at the end of the cooling step. Note that the Fig. 2.10 was obtained after the annealing step. Therefore, the graphene morphology under each growth condition could be associated with the surface feature of Cu that evolved during the annealing. First, multilayer graphene aligned to the rolling direction, as shown in Fig. 2.9(a)-(b), could be attributed to the rough foil surface caused by the H_2 introduction in the heating and annealing step. The expectation that a rougher substrate surface will give rise to form more multilayer graphene can be understood by the postulation regarding a dominant kinetics. In other words, the general rate-limiting step of the APCVD is not the surface reaction on the Cu, but rather the mass transport from the bulk region to the surface region [2]. Furthermore, the graphene growth under APCVD is not self-limiting (in contrast to LPCVD), so that the roughness on the surface can cause a different boundary layer thickness, and thus the growth rate is not uniform over the substrate. Therefore in this kinetic regime, the process is sensitive to the surface feature, thereby leading to form multilayer graphene through an accumulated nucleation along the rolling direction [3].

In contrast to this, when a typical LPCVD (1.70 Torr) was performed with the same type of rough Cu foil (*i.e.*, annealed with H_2 and Ar under AP, Fig. 2.10(c) and (g)), MLG resulted from the growth, as

shown in Figure 2.11(a). The optical transmittance here was 96.5%, consistent with the results from sample A3 in Fig. 2.9(c). This is because the kinetics of the LPCVD process is dominated by the surface reaction on the Cu surface, and the graphene growth is self-limiting [2]. Thus, the effect of surface feature turned out to be not so important. This allowed our understanding that the dependence of the Cu roughness on the morphology of graphene is arising from the growth kinetics. In this respect, it was elucidated how a uniform MLG can be obtained under the A3 condition, through the hydrogen-excluded APCVD process. Interestingly, as can be seen in Fig. 2.11(b), when the Cu foil with the rough surface of Fig. 2.10(c) was used for A3 condition, we also obtained a close-to-MLG material with a trace amount of multilayer flakes. This suggested that the hydrogen-excluded growth likely has similar growth kinetics to the LPCVD growth, that is, a surface reaction limiting growth process.

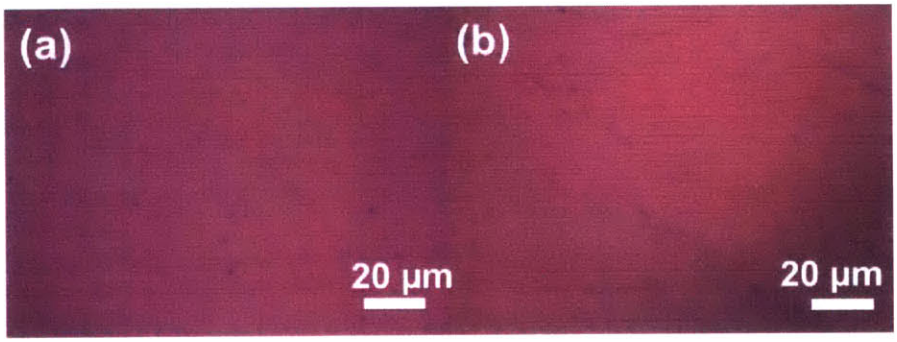

Figure 2.11 OM image of transferred graphene samples on a SiO_2/Si substrate. The graphene was synthesized by using a Cu foil with a rough surface as shown in Fig. 2.10(c) where (a) the LPCVD condition was applied and (b) the A3 condition (hydrogen-excluded APCVD) was applied.

Since the graphene synthesis by a typical APCVD growth process is generally found not to be self-limiting, the formation of multilayer graphene more than a single layer is probable. One sensitive parameter to determine the number of graphene layers in an APCVD process is the CH_4 concentration, or more precisely, the partial pressure of CH_4. Consequently, the most successful strategies to achieve MLG

in APCVD were to employ an extremely low CH_4 concentration on a highly flat Cu surface [2, 44]. However, the results we obtained here suggested that the hydrogen-excluded APCVD process had a different kinetic barrier from that in a usual APCVD process. In order to gain further understanding on this behavior, the concentration of CH_4 was first varied, by fixing the A3 growth conditions.

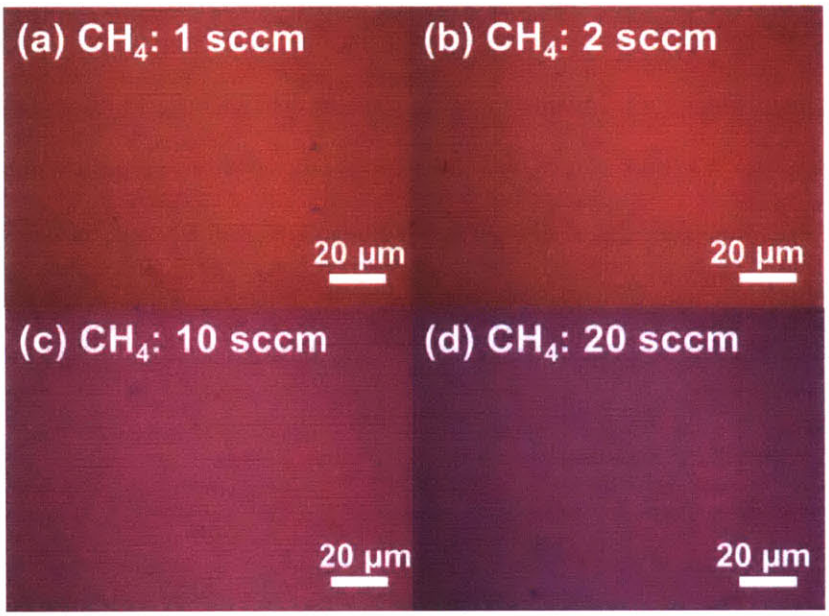

Figure 2.12 OM image of transferred graphene samples on a SiO_2/Si substrate. The samples were prepared by applying the A3 condition where hydrogen was excluded in all the steps, and by varying the CH_4 flow rate. The flow rate of CH_4 feedstock of (a)–(d) is, 1, 2, 10, and 20 sccm, respectively.

Although the CH_4 flow rate changed by 1, 2, 10, and 20 sccm, there was no significant difference in the resulting morphology, but MLG was commonly obtained like in Fig. 2.9(c), as shown in Figure 2.12(a)-(d). This was contrasted with a previous APCVD result [2] that the graphene morphology was highly sensitive to the CH_4 concentration. Conversely, the graphene growth in the hydrogen excluded process appears to have a self-limiting nature even though it was carried out in AP. It should also be noted that within the experimented CH_4 concentration range, a "conditioned" quartz tube, whereby a thin Cu

layer was deposited on the inner wall by a LPCVD process helped in obtaining a uniform MLG reliably. Together with the result of Fig. 2.11(b), the experiment gives further evidence that the kinetics of the hydrogen-excluded APCVD was mainly dominated by the surface reaction. In other words, it can be inferred that by excluding hydrogen in the APCVD process, the dominant kinetic barrier is converted from the mass transport of gas molecules to a surface reaction, like the decomposition of CH_4.

2.3.3.6 Understanding of the growth mechanism of the hydrogen-excluded APCVD process

- The investigation of the domain shape of graphene samples at the initial growth stage

To confirm this change of the main kinetic regime by using hydrogen, the domain shape of graphene was investigated by ceasing the growth within a short time, before the coalescence of nuclei. First, SEM images of graphene grown on a Cu foil for just 3 min with the A1 and A3 conditions are shown in Figure

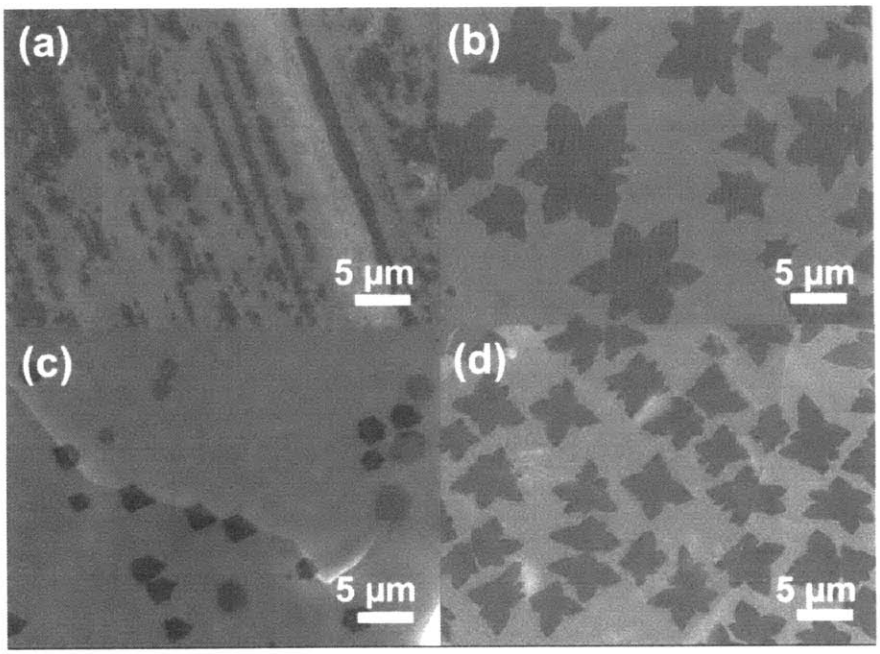

Figure 2.13 SEM image of partially grown graphene on a Cu foil. (a)-(b) graphene grown for 3 min with the A1 and A3 conditions, respectively. (c)-(d) graphene grown on a 127 μm-thick Cu foil for 5 min with the A1 and a LPCVD condition, respectively.

2.13(a) and (b), respectively. Figure 2.13(c) and (d) show other partially grown graphene samples on a 127 μm-thick Cu foil (127 μm, Alfa Aesar) for comparison. Like the one in sec. 2.2.2, this thick foil was electropolished in advance by a 75 vol. % phosphoric acid. The graphene shown in Fig. 2.13(c) was obtained after 5 min of growth time, where a similar reactor condition to A1 was applied. Fig. 2.13(d) was taken after 5 min growth of the LPCVD process at 1035 °C with H_2 and CH_4.

As can be seen in Fig. 2.13(a), in the partially grown graphene with A1, the domain shape was not distinguishable, but instead flakes aligned to the rolling direction were observed. This directional growth continues across the Cu grain boundaries. The observation here that nucleation prevailed on rough sites along the rolling line is consistent with the understanding that the dominant rate-limiting step for this condition (A1) was the mass transport of gas molecules. In this sample, because the nucleation density was too high, the shape of the graphene flakes could not be recognized. Thus, a highly flat and clean Cu foil was prepared by an electrochemical polishing process (rms roughness: 1.5 nm) as a growth substrate. When the similar growth condition to A1 was applied to this foil, mostly hexagon-shaped graphene nuclei were observed as shown in Fig. 2.13(c). In order to minimize the roughening effect by H_2, the annealing step was skipped in this process.

On the other hand, the partially grown graphene in the hydrogen-excluded process showed a lobe-shape with six folds, illustrated in Fig. 2.13(b). In other attempts, four-fold morphology was also observed. Furthermore, as compared to Fig. 2.13(c) grown for 5min, the size of each nucleus was much larger in spite of the shorter growth time of 3 min; besides, the nuclei density was also low. These characteristics were consistent with the partially grown graphene in Fig. 2.13(d) prepared by a LPCVD process.

In the meantime, there have been reports on the domain shape of graphene grown by Cu-mediated CVD [5, 8, 13, 22-24]. Generally, a hexagon-shape was commonly observed in the APCVD [5, 23, 24], as in Fig. 2.13(c), while lobe-shaped dendritic morphology was noted in the LPCVD [8, 22] like in Fig. 2.13(d). The hexagonal shape was interpreted as an equilibrium form for correlation with the hexagonal

atomic structure of graphene. To account for this morphology, little effect from the Cu substrate on a graphene flake was considered [23] and a low enough initial growth rate was suggested as a process requirement [24]. In contrast, the lobe shape shown in the LPCVD was attributed to the different crystallographic symmetry between a four-fold (100) Cu substrate and a six-fold graphene flake [22]. Although the shape of the graphene flakes appear to be influenced by many different factors, such as pressure [23], choice of substrate [22], H_2/CH_4 ratio [13], the similar domain shape between the A3 condition and LPCVD suggested that the growth kinetics of both are alike each other, as discussed earlier.

- The role of hydrogen in hydrogen-excluded APCVD

Vlassiouk *et al.*[13] provides insights to understand the role of hydrogen in the APCVD. It was found that no matter whether the growth ambient is AP or LP, the shape of the nuclei could evolve from a random shape into a hexagonal shape with an increase of H_2 concentration, as shown in Fig. 2.4. For the growth under AP, they used a highly diluted CH_4 (30 ppm) in Ar [13]. In that regime, hydrogen serves both as an auxiliary catalyst and as an etchant for graphene, leading to form a hexagonal shape by the balance between these two roles with sufficient hydrogen concentration.

In fact, our APCVD process appeared to be outside the regime discussed by Vlassiouk *et al.* in the respect of having excessive CH_4 concentration. Nevertheless, much light is shed upon the current result from the discussion there. It is known that without H_2 in the reaction mixture, CH_4 has to chemisorb on the Cu surface to form active carbon species to produce graphene. Such dehydrogenation reactions are not thermodynamically favorable, thus constituting the rate limiting step [14]. As a result, the growth kinetics of A3 (hydrogen-excluded growth) becomes surface reaction-limited. The insensitivity of the graphene morphology to the Cu surface feature is one of the proofs of this interpretation. The hexagonal shape was favored in the kinetically mass transport-limiting regime where a lower interaction between graphene and Cu was expected [23, 24]. On the other hand, the lobed shape or the dendritic shape was mostly observed

in the kinetically surface reaction-limiting regime, where the graphene growth along a specific direction could be limited by an interaction with the Cu [22].

2.3.3.7 The characterization of the electrical properties along with a graphene passivated etch test

Finally, the electrical properties of a MLG grown by the A3 condition (A3-graphene) were investigated. A MLG sample grown by a LPCVD process (LPCVD-graphene) at P=1.70 Torr was used for comparison. 1 cm^2 sized each graphene sample was transferred onto a SiO_2/Si substrates for a four-point probe measurement. For the A3-graphene, the extracted sheet resistance and mobility were 289.8 Ω $sq.^{-1}$ and 1271.8 cm^2 $V^{-1}s^{-1}$, respectively, while for the LPCVD-graphene, the corresponding values were 305.3 Ω $sq.^{-1}$ and 825.9 cm^2 $V^{-1}s^{-1}$, respectively. Further measurements consistently exhibited relatively better performances in the A3-graphene samples.

Furthermore, a graphene passivated etch test was carried out to evaluate the openings in the graphene film [45]. The technique was simple that a Cu etchant (Transence APS-100) droplet was brought onto an as-grown graphene flakes on a Cu foil using a plastic pipette. After 5s, the drop of etchant was rinsed

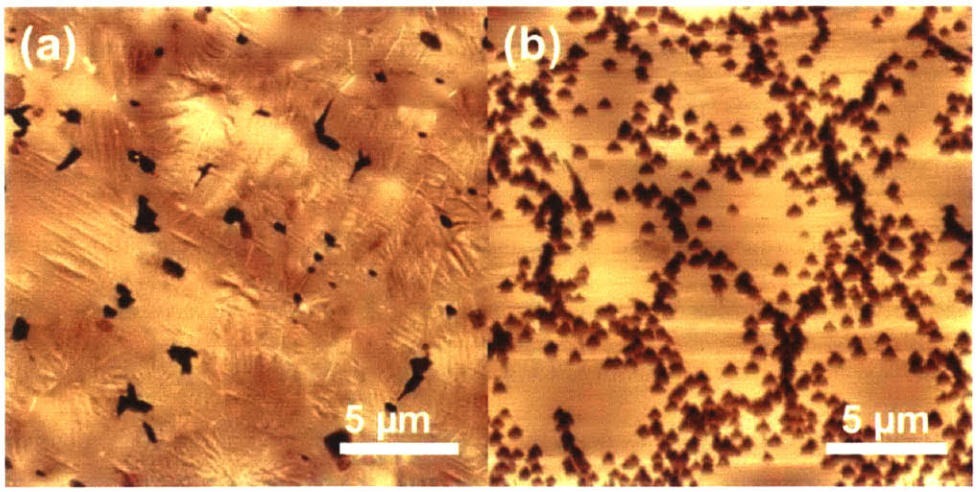

Figure 2.14 AFM height image taken after a graphene passivated etch test on a Cu foil. (a) A3-graphene, (b) LPCVD-graphene showing a higher density of the etch pits and their clustered location.

away with deionized (DI) water and the sample was quickly dried by blowing compressed N_2. Figure 2.14(a) and (b) show the results of this etching test conducted on an A3-graphene and a LPCVD-graphene on a Cu foil, respectively.

Remarkably, the etch pits were commonly observed, although the density of pits in Fig. 2.14(a) was much lower than in Fig. 2.14(b). This observation informed us that the graphene grown by the CVD process is basically not possible to perfectly passivate the Cu surface, different from the expectation [46]. The origin of these pits was attributed to an incomplete coverage of graphene [8] or to nanoparticles presumed to be an oxide [13]. Since structural defects can be regarded as the most sensitive factor to the process conditions, the difference of the density of etch pit shown in Fig. 2.14 could be correlated with the domain size to a certain extent. In fact, the distribution of etch pit in Fig. 2.14(b) appeared to form borders between distinct regions, but no certain evidence was yet found that these regions actually denoted the graphene domains. Nevertheless, it is still valid that the lower density of structural irregularities observed in the A3-graphene indicates a better graphene quality. Together with a relatively larger domain size shown in Fig. 2.13, this etch test result supports a higher electrical property of the A3-graphene than that of the LPCVD-G.

2.3.3.8 Conclusion

In conclusion, the graphene morphology grown by the APCVD process was investigated with respect to the hydrogen introduction in each synthesis step. Remarkably, a pristine MLG resulted when the simplest condition was applied where hydrogen was excluded in all the synthesis steps. This morphology variation of graphene was understood by identifying the role of hydrogen in APCVD. The multilayer graphene formed was attributed to the combination of surface roughening of Cu by hydrogen-induced annealing and the mass transport-limiting kinetics in the growth. On the other hand, a pristine MLG observed in the hydrogen-excluded process appeared that the dominant kinetics is surface reaction limiting, which is similar to LPCVD. This was confirmed by comparing the domain shapes of various

partially grown graphene samples. We concluded that the shape of the nuclei for growing MLG was closely associated with the dominating kinetics determined by hydrogen in the APCVD, refining a previous report on the role of hydrogen. Finally, we obtained a better quality of the graphene prepared by the hydrogen-excluded APCVD process than the MLG obtained by a typical LPCVD, as verified by material characterization. This process development in the present work is expected to provide a simpler way to synthesize high quality graphene in large area.

2.4 Characterization of nucleation sites of graphene

2.4.1 Introduction

As stated earlier, one of the factors lowering the electric properties of CVD-G compared to Exf-G is the existence of domain boundaries that scatter electrons and holes which transport charges [5]. This domain boundary as an atomic imperfection also deteriorates the thermal [6] and mechanical [7] properties of graphene. Therefore, researchers working on improving the transport properties of graphene have attempted to prepare CVD-G with a domain size as large as possible, aiming for a mono-domain single sheet of graphene in the end. Apart from such efforts, however, a simple method to determine the size of each domain is still needed. In this regard, there can be two approaches to measure the domain size of graphene. One is to directly observe through microscopy (e.g. TEM [29], STM [47]) and the other is to indirectly estimate. The former approach can obtain the structural information of a given CVD-G sample exactly, but has an aerial limit to implement because the typical domain size of CVD-G is several μm-scale while microscopy allows analysis on the hundreds of nm scale at most. The latter approach takes advantage of the relative crystallinity or defectiveness of CVD-G. For example, Raman spectroscopy mapping obtained on a single crystalline graphene flake shows a relatively high I_D/I_G on both its edge and nucleation site, implying that these are more defective [5]. However, this indirect method can be a misleading interpretation in a continuous graphene sample because as well as the boundaries and

nucleation sites, graphene wrinkles and PMMA residues left by the transfer process can also show a high I_D/I_G [26].

We have attempted in this thesis to develop a method to directly determine the graphene domain size suitable for typical CVD-G samples. Three main hypotheses were assumed. First, each domain has one nucleation site. Second, the domain sizes will have the same length scale as the distance between nucleation sites. Finally, the nucleation sites will be more susceptible to a chemical reaction than the surrounding crystalline region. Based on these, I applied a simple chemical treatment, oxidation, to a transferred graphene with different coverages and domain sizes. As a result, each nucleation sites of graphene domains could be optically pointed out, which resulted in agreement with the Raman spectroscopy results.

2.4.2 Experimental

Four types of MLG samples with different domain sizes and coverages on a 25 μm-thick Cu foil (99.8%, Alfa Aesar) were prepared using LPCVD. The domain size was controlled *via* the H_2/CH_4 ratio and the growth temperature after following the criteria provided in sec. 2.2.2. Single crystalline graphene flakes were obtained by stopping the growth in minutes before merging the flakes together while continued growth resulted in a continuous graphene sample. Table 2.3 shows the growth conditions of each sample.

Table 2.3 Four types of samples with respect to the domain size and coverage and their growth conditions

Sample	**Big/Partial**	**Big/Full**	**Small/Partial**	**Small/Full**
H_2: CH_4 (sccm), Growth temperature (°C)	5:2, 1035	5:2, 1035	50:20, 1000	50:20, 1000
Growth time (min)	5	10	2.5	40
Domain size (μm)	20	20	5	5
Coverage over Cu	Partial	Full	Partial	Full

The graphene samples grown on a Cu foil were transferred onto a SiO_2/Si substrate with the established PMMA-supported wet transfer method [2]. The final step of the transfer process was to peel off the PMMA by atmospheric annealing in H_2/Ar for two hours at 500 °C. As can be seen in Figure 2.15, for both of the partially grown single crystalline graphene flakes, there was no change in the graphene morphology after transfer. All the experiments and analyses in this section were performed with the transferred graphene samples on the SiO_2/Si substrate.

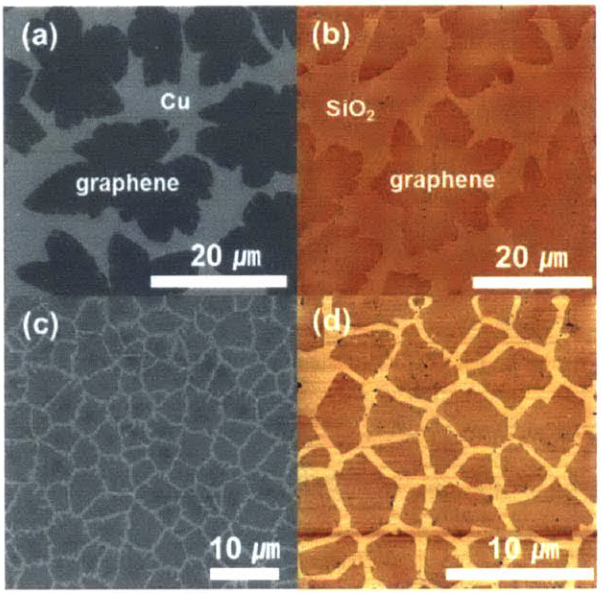

Figure 2.15 (a)-(b) SEM image of a Big/Partial graphene on a Cu foil and the corresponding AFM phase image after being transferred onto a SiO_2/Si substrate, respectively. (c)-(d) SEM image of a Small/Partial graphene on a Cu foil and the corresponding AFM phase image after the graphene was transferred onto a SiO_2/Si substrate, respectively.

2.4.3 Preliminary results

2.4.3.1 Setting up an oxidation condition

First, preliminary experiments were carried out to set a condition to bring on a structural morphology change in graphene. As a reference sample, the Big/Partial samples shown in Fig. 2.15(b) were selected.

As a chemical treatment, the oxidation of graphene was considered. Graphene itself is chemically stable in an ambient environment, but the formation of CO_2 by the reaction with O_2 is spontaneous,

$$C(s)+O_2(g) \longrightarrow CO_2(g), \quad \Delta H = -393.51\,\text{kJ mol}^{-1}\ (25°C) \tag{2.5}$$

Since the use of O_2 plasma can cause a severe structural modification, the change of the graphene morphology was monitored by annealing the samples in air at elevated temperatures.

As illustrated in Figure 2.16, each flake began to burst in the center when annealed at 500 °C, which feature was the most prominent with a process time of 30 min in (g). The longer annealing time at 500 °C damaged adjacent regions shown in Fig. 2.16(h). Moreover, the annealing at a higher temperature than 500 °C resulted in etching away of whole graphene flakes, even though the annealing was conducted for a short time, less than 10 min. Therefore, the annealing condition was set to 500 °C for 30 min, which was consistent with the earlier method that was used to reveal the domain boundaries of graphene [48].

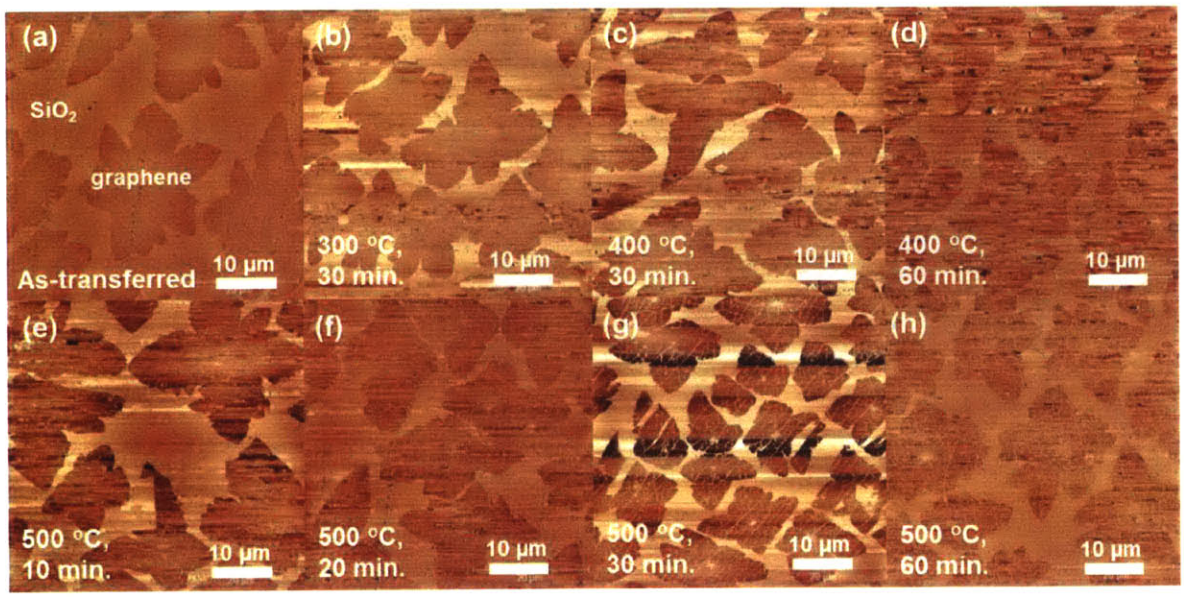

Figure 2.16 AFM height image of the preliminary oxidation results with respect to the heating conditions. Each graphene flake started to burst in the center at 500 °C while harsher oxidation conditions either damaged or etched away the flakes.

2.4.3.2 Morphology characterization

As a result of the annealing treatment, regions that looked like volcano craters were observed in the center of each flake. When this treatment was applied to a continuous graphene sample, not only *the craters*, but also sharp lines were observed. As can be seen in Figure 2.17(a)-(b), the morphology change of seemingly pristine graphene was generated by the annealing at 500 °C for 30 min. This behavior was similar to the previous result where experimented with a graphene sample transferred onto a mica substrate [48]. However, this was the first time that the creation of craters was found. In fact, these features were hardly seen in the AFM height image due to the atomically thin thickness of the graphene, while the AFM phase image, however, provided a distinctive contrast. Interestingly, some craters have unetched regions at the center, indicated by the white dotted circle in Fig. 2.17(b). These turned out to be BLG, and this will be discussed later in detail. The sharp lines surrounding craters were suspected since

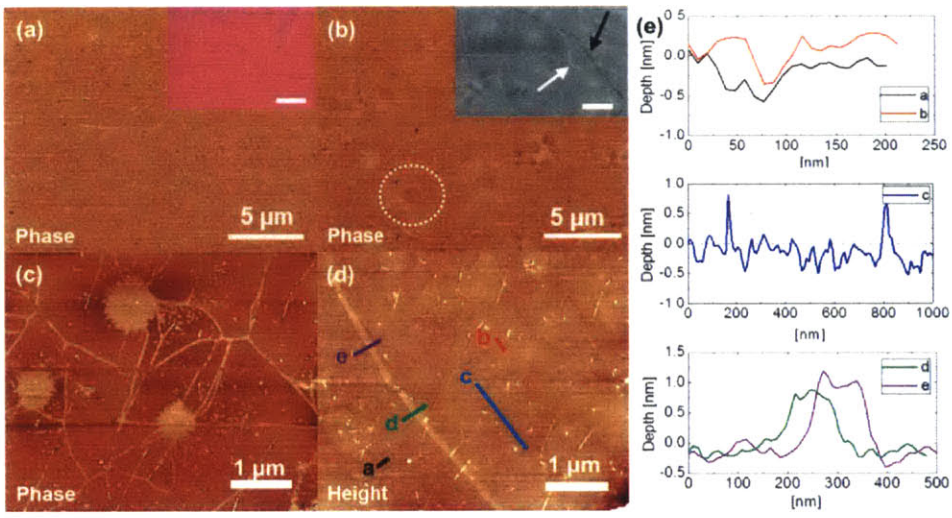

Figure 2.17 (a)-(b) AFM phase image of graphene on a SiO_2/Si substrate before and after an annealing treatment (500 °C, 30 min), respectively. The corresponding OM and SEM images are insets, respectively. (c)-(d) AFM phase and height images taken on a location in (b), respectively. (e) Height profiles of the selected regions in (d), showing a collapsed feature in a-c (line and crater) and a protruding feature in d-e (wrinkle). The scale bar insets in (a)-(b) are 20 μm and 2 μm, respectively.

graphene wrinkles typically formed during the growth and transfer process. The SEM image in Fig. 2.17(b), however, showed that these lines (indicated by the white arrow) were different from the wrinkle (indicated by the black arrow). Further AFM characterization in 2.17(c)-(e) confirmed that both of the lines (a-b in (d)) and lines (c in (d)) were proven to be empty spaces, *i.e.* a SiO_2 surface, which was clearly distinguished by the graphene wrinkles (d-e in (d)), showing higher topography.

2.4.4 Analysis with Raman spectroscopy

2.4.3.1 Partially grown samples

Based on the preliminary results, the morphology change of partially grown graphene with different domain sizes in Fig. 2.15 (b) and (d) were investigated. To explore the nature of the craters, Raman mapping was carried out in advance. First, for the Big/Partial sample, a location of interest was defined and characterized through OM and AFM, as shown in Figure 2.18 (a)-(b). Then, Raman maps that consist of a number of point Raman spectra were completed at the defined location. Considering that I_D is sensitive to the defectiveness of graphene [49], it was characterized with two types of Raman maps: I_D-I_{BKG}, the intensity subtraction of the background (I_{BKG}) from the D-band, and I_D/I_G as shown in Fig. 2.18(c)-(d), respectively. In this single domain, the Raman map showed a relatively high I_D-I_{BKG} and I_D/I_G on the edge of the domain and at the center. As indicated in Fig. 2.18 (e), the point Raman spectra also showed relatively higher I_D at the center (a-b in Fig. 2.18(d)) than in the adjacent region (c-d in Fig. 2.18(d)). Therefore, it was expected there was a defective region at the center of a single graphene domain.

The result of the annealing treatment at 500 °C in air for 30 min was in accord with this expectation from the Raman spectroscopy. Although the treatment on this sample was a little severe, it created a crater at the center of the defined domain as shown in Fig. 2.18(g). Not just in this domain, as shown in Fig. 2.19(f), every domain was found to have a crater at each center. Since a graphene domain started from one nucleation site, it is reasonable to presume that these craters correspond to nucleation sites. In other words, each nucleation site could be selectively verified on an OM scale.

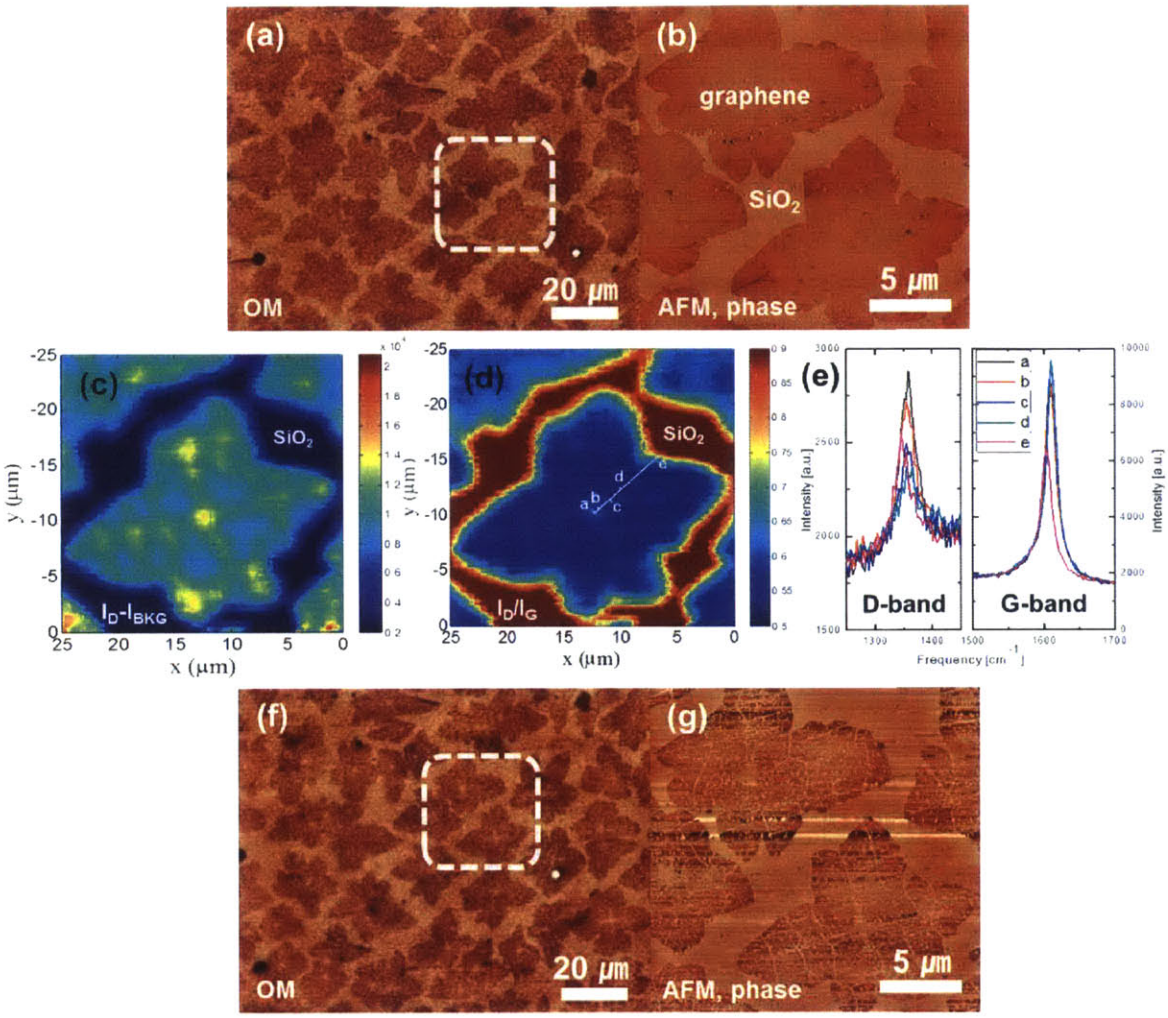

Figure 2.18 (a)-(b) OM and AFM phase images of a Big/Partial sample, respectively. (b) is the white dotted region in (a). (c)-(d) I_D-I_{BKG} and I_D/I_G of the Raman mapping performed on the bottom-right graphene flake in (b), respectively. (e) The point Raman spectra on the locations in (d) (a-e) in terms of the D-band and G-band. (f)-(g) OM and AFM phase images of a Big/Partial sample, respectively, after the annealing treatment at 500 °C for 30 min. (g) is the white dotted region in (f) and the identical location of (b). The OM images, (a) and (f), here were processed by a program (Gwyddion) to increase the contrast.

To confirm if the annealing treatment gave rise to the creation of one crater per one domain, the same

experiment was conducted on the Small/Partial sample. Like the Big/Partial sample, a region of interest in the sample was mapped through Raman spectroscopy as shown in Figure 2.19 (a)-(b). As a result, relatively high I_D/I_G at each domain center was observed. While the I_D/I_G at the center was indicated as yellowish in the map, the I_D/I_G at the most adjacent regions was presented as greenish. In other words, the Raman mapping confirmed that each domain owned a relatively defective region at the center, regardless of the domain size. Interestingly, the I_D/I_G at the center of some domains, on the contrary, was lower than in the adjacent regions, and is here indicated as bluish. It turns out in the AFM that these graphene domains contained BLG at the center.

In the same way as the Big/Partial sample, a location on the Small/Partial sample was defined as characterized with AFM shown in Fig. 2.19(c)-(d). The result of the annealing treatment at 500 °C in air for 30 min on this location was similar to the Big/Partial sample, creating a crater per each domain, as shown in Fig. 2.19(e)-(f). Therefore, it was believed that no matter what the domain size is, the center of domain is susceptible to oxidation due to the relative defectiveness and is regarded as the nucleation site. Besides, it was also noted that there were domains showing a different behavior, which contained BLG. The BLG was commonly located at the domain center and surprisingly, was not damaged by the annealing treatment, while the very adjacent region created a crater, indicated as a white arrow in Fig. 2.19(f).

This behavior in the BLG could be understood by examination through Raman spectroscopy. As can be seen in Figure 2.20 (a)-(b) and Table 2.4, the point Raman spectra of monolayer domain A and bilayer domain B were compared with mechanically exfoliated monolayer (Exf-MLG) and AB-stacked bilayer (Exf-BLG). Both Exf-MLG and Exf-BLG showed characteristic features: Exf-MLG has a high I_{2D}/I_G with a narrow 2D peak width, while Exf-BLG has a suppressed I_{2D}/I_G with a wider 2D peak [50]. In contrast, in the A and B locations, such features were reversed and moreover, both of the ω_G were highly blue shifted, implying a heavily doped area [51]. As stated earlier, the PMMA used as a supporting layer in the transfer process was removed by atmospheric annealing in H_2/Ar for two hours at 500 °C.

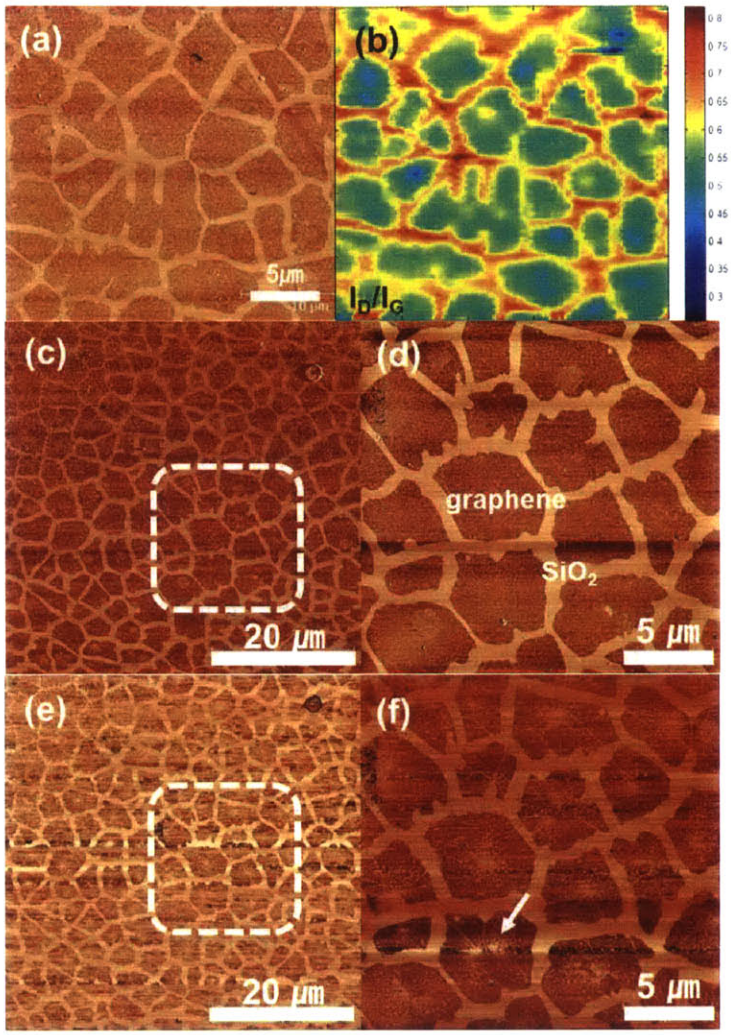

Figure 2.19 (a)-(b) AFM phase image of a Small/Partial sample and the corresponding I_D/I_G of the Raman mapping, respectively, (c)-(d) AFM phase image of a defined location in the sample. (d) is the white dotted region in (c), (e)-(f) AFM phase image of the same regions in (c)-(d), respectively, after the annealing treatment at 500 °C for 30 min.

Reportedly, the annealing process can give rise to the blue-shifted ω_G and a lowered I_{2D}/I_G by the interaction of graphene with the underlying SiO_2/Si substrate [52]. This behavior will be discussed more in detail in Chapter 4. Nonetheless, as presented in Table 2.4, the Raman characteristics of the BLG were different from those of the MLG to some extent, showing a relatively less blue-shifted ω_G and a higher

I_{2D}/I_G (indicated as red arrows in Fig. 2.20(a) and (c)), together with the highly suppressed I_D/I_G discussed with Fig. 2.19(b). Besides, from the shape of the 2D peak, different from that for an AB-stacked BLG, the stacking order of this BLG was regarded as turbostratic. Based on the assumption that the second graphene layer forms under the firstly synthesized layer [53], it can be speculated how the BLG was undamaged by the annealing treatment. First, graphene is nucleated on defective sites like impurities on a Cu foil. Depending on the growth condition, the second layer can form. In this case, the nucleation site for

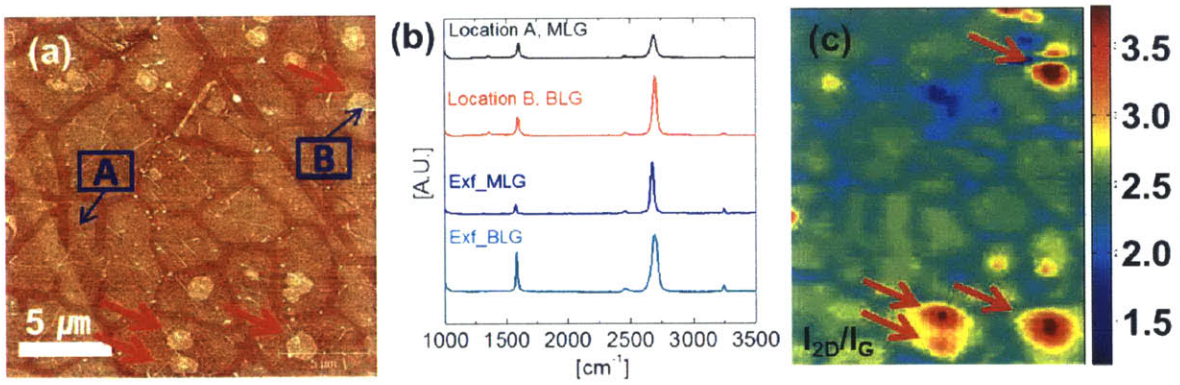

Figure 2.20 (a) AFM phase image of a Small/Partial sample (b) Point Raman spectra of A and B regions indicated in (a) together with spectra Exf-MLG and Exf-BLG. Corresponding values of ω_G, ω_2, and I_{2D}/I_G of each sample are provided in Table 2.4 below. (c) Raman map of I_{2D}/I_G obtained in (a) region, respectively.

the second layer will be the same as the sites where the first layer nucleated, because it is energetically favorable for this to occur. After transfer onto a SiO_2/Si substrate, the second layer passivates the interaction between the upper graphene layer and the SiO_2. Consequently, the upper layer can keep the original state, while adjacent regions were heavily doped during the annealing to remove PMMA. The BLG region shows a rather lower I_D/I_G than neighboring regions, as indicated in Fig. 2.19(b). In the end, this passivation by the second layer allows the graphene at the center to survive during the annealing

treatment. However, this relative stability of the BLG was not permanent. More severe conditions such as an annealing at 600 °C resulted in burning away entire graphene flakes.

Table 2.4 Values of ω_G, ω_{2D}, and I_{2D}/I_G of the point Raman spectra in Fig. 2.20(b)

	ω_G (cm^{-1})	ω_{2D} (cm^{-1})	I_{2D}/I_G
Location A, MLG	1607.3	2690.5	3.39
Location B, BLG	1600.5	2698.3	5.80
Exf_MLG	1581.3	2674.4	8.70
Exf_BLG	1584.5	2693.9	4.60

2.4.3.2 Fully grown samples

The goal of the experiment was to develop a method to measure the domain size of a given graphene flake without having any other information. One major assumption was that the domain size will have the same length scale as the distance between nucleation sites. To confirm the effectiveness of this annealing treatment, measurements on both Big/Full and Small/Full samples with full graphene coverage on a Cu foil were also attempted. As illustrated in Figure 2.21(a), it was impossible to figure out the locations of the domain boundaries or the nucleation sites from AFM characterization for a Big/Full sample. It was also hard to tell such sites through the I_D/I_G of the Raman map in Fig. 2.21(b) because the information from other defective sites like graphene wrinkles or PMMA residues were mixed together. However, by the annealing treatment in air, two craters, namely, nucleation sites were observed as shown in Fig. 2.21(c) and indicated as white arrows. It was obviously hard to predict both of the craters in the Raman map in Fig. 2.21(b). The length scale of the distance between the carters was consistent with the Big/Partial samples.

For a Small/Full sample, the Raman map fortunately revealed local defective sites selectively as shown in Fig. 2.21(e). As shown in Fig. 2.21(f), the following annealing treatment expectedly resulted in the creation of craters on the exact locations showing higher I_D/I_G. Furthermore, it was also intriguing to

find lines centering on the craters through a careful observation of the AFM image. It was thus reasonable to consider these lines as domain boundaries because such boundaries are also defective and thus would be susceptible to the oxidation in a similar manner to the nucleation sites. Certainly, the length scale of the distances among the craters was consistent with the Small/Partial samples. Therefore, it is worth noting that this method not just determines the domain size of a given graphene sample, but provides information about how each domain merges together with another domain by revealing the domain boundaries.

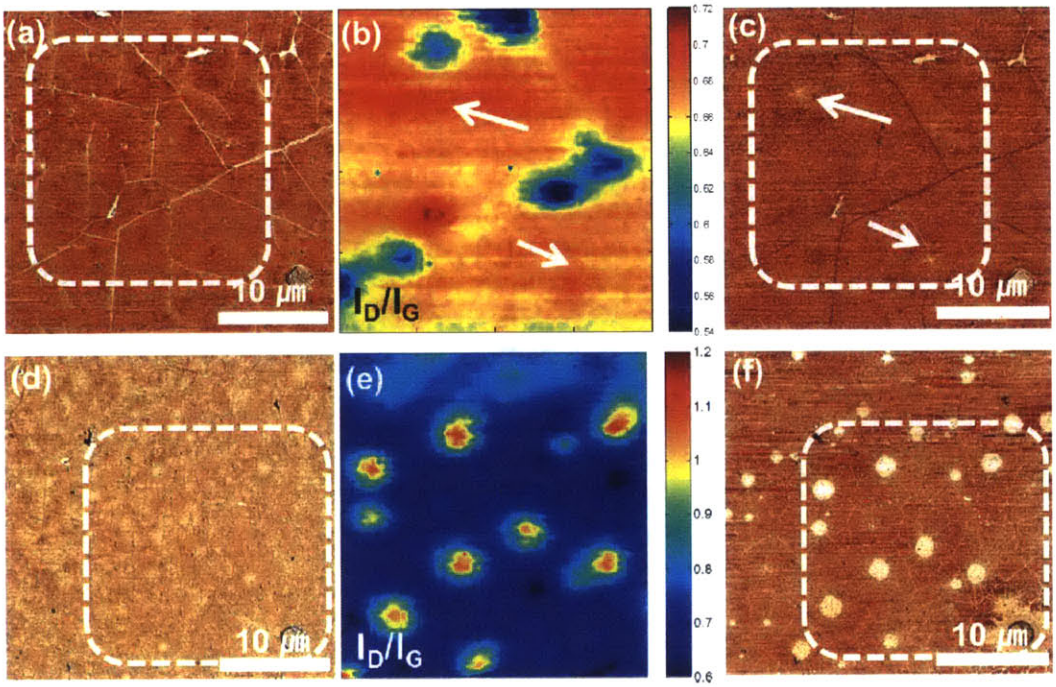

Figure 2.21 (a)-(b) AFM phase image of a Big/Full sample and the I_D/I_G of the Raman mapping performed in the white dotted region in (a), respectively, (c) AFM phase image of (a) after the annealing treatment at 500 ℃ for 30 min. (d)-(e) AFM phase image of a Small/Full sample and I_D/I_G of the Raman mapping performed in the white dotted region in (d), respectively, (f) AFM phase image of (d) after the annealing treatment at 500 ℃ for 30 min.

2.4.5 The nature of nucleation sites

Together with how to point out the nucleation sites, it is also worthwhile to study the nature of the nucleation sites. It has been widely observed that the nucleation of graphene has nothing to do with the grain boundary of a Cu foil. Instead, impurities like oxide particles can serve as a nucleation center [33]. In this respect, we attempted to find out if the nucleation center could be selectively located before transfer through the established graphene passivated etch test [45] using Big/Partial graphene samples on a Cu foil. As shown in Figure 2.22 (a)-(e), by using a droplet of a Cu etchant, each domain retained their own morphology, passivating the Cu underneath. Meanwhile, a bare Cu surface outside the domains continuously collapsed at the rate of ~8.5 μm/s. Interestingly, the center of each graphene flake was physically dimpled as illustrated in Fig. 2.22(f)-(g), but was not etched as the etch test continued. In other

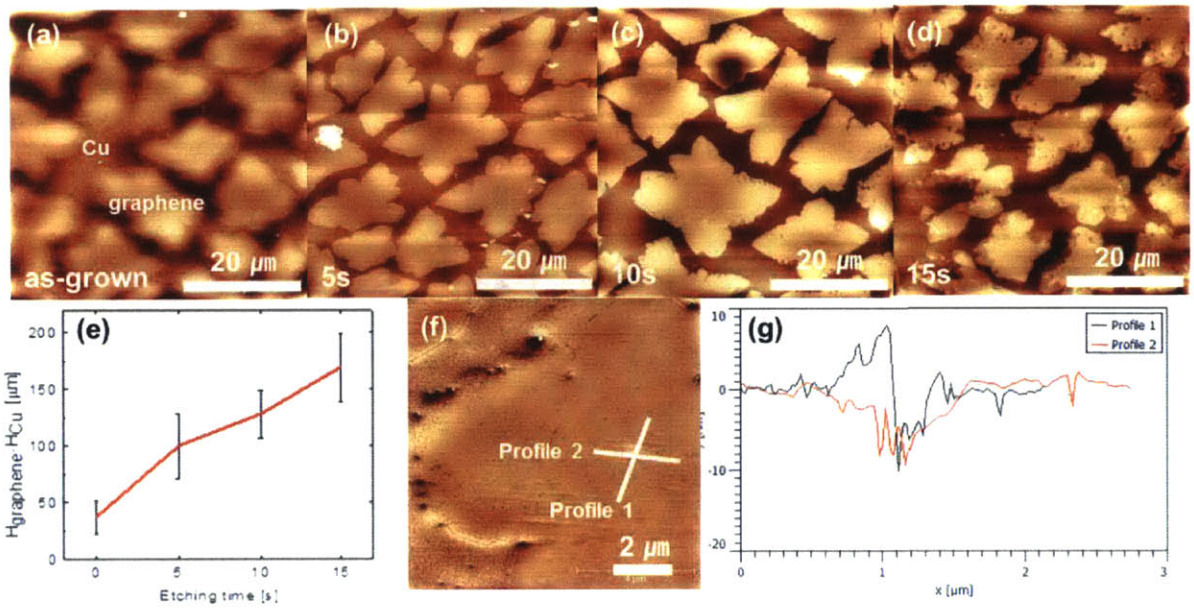

Figure 2.22 (a)-(d) AFM height image of the Big/Partial samples on a Cu foil with the graphene undergoing a passivated etch test for 0s, 5s, 10s, and 15s, respectively. (e) Corresponding height change of graphene relative to Cu by the test, (f) Highly magnified AFM height image of (a). (g) Height profile along the two lines in (f). The domain center was dimpled.

words, the nucleation sites were neither holes nor oxides in this case. As shown in Fig. 2.22(d), etch pits in graphene started to appear near the edge of the domains.

Hence, it is yet hard to figure out the nature of the nucleation on these microscopic scales. Although it will be quite challenging to locate the exact nucleation sites, a further TEM study would be expected to help elucidate the nucleation sites on the atomic scale.

2.4.6 Conclusion

A simple technique to measure the domain size of a graphene sample was developed. Instead of the direct observation of each graphene domain, an attempt was made to bring a morphology change selectively on to the nucleation sites to measure the distance between them. This information enabled us to estimate the domain size of the graphene sample with a similar length scale to the actual domain size. Assuming that each nucleation site will be more susceptible to an oxidation reaction, an annealing condition to selectively etch out nucleation sites was optimized in air. The experiments carried out on the graphene samples having different graphene coverage and domain sizes confirmed the effectiveness of this method, consistent with the Raman spectroscopy mapping tests.

2.5 Synthesis of graphene on a Pt foil

2.5.1 Introduction

Cu, more exactly, a Cu foil has known as the best substrate material to synthesize MLG in large area by using a CVD synthesis method. As well as its catalytic activity to promote the decomposition of hydrocarbon, negligible carbon solubility at the typical growth temperature at around 1000 °C prevented the formation of multilayer graphene in the cooling step by precipitation. However, wet-etching based transfer process of graphene grown on a Cu foil necessarily involves a hazardous Cu etchant containing Cu wastes at the end of the process. Thus, the cost of Cu-foil based graphene synthesis by CVD should include the discarding expense of the waste of Cu etchant as long as the Cu foil is not recycled.

Certainly, this drawback can be tackled by changing the transfer process by introducing either dry transfer [54] or (wet) bubble-transfer [55]. However, the dry transfer not only has a limitation of the target substrate that should be highly flat, but also results in yet inferior quality of the transferred graphene due to mechanically damages during the transfer. On the other hand, it is true that the bubble transfer method introduced in sec. **1.4.2** is environmentally more favorable than the wet transfer using a Cu etchant. In fact, some researchers are exploiting this transfer method for the graphene grown on a Cu foil [56]. In this case, the electrolyte used in the transfer needs to be mild in order for the Cu neither to be corroded nor to be etched by itself.

However, the use of Cu itself has a limit in term of the recycle of a growth substrate. After a graphene growth on a Cu foil by a LPCVD process, we typically witness the deposition of Cu on the chamber wall (*eg.* quartz tube) while such a deposition of Cu is not observed in an APCVD process. This is arising from the vapor pressure of Cu. From the vapor pressure equation given by [57],

$$\log(p / Pa) = 5.006 + A + BT^{-1} + C\log T + DT^{-3} \qquad \text{(Eq. 2.9)}$$

where T denotes the temperature (K). At 1000 °C, the typical graphene growth temperature, the vapor pressure of Cu is calculated to 6.17×10^{-5} Torr, which is quite agreement of an earlier result of 4.71×10^{-5} Torr at 1000 °C [58]. Accordingly, the Cu should be consumed in every LPCVD growth process where a typical ambient pressure ranges from 450 mTorr to 1.6 Torr. Furthermore, when the Cu foil is thinned by a few μm, we observed the Cu foil becomes very susceptible to the growth temperature and the time. Since the foil is basically poly-crystalline, the facilitated surface diffusion leads to the wetting of the foil by agglomerating grain by grain. Consequently, strictly speaking, Cu is not a suitable growth substrate of graphene for recycling.

For these reasons, a new growth substrate has been sought. The requirements were 1) to allow for growing MLG with a better quality than that was grown by Cu, 2) recyclability with a low vapor pressure, 3) compatibility with the bubble-transfer method, and 4) relatively low carbon solubility, and 5) weak interaction with graphene in order to make the ease of taking of graphene. In this respect, first of all,

various metals that can catalyze the decomposition of hydrocarbon were considered to meet the criteria 1), such as Fe, Co, Ni, Ru, Rh, Pd, Au, Ta, W, Ir, or Pt. In the followed criteria, the candidate materials were narrowed to Ni, Pd, and Pt. Among these materials, Ni is challenging to obtain a MLG due to the carbon solubility (~1.1 at. % at 1000 °C [19]) and has a strong interaction with graphene [59] while Pd has a significantly large carbon solubility up to 3.5 at. % at 1000 °C that mostly results in the formation of multilayer graphene [20]. In contrast, Pt was believed to satisfy all the criteria. Pt has a low vapor pressure ranging from 2.10×10^{-21} Torr to 7.87×10^{-18} Torr at a temperature range from 900 °C to 1100 °C [57]. Pt is also weakly bound to graphene, similar to Cu [59] and is an excellent catalyst itself for proton reduction that is advantageous in the bubble-transfer process. Finally, its strong catalytic capability to decompose hydrocarbon on the surface was believed to achieve MLG by modulating the process parameters in spite of specific carbon solubility (1.26 at. % at 1100 °C [60]).

2.5.2 Experimental and Discussion

As a growth substrate, 127 μm-thick, (100)-textured poly-crystalline Pt foil (99.99%, Sigma-Aldrich) was used. The crystallographic orientation was confirmed through an XRD measurement. Like the Cu-mediated graphene growth, a typical LPCVD process was carried out with varied growth temperatures up to 1100 °C, varied CH_4/H_2 ratios during either growth or cooling step, and growth times. When further analysis was required, the graphene grown on a Pt foil was transferred onto a SiO_2/Si substrate by the bubble-transfer method introduced earlier. A Pt mesh was used as a counter electrode while 1 M NaOH solution was used as an electrolyte. The graphene with spin-coated PMMA on top was isolated from the Pt foil by reducing H_2 bubbles at the interface by applying a cathodic voltage of 1.5-2.0 V to the foil. If it was the case that aimed to check the morphology of graphene through SEM, the graphene was removed by applying excessive cathodic voltage more than 5.0 V that resulted in an aggressive generation of H_2 bubbles on the surface. This process was sufficient to take off all the graphene flakes on the Pt surface that was confirmed through a subsequent SEM imaging. It should be noted that throughout this thesis

study, only one piece of Pt foil (1 in. by 1 in.) was used over and over again more than 300 times. The morphology of graphene was reproducible regardless of the number of the growths.

2.5.2.1 Graphene growth with respect to the temperature

Fixing the CH_4/H_2 ratio to 10:1 (in sccm) and the growth time to 40 min, the graphene morphologies with respect to the growth temperature were investigated. In the cooling step, 10 sccm of H_2 were flowed. Figures 2.23 show the corresponding OM images of graphene after transferring onto a SiO_2/Si substrate. There was a clear difference in the graphene morphology with the growth temperatures. At 1100 °C illustrated in Fig. 2.23(a), loop-shaped thick multilayers were observed on the background of MLG. As the growth temperature was lowered, such a loop-shaped multilayer became dimmed and BLGs were appeared. These BLGs were appeared by the growth temperature at 950 °C (see Fig. 2.23(d)) and finally only pristine uniform MLG was obtained at both 900 °C and 800 °C, as shown in Fig. 2.23(e) and (f), respectively. This temperature dependence on the graphene morphology is not observable in the typical Cu-mediated LPCVD process exhibiting MLG regardless of the growth temperatures. In fact, at a high growth temperature, the graphene coverage on a Cu foil is likely to be less than 100% even with a long time exposure of CH_4 as 40 min because the rate-limiting step can be desorption of carbons [10]. In other words, the growth mechanism of graphene on a Pt foil is not purely a surface reaction like the Cu-mediated growth and the precipitation should be considered arising from the carbon solubility in Pt.

In fact, the carbon precipitation in Pt has been studied for decades as a carbon-poisoning effect which is detrimental to the catalytic activity of Pt decomposing hydrocarbon [61-65]. Most of the works were to elucidate the formation mechanism of graphitic layer on Pt upon cooling of carbon-doped Pt. It turns out that the carbons were not segregated out of the Pt, but precipitated because carbon atoms tend to be bound inside the bulk Pt [60, 66]. This gave rise to the loosely bound carbon atoms on the Pt surface, which is consistent with the weak binding energy of graphene on Pt [67].

In these earlier studies, I remarked an experiment that monitored peak-to-peak Auger signals upon

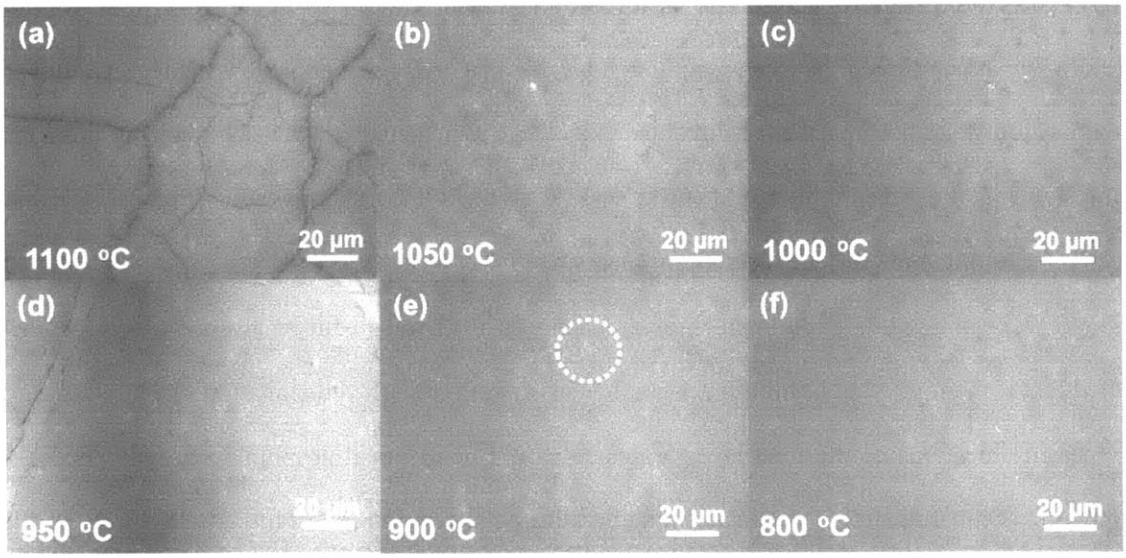

Figure 2.23 (a)-(f) Grayscale OM image of graphene samples transferred onto a SiO_2/Si substrate. The graphene was grown on an identical Pt foil with varied growth temperature from 1100 °C to 800 °C, respectively. The pristine MLG without any multilayer formation was started to obtain at T=900 °C. The uniformity of the MLG was remarked by contrasting with a hole inside a dotted circle in (e).

cooling of carbon-doped Pt from 1200 °C to 800 °C [66]. It turns out that regardless of the dopant concentration of carbon in Pt, the precipitation was saturated at 900 °C. Since the precipitation is a diffusion process, the temperature plays a significant role. The carbon diffusivity in a poly-crystalline bulk Pt can be empirically expressed as,

$$D_C^{Pt} = 0.017\exp(-1.084eV/kT)\,[68]. \qquad \text{(Eq. 2.10)}$$

Accordingly, the corresponding carbon diffusivity at 1100 °C, 1050 °C, 1000 °C, 950 °C, 900 °C and 800 °C is calculated to be, 1.78×10^{-6} $cm^2 s^{-1}$, 1.26×10^{-6} $cm^2 s^{-1}$, 0.87×10^{-6} $cm^2 s^{-1}$, 0.58×10^{-6} $cm^2 s^{-1}$, 0.37×10^{-6} cm^2 s^{-1}, and 0.14×10^{-6} cm^2 s^{-1}, respectively. Due to the strong temperature dependence, the carbon diffusivity drops almost one order of magnitude from 1100 °C to 800 °C. In other words, one main reason why the formation of BLG is suppressed is due to the sluggish precipitation of carbon at this growth condition. Furthermore, the carbon solubility in Pt is found to be 1.26 at. % at 1100 °C and 0.75% at 900

°C [60]. Therefore, the carbon reservoir inside the Pt is also reduced by about 40% for precipitation. Therefore, it can be inferred that the precipitation mechanism does not work below the temperature at 900 °C, thereby only surface reaction is involved like the Cu-mediated growth. The self-limiting growth feature showing the same uniform MLG at 900 °C and 800 °C, as shown in Fig. 2.23(e) and (f), respectively, supports the surface reaction mechanism.

Figure 2.24 shows the SEM images of graphene on a Pt foil obtained at a defined location. We assumed that if the formation of multilayer graphene is arising from the precipitation, the morphology and the appearing locations of the multilayer graphene would be identical at multiple growths because the precipitation is subordinated by the underlining bulk Pt. As shown in Fig. 2.24(a), after gaining multilayer graphene at a growth at 1100 °C, it was cleanly removed by generating excessive H_2 bubbles at

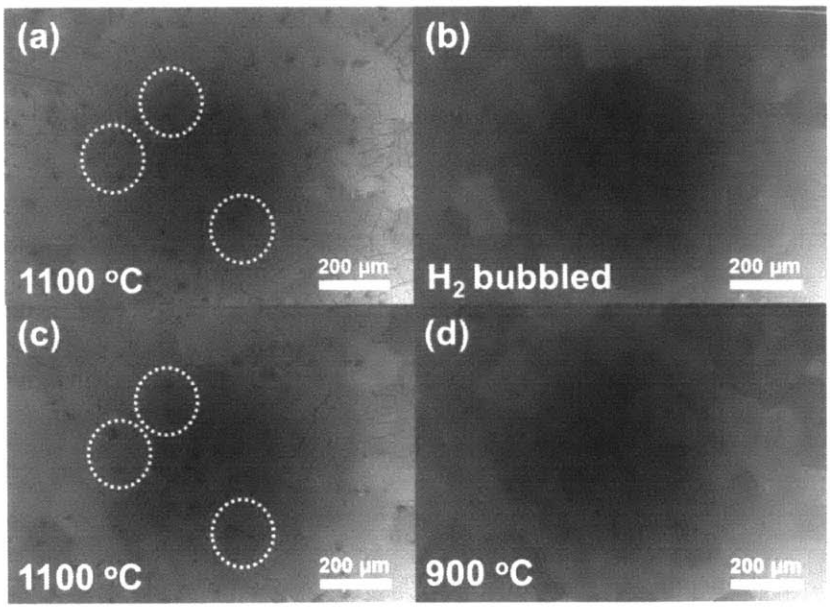

Figure 2.24 SEM images of graphene grown on a Pt foil at a defined location. (a) Growth at 1100 °C, (b) Bare surface of the Pt foil after taking off the graphene in (a) with excessive H_2 bubbles, (c) Regrowth at 1100 °C, (d) Growth at 900 °C. The multilayer formed at the same locations were indicated as dotted circles in (a) and (c).

graphene/Pt interface, as shown in Fig. 2.24(b). In the subsequent growth at 1100 °C, the expected multilayer graphene was observed. As shown in Fig. 2.24(c), although the morphology and the location of the multilayer were not completely identical to an earlier growth at 1100 °C in Fig. 2.24(a), we could find the agreeable consistency marked as dotted circles. This result supports the precipitation mechanism accounting for the multilayer formation at the growth temperature > 900 °C. As shown in Fig. 2.24(d), the growth at 900 °C exhibited a uniform graphene layer without any multilayer so that it was hard to figure out to distinguish with a bare Pt foil in Fig. 2.24(b).

- Growth at 900 °C

From the uniform morphology of graphene obtained in the growth at, the formation of MLG was strongly suggested. Nevertheless, it requires further characterizations to confirm the MLG were required because such a continuously uniform MLG growth on a Pt foil has been yet to achieve [55, 69-71]. For comparison, a MLG sample grown on a Cu foil using a typical LPCVD process (P=1.6 Torr) was prepared. Figure 2.25 shows the various characterization results indicating that the graphene grown on a Pt foil at 900 °C is a monolayer. The subsequent Table 2.5 presents quantitative data of the Raman spectroscopy and the transmittance characterization. As shown in Fig. 2.25(a), the TEM images obtained on multiple edge regions directly confirmed the graphene of a monolayer together with one clear set of six-fold diffraction pattern in Fig. 2.25(b). Moreover, the quality of this MLG grown by a Pt foil was compared with a MLG grown by a Cu foil. Interestingly, the graphene wrinkles were hardly observed on the graphene by a Pt foil (see Fig. 2.25(c)), which are typically appearing on the graphene by a Cu foil (see white arrows in Fig. 2.25(d)). This is arising not only from the relatively lower thermal expansion coefficient (TEC) of Pt ($.0\times10^{-6}$ m $m^{-1}K^{-1}$) than that of Cu (TEC: 16.6×10^{-6} m $m^{-1}K^{-1}$), but also from the lower growth temperature on the Pt than the Cu-mediated growth at 1030 °C.

The Raman spectroscopy characterization results shown in Fig. 2.25(e) and Table 2.5 provide an intriguing feature in terms of the doping level among the graphene samples prepared with different

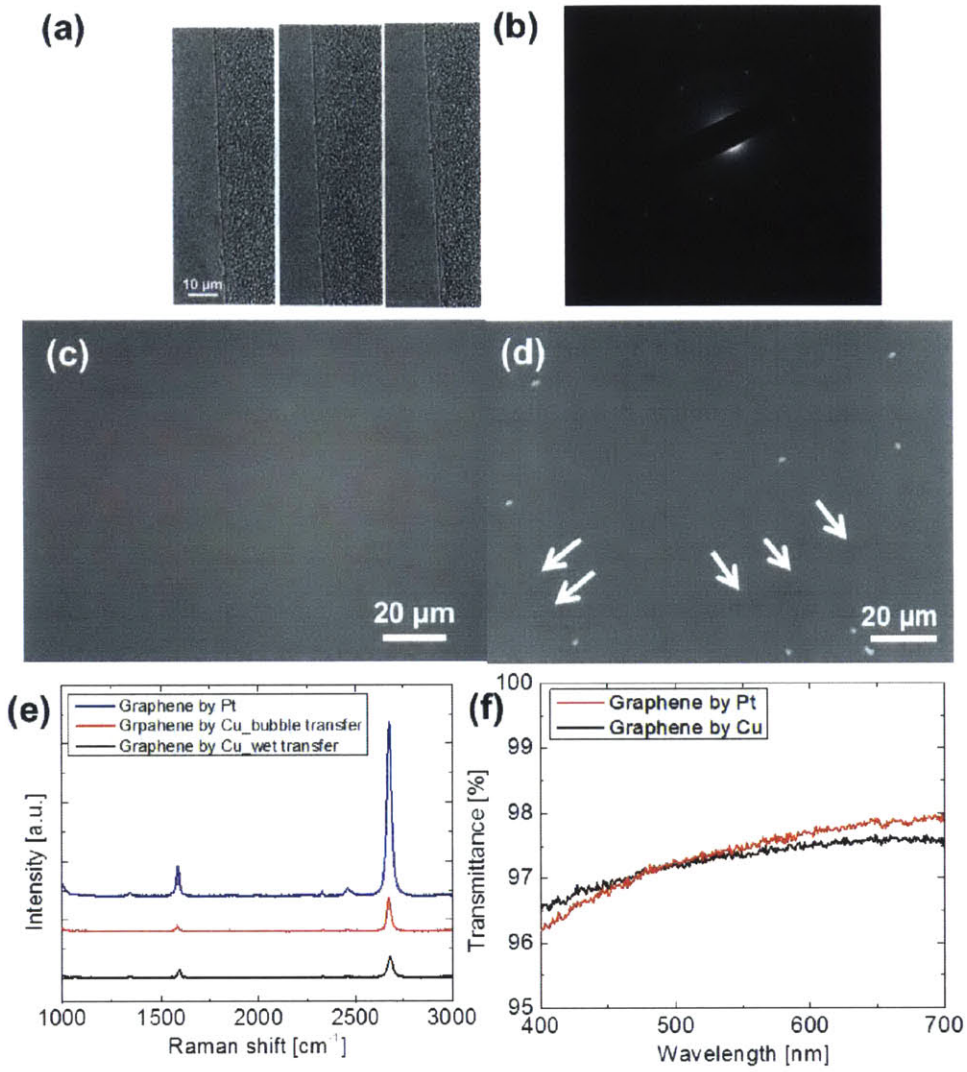

Figure 2.25 (a) TEM images obtained on the edges of a graphene sample grown by a Pt foil. A monolayer was confirmed. (b) Diffraction pattern of graphene clearly indicating a monolayer. (c)-(d) OM images of a graphene sample transferred onto a SiO_2/Si substrate where the growth substrate was a Pt foil and a Cu foil, respectively. (c) is the reproduced image of Fig. 2.23(e). Graphene wrinkles are indicated as arrows in (d). (e) Raman spectrum of graphene samples with respect to the growth substrate and the transfer method. (f) Transmittance characterization of graphene samples grown by a Pt foil and a Cu foil.

Table 2.5 Characterization results of the Raman spectroscopy and the transmittance in the graphene samples in Fig. 2.25 (e) and (f).

Sample	ω_G [cm^{-1}]	I_{2D}/I_G	Transmittance at λ=550 nm [%]
Graphene by Pt	1586.1±1.8	9.06±1.0	97.4
Graphene by Cu_bubble transfer	1584.3±1.8	6.83±3.0	N/A
Graphene by Cu_wet transfer	1591.4±2.6	5.39±0.4	97.3

growth substrates and the transfer methods. Apparently, the graphene sample grown on a Pt foil was less hole-doped than that on a Cu foil, indicated by lower ω_G and much larger I_{2D}/I_G. In this case, the graphene sample by Cu was transferred onto a SiO_2/Si substrate by a wet-etching process. Since the Cu etchant used in the wet transfer was $FeCl_3$-baed (CE-100, TRANSENE), the graphene sample could be hole-doped by the interaction with Cl ions during the wet etching step. To rule out the hole-doping by the Cu etchant, a bubble-transferred graphene sample that had been grown on a Cu foil was characterized with Raman spectroscopy. Interestingly, the ω_G was highly red-shifted from 1591.4±2.6 cm^{-1} to 1584.3±1.8 cm^{-1}, indicating that the hole-doping in graphene was significantly mitigated. Nonetheless, the I_{2D}/I_G value, 6.83±3.0, was still lower than the graphene sample grown by a Pt foil (I_{2D}/I_G: 9.06±1.0). In other words, the Pt-mediated growth inherently results in a graphene sample less hole-doped than the Cu-mediated growth. Otherwise, since the SiO_2 substrate generally contributes to the hole-doping in graphene, the less hole-doped feature in graphene grown by Pt can be a compensation effect by an electron-doping in graphene.

According to Giovannetti *et al.* [72], for metal-graphene equilibrium separations graphene is electron-doped by the interaction with Al, Ag, and Cu while graphene is hole-doped by Au and Pt. The type of doping is determined by the relative work function of a metal to that of graphene, 4.5 eV. However, when the formation of interfacial dipole is considered, it can result in a potential step to favor n-type doping in graphene on Pt [73]. In particular, the work function of Pt (100) is 0.5 eV lower than for Pt (111) [74],

this crossover can be applied to our case using a (100)-textured Pt foil [75]. The suppressed hole-doping doping in graphene by Pt in this thesis study was believed to result in a better carrier transport with reduced charged impurity scatterings on graphene.

Besides, the I_D/I_G of the graphene grown by a Pt foil was found to be larger than for the graphene sample prepared by a Cu foil. This appears to be due to structural damages on graphene during the bubble-transfer process where the generated H_2 bubbles at graphene/Pt interface cause the delaminated PMMA/graphene stack to be mechanically deformed. A milder bubble transfer process or the choice of a more flexible supporting layer over PMMA can be expected to lower the I_D/I_G.

Finally, the transmittance characterization results obtained in both the graphene samples by a Pt foil and a Cu foil exhibited the closer values to the expecting value of MLG, 97.7% at 550 nm, reassuring the formation of MLG on the Pt foil.

- Growth at lower than 800 °C

After gaining graphene on a Pt foil at 800 °C, we attempted to growth graphene at lower temperatures from 700 °C to 300 °C. Figure 2.26 shows the corresponding results. We could not obtain any carbon material at 300 °C. Interestingly, uniform carbon materials that appear to be graphene were achieved through the temperature range from 700 °C to 400 °C, as presented in Fig. 2.26(a)-(c). The Raman spectroscopy characterization on these materials in order to identify their nature indicated that they are not graphene, as shown in Fig. 2.26(d). Although a graphene-like feature was obtained on the region 1 at 700 °C (see Fig. 2.26(a) and (d)), the I_D/I_G was considerably large because the temperature was not sufficient to form a complete sp^2-carbon structure. The Raman spectra below this temperature were consistent with that of nanocrystalline graphite (NCG), distinguished from a completely amorphous carbon [76, 77].

Besides the Raman spectroscopy, the NCG material was characterized with other methods. Figures 2.27(a)-(b) show the AFM height images of NCG transferred onto a SiO_2/Si substrate where the PMMA

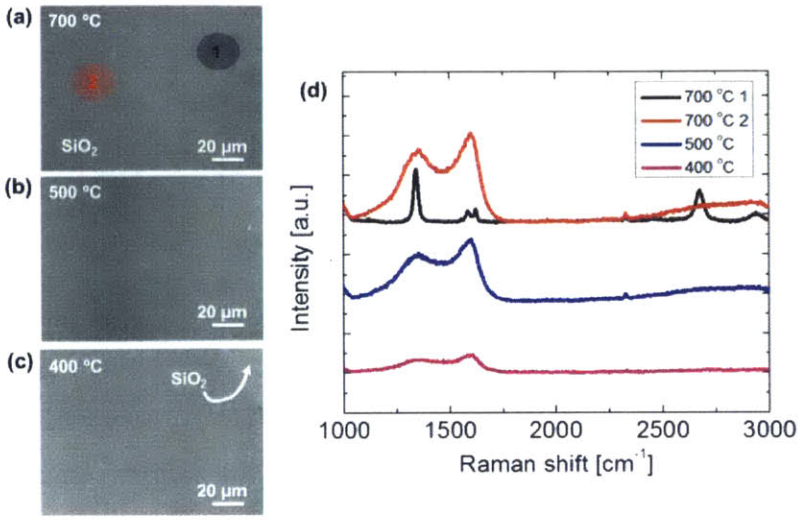

Figure 2.26 (a)-(c) Grayscale OM images of the carbon samples transferred onto a SiO_2/Si substrate. These carbon materials were grown on an identical Pt foil with varied growth temperatures of 700 °C, 500 °C, and 400 °C, respectively. (d) Raman spectrum of the graphene samples in (a)-(c).

was removed by acetone and by atmospheric annealing at 500 °C under Ar/H_2 ambient, respectively. As indicated in both the top images in Fig. 2.27(a)-(b), the thickness of the NCG was reduced by about 50 % by the annealing process. This was interpreted that the PMMA on this NCG was not efficiently removed by acetone due to the amorphousness of NCG, different from graphene. After the annealing, some locally brighter regions were observed in the AFM height image in the bottom of Fig. 2.27(b), but it was still challenging to exactly figure out the nature of NCG. The following TEM characterization confirmed the NCG through a dim crystalline ring in the diffraction pattern of the inset in Fig. 2.27(c). With this ring as a basis, the bright and dark field images were compared, as shown in Fig. 2.27(c)-(d), respectively. From the dark field image in Fig. 2.27(d), the locally brighter regions in the bottom of Fig. 2.27(b) were confirmed to the crystalline regions with tens of nm scale.

Interestingly, the NCG was obtained even without the flow of CH_4 during the growth. The formation of these carbon materials without a carbon source was believed by the segregation of carbons in the bulk of Pt which had been dissolved in the previous growths. To confirm the origin of the NCG, we attempted

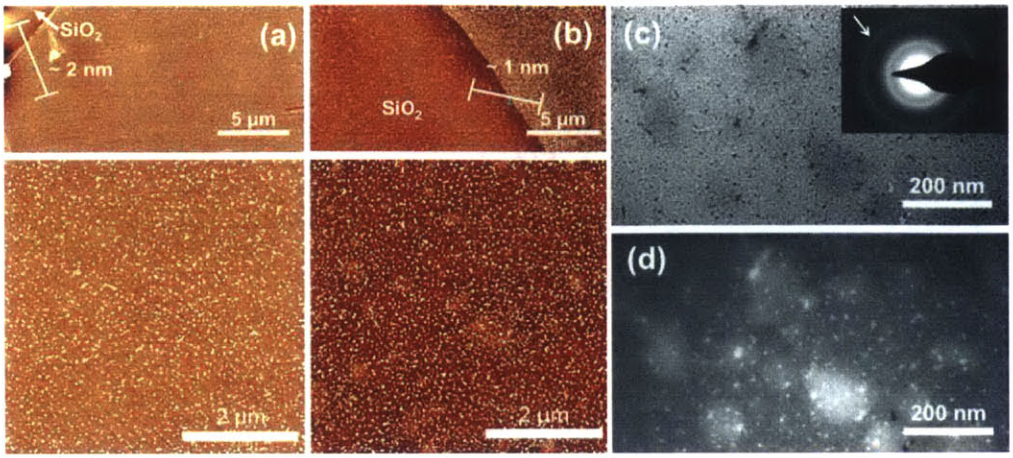

Figure 2.27 (a)-(b) AFM height images of NCG transferred onto a SiO_2/Si substrate where at the final transfer step, the PMMA was removed by acetone and atmospheric annealing at 500 °C under Ar/H_2 ambient, respectively. (c)-(d) Bright and dark field TEM images of the NCG material, respectively. The corresponding diffraction pattern is in the inset in (c) with a white arrow indicating the basis for both the TEM images.

to study with an isotope of CH_4, $^{13}CH_4$. Firstly, a ^{12}C-MLG sample was synthesized with a growth at 900 °C on a Pt foil while a ^{13}C-MLG sample was grown on a fresh Pt foil by applying the same growth condition at 900 °C. It was impossible to optically figure out the difference between ^{12}C-MLG and ^{13}C-MLG, as presented in Figure 2.28(a) and (b), respectively. However, the Raman spectrum on each sample clearly exhibited a red shift of both G-band and 2D-band on the ^{13}C-MLG, as shown in Fig. 2.28(e). Then, both of the Pt foils where graphene was transferred out were placed in a growth chamber and the growths of NCG were carried out by flowing only H_2 without the supply of a carbon source. As a result, the uniformly formed NCG were obtained on both of the Pt foils and then were transferred onto a SiO_2/Si substrate, as shown in Fig. 2.28(c)-(d), respectively. In the NCG, a broad carbon peak around 1600 cm^{-1} is generally found. Accordingly, if the NCG was originated from the dissolved carbons in the previous growth in our case, the carbon peak should be shifted in the NCG grown on a Pt foil where the growth of ^{13}C-MLG was performed. However, as shown in Fig. 2.28(e), the almost same Raman spectra were

obtained in both the NCG samples. In other words, the origin of the NCG is not coming from the dissolved carbons in Pt, but from solid carbon sources existing as impurities in the growth setup. The strong catalytic activity of Pt appears to enable to form nanocrystalline carbon materials at a low temperature range. Otherwise, the Pt foil could be contaminated by carbon impurities in the recycling process. After transferring off the graphene, in general the Pt foil was carefully rinsed with DI water, dried in an oven, and then stored in a vacuum container. Nevertheless, when the NCG growth process at 500 °C was performed by annealing at 1100 °C instead of the annealing at 500 °C, any carbon material was not obtained on the Pt. This result may suggest that the formation of NCG is arising from the carbon impurities adhered onto a Pt foil.

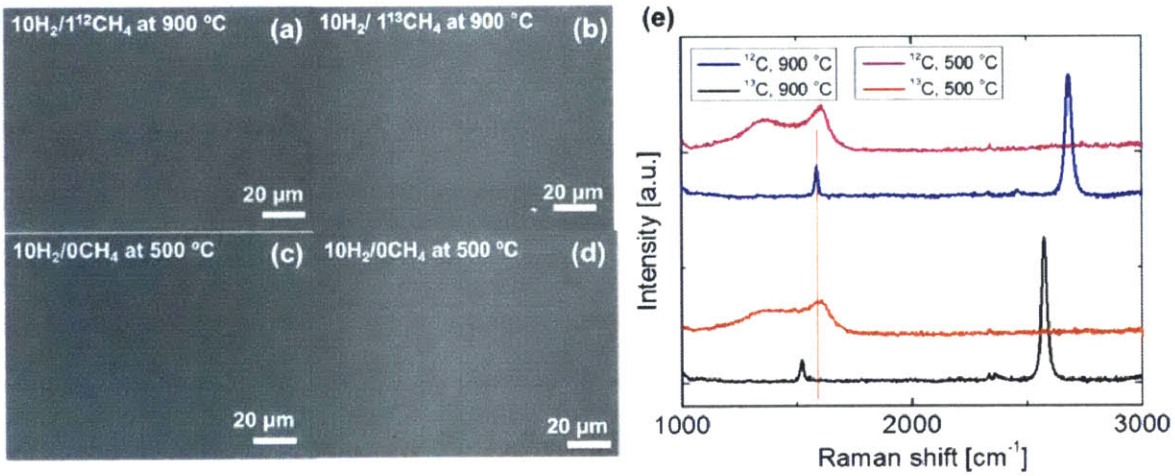

Figure 2.28 (a)-(b) Grayscale OM images of graphene samples transferred onto a SiO_2/Si substrate. Each graphene was grown on a Pt foil at 900 °C with $^{12}CH_4$ and $^{13}CH_4$ as a precursor, respectively. (c)-(d) Grayscale OM images of NCG samples transferred onto a SiO_2/Si substrate. These samples were prepared right after taking off the graphene in (a) and (b), respectively. (e) The corresponding Raman spectra of the samples of (a)-(d). The vertical red line confirms the G-band shift of ^{13}C-graphene.

2.5.2.2 Graphene growth with respect to the growth time

It is also of interest to monitor how the graphene proceeds. This provides the relevant information of the graphene domain size and morphology change to the modulation of process parameters. In particular, since the graphene growth on a Pt foil appears to have a strong relation with the underling Pt substrate, the information of the Pt grains should also be correlated. In this regard, we defined a location on a Pt foil, and then obtained the information of the crystallographic orientation of Pt grains at the location by taking EBDS, which are shown in Figure 2.29(a) and (b), respectively. By fixing the growth condition at 900 °C, the graphene morphology was monitored with respect to the growth time from 5 min. to 40 min., as presented in Fig. 2.29(c)-(f). As can be seen in the growth for 5 min. in Fig. 2.29(c), the growth feature was different from the typical Cu-mediated growth. While the graphene growth on a Cu foil started with the nucleation occurring all over the foil, regardless of what the Cu grains are (see Fig. 2.3 and Fig. 2.13), the initial graphene growth on a Pt foil was preferred along specific Pt grains. By superposing the initial growth SEM images onto the EBSD map in Fig. 2.29(b), we could mark the Pt grains showing preferential graphene growth on top, as indicated by black circles. The graphene formed like one or two hundreds of μm-wide streaks along the Pt grains rather than the formation of nuclei. It was also hard to tell that there is an exact correlation between the graphene growth rate and the crystallographic orientation of Pt in this scheme. Nevertheless, looking into the graphene morphology change upon the growth time, we could find an agreeable trend that the graphene growth rate on (110) grains were the highest while the graphene growth was finally completed on (100) grains. The activation energy of the dissociation of CH_4 on Pt (100), Pt (110), and Pt(111) is found to be 0.54 eV, 0.51 eV, and 0.61-0.84 eV [78]. Hence, the graphene growth shown in Fig. 2.29 can be accounted for the initial graphene growth along a series of (111) grains and the extension to adjacent grains. However, it is yet to come to a conclusion that graphene is growing on a Pt foil in this manner. Further investigation to elucidate how graphene grow on a Pt foil should be followed together with exploring the graphene domain size.

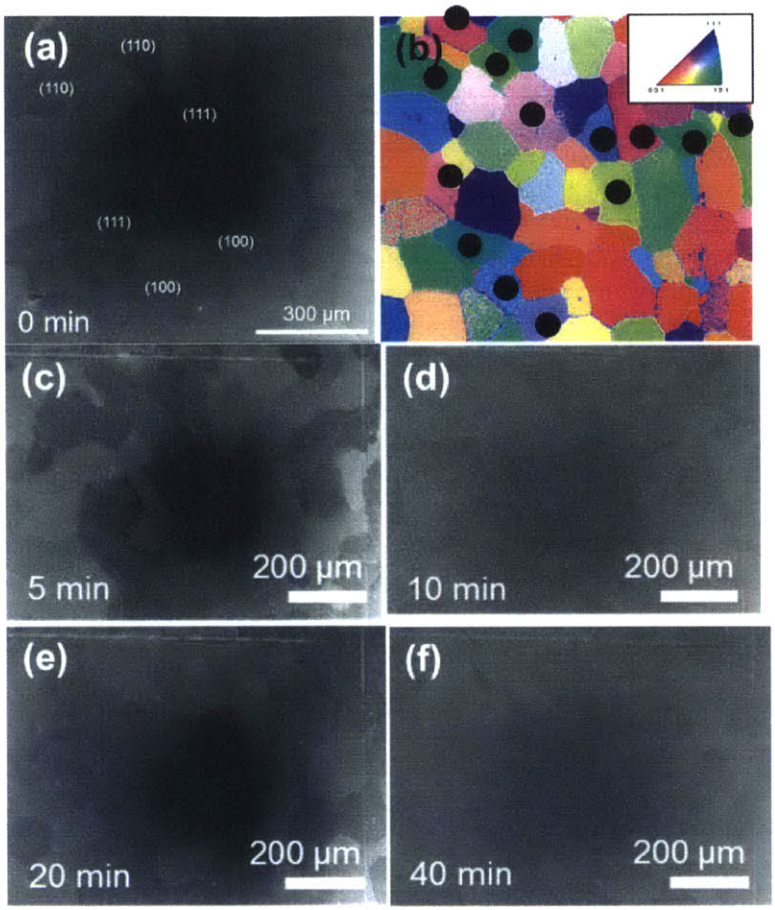

Figure 2.29 (a) SEM image scanned at a defined location of a bare Pt foil. (b) The corresponding EBSD map indicating inverse pole figures. The index to correlate the colors of the map to the crystallographic orientations is in the inset. (c)-(f) SEM images of graphene on the Pt foil scanned at the defined location with the growth time of 5 min, 10 min, 20 min, and 40 min, respectively. The partially grown graphene along the Pt

2.5.2.3 The effect of hydrogen in the cooling step

Like the Cu-mediated growth, hydrogen serves as an assisting role to decompose CH_4 on the Pt surface. In the cooling step when the supply of CH_4 is ceased, the balance between CH_4 and H_2 maintained during the steady-state becomes upset. In this case, the hydrogen starts to react with carbons to reduce or hinder the graphene growth. In this respect, the effect of hydrogen in the cooling step was

studied by varying the cooling conditions. Figure 2.30(a)-(b) shows the SEM images of graphene on a Pt foil that was cooled down to RT only with hydrogen with 10 and 100 sccm of flow rates, respectively. Since they shared the same growth conditions, the more empty regions in Fig. 2.30(b) is believed to occur by the severe carbon reduction reaction by the 10-fold increase of H_2 flow during the cooling. As shown in Fig. 2.30(c)-(d), either the conservation of the steady state by keeping the same gases composition as the growth step or the cease of all the gases allowing for vacuuming down to the base pressure (~30 mTorr), respectively, could help preventing from the reduction of carbons, *i.e.*, the etching of graphene. In particular, flowing CH_4 in the cooling step (Fig. 2.30(c)) was better to obtain a conformal graphene layer over the Pt foil. It should be also noted that the almost complete graphene coverage found in Fig. 2.30(d) implied the graphene growth on the Pt finished more or less than 10 min. Furthermore, the incomplete

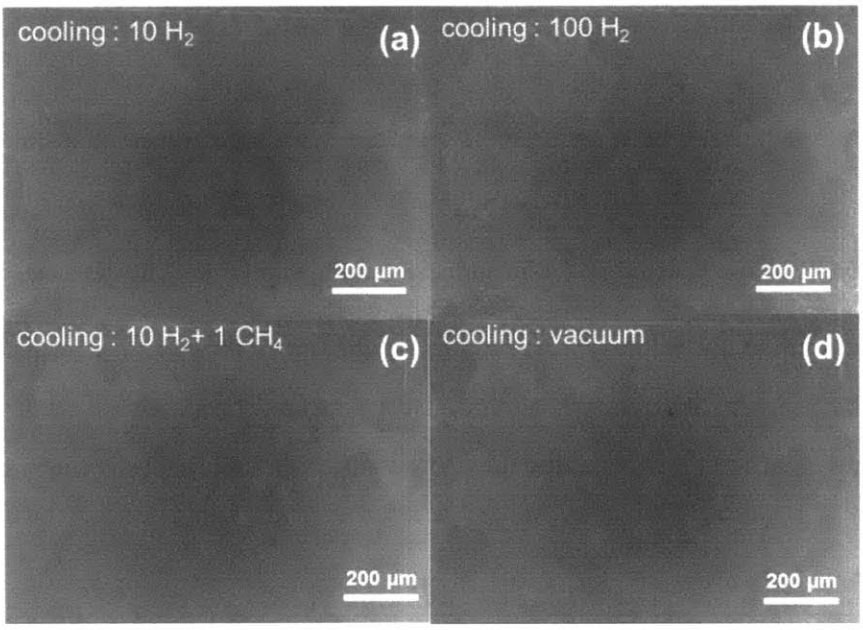

Figure 2.30 (a)-(d) SEM images of graphene on a Pt foil with respect to the cooling conditions. (a) only hydrogen with 10 sccm, (b) only hydrogen with 100 sccm, (c) hydrogen and methane with 10 sccm and 1 sccm, respectively, (d) without flowing gases, the pressure was hold at a base pressure (~30 mTorr). The growth time was 10 min while (a) is the reproduced image of Fig. 2.29(d).

regions in Fig. 2.30(a)-(b) can be arising from the preferential attacks by hydrogen during the cooling step. In other words, the reason why the graphene growth was finally completed on Pt (100) grains discussed earlier is not that the graphene growth rate is the lowest on the (100) grains, but that the dissociative hydrogen adsorption reaction to decompose graphene can be the most active on the (100) grains.

2.5.3 Device characteristics

More than 70 graphene FET devices were fabricated with a MLG sample grown by using a Pt foil at 900 °C and compared with the graphene FET devices with the MLG sample synthesized using a Cu foil. The corresponding electrical characterization results are shown in Figure 2.31. Apparently, about 50% of the improvement of the carrier mobility was obtained by growing graphene on a Pt foil. Recalling the Matthiessen's rule (Eq. 2.8), the electron-hole scattering is ignored in this case because the substrate of

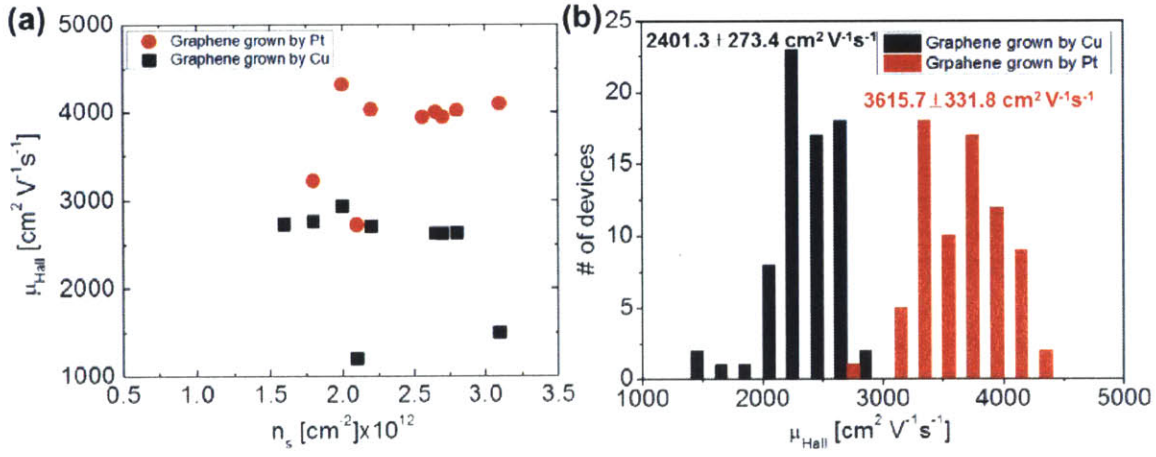

Figure 2.31 (a) Carrier density and the corresponding μ_{Hall} of 10 devices of each graphene sample grown by a Pt foil and a Cu foil. (b) Entire μ_{Hall} of the fabricated FET devices each graphene sample grown by a Pt foil and a Cu foil. The average values of μ_{Hall} of each type of graphene FET devices are included. The data of the sample, graphene grown by Cu, is the reproduced one in Fig. 2.8, the continuous graphene sample.

the devices was a commonly SiO_2/Si. From the comparison of the Raman spectra of each sample presented in Fig. 2.25(e) and Table 2.5, the mitigated hole-doping in the graphene sample grown by a Pt foil over the one by a Cu foil was confirmed and the underling mechanism was discussed. Accordingly, the suppressed charged impurity scattering is regarded as the main rationale for the enhancement of electrical properties of graphene. In addition, the relatively wider distribution of carrier density than that of the carrier mobility of the Pt-grown graphene sample was found in Fig. 2.31(a). This is interpreted that the factor to limit the carrier mobility is carrier density-independent lattice disorders. Hence, to increase the carrier mobility of graphene samples grown by the Pt-mediated growth, it is highly required to reduce the structural damage of graphene, characterized as I_D/I_G in Raman spectroscopy.

2.5.4 Conclusion

The CVD process to grow graphene was explored by using a Pt foil instead of the widely used Cu foil. The choice of the Pt as a new growth substrate was favored by enabling the repeated use of a substrate without involving hazardous substances generated by the typical wet-etching based transfer process. However, it has been challenging to obtain MLG over a Pt foil by LPCVD process up to now because Pt has a significant carbon solubility that leads to the precipitation of carbons during the cooling step, allowing for the formation of multilayer graphene. In this study, by modulating the growth temperature, we could suppress the precipitation of carbons, thereby obtaining a highly uniform and pristine MLG over the Pt substrate. Moreover, the quality of graphene was found to be better than one grown by the Cu-mediated growth process and was confirmed by the superior carrier mobility in the fabricated graphene FET devices. Pt is known as one of the most versatile materials. We explored another capability of Pt as a good graphene substrate. We believe further investigation on this Pt-mediated graphene growth will be able to improve the quality of resulting graphene samples.

References

[1] Reina A, Jia X, Ho J, Nezich D, Son H, Bulovic V, et al. Large Area, Few-Layer Graphene Films on Arbitrary Substrates by Chemical Vapor Deposition. Nano Letters. 2009;9(1):30-5.

[2] Bhaviripudi S, Jia X, Dresselhaus MS, Kong J. Role of Kinetic Factors in Chemical Vapor Deposition Synthesis of Uniform Large Area Graphene Using Copper Catalyst. Nano Letters. 2010;10(10):4128-33.

[3] Luo Z, Lu Y, Singer DW, Berck ME, Somers LA, Goldsmith BR, et al. Effect of Substrate Roughness and Feedstock Concentration on Growth of Wafer-Scale Graphene at Atmospheric Pressure. Chemistry of Materials. 2011;23(6):1441-7.

[4] Han GH, Guenes F, Bae JJ, Kim ES, Chae SJ, Shin H-J, et al. Influence of Copper Morphology in Forming Nucleation Seeds for Graphene Growth. Nano Letters. 2011;11(10):4144-8.

[5] Yu Q, Jauregui LA, Wu W, Colby R, Tian J, Su Z, et al. Control and characterization of individual grains and grain boundaries in graphene grown by chemical vapour deposition. Nature Materials. 2011;10(6):443-9.

[6] Bagri A, Kim S-P, Ruoff RS, Shenoy VB. Thermal transport across Twin Grain Boundaries in Polycrystalline Graphene from Nonequilibrium Molecular Dynamics Simulations. Nano Letters. 2011;11(9):3917-21.

[7] Grantab R, Shenoy VB, Ruoff RS. Anomalous Strength Characteristics of Tilt Grain Boundaries in Graphene. Science. 2010;330(6006):946-8.

[8] Li X, Magnuson CW, Venugopal A, An J, Suk JW, Han B, et al. Graphene Films with Large Domain Size by a Two-Step Chemical Vapor Deposition Process. Nano Letters. 2010;10(11):4328-34.

[9] Porter DA, Easterling KE. Phase transformations in metals and alloys: Chapman & Hall; 1992.

[10] Kim H, Mattevi C, Calvo MR, Oberg JC, Artiglia L, Agnoli S, et al. Activation Energy Paths for Graphene Nucleation and Growth on Cu. Acs Nano. 2012;6(4):3614-23.

[11] Mehdipour H, Ostrikov K. Kinetics of Low-Pressure, Low-Temperature Graphene Growth: Toward Single-Layer, Single-Crystalline Structure. Acs Nano. 2012;6(11):10276-86.

[12] Plummer JD, Deal MD, Griffin PB. Silicon VLSI Technology: Fundamentals, Practice and Modeling: Prentice Hall; 2000.

[13] Vlassiouk I, Regmi M, Fulvio PF, Dai S, Datskos P, Eres G, et al. Role of Hydrogen in Chemical Vapor Deposition Growth of Large Single-Crystal Graphene. Acs Nano. 2011;5(7):6069-76.

[14] Zhang W, Wu P, Li Z, Yang J. First-Principles Thermodynamics of Graphene Growth on Cu Surfaces. Journal of Physical Chemistry C. 2011;115(36):17782-7.

[15] Terasawa T-o, Saiki K. Growth of graphene on Cu by plasma enhanced chemical vapor deposition. Carbon. 2012;50(3):869-74.

[16] Yao Y, Li Z, Lin Z, Moon K-S, Agar J, Wong C. Controlled Growth of Multilayer, Few-Layer, and Single-Layer Graphene on Metal Substrates. Journal of Physical Chemistry C. 2011;115(13):5232-8.

[17] Li Z, Wu P, Wang C, Fan X, Zhang W, Zhai X, et al. Low-Temperature Growth of Graphene by Chemical Vapor Deposition Using Solid and Liquid Carbon Sources. Acs Nano. 2011;5(4):3385-90.

[18] Lopez GA, Mittemeijer E. The solubility of C in solid Cu. Scripta Materialia. 2004;51(1):1-5.

[19] Natesan K, Kassner TF. THERMODYNAMICS OF CARBON IN NICKEL, IRON-NICKEL AND IRON-CHROMIUM-NICKEL ALLOYS. Metallurgical Transactions. 1973;4(11):2557-66.

[20] Ma D, Liu M, Gao T, Li C, Sun J, Nie Y, et al. High-Quality Monolayer Graphene Synthesis on Pd Foils via the Suppression of Multilayer Growth at Grain Boundaries. Small (Weinheim an der Bergstrasse, Germany). 2014;10(19):4003-11.

[21] Vill V. Landolt-Börnstein: Group 4 - Physical Chemistry: Springer; 1996.

[22] Wofford JM, Nie S, McCarty KF, Bartelt NC, Dubon OD. Graphene Islands on Cu Foils: The Interplay between Shape, Orientation, and Defects. Nano Letters. 2010;10(12):4890-6.

[23] Robertson AW, Warner JH. Hexagonal Single Crystal Domains of Few-Layer Graphene on Copper Foils. Nano Letters. 2011;11(3):1182-9.
[24] Wu B, Geng D, Guo Y, Huang L, Xue Y, Zheng J, et al. Equiangular Hexagon-Shape-Controlled Synthesis of Graphene on Copper Surface. Advanced Materials. 2011;23(31):3522-+.
[25] Wood JD, Schmucker SW, Lyons AS, Pop E, Lyding JW. Effects of Polycrystalline Cu Substrate on Graphene Growth by Chemical Vapor Deposition. Nano Letters. 2011;11(11):4547-54.
[26] Li X, Cai W, Colombo L, Ruoff RS. Evolution of Graphene Growth on Ni and Cu by Carbon Isotope Labeling. Nano Letters. 2009;9(12):4268-72.
[27] Fan L, Zou J, Li Z, Li X, Wang K, Wei J, et al. Topology evolution of graphene in chemical vapor deposition, a combined theoretical/experimental approach toward shape control of graphene domains. Nanotechnology. 2012;23(11).
[28] Chavez KL, Hess DW. A novel method of etching copper oxide using acetic acid. Journal of the Electrochemical Society. 2001;148(11):G640-G3.
[29] Huang PY, Ruiz-Vargas CS, van der Zande AM, Whitney WS, Levendorf MP, Kevek JW, et al. Grains and grain boundaries in single-layer graphene atomic patchwork quilts. Nature. 2011;469(7330):389-+.
[30] Petrone N, Dean CR, Meric I, van der Zande AM, Huang PY, Wang L, et al. Chemical Vapor Deposition-Derived Graphene with Electrical Performance of Exfoliated Graphene. Nano Letters. 2012;12(6):2751-6.
[31] Tsen AW, Brown L, Levendorf MP, Ghahari F, Huang PY, Havener RW, et al. Tailoring Electrical Transport Across Grain Boundaries in Polycrystalline Graphene. Science. 2012;336(6085):1143-6.
[32] Yan Z, Lin J, Peng Z, Sun Z, Zhu Y, Li L, et al. Toward the Synthesis of Wafer-Scale Single-Crystal Graphene on Copper Foils. Acs Nano. 2012;6(10):9110-7.
[33] Wang H, Wang G, Bao P, Yang S, Zhu W, Xie X, et al. Controllable Synthesis of Submillimeter Single-Crystal Monolayer Graphene Domains on Copper Foils by Suppressing Nucleation. Journal of the American Chemical Society. 2012;134(8):3627-30.
[34] Wu T, Ding G, Shen H, Wang H, Sun L, Jiang D, et al. Triggering the Continuous Growth of Graphene Toward Millimeter-Sized Grains. Advanced Functional Materials. 2013;23(2):198-203.
[35] Li X, Magnuson CW, Venugopal A, Tromp RM, Hannon JB, Vogel EM, et al. Large-Area Graphene Single Crystals Grown by Low-Pressure Chemical Vapor Deposition of Methane on Copper. Journal of the American Chemical Society. 2011;133(9):2816-9.
[36] Geng D, Wu B, Guo Y, Huang L, Xue Y, Chen J, et al. Uniform hexagonal graphene flakes and films grown on liquid copper surface. Proceedings of the National Academy of Sciences of the United States of America. 2012;109(21):7992-6.
[37] Fang W, Hsu AL, Song Y, Birdwell AG, Amani M, Dubey M, et al. Asymmetric Growth of Bilayer Graphene on Copper Enclosures Using Low-Pressure Chemical Vapor Deposition. Acs Nano. 2014;8(6):6491-9.
[38] Heijnen LM. MODEL DESCRIPTION AND EXPERIMENTS ON CARBON DIFFUSION THROUGH PROTECTIVE LAYERS. PhD Thesis. 1987.
[39] Katz L, Guinan M, Borg RJ. DIFFUSION OF H2, D2, AND T2 IN SINGLE-CRYSTAL NI AND CU. Physical Review B-Solid State. 1971;4(2):330-&.
[40] Skakalova V, Kaiser AB. Graphene: Properties, Preparation, Characterisation and Devices: Elsevier Science; 2014.
[41] Nair RR, Blake P, Grigorenko AN, Novoselov KS, Booth TJ, Stauber T, et al. Fine structure constant defines visual transparency of graphene. Science. 2008;320(5881):1308-.
[42] Li X, Zhu Y, Cai W, Borysiak M, Han B, Chen D, et al. Transfer of Large-Area Graphene Films for High-Performance Transparent Conductive Electrodes. Nano Letters. 2009;9(12):4359-63.
[43] Hutchings FR, Unterweiser PM. Failure analysis: the British Engine technical reports: American Society for Metals; 1981.

[44] Kim KS, Zhao Y, Jang H, Lee SY, Kim JM, Kim KS, et al. Large-scale pattern growth of graphene films for stretchable transparent electrodes. Nature. 2009;457(7230):706-10.
[45] Hofmann M, Shin YC, Hsieh Y-P, Dresselhaus MS, Kong J. A facile tool for the characterization of two-dimensional materials grown by chemical vapor deposition. Nano Research. 2012;5(7):504-11.
[46] Chen GH, Wu DJ, Weng WU, Wu CL. Exfoliation of graphite flake and its nanocomposites. Carbon. 2003;41(3):619-21.
[47] Gao L, Guest JR, Guisinger NP. Epitaxial Graphene on Cu(111). Nano Letters. 2010;10(9):3512-6.
[48] Nemes-Incze P, Yoo KJ, Tapaszto L, Dobrik G, Labar J, Horvath ZE, et al. Revealing the grain structure of graphene grown by chemical vapor deposition. Applied Physics Letters. 2011;99(2).
[49] Cancado LG, Jorio A, Martins Ferreira EH, Stavale F, Achete CA, Capaz RB, et al. Quantifying Defects in Graphene via Raman Spectroscopy at Different Excitation Energies. Nano Letters. 2011;11(8):3190-6.
[50] Ferrari AC, Meyer JC, Scardaci V, Casiraghi C, Lazzeri M, Mauri F, et al. Raman spectrum of graphene and graphene layers. Physical Review Letters. 2006;97(18).
[51] Das A, Pisana S, Chakraborty B, Piscanec S, Saha SK, Waghmare UV, et al. Monitoring dopants by Raman scattering in an electrochemically top-gated graphene transistor. Nature Nanotechnology. 2008;3(4):210-5.
[52] Cheng Z, Zhou Q, Wang C, Li Q, Wang C, Fang Y. Toward Intrinsic Graphene Surfaces: A Systematic Study on Thermal Annealing and Wet-Chemical Treatment of SiO2-Supported Graphene Devices. Nano Letters. 2011;11(2):767-71.
[53] Li Q, Chou H, Zhong J-H, Liu J-Y, Dolocan A, Zhang J, et al. Growth of Adlayer Graphene on Cu Studied by Carbon Isotope Labeling. Nano Letters. 2013;13(2):486-90.
[54] Caldwell JD, Anderson TJ, Culbertson JC, Jernigan GG, Hobart KD, Kub FJ, et al. Technique for the Dry Transfer of Epitaxial Graphene onto Arbitrary Substrates. Acs Nano. 2010;4(2):1108-14.
[55] Gao L, Ren W, Xu H, Jin L, Wang Z, Ma T, et al. Repeated growth and bubbling transfer of graphene with millimetre-size single-crystal grains using platinum. Nature Communications. 2012;3.
[56] Wang Y, Zheng Y, Xu X, Dubuisson E, Bao Q, Lu J, et al. Electrochemical Delamination of CVD-Grown Graphene Film: Toward the Recyclable Use of Copper Catalyst. Acs Nano. 2011;5(12):9927-33.
[57] Alcock CB, Itkin VP, Horrigan MK. VAPOR-PRESSURE EQUATIONS FOR THE METALLIC ELEMENTS - 298-2500-K. Canadian Metallurgical Quarterly. 1984;23(3):309-13.
[58] Hersh HN. THE VAPOR PRESSURE OF COPPER. Journal of the American Chemical Society. 1953;75(7):1529-31.
[59] Preobrajenski AB, Ng ML, Vinogradov AS, Martensson N. Controlling graphene corrugation on lattice-mismatched substrates. Physical Review B. 2008;78(7).
[60] Hamilton JC, Blakely JM. CARBON SEGREGATION TO SINGLE-CRYSTAL SURFACES OF PT,PD AND CO. Surface Science. 1980;91(1):199-217.
[61] Selman GL, Ellison, P. J., and Darling, A. S. Carbon in Platinum and Palladium. Journal of Platinum Metals Review. 1970;14(1):14-20.
[62] May JW. Platinum surface LEED rings. Surface Science. 1969;17(1):267-70.
[63] Lang B. A LEED study of the deposition of carbon on platinum crystal surfaces. Surface Science. 1975;53(1):317-29.
[64] Yang RT, Goethel PJ, Schwartz JM, Lund CRF. Solubility and diffusivity of carbon in metals. Journal of Catalysis. 1990;122(1):206-10.
[65] Reeves CT, Seets DC, Mullins CB. Low translational energy mechanisms in the dissociative chemisorption of methane on iridium and platinum surfaces. Journal of Molecular Catalysis A: Chemical. 2001;167(1–2):207-15.
[66] Hamilton JC, Blakely JM. Carbon layer formation on the Pt (111) surface as a function of temperature. Journal of Vacuum Science & Technology. 1978;15(2):559-62.

[67] Vanin M, Mortensen JJ, Kelkkanen AK, Garcia-Lastra JM, Thygesen KS, Jacobsen KW. Graphene on metals: A van der Waals density functional study. Physical Review B. 2010;81(8).
[68] Watson EB. DIFFUSION AND SOLUBILITY OF C IN PT. American Mineralogist. 1987;72(5-6):487-90.
[69] Sutter P, Sadowski JT, Sutter E. Graphene on Pt(111): Growth and substrate interaction. Physical Review B. 2009;80(24).
[70] Gao J-H, Sagisaka K, Kitahara M, Xu M-S, Miyamoto S, Fujita D. Graphene growth on a Pt(111) substrate by surface segregation and precipitation. Nanotechnology. 2012;23(5).
[71] Sun J, Nam Y, Lindvall N, Cole MT, Teo KBK, Park YW, et al. Growth mechanism of graphene on platinum: Surface catalysis and carbon segregation. Applied Physics Letters. 2014;104(15).
[72] Giovannetti G, Khomyakov PA, Brocks G, Karpan VM, van den Brink J, Kelly PJ. Doping graphene with metal contacts. Physical Review Letters. 2008;101(2).
[73] Pi K, McCreary KM, Bao W, Han W, Chiang YF, Li Y, et al. Electronic doping and scattering by transition metals on graphene. Physical Review B. 2009;80(7).
[74] Sinsarp A, Yamada Y, Sasaki M, Yamamoto S. Local tunneling barrier height imaging of a reconstructed Pt(100) surface. Applied Surface Science. 2004;237(1-4):587-92.
[75] Ulstrup S, Nilsson L, Miwa JA, Balog R, Bianchi M, Hornekaer L, et al. Electronic structure of graphene on a reconstructed Pt(100) surface: Hydrogen adsorption, doping, and band gaps. Physical Review B. 2013;88(12).
[76] Chu PK, Li LH. Characterization of amorphous and nanocrystalline carbon films. Materials Chemistry and Physics. 2006;96(2-3):253-77.
[77] Ferrari AC, Robertson J. Raman spectroscopy of amorphous, nanostructured, diamond-like carbon, and nanodiamond. Philosophical Transactions of the Royal Society a-Mathematical Physical and Engineering Sciences. 2004;362(1824):2477-512.
[78] Moussounda PS, Haroun MF, Rakotovelo G, Legare P. A theoretical study of CH4 dissociation on Pt(100) surface. Surface Science. 2007;601(18):3697-701.

Chapter 3. Synthesis of h-BN by CVD

3.1 Background

C. R. Dean *et al.* has reported the use of mechanically exfoliated h-BN as an excellent dielectric substrate for graphene, demonstrating extremely high carrier mobility up to 250,000 $cm^2V^{-1}s^{-1}$ [1]. However, like the mechanically exfoliated graphene from HOPG, this route has a limit to scale up in spite of the ultraflatness (rms roughness: 50-100 pm) and the absence of dangling bonds on the surface. In fact, the history of the synthesis of h-BN can be traced back to the 1980s [2] for other applications like use as a lubricant. Various h-BN synthesis processes have been explored. For example, Kubota *et al.* demonstrated a precipitation method to produce a highly crystalline h-BN from h-BN powder [3]. They used Ni and Mo that have a specific solubility of B and N, respectively, and obtained h-BN hundreds of μm in size by cooling those metals from 1400 °C to 1200 °C. Because of the drawbacks, such as the high process temperature, the difficulty of thickness control, and the low throughput, this h-BN is only being used to serve as a source material for mechanical exfoliation. Like the synthesis of graphene, epitaxial growth on a Ni (111) [4], Pt (111) [5], Pd (111) [6], Cu (111) [7], and Ru (0001) substrate [8] is another route to produce high quality h-BN films under UHV.

Samples of h-BN also can be prepared through polymerization and recrystallization of a precursor containing B and N, borazine $(BHNH)_3$ [9]. This borazine can easily dehydropolymerize at an elevated temperature to form polyborazylene. Subsequent dehydrogenation and followed by recrystallization at 1000 °C in AP could result in few layer h-BN on a Ni substrate in large area [10]. Afterward, like the metal-catalyzed CVD-graphene, this h-BN can be transferred onto an arbitrary substrate for further process steps. This CVD route has been widely accepted as a simple method to produce to h-BN in large area. More recently, a solid precursor, ammonia borane (BH_3NH_3) have also been used instead of borazine (liquid at RT) to avoid a bubbling step requiring to activate it. The use of ammonia borane resulted in few layer h-BN films by Cu-catalyzed APCVD processes [11, 12] like the borazine-CVD process, but enabled to obtain monolayer h-BN on a Cu foil through a LPCVD process [13] and on a Pt

foil through both AP- [14] and LPCVD [15] processes. Nevertheless, the quality of the *produced* monolayer CVD-h-BN is far poorer than the mechanically exfoliated one, and is yet to be used as a device component. The optical microscopy image and AFM image of the monolayer h-BN transferred onto a SiO_2/Si substrate [13] are shown in Figure 3.1.

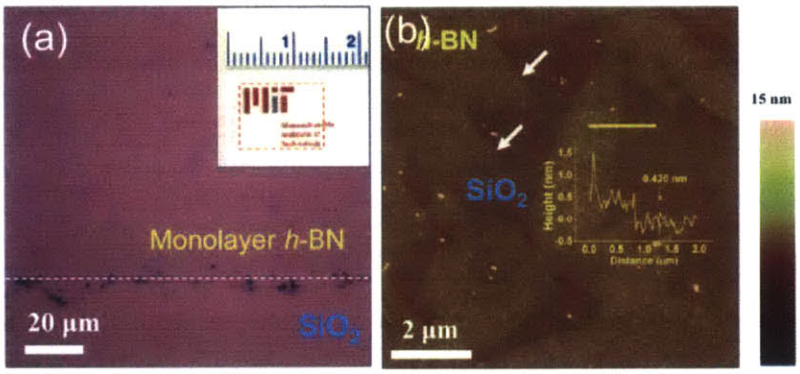

Figure 3.1 (a) OM image of monolayer h-BN transferred onto a SiO_2/Si substrate from a growth substrate, Cu foil. (b) Corresponding AFM height image. The monolayer was confirmed through measurement a thickness of 0.420 nm. Reprinted with permission from [13]. ©2012 American Chemical Society.

Different from few layer h-BN to be used as a graphene substrate or a tunneling barrier, the monolayer h-BN has more feasible applications, such as used as a tunneling device or for molecular membranes. Particularly, it should be noted that the synthesis of monolayer h-BN opened a path to study and develop a hybrid structure with other 2-D materials in large area, for example, graphene. This hybrid structure can be either stacked [1] or in-plane [16, 17]. For the stacked structure, depending on the stacking orientation, interesting characteristics like opening up a band gap ~50 meV in graphene can be observed [18]. One can achieve this hybridd structure by either sequentially transferring each 2-D material or patterning existing material [16]. Above all, it would be the most desirable if this hybrid structure could be realized in one growth flow in order not to be contaminated by impurities or an ambient environment.

In this chapter, based on the accumulated experiences and knowledge from the graphene synthesis by CVD, the synthesis of h-BN will be investigated through the LPCVD process. Since the process goal was limited to obtaining monolayer h-BN, ammonia borane was used as a precursor, while both Cu and Pt foils were used as a growth substrate. Besides, after an established process [19], we also attempted to synthesize a hybrid structure: h-BN/graphene.

3.2 Synthesis of monolayer h-BN

3.2.1 Experimental

Regardless of the growth substrate used, the CVD setup for h-BN synthesis was common as a two-zone system. Figure 3.2 [15] depicts almost as same setup as the one used in our study, except that I used a heating belt that was wound around the activation chamber (quartz tube) in our case for ammonia borane instead of the hot plate in the figure.

The experiments were carried out in the following sequences. First, after placing ammonia borane precursor (50 mg, 97%, Sigma-Aldrich) and a growth substrate in the activation zone and in the growth zone, respectively, all the chambers were evacuated down to a base pressure of ~50 mTorr. Like the graphene synthesis, the h-BN growth process consisted of a heating, annealing, growth, and a cooling step, while certain amounts of H_2 were introduced into the both chambers during the entire growth. In the growth step after heating for 30 min and annealing for 1 hour, the temperature of the activation zone was ramped up from RT to a moderate temperature of less than 104 °C, the melting point of ammonia borane. As a result, in the activation zone, the following decomposition reaction occurred,

$$4(BH_3NH_3)(s) \xrightarrow{RT<T<104°C} 7H_2(g) + (BHNH)_3(g) + BH_2NH_2(g) \quad (3\text{-}1)$$

resulting in hydrogen, borazine, and aminoborane, respectively [13]. This borazine that was diffused into the growth zone was recrystallized to form h-BN on the growth substrate heated at T >1000 °C. When the growth finished, the precursor supply from the activation zone quickly ceased and the growth zone was cooled down to RT as fast as possible. This was to prevent the formed h-BN from being etched by H_2

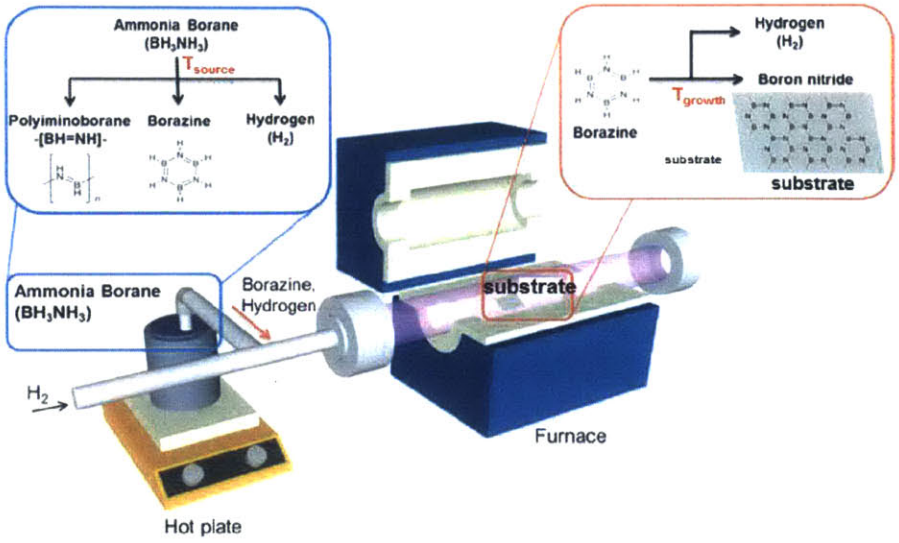

Figure 3.2 The CVD setup for h-BN synthesis. As well as the growth zone inside the furnace, another zone was installed in my case to activate the ammonia borane precursor. In our study, instead of the hot plate, a heating belt was used, wound on the activation chamber (quartz tube). Reprinted with permission from [15]. ©2013 American Chemical Society.

during the cooling step. Besides, a cold trap was installed in the exhaust line ahead of the vacuum pump and was filled with liquid N_2 during the growth step. This allowed for activated ammonia borane to be condensed inside the trap, thereby protecting the pump from damage by the precursor. As process parameters to determine the morphology of h-BN, we considered the source activation temperature, T_{src}, the substrate temperature, T_{sub}, the growth time, and the flow rate of H_2.

3.2.2 Monolayer h-BN growth on a Cu foil

3.2.2.1 Substrate preparation

The Cu foil used for the h-BN growth was 127 μm-thick (99.9%, Alfa Aesar) to take advantage of its high purity. Since as-received Cu foil of this type has rolling lines that can serve as preferential nucleation

sites, the foil was electropolished in advance using phosphoric acid. The detailed process is described in sec **2.3**. The anodic voltage was maintained at 2.0 V for 30 min of the polishing time. As a result, a highly flat Cu foil was prepared as a growth substrate after the foil was carefully cleaned by DI water.

3.2.2.2 Characterization of monolayer h-BN

First, the synthesized monolayer h-BN was characterized to confirm its physical structure. Figure 3.3 shows the AFM images obtained on an h-BN sample and the corresponding Raman spectra. The AFM images in (a)-(d) were taken with an as-grown h-BN sample on a Cu foil, while the Raman spectra in (e) was obtained after transferring the h-BN onto a SiO_2/Si substrate using the established PMMA-supported wet transfer process. The T_{src}, T_{sub}, the growth time, and the H_2 flow rate as a growth condition for preparing this sample were 60 °C, 1020 °C, 15 min, and 10 sccm, respectively.

As can be seen in Fig. 3.3 (a)-(d), the shape of each h-BN domain was triangular like earlier observations [13, 20], different from the hexagon-shaped graphene flakes. Atomically, these triangular domains have zig-zag edges, either B-terminated or N-terminated. With the analogy to the triangular shape of h-BN grown on a Ni substrate [20], N-terminated zig-zag edges are more likely to form than the B-terminated because they are energetically favorable in terms of the edge energy [21, 22] . In the initial stage of the growth, only triangular shaped domains were observed, but hexagonal domains were also shown as the growth proceeded, which will be discussed later.

The thickness of the h-BN measured on a SiO_2/Si substrate by AFM was ~0.45 nm. Although this was a little thicker than the theoretical value of 0.33 nm, the length scale was almost the same as that a monolayer of h-BN based on earlier reports [13, 15]. This can be attributed to the roughness of the SiO_2 surface and possible PMMA residue on the h-BN surface that was not completely removed after the transfer process.

Raman spectroscopy is another method to characterize the number of h-BN layers. As introduced in Chapter 1, there is a characteristic peak due to the B-N vibrational mode (E_{2g} phonon mode) around 1365

cm^{-1} [23, 24], that is like the G peak in graphene. As reported previously [24], the E_{2g} peak position for monolayer h-BN tends to be upshifted to ~1370 cm^{-1} or higher, while adding an additional layer gradually downshifts this feature toward the bulk E_{2g} peak at around 1365 cm^{-1}. As can be seen in the Fig. 3.3(e), the prominent peak at ~~1370 cm^{-1} confirmed that these h-BN flakes were all monolayers. Another peak turned up between 1400-1500 cm^{-1} was accounted for as the Raman mode from the SiO_2/Si substrate because the same peak was observed on blank SiO_2/Si.

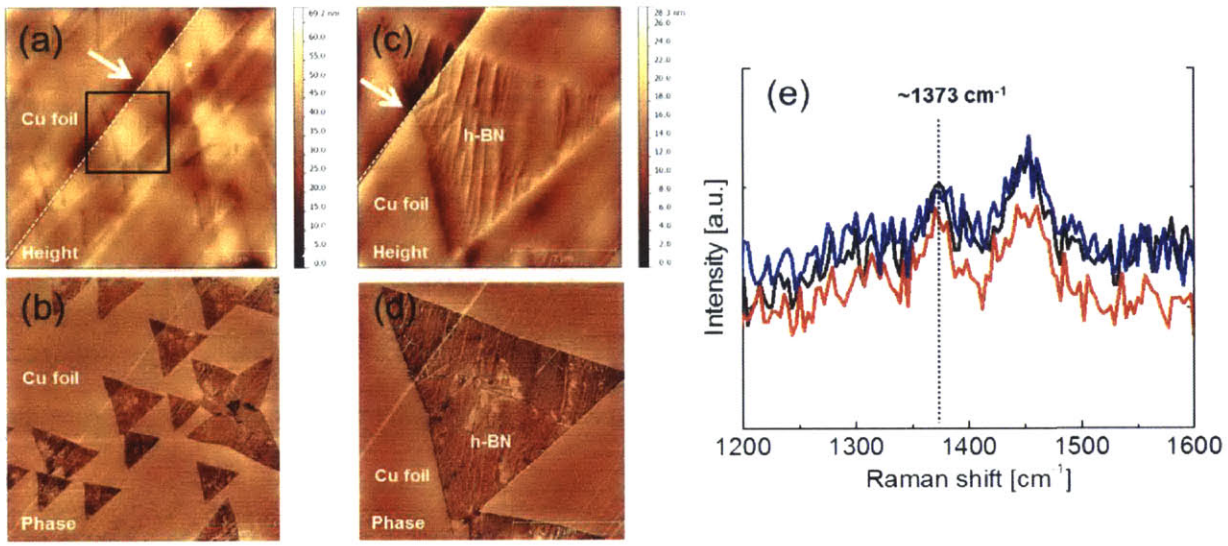

Figure 3.3 (a)-(d) AFM image of monolayer h-BN flakes taken with an as-grown sample on a Cu foil substrate. The region inside a black square in (a) is magnified in (c). (b) and (d) are the phase images of (a) and (c), respectively. The dotted line observed in both (a) and (c), indicated by a white arrow, is a grain boundary of the Cu foil. (e) The Raman spectra on these flakes obtained after transferring them onto a SiO_2/Si substrate.

3.2.2.3 Effect of process parameters

After the confirmation of monolayer h-BN, the morphologies of h-BN with respect to the process parameters were investigated. Throughout this study, it was ultimately desired to develop a process to

synthesize a continuous monolayer h-BN on a Cu foil. As illustrated in Figure 3.4, since Cu has a very limited solubility of both B and N, like C for graphene, the growth behavior could be understood as simply surface deposition, neglecting the segregation of supersaturated $(BN)_x$ from the bulk to the surface of Cu during the cooling step. Furthermore, the grain boundaries of a Cu foil did not serve as preferential nucleation sites of h-BN, as can be seen in Fig. 3.5(a) and (c). Like the graphene growth by LPCVD process, it was quite often that were observed h-BN being nucleated inside Cu grains crossing over Cu grain boundaries as the growth proceeded.

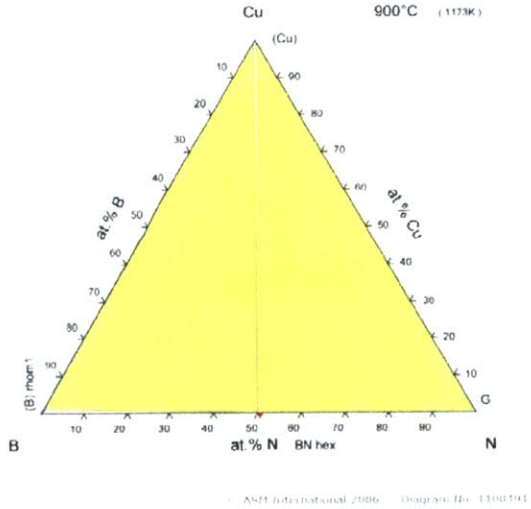

Figure 3.4 Cu-B-N ternary phase diagram

- Effect of the source activation temperature, T_{src}

Ammonia borane can be easily decomposed at a moderate temperature higher than RT, yielding vaporized borazine by the reaction (see 3.1). This borazine subsequently flows into the growth chamber and participates in the h-BN growth as a precursor. Therefore, the T_{src} can be regarded as a factor to determine the flux of borazine in the growth zone, thereby affecting the morphology of h-BN. Figure 3.5 shows the SEM images of as-grown h-BN samples on Cu foils with respect to the T_{src}. The T_{sub}, the growth time, and the H_2 flow rate were fixed for this growth at 1050 °C, 10 min, and 10 sccm,

respectively while the T_{src} was varied from 20 °C to 80 °C. The coverage of h-BN on the Cu increased as T_{src} increased by the facilitated borazine concentration. The decomposition of ammonia borane took place at a temperature as low as 40 °C in Fig. 3.5(b), but RT was still insufficient for this decomposition as shown in Fig. 3.5(a). While monolayer h-BN with local multilayers could be synthesized at T_{src}=60 °C, a further increase of T_{src} gave rise to multilayer formation caused by the excessive supply of the borazine source. It was remarked that these multilayers were observable before forming a monolayer. This meant that certain h-BN domains were started from multilayer h-BN nuclei. Particularly, at T_{src}=80 °C, bilayer h-BN flakes were observed with a coverage >80%. The existence of a monolayer background could be identified by wrinkles as indicated by arrows in Fig. 3.5(f). This morphology change implied that the h-BN growth on a Cu foil is not self-limiting as occurs for graphene, even if LPCVD is used. Thus, all the process parameters should be carefully controlled to synthesize the desired h-BN.

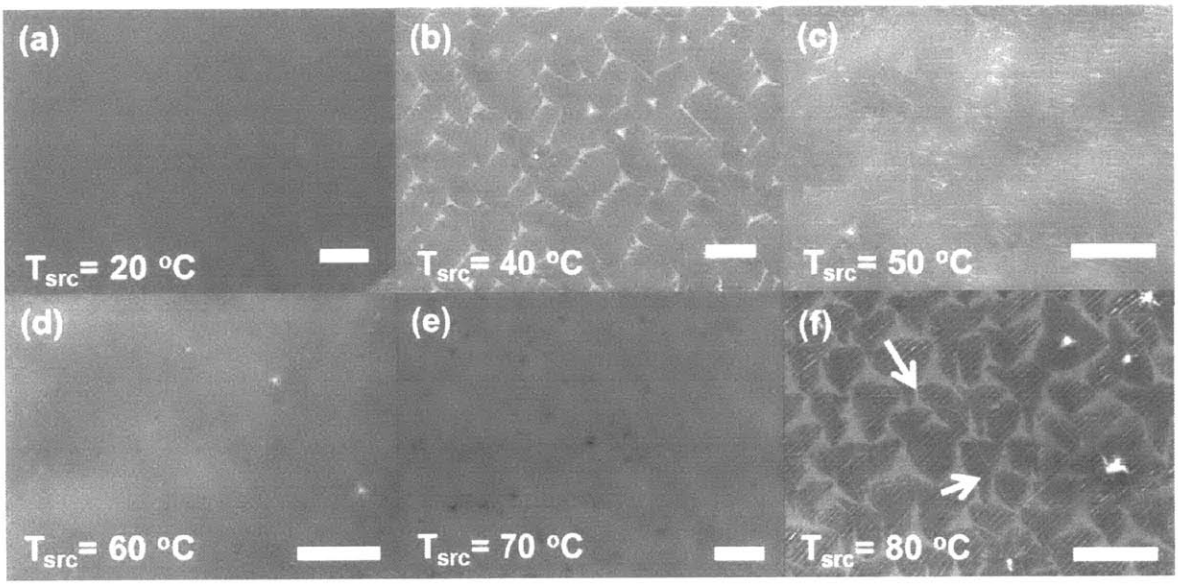

Figure 3.5 SEM images of as-grown h-BN on Cu foils with respect to the T_{src}. The T_{sub}, the growth time, and the H_2 flow rate were fixed at 1050 °C, 10 min, and 10 sccm, respectively. Only blank Cu was seen at T_{src}=20 °C in (a), while h-BN covered the Cu partially or fully at a higher T_{src} in (b)-(f). Scale bars are 5 μm.

- Effect of the substrate temperature, T_{sub}

While the T_{src} determines the concentration of the precursor (borazine) introduced into the growth zone, T_{sub} controls the kinetics of the h-BN formation reaction provided by,

$$(BHNH)_3(g) \xrightarrow[T_{sub}>1000^{\circ}C]{Cu} hBN(s)+3H_2(g). \quad (3.2)$$

Since this decomposition is thermally activated, a slight change of the growth temperature can drastically change the growth rate of h-BN. Figure 3.6 shows the SEM images of as-grown h-BN samples on Cu foils at T_{src} was varied from 50 °C to 80 °C. As compared to Fig. 3.5, the T_{sub} was down to 1020 °C, while the 15 min of the growth time was increased by 5 min. Apparently, the growth rate was quite sluggish so that the each h-BN domain was not yet coalesced even at T_{src} =80 °C in Fig. 3.6(c), while the coverage of additional layer over a monolayer h-BN background was >80% at T_{sub}=1050 °C, as can be seen in Fig. 3.5(f). Control of the growth rate, however, could not lead to the increase of h-BN domain size. Like graphene, the domain boundaries of h-BN are likely to be atomically imperfective sites. To use the insulating characteristics of h-BN in device applications, the density of the domain boundaries should be minimized. Throughout the study, it was challenging to synthesize h-BN with a domain size that was larger than 5 μm. Nevertheless, it is also true that single crystalline h-BN flakes with this size level can be acceptable in microelectronics.

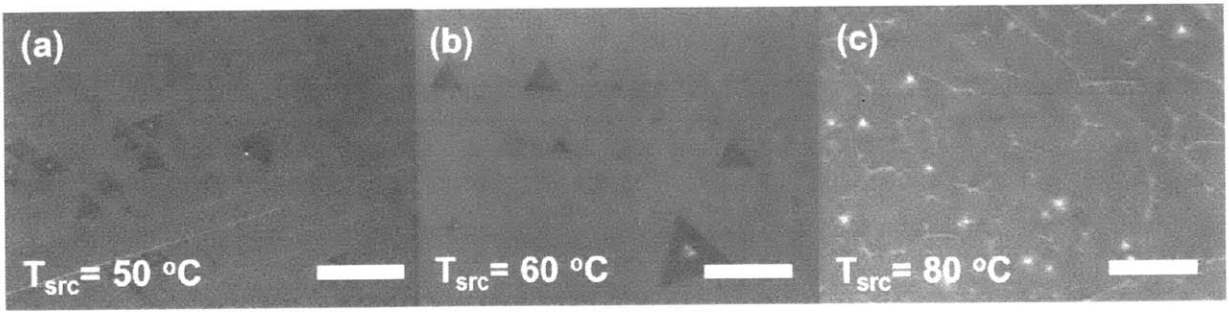

Figure 3.6 SEM images of as-grown h-BN on Cu foils with respect to the T_{src}. Note that this time, the T_{sub} and the growth time were fixed at 1020 °C and 15 min, respectively, while the H_2 flow rate was 10 sccm. Scale bars are 5 μm.

- Morphology change upon growth time

It is of interest to trace how each h-BN domain grows and meets another domain as the growth proceeds. Figure 3.7 shows the SEM images of as-grown h-BN samples on Cu foils with respect to the growth time. The growths were stopped at 10 min, 15 min, and 20 min as shown in the figure, respectively, where the T_{sub}, T_{src}, and the H_2 flow rate were fixed at 1020 °C, 80 °C, and 10 sccm, respectively. As discussed earlier, triangular shaped nuclei can be observed in the initial stage of the growth in Fig. 3.7(a). Then, with the continued injection of the BN source, the nuclei kept growing and formed a continuous layer. Further growth ended up with the formation of multilayers on top of the monolayer as shown in Fig. 3.7(c). It was remarked that each triangular nucleus appeared to be aligned inside a single Cu grain, which was not found in a typical graphene growth. This was understood in terms of h-BN being more strongly bound to the underlying Cu than graphene. The difference of the binding energies between C-Cu(111) [25] and h-BN-Cu(111) [26] being one order of magnitude supports this argument. Still, it is hard to tell whether or not the growth is epitaxial because there is a 2% lattice mismatch between Cu (111) and crystalline h-BN.

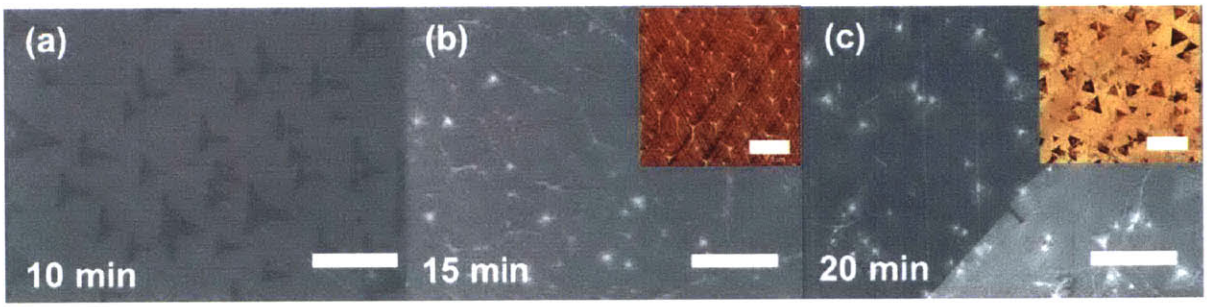

Figure 3.7 SEM images of as-grown h-BN on Cu foils with respect to the growth time as it was varied from 10 min to 20 min. The T_{sub}, T_{src} and the H_2 flow rate were fixed at 1020 °C, 80°C, and 10 sccm, respectively. (b) is the reproduction of Fig. 3.6(c). Insets are the corresponding AFM phase images. Scale bars are 5 μm.

It was fortunate to catch the growth process just at the moment right before each h-BN domain is stitched up, as shown in Fig. 3.7(b). Interestingly, the domain shape evolution from triangles to hexagons was observed while some local multilayers were still triangular. The alignment of the nuclei was still valid at this point. Furthermore, the 3-fold symmetry among the domains appeared to indicate that the growth proceeded in a manner of close packing. Since the edge of the hexagon shaped h-BN can be either N-terminated or B-terminated [13], the domain boundary can be either seamless or stacking-faulted. Considering the domain boundary as a defect that causes deterioration of the electronic (insulating), thermal, and mechanical properties of h-BN, this low angle boundary can also be beneficial for minimizing carrier and phonon scatterings across the domain boundaries. Further analysis at the atomic scale of domain boundaries can be expected in connection with exploring the physical and chemical structure of h-BN.

- Effect of hydrogen

Similarly to the graphene growth process, hydrogen serves not only for removing the native oxide on a metal substrate during annealing, but also for controlling the growth kinetics by participating in the growth process shown in (3.2). Figure 3.8 shows the SEM images of as-grown h-BN samples on Cu foils showing the effect of hydrogen on the growth. At a given growth condition with the same T_{sub}, T_{src}, and growth time of 1020 °C, 60 °C, and 15 min, the growth rate of h-BN decreased by the increase of the H_2 flow rate, as shown in Fig. 3.8(a)-(d). Looking into the chemical reaction, (3.2), the decomposition reaction rate will be the same as the desorption rate of H_2 on the surface at the steady state. When the partial pressure of hydrogen is increased by the introduction of H_2 gas, the H_2 desorption rate limits the decomposition rate, thereby making the growth rate of h-BN more sluggish. Although the growth rate with the lowest H_2 flow rate in (a) was higher than ones with higher flow rate (b)-(d), the edges of the flakes were finger-shaped while the others were of a sharply defined triangular shape. From this dendritic shape, we concluded that the reverse reaction, *i.e.* etching of h-BN by hydrogen, was not balanced with

the h-BN formation reaction, with a higher growth rate at the growth fronts. However, since the adatom attachment energy barrier is less than the nucleation energy barrier, a bigger domain size of h-BN would be expected with a lower H_2 flow rate. Keeping this observation in mind, we attempted to dynamically change the H_2 flow rate in the growth step. As a result, h-BN flakes with sharp triangular edges whose domain size is larger than 5 μm were obtained, as shown in Fig. 3.8(f). Although further process optimization is required toward full h-BN coverage on a Cu foil and negligible multilayer density, this approach is still valid with regard to controlling the growth kinetics using hydrogen. When argon was used in the growth step instead of hydrogen, an aggregated structure was obtained, as shown in Fig. 3.8(g), implying an assisting role of hydrogen to decompose borazine on the Cu surface.

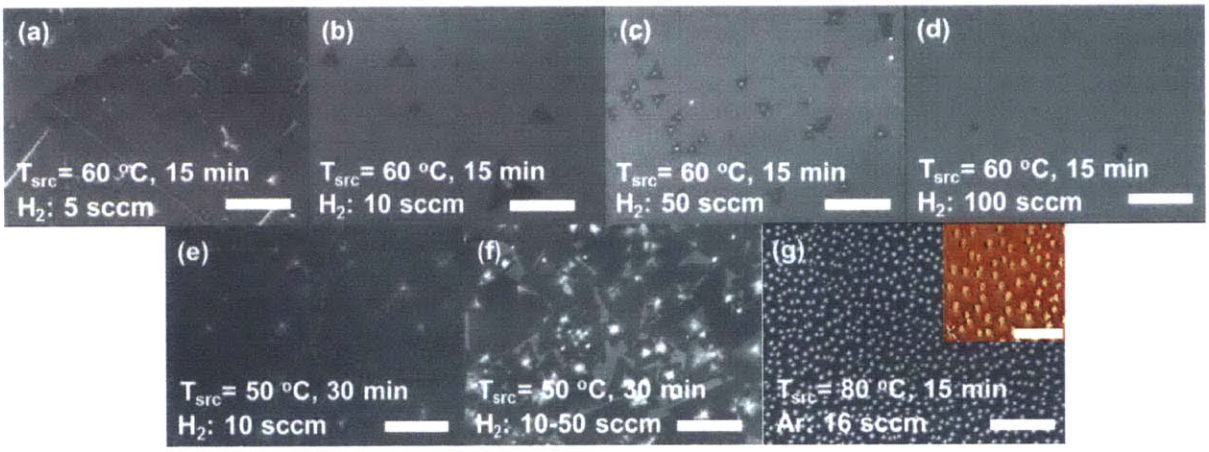

Figure 3.8 SEM images of as-grown h-BN on Cu foils with respect to the hydrogen flow rate. (a)-(d) varied the flow rate of hydrogen from 5 to 100 sccm where T_{src} was held at 60 °C for 15 min, respectively. (b) is the reproduced image of Fig. 3.6(b). The h-BN in (e) and (f) has the same growth conditions with T_{src}=60 °C for 30 min, but while the flow rate of H_2 was fixed at 10 sccm in (e), the one in (f) was dynamically increased from 10 to 50 sccm during the growth. (g) h-BN synthesized by flowing Ar in the growth step. The dark grayed background is a bare Cu surface. The inset figure is an AFM phase image. All the growths in this figure were implemented at T_{sub}=1020 °C. Scale bars of the SEM images are 5 μm while the scale bar for the inset in (g) is 2 μm.

3.2.2.4 Challenges

Basically, as discussed throughout this chapter, the main challenge of the h-BN growth on a Cu substrate is the difficulty in obtaining a uniform single layer. This is because the growth is not self-limiting like it is in the graphene synthesis. Furthermore, since the growth process is greatly susceptible to all the process parameters, such as the T_{sub}, T_{src}, growth time, and hydrogen flow rate, the process window to achieve the desired h-BN morphology is very narrow. Consequently, CVD-h-BN has not been actively applied to devices like graphene or TMDs.

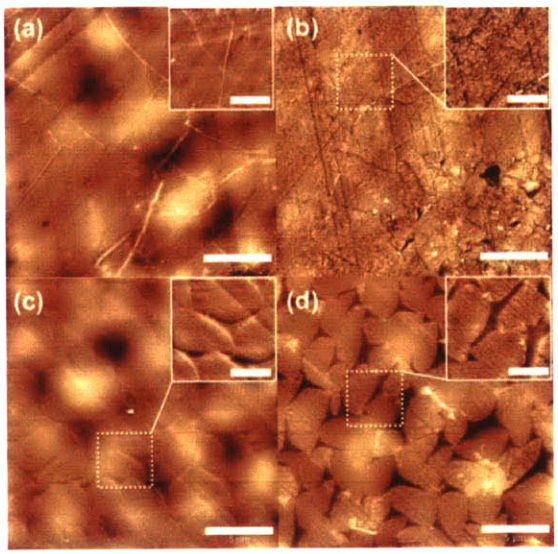

Figure 3.9 AFM height images of a continuous h-BN sample on a Cu foil before (a) and after (b) the graphene passivated etch test for 5s of using a Cu etchant droplet (Transence APS-100). (c) and (d) are AFM height images of a discontinuous h-BN sample on a Cu foil before and after the same etch test, respectively. Insets are the magnified images of each sample, respectively. Scale bars are 5 μm, while in the insets they are 2 μm.

Moreover, for applications like a tunneling barrier taking advantage of the h-BN's insulating property, the density of defects should be minimized. In this regard, the quality of the h-BN samples was

characterized using the earlier graphene passivated etch test by placing an Cu etchant droplet for 5s on the samples on a Cu foil [27]. As shown in Figure 3.9, regardless of the coverage of h-BN on the Cu, etch pits were found. No particular alignment of these pits suggested that a domain boundary was not observed while there were holes inside the region made by the etching test in Fig. 3.9(b) and (d). This indicated that the h-BN grown on a Cu foil was porous to some extent, thereby making it leaky in electronic devices. Correlating the density of etch pits with the crystalline structure of synthesized h-BN is under investigation.

3.2.3 Monolayer h-BN growth on a Pt foil

3.2.3.1 Introduction

To tackle the challenges addressed in the Cu-mediated h-BN growth, a Pt foil was also attempted as the growth substrate, like in the graphene growth study. Until now, very few researchers have reported the h-BN CVD growth on a Pt substrate. They either used ammonia borane [14, 15] or borazine [28] as a h-BN precursor where a monolayer h-BN was presented [15, 28], or a mono- to few-layered h-BN growth was discussed [14], using LPCVD and APCVD, respectively. Interestingly, the resulting monolayer h-BN obtained in these LPCVD processes was uniform and continuous, different from the Cu-mediated growth results. This feature was maintained even with the variance of the process parameters, implying that the growth is self-limiting. In the APCVD approach, however, the h-BN thickness could be controlled by the growth parameters, like the T_{src} and growth time, similarly to the APCVD graphene growth discussed in Chapter 2.

In this study, LPCVD h-BN growths using ammonia borane were mostly investigated. Like earlier demonstrations, the growth of uniform and continuous monolayer h-BN was confirmed. Particularly, noting that this high quality could be used as a good substrate for graphene, the electronic properties of a CVD-graphene transferred on this h-BN were characterized at the device level. Like the graphene growth, a 127 μm-thick, (100)-textured poly-crystalline Pt foil (99.99%, Sigma-Aldrich) was used. No particular

pre-treatment was applied for the growth. As introduced in the graphene growth with Pt, the h-BN synthesized was thus transferred using a bubble transfer method in order to reuse the substrate. PMMA was used as a supporting layer. The transfer condition was almost the same as the bubble transfer conditions for graphene, where -2.0V was applied to the sample dipped in a 1 M NaOH solution.

3.2.3.2 Characterization of monolayer h-BN

Figure 3.10 shows the SEM, OM, and AFM images of an h-BN sample grown on a Pt foil where T_{src}=80 °C and T_{sub}=1100 °C and a H_2 flow rate of 10 sccm were applied for 20 min. Compared to the h-BN grown on a Cu foil with a similar growth condition as indicated in Fig. 3.7(c), the h-BN grown on a Pt foil showed a uniform layer without multilayer formation even with much higher T_{sub} than the Cu foil case. Since the layer was continuous, the number of layers was explored with various characterization methods. First, as shown in Fig. 3.10 (a)-(b), it was hard to figure out even if h-BN was grown or not on the Pt foil because no wrinkle was observable. Since the thermal expansion coefficient (TEC) of a monolayer h-BN is found to be positive 7.2×10^{-6} m $m^{-1}K^{-1}$ [29], h-BN appeared to relatively match with that of Pt (TEC: 9.0×10^{-6} m $m^{-1}K^{-1}$) better than for the case of Cu (TEC: 16.6×10^{-6} m $m^{-1}K^{-1}$). The lack of wrinkles in h-BN can be beneficial because the wrinkles are also considered as one of the defects degrading the material properties. This will be further discussed in Chapter 4. The transferred h-BN remained intact on a SiO_2/Si substrate and confirmed the existence of the h-BN shown in optical and AFM images in Fig. 3.10 (c)-(d) and (e)-(f), respectively. Particularly, the roughness of the h-BN surface could be reduced down to ~800 pm. This sample is still rougher than a SiO_2 surface (rms: 250 pm) or a mechanically exfoliated h-BN (rms: 50 pm) samples, but the surface can be improved because the roughness was mainly attributed to the PMMA residue on the surface. The thickness measured on the edge region was calculated to be 0.370 nm. This confirmed that the synthesized pristine h-BN layer was a monolayer.

The formation of monolayer h-BN on a Pt foil was also characterized in a direct way through TEM

images, like the graphene grown on a Pt foil. The sample was prepared by transferring a PMMA/h-BN stack onto a TEM grid and taking off the PMMA by annealing with Ar and H_2 flow at 450 °C for 2 hours

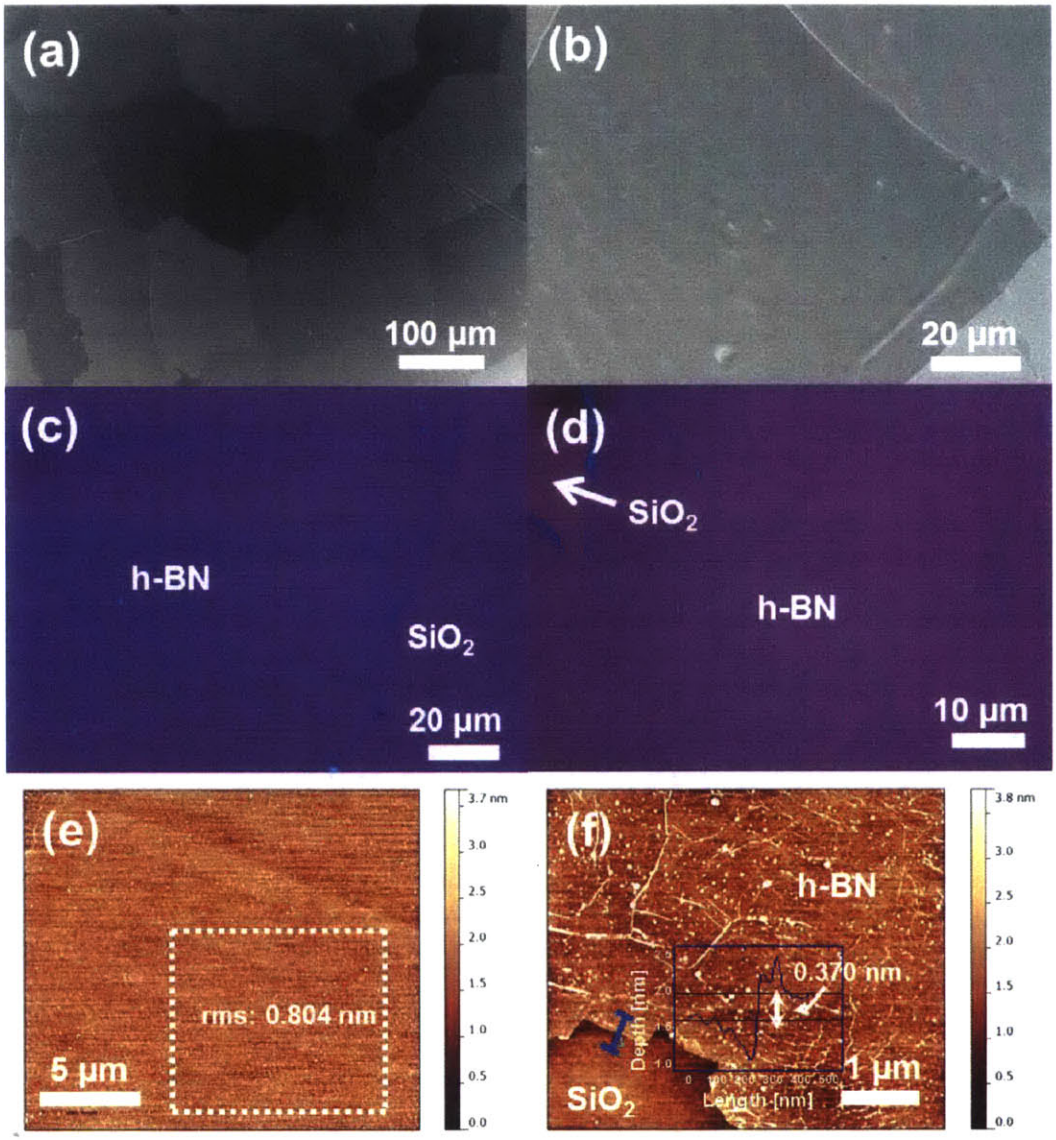

Figure 3.10 (a)-(b) SEM image of an as-grown monolayer of h-BN on a Pt foil. (c)-(d) OM image of the monolayer h-BN transferred onto a SiO_2/Si substrate. (e)-(f) Corresponding AFM height images. The rms roughness of the inside h-BN was 0.804 nm in (e). The thickness of this h-BN was calculated by measuring the depth on the edge region of this h-BN (blue line), which was 0.370 nm in (f).

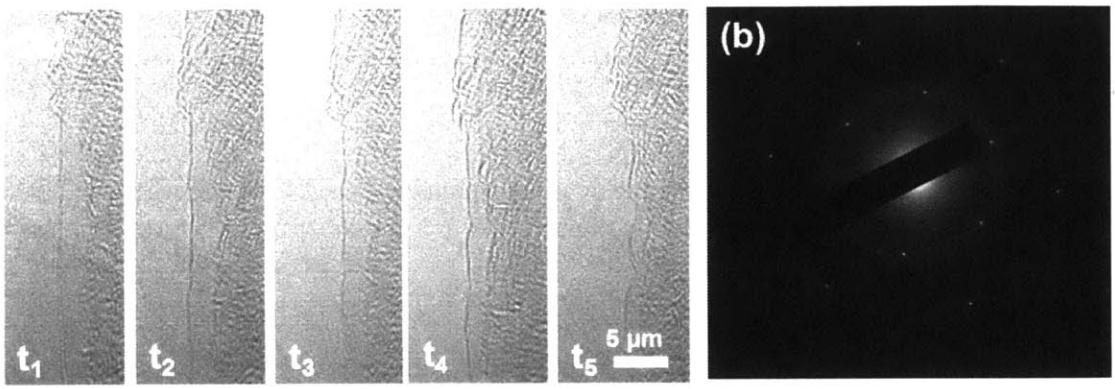

Figure 3.11 TEM image of an h-BN sample grown on a Pt foil. (a) Monolayer growth was confirmed on the edge. Different from graphene, h-BN had been damaged by the electron beam (200 kV) for multiple scans at one location from t_1 to t_5. (b) Diffraction pattern of h-BN clearly indicating a monolayer.

under AP. As can be seen in Figure 3.11 (a), an h-BN monolayer was confirmed on the edge region. Different from graphene, h-BN had been damaged by the electron beam (200 kV) for multiple scans at a particular location. One clear set of a six-fold diffraction pattern, shown in Fig. 3.11(b), confirmed the monolayer h-BN growth.

Finally, the h-BN was characterized with Raman spectroscopy and UV-Vis-IR spectroscopy. For continuous h-BN samples using a Cu foil, due to the locally distributed multilayers, a variance in the peak position and shape could be found in the Raman spectra. However, as shown in Figure 3.12 (a), the only characteristic E_{2g} peak of monolayer h-BN occurring at around 1372 cm^{-1} was obtained at multiple sample locations in the Raman spectra. Besides, regardless if the supported PMMA was removed by either annealing or acetone, the peak position remained invariant. Furthermore, the optical band gap (OBG) of h-BN was derived using its absorbance. For a direct band gap material, the absorption coefficient, α is given by,

$$\alpha = \frac{A}{t} = \frac{a(E - E_g)^{1/2}}{E}, \qquad \text{(Eq. 3.1)}$$

where A, t, a, E, and E_g are absorbance, thickness, proportionality constant, photon energy, and optical band gap, respectively [30]. By plugging the h-BN thickness obtained through AFM into Eq. 3.1, the optical band gap, E_g, can be extracted as shown in Fig. 3.12 (b) inset. The value found was 6.07 eV was consistent with the one of monolayer h-BN, while bi-, few-, and bulk h-BN have E_g values of 5.94, 5.84, and 5.2-5.4 eV, respectively [14].

Thus, from all the characterizations of the uniform h-BN layer synthesized using a Pt foil, we concluded that the formation of monolayer had been achieved; the growth condition (T_{src}=80 °C, T_{sub}=1100 °C, t_{growth}=20 min) was more excessive than the Cu-mediated h-BN growth to yield multilayer h-BN (T_{src}=80 °C, T_{sub}=1020 °C, t_{growth}=20 min, see Fig. 3.7(c)). Therefore, the h-BN growth on a Pt foil was regarded as self-limiting. The morphology change of h-BN with respect to the process parameters was followed with this Pt foil as discussed below.

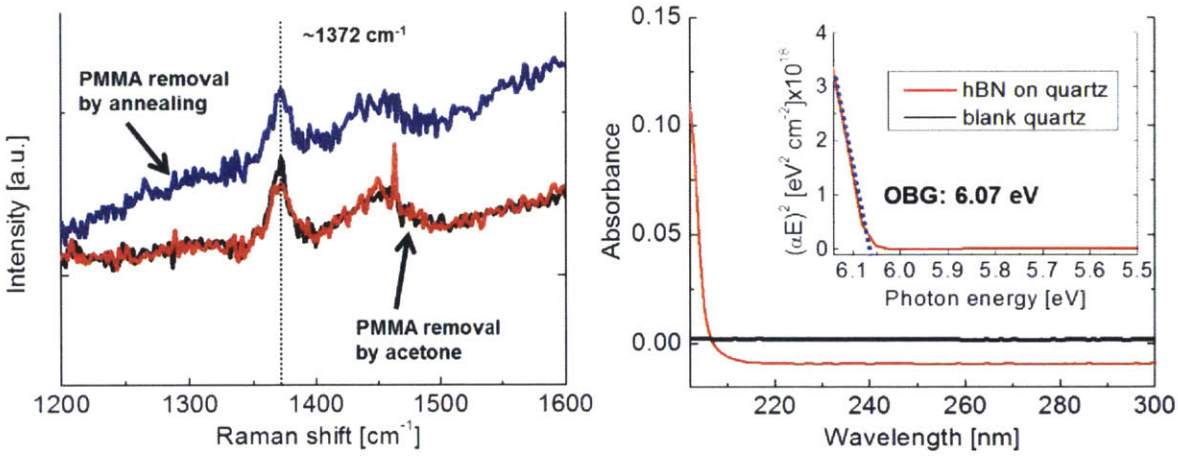

Figure 3.12 (a) Raman spectroscopy of h-BN transferred onto a SiO_2/Si substrate. Regardless of how the supported PMMA was removed, the E_{2g} peak of monolayer h-BN was observed at around 1372 cm^{-1}. (b) Absorbance of h-BN transferred onto a quartz substrate and a blank quartz substrate as a reference. From the result, a value of 6.07 eV for the optical band gap (OBG) was extracted, which is consistent with the one of monolayer h-BN.

3.2.3.3 Effect of the source activation temperature, T_{src}, and growth time

Different from the h-BN grown using a Cu foil, there was no change in the h-BN morphology with respect to the T_{src} and growth time as shown in Figure 3.13. In this study, the effects of other parameters, such as the T_{sub} or the hydrogen flow rate, were not investigated. Like an earlier observation [15], additional multilayer h-BN was not created, once monolayer formed. Besides, there was no particular difference in the h-BN morphology as the T_{src} was varied. In addition to the self-limiting growth characteristics, one difference from the Cu-mediated h-BN growth was the high growth rate of h-BN. Even under the mildest growth condition, like T_{src} at 40 °C for 2 min, the monolayer already formed. In fact, a lower T_{src} than 40 °C, h-BN did not form. Therefore, the shape of h-BN nuclei on Pt could not be identified although the tests T_{sub} is lower than 1100 °C may help to figure this out.

These self-limiting growth behaviors and the high growth rate of h-BN may be understood by the strong interaction between Pt and h-BN and by the high catalytic activity of Pt to help decomposing borazine, respectively. The binding energy between Pt and h-BN was calculated to be 0.34 eV while the one with Cu was 0.19 eV [26]. This difference may give rise to the suppression of multilayer h-BN nucleation on the Pt surface. Note that for the Cu-mediated growth, the multilayer did not form as a layer-by-layer-like atomic layer deposition (ALD), but rather started from multilayer nuclei in a manner of the Volmer-Weber growth. Hence, the lack of the multilayer nuclei on the Pt surface only allowed for growth in the lateral direction to form a monolayer. In addition, the high catalytic activity of Pt for dissociative hydrogen adsorption promoted the rate of decomposition of borazine by the help of reactive hydrogen atoms. While the activation energy for the dissociation of hydrogen on Cu surface is 0.5 eV-0.57 eV [31], the hydrogen dissociation on Pt surface is almost barrier-less [32]. In the competition of surface reactions occurring on the metal surface between the decomposition of borazine and the dissociative adsorption of hydrogen, Pt surface appears to facilitate the generation of reactive hydrogen atoms and increase the growth rate of h-BN. Once the Pt surface is covered by a monolayer of h-BN, there is no surface site of Pt to catalyze the decomposition reaction of hydrogen, thus attaining the self-limiting growth.

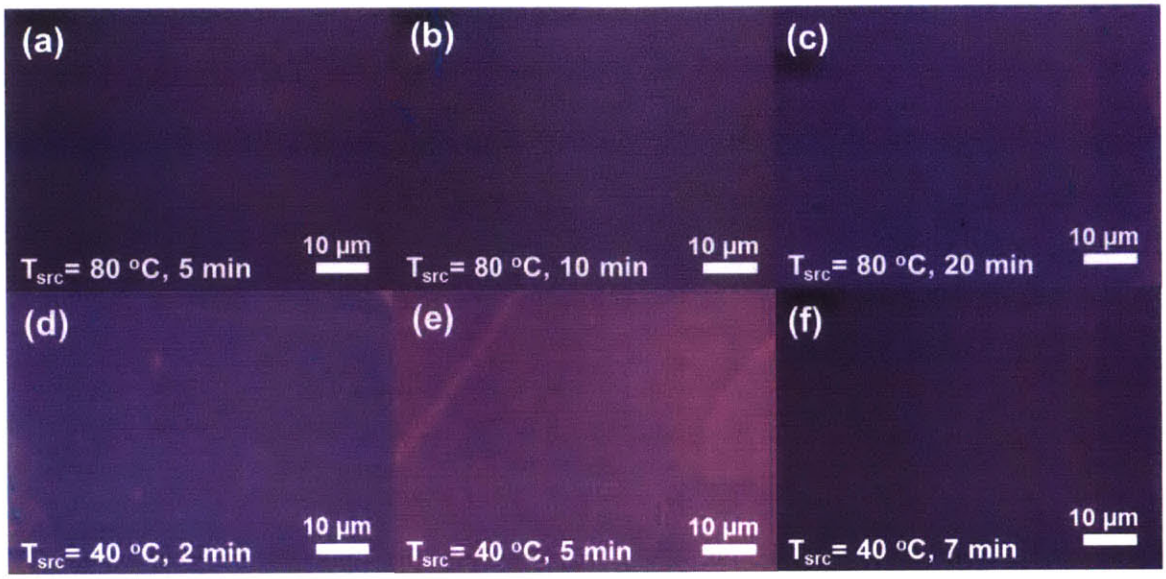

Figure 3.13 OM images of h-BN samples grown using a Pt foil transferred onto a SiO_2/Si substrate. The T_{src} and growth time changed, while T_{sub} and the flow rate of H_2 were held at 1100 °C and 10 sccm, respectively.

3.2.3.4 Microstructure of h-BN

Since the h-BN was a monolayer, its morphology followed the surface corrugation of the underlying Pt as can be seen in Figure 3.14(a) and (b). Like the SEM images in Fig. 3.10(a)-(b), it was challenging to identify as-grown h-BN on the Pt substrate. After transferring the h-BN onto a SiO_2/Si substrate and removing the supporting PMMA using acetone, the surface feature of h-BN appeared to have local multilayers and to be rough in general, as illustrated in Fig. 3.14(c). However, after annealing with H_2 and Ar at 500 °C for 2 hours under AP, the surface was drastically smoothened and no features that looked a multilayer were observed, as presented in Fig. 3.14(d). In other words, the PMMA on h-BN was not completely removed by acetone and the annealing process should be the last step to prepare a pristine h-BN on a target substrate. This annealing process was inert to h-BN, as indicated in Fig. 3.12(a).

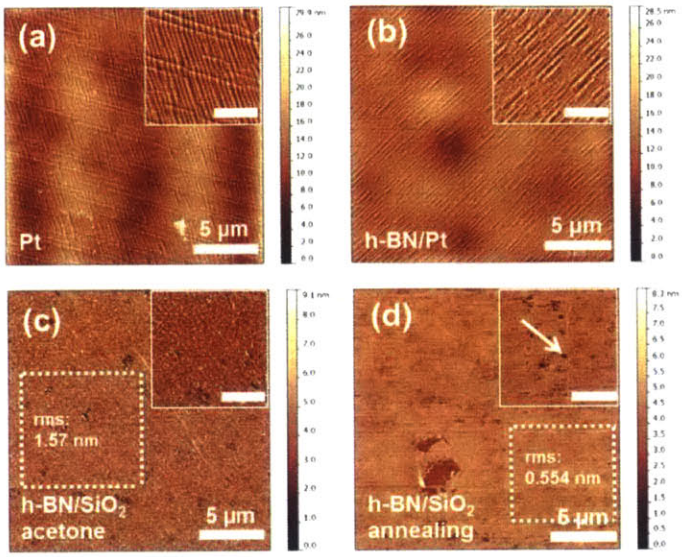

Figure 3.14 AFM height images of (a) a bare Pt foil, (b) An as-grown h-BN layer on the Pt foil with the growth conditions of Fig. 3.13 (e), (c) as-transferred h-BN on a SiO_2/Si substrate where the supported PMMA was removed by acetone, and (d) h-BN on a SiO_2/Si substrate after annealing with H_2 and Ar at 500 °C for 2 hours in AP. Insets are the magnified images of each sample, respectively, whose scale bars are 2 μm. A wrinkle of h-BN is indicated as an arrow in the inset in (d).

3.2.3.5 h-BN and underlying Pt

When the h-BN was transferred onto a SiO_2/Si substrate, sharply and linearly defined breakages of h-BN were observed quite often like that showed in Fig. 3.13(e). As can be seen in Figure 3.15, in low magnification OM images, such broken regions appeared to be cracked around h-BN regardless of the growth condition. Interestingly, the shape and length scales of each h-BN island were the same as the underlying Pt grains shown in Fig. 3.10(a). In other words, h-BN can be separated from the underlying Pt grains in a few hundreds of μm scale. There can be two explanations for this effect. First, the h-BN inside a single Pt grain is single crystalline so that the domain boundary of h-BN is coincident with the grain boundary of Pt. This is supported by observation elsewhere [28] that the growth rate of h-BN appears to be dependent to the crystallographic orientation of Pt. In this regard, further study to check whether or not

a single h-BN island has an identical in-plane orientation is required. Another explanation is the bubble transfer. During the bubble transfer, the PMMA/h-BN stack is stripped from the Pt surface, being pushed out by H_2 gas bubbles that are generated on the Pt surface. The grain boundaries had a grooved structure where the density of H_2 bubbles was locally concentrated. Consequently, stronger collisions of H_2 bubbles to the h-BN could break the layer along the grain boundaries. If the first scenario is valid, it will be of interest in the application of h-BN as a device component because single crystalline h-BN on a hundreds of μm scale is sufficiently large for such applications.

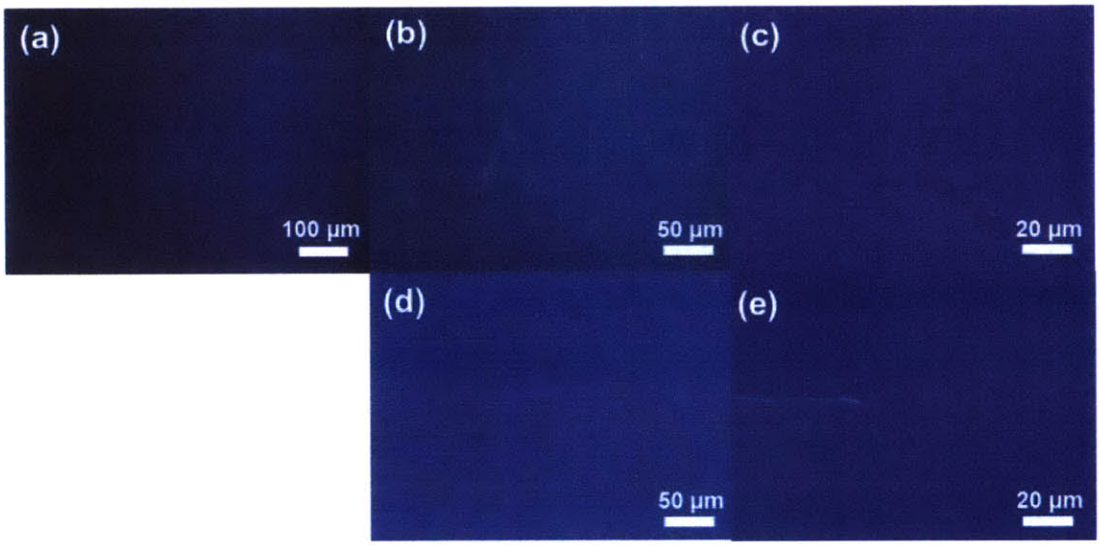

Figure 3.15 Low magnification OM images of h-BN samples grown using a Pt foil transferred onto a SiO_2/Si substrate. The h-BN in (a)-(c) was obtained with T_{sub} and T_{src} at 1100°C and 60 °C for 10 min of growth time, respectively. The h-BN in (d)-(e) was obtained with T_{sub} and T_{src} at 1050°C 40 °C for 4 min of growth time, respectively. The flow rate of H_2 was commonly fixed at 10 sccm, respectively.

3.2.3.6 h-BN as a graphene substrate

The uniform monolayer h-BN obtained with a Pt foil provides a potential to use the h-BN as a graphene substrate like a mechanically exfoliated h-BN [1]. After confirming the feasibility through

Raman spectroscopy of graphene transferred on an h-BN sample, the electronic properties were characterized by fabricating field effect transistor (FET) devices.

- Raman spectroscopy

To compare the Raman spectra of graphene with respect to the underlying substrates, a monolayer h-BN sample synthesized on a Pt foil was transferred onto a SiO_2/Si substrate at first. After taking off the supporting PMMA on h-BN, a larger monolayer graphene sheet prepared using a Cu foil was transferred on top of the h-BN. As a result, as can be seen in Figure 3.16, graphene was either overlapped on the h-

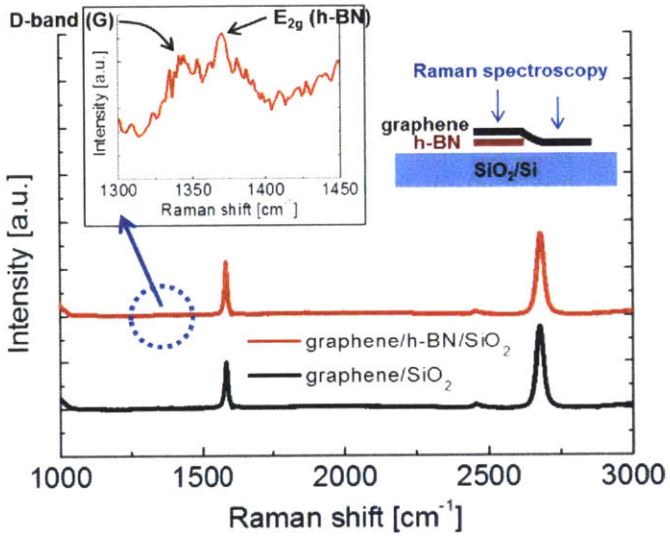

Figure 3.16 Raman spectroscopy of graphene transferred onto two regions: (red) on monolayer h-BN transferred from a Pt growth substrate and (black) on a bare SiO_2/Si substrate. The graphene studied here was prepared using a Cu foil. For graphene on h-BN, the characteristic E_{2g} peak of h-BN could be deconvoluted by the D-band of graphene between 1300 and 1400 cm^{-1} (see inset).

BN or placed on a bare SiO_2 surface. Corresponding Raman spectra on both locations are shown in the figure together. For the graphene on h-BN, the characteristic E_{2g} peak from h-BN was confirmed, and

distinguished from the D-band of graphene in between 1300 and 1400 cm^{-1}. Interestingly, from the Raman spectra obtained on multiple locations in each region, ω_G and I_D/I_G of the graphene on SiO_2 were found to be 1588.3±2.7 cm^{-1} and 0.18±0.06, respectively, while those of the graphene on h-BN were 1584.9±0.8 cm^{-1} and 0.11±0.06, respectively. The redshift in ω_G of about 4 cm^{-1} by the insertion of h-BN between graphene and SiO_2 is considered to be a slight but significant change. Moreover, even though the E_{2g} peak intensity was included, the I_D/I_G of the graphene on h-BN was smaller than for the graphene on SiO_2. Therefore, it was inferred that this graphene sample transferred on h-BN was less doped and less defective, thereby expecting relatively higher carrier mobility on this graphene sample.

- Device fabrication

Based on the observations from Raman spectroscopy, the electronic properties of graphene were investigated by fabricating FET devices. To exclude the scatterings caused by the domain boundary of graphene, several single crystalline graphene flakes a few hundreds of μm-wide were synthesized inside a Cu enclosure, as shown in Figure 3.17(a), and this topic was introduced in Chapter 2. Furthermore, since the PMMA residue on a h-BN surface can act as a scattering center for graphene as discussed above, the

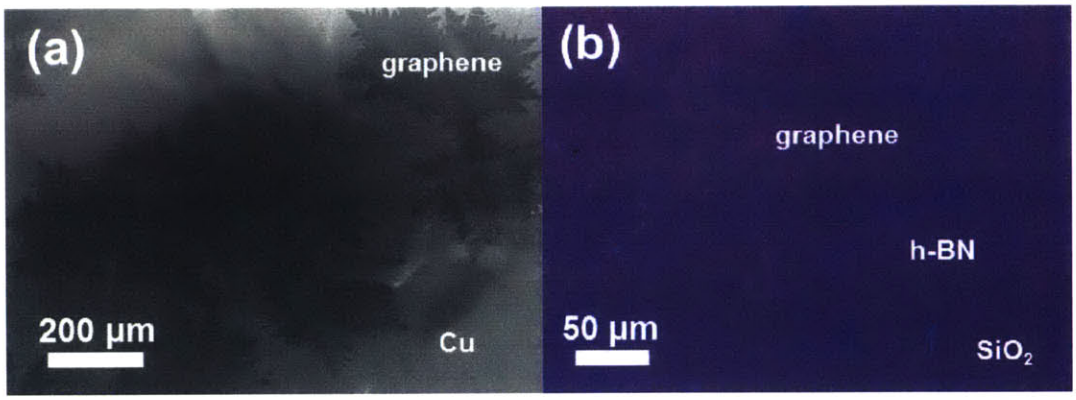

Figure 3.17 (a) SEM image of as-grown graphene flakes on a Cu foil. (b) OM image of the graphene of (a) after being transferred onto a SiO_2/Si substrate where monolayer h-BN synthesized using a Pt foil had been transferred previously.

PMMA/graphene stack, prepared by the wet-transfer method, was directly transferred onto a monolayer h-BN on a Pt foil. Subsequently, the PMMA/graphene/h-BN stack was peeled off from the Pt foil by the bubble transfer method, and then the stack was placed on a 300 nm-thick SiO_2/Si substrate. Finally, the PMMA on graphene was removed by acetone, leaving the graphene/h-BN on the SiO_2/Si substrate, as shown in Fig. 3.17(b).

In the following, graphene FET device were fabricated after the process steps discussed in the earlier sec. **2.3.2**. Figure 3.18 shows the corresponding electrical characterization results. In the earlier section, the notable improvement of carrier mobility of graphene was highlighted by just using a single crystalline graphene flakes with a big domain. However, by placing such single crystalline flakes onto a monolayer h-BN, further enhancement of carrier mobility by ~30% was obtained. The corresponding carrier mobility was achieved to be 9519.2±884.9 $cm^2\ V^{-1}s^{-1}$. This value is highly remarkable because the measurement was carried out in an ambient air at RT. If the devices are placed in a controlled environment free from polar adsorbates, a far better device performance can be expected. Recalling the Matthiessen's rule (Eq. 2.8), the improvement of carrier mobility in this case is regarded as mainly arising from the mitigation of the electron-phonon scattering. It is true that the h-BN substrate passivates the polar –OH group of SiO_2 partially responsible for the hole-doping in graphene, thereby suppressing the charged impurity scattering. However, as can be seen in Fig. 3.18(a), the carrier density was not significantly reduced with the passivation by h-BN at graphene/SiO_2 interface. When the SiO_2 was treated by hexamethyldisilazane (HMDS) converting the polar –OH groups into non-polar $–CH_3$ groups, a prominent shift in the G-band was not observed in Raman spectroscopy, which will be discussed in the sec. **4.2.2**.

Consequently, it is inferred that one monatomic layer of h-BN effectively negates the charge puddles from the SiO_2 phonons that scatter carrier transport. This result encourages further experiments to use the monolayer h-BN as an excellent graphene passivation layer. For example, it is of interest to see the difference of carrier mobility with two sheets of monolayer h-BN at the graphene/SiO_2 interface. Otherwise, the monolayer h-BN can be used as a capping layer over the surf ace of graphene to protect

from ambient adsorbates.

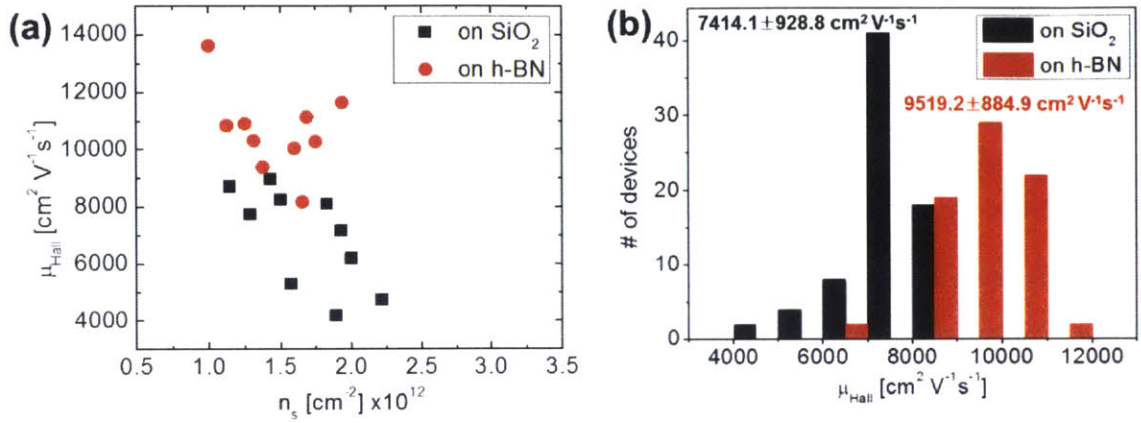

Figure 3.18 (a) Carrier density and the corresponding μ_{Hall} of each 10 devices fabricated on a SiO_2/Si substrate and an h-BN sample grown by a Pt foil, (b) Entire μ_{Hall} of the fabricated FET devices fabricated on a SiO_2/Si substrate and an h-BN sample grown by a Pt foil. The average values of μ_{Hall} of each type of graphene FET devices are included. The data of the sample, graphene devices fabricated on a SiO_2/Si substrate is the reproduced one in Fig. 2.8, the single crystalline graphene flakes.

3.2.3.7 Conclusion

Perceiving the challenges in the Cu-mediated h-BN growth, a Pt foil was attempted for use as a growth substrate of h-BN. Different from the growth by using a Cu foil, as a result, when using a Pt foil a continuous monolayer of h-BN was simply obtained with a wide process window. Interestingly, the growth feature was also self-limiting. Even if more severe conditions had been applied than a Cu-mediated growth by which lots of multilayer h-BN resulted, with the Pt foil a pristine monolayer was grown without any multilayer formation. This self-limiting growth was attributed to the high catalytic activity of Pt to dissociate hydrogen for helping the decomposition of borazine. The quality of this monolayer h-BN was confirmed as reasonably good through various characterization procedures. This allowed the growth of h-BN with a high enough quality for potentially being used as a graphene substrate.

Remarkably, the carrier mobility of graphene devices fabricated on the h-BN was improved by ~30% relation to what was achieved using a SiO_2 surface. This result demonstrated that h-BN grown on a Pt foil can be used as an effective device component in graphene-based applications. Furthermore, as an atomic layered insulator, a new type of application like a tunneling device could be expected with this type of h-BN, along with other possibilities.

3.3 Synthesis of a Graphene/h-BN hybrid structure

3.3.1 Introduction

The growth of graphene/h-BN hybrid structure is of interest in terms of its unusual physical property like opening a band gap with a special stacking orientation [18] or the isolation of an h-BN surface from the surrounding contamination. Considering the graphene/h-BN hybrid structure that was obtained by multiple transfer processes, this contamination can include both a PMMA residue and moisture adsorption, thereby degrading the property of the graphene that is transferred on top.

It was amenable to set up the growth system for the graphene/h-BN hybrid structure by slightly modifying the established h-BN growth system as described with Fig. 3.2. All we needed to do was to add a CH_4 gas line to the system. In this study, based on the earlier result [19], the graphene/h-BN hybrid structure was demonstrated in a single growth process.

3.3.2 Experimental

Like the h-BN growth, a 127 μn-thick Cu foil (99.9%, Alfa Aesar) was used as a substrate. As a pre-treatment, the Cu surface was electropolished with a phosphoric acid solution. Since the nucleation of graphene requires Cu surface for its catalytic activity, the firstly growing h-BN should be discontinuous. Such h-BN flakes could be obtained with the various conditions discussed earlier, but we attempted to exploit the backward reaction of (3.2) by using hydrogen as an etching agent for h-BN. As can be seen in Figure 3.19(a), well-aligned triangular h-BN flakes were obtained with a growth condition where the T_{sub},

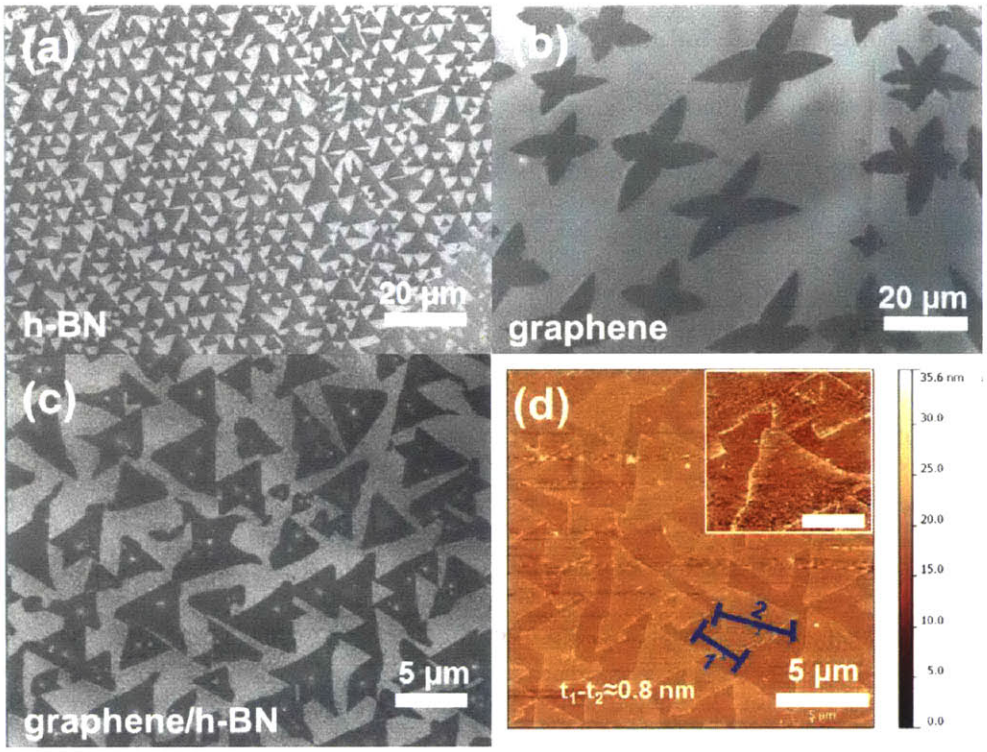

Figure 3.19 (a) SEM image of as-grown h-BN on a Cu foil where the T_{sub}, T_{src} and the H_2 flow rate were fixed at 1050 °C, 60°C, and 10 sccm, respectively, for 9.5 min of growth time. The h-BN precursor was supplied for the first 9 min. (b) SEM image of as-grown graphene on a Cu foil where T_{sub} was fixed at 1050 °C with the flow of CH_4 and the H_2 flow at 10 sccm and 1 sccm, respectively, for 1 min. (c) SEM image of the graphene/h-BN hybrid structure on a Cu foil. After the h-BN growth where T_{sub} was at 60°C for 10 min, the process was paused for 10 s, and then 2 sccm of CH_4 was flowed for 15 s. The T_{sub} and the flow rate of H_2 were fixed at 1050 °C and 10 sccm, respectively, through the whole process. (d) AFM height image of the transferred graphene/h-BN hybrid structure in (c) onto a SiO_2/Si substrate. The hybrid region was thicker than the inside h-BN region by ~0.8 nm. A high magnification image is shown in the inset with a scale bar of 2 μm.

T_{src} and the H_2 flow rate were fixed at 1050 °C, 60°C, and 10 sccm, respectively, for 9.5 min of growth time. This growth condition was similar to the one in Fig. 3.6(a), but the h-BN precursor was supplied for

the first 9 min. In other words, only 10 sccm of hydrogen was flowed for the last 30s before cooling. This hydrogen flow contributed to etch the h-BN which was supposed to be continuous. Because the survived h-BN regions were considered as relatively stable, it was inferred that the hydrogen preferentially attacked the unstable defective regions between the domains, *i.e.*, the domain boundaries.

After setting up the condition to prepare graphene flakes shown in Fig. 3.19(b), the growth of the graphene/h-BN hybrid structure was implemented. For the first h-BN growth, T_{src} was 60°C as before, but the growth time and the pausing time was 10 min and 10s, respectively. This was because the h-BN could be etched in the subsequent graphene growth. As a result of the subsequent CH_4 flow of 2 sccm for 15 s, the structure shown in Fig. 3.19(c) was obtained. Looking into the shape that was obtained carefully, it was found that each triangular point of the h-BN flakes turned blunt. The AFM height image of this sample transferred onto a SiO_2/Si substrate in Fig. 3.19(d) proved that the blunt vertex regions were a little thicker than the inside h-BN region by ~0.8 nm. This thickness certainly corresponded to the thickness of graphene with two layers at least, but the thickness difference confirmed the formation of a hybrid structure on each vertex. Further characterizations like scanning kelvin probe microscopy (SKPM), Raman spectroscopy, or TEM will be able to determine the structure more exactly.

References

[1] Dean CR, Young AF, Meric I, Lee C, Wang L, Sorgenfrei S, et al. Boron nitride substrates for high-quality graphene electronics. Nature Nanotechnology. 2010;5(10):722-6.

[2] Adams AC. CHARACTERIZATION OF FILMS FORMED BY PYROLYSIS OF BORAZINE. Journal of the Electrochemical Society. 1981;128(6):1378-9.

[3] Kubota Y, Watanabe K, Tsuda O, Taniguchi T. Deep ultraviolet light-emitting hexagonal boron nitride synthesized at atmospheric pressure. Science. 2007;317(5840):932-4.

[4] Auwarter W, Kreutz TJ, Greber T, Osterwalder J. XPD and STM investigation of hexagonal boron nitride on Ni(111). Surface Science. 1999;429(1-3):229-36.

[5] Muller F, Stowe K, Sachdev H. Symmetry versus commensurability: Epitaxial growth of hexagonal boron nitride on Pt(111) from B-trichloroborazine (ClBNH)(3). Chemistry of Materials. 2005;17(13):3464-7.

[6] Morscher M, Corso M, Greber T, Osterwalder J. Formation of single layer h-BN on Pd(111). Surface Science. 2006;600(16):3280-4.

[7] Joshi S, Ecija D, Koitz R, Iannuzzi M, Seitsonen AP, Hutter J, et al. Boron Nitride on Cu(111): An Electronically Corrugated Monolayer. Nano Letters. 2012;12(11):5821-8.

[8] Sutter P, Lahiri J, Albrecht P, Sutter E. Chemical Vapor Deposition and Etching of High-Quality Monolayer Hexagonal Boron Nitride Films. Acs Nano. 2011;5(9):7303-9.

[9] Fazen PJ, Remsen EE, Beck JS, Carroll PJ, McGhie AR, Sneddon LG. SYNTHESIS, PROPERTIES, AND CERAMIC CONVERSION REACTIONS OF POLYBORAZYLENE - A HIGH-YIELD POLYMERIC PRECURSOR TO BORON-NITRIDE. Chemistry of Materials. 1995;7(10):1942-56.

[10] Shi Y, Hamsen C, Jia X, Kim KK, Reina A, Hofmann M, et al. Synthesis of Few-Layer Hexagonal Boron Nitride Thin Film by Chemical Vapor Deposition. Nano Letters. 2010;10(10):4134-9.

[11] Song L, Ci L, Lu H, Sorokin PB, Jin C, Ni J, et al. Large Scale Growth and Characterization of Atomic Hexagonal Boron Nitride Layers. Nano Letters. 2010;10(8):3209-15.

[12] Lee KH, Shin H-J, Lee J, Lee I-y, Kim G-H, Choi J-Y, et al. Large-Scale Synthesis of High-Quality Hexagonal Boron Nitride Nanosheets for Large-Area Graphene Electronics. Nano Letters. 2012;12(2):714-8.

[13] Kim KK, Hsu A, Jia X, Kim SM, Shi Y, Hofmann M, et al. Synthesis of Monolayer Hexagonal Boron Nitride on Cu Foil Using Chemical Vapor Deposition. Nano Letters. 2012;12(1):161-6.

[14] Gao Y, Ren W, Ma T, Liu Z, Zhang Y, Liu W-B, et al. Repeated and Controlled Growth of Monolayer, Bilayer and Few-Layer Hexagonal Boron Nitride on Pt Foils. Acs Nano. 2013;7(6):5199-206.

[15] Kim G, Jang AR, Jeong HY, Lee Z, Kang DJ, Shin HS. Growth of High-Crystalline, Single-Layer Hexagonal Boron Nitride on Recyclable Platinum Foil. Nano Letters. 2013;13(4):1834-9.

[16] Liu Z, Ma L, Shi G, Zhou W, Gong Y, Lei S, et al. In-plane heterostructures of graphene and hexagonal boron nitride with controlled domain sizes. Nature Nanotechnology. 2013;8(2):119-24.

[17] Liu L, Park J, Siegel DA, McCarty KF, Clark KW, Deng W, et al. Heteroepitaxial Growth of Two-Dimensional Hexagonal Boron Nitride Templated by Graphene Edges. Science. 2014;343(6167):163-7.

[18] Giovannetti G, Khomyakov PA, Brocks G, Kelly PJ, van den Brink J. Substrate-induced band gap in graphene on hexagonal boron nitride: Ab initio density functional calculations. Phys Rev B. 2007;76(7).

[19] Kim SM, Hsu A, Araujo PT, Lee Y-H, Palacios T, Dresselhaus M, et al. Synthesis of Patched or Stacked Graphene and hBN Flakes: A Route to Hybrid Structure Discovery. Nano Lett. 2013;13(3):933-41.

[20] Bokdam M, Brocks G, Katsnelson MI, Kelly PJ. Schottky barriers at hexagonal boron nitride/metal interfaces: A first-principles study. Physical Review B. 2014;90(8).
[21] Auwarter W, Suter HU, Sachdev H, Greber T. Synthesis of one monolayer of hexagonal boron nitride on Ni(111) from B-trichloroborazine (ClBNH)(3). Chemistry of Materials. 2004;16(2):343-5.
[22] Liu Y, Bhowmick S, Yakobson BI. BN White Graphene with "Colorful" Edges: The Energies and Morphology. Nano Letters. 2011;11(8):3113-6.
[23] Reich S, Ferrari AC, Arenal R, Loiseau A, Bello I, Robertson J. Resonant Raman scattering in cubic and hexagonal boron nitride. Physical Review B. 2005;71(20).
[24] Gorbachev RV, Riaz I, Nair RR, Jalil R, Britnell L, Belle BD, et al. Hunting for Monolayer Boron Nitride: Optical and Raman Signatures. Small. 2011;7(4):465-8.
[25] Xu Z, Buehler MJ. Interface structure and mechanics between graphene and metal substrates: a first-principles study. Journal of Physics-Condensed Matter. 2010;22(48).
[26] Laskowski R, Blaha P, Schwarz K. Bonding of hexagonal BN to transition metal surfaces: An ab initio density-functional theory study. Physical Review B. 2008;78(4).
[27] Hofmann M, Shin YC, Hsieh Y-P, Dresselhaus MS, Kong J. A facile tool for the characterization of two-dimensional materials grown by chemical vapor deposition. Nano Research. 2012;5(7):504-11.
[28] Park J-H, Park JC, Yun SJ, Kim H, Luong DH, Kim SM, et al. Large-Area Monolayer Hexagonal Boron Nitride on Pt Foil. Acs Nano. 2014;8(8):8520-8.
[29] Singh SK, Neek-Amal M, Costamagna S, Peeters FM. Thermomechanical properties of a single hexagonal boron nitride sheet. Physical Review B. 2013;87(18).
[30] Yuzuriha TH, Hess DW. STRUCTURAL AND OPTICAL-PROPERTIES OF PLASMA-DEPOSITED BORON-NITRIDE FILMS. Thin Solid Films. 1986;140(2):199-207.
[31] Sakong S, Gross A. Dissociative adsorption of hydrogen on strained Cu surfaces. Surface Science. 2003;525(1-3):107-18.
[32] Zhou C, Wu J, Nie A, Forrey RC, Tachibana A, Cheng H. On the sequential hydrogen dissociative chemisorption on small platinum clusters: A density functional theory study. Journal of Physical Chemistry C. 2007;111(34):12773-8.

Chapter 4. Transfer process

4.1 Background

Since graphene is basically a monatomic layer, when it is transferred onto a target substrate, a supporting layer (also referred to as protective layer or sacrificial layer) providing mechanical robustness and handling convenience is typically required. For the mechanical exfoliation of graphene from HOPG, an adhesive tape plays a supporting role. This mechanical transfer process can also be employed on the large-sized CVD-G grown on metallic substrates. However, since it is challenging to homogeneously control the relative adhesion between the tape/graphene and graphene/metal substrate, such transfer tends to result in holes and cracks in the graphene layer, which are detrimental to the graphene quality as a large-area film. Therefore, instead of the mechanical exfoliation, the most straightforward transfer process is to isolate the protective layer/graphene stack by chemically etching the underlying metal substrate and then to transfer the stack onto a target substrate, and finally to remove the protective layer, leaving the graphene on the target substrate. There are two basic requirements for the protective layer: first, it should be resistant to the metal etchant and second, it should be able to be removed without damaging the graphene. Polymers have been found to be very suitable for this purpose, and the most commonly used polymer has been PMMA.

In this chapter, the PMMA-supported transfer process will be carefully investigated. By comparing a CVD-G sample with an Exf-G sample, it will be verified that one of the main reasons that the quality of CVD-G fails during the transfer is the interaction of graphene with the surrounding environments. Afterwards, an optimized transfer process to have a clean graphene surface and to suppress hole-doping in graphene will be presented. Furthermore, by adopting a new supporting polymer, ethylene-vinyl acetate (EVA), we will attempt to challenge the issues connected with the PMMA-supported transfer, such reducing wrinkles on graphene and providing a conformal graphene transfer onto an uneven surface.

4.2 PMMA-supported graphene transfer

4.2.1 Introduction

The PMMA-supported transfer method is the most widely used transfer process for graphene prepared by CVD because it better fulfills the criteria for a supporting layer than other polymers: being inert for the entire transfer process and being selectively and efficiently removable without modifying the properties of the underlying graphene. Figure 4.1 is a schematic diagram illustrating the step-by-step process of the PMMA-supported graphene transfer.

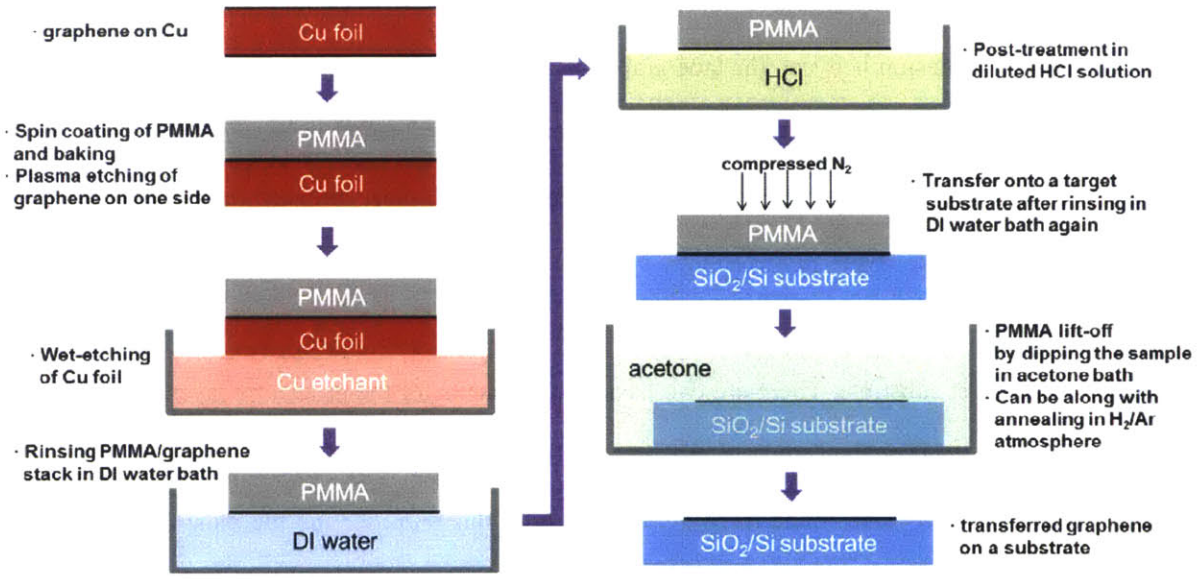

Figure 4.1 Illustration of the general PMMA-supported graphene transfer process onto an arbitrary substrate. In this case, the example was based on the transfer of graphene grown on a Cu foil onto a SiO_2/Si.

First, a PMMA layer with hundreds of nm up to 1 μm in thickness is spun onto an as-grown graphene/metal stack. The thickness of the PMMA layer can be adjusted by changing the spinning rate and the concentration of PMMA solution. To evaporate the solvent in this PMMA layer, the PMMA/graphene/metal stack is baked at a moderate temperature at around 80 °C. Subsequently, this stack is placed into an aqueous metal-specific etchant bath to etch away the metal substrate. When

graphene is grown on a Cu foil by CVD, the entire surface of the Cu foil is covered with graphene. The graphene grown on the back side of the Cu foil thus needs to be removed by O_2 plasma before the etching step [1]. Otherwise, after the Cu is etched, the broken fragments of graphene from the back side (which are not protected by the PMMA layer) will float in the solution and later adhere to the (front side) graphene/PMMA layer. The etching typically takes 20 min to 1 hour, depending on the metal layer thickness and the type of an etchant. Afterwards, the PMMA/graphene stack will float on the etchant due to the hydrophobicity of the stack. Although the etching time is determined by the thickness of the metal substrate and the aggressiveness of the etchant, over-etching is quite often carried out (especially with Cu etchants, such as $FeCl_3$, $Fe(NO_3)_3$ or $(NH_4)_2S_2O_8$). It has not been noticed that there is a clear degradation on the graphene quality even if the etching is carried out much longer than 1 hour. After the metal is etched away, the PMMA/graphene stack is scooped from the etchant and brought to a DI water bath to be rinsed multiple times for an hour up to overnight soaking. Since some etchants (especially $FeCl_3$, $Fe(NO_3)_3$) could leave residues on the graphene in the form of a metallic salt, one additional treatment with HCl, is sometimes used in between the DI water rinsing steps [1]. In the following step, the PMMA/graphene stack floating on the DI water bath is scooped by using the desired target substrate. To remove any possibly trapped water between the PMMA/graphene and the substrate, compressed N_2 is gently blown perpendicular to the PMMA/graphene/substrate stack, pushing out the water droplets through the sides of the PMMA/graphene layer. After this step, the stack is dried to let the PMMA/graphene form a conformal adhesion on the substrate surface. Finally, the PMMA layer is removed by solvents such as acetone, or by annealing under elevated temperature (350-500 °C) and Ar/H_2 gas ambient, or by a combination of both. In fact, the processes described here are the most basic steps for graphene transfer using a PMMA protective layer.

In order to avoid any degradation and to maintain the original quality of the graphene, various approaches were used to improve the transfer procedures. For example, for the graphene surface that is in contact with the target substrate, it is desirable to avoid carrying over any contaminants or impurities from

the etching process. Liang *et al.* [2] reported that a modified treatment from the RCA clean could effectively remove metal nanoparticles and organic contaminants created on graphene surface during the transfer process, resulting in better performance of the fabricated devices. The RCA clean is a standard wafer cleaning steps widely used in microelectronics. This modified RCA (mRCA) process is different from a typical RCA cleaning to clean Si wafers [3], only involving two cleaning steps using diluted H_2O_2/HCl and H_2O_2/NH_4OH solutions in order. The corresponding process flow is shown in Figure 4.2 [2].

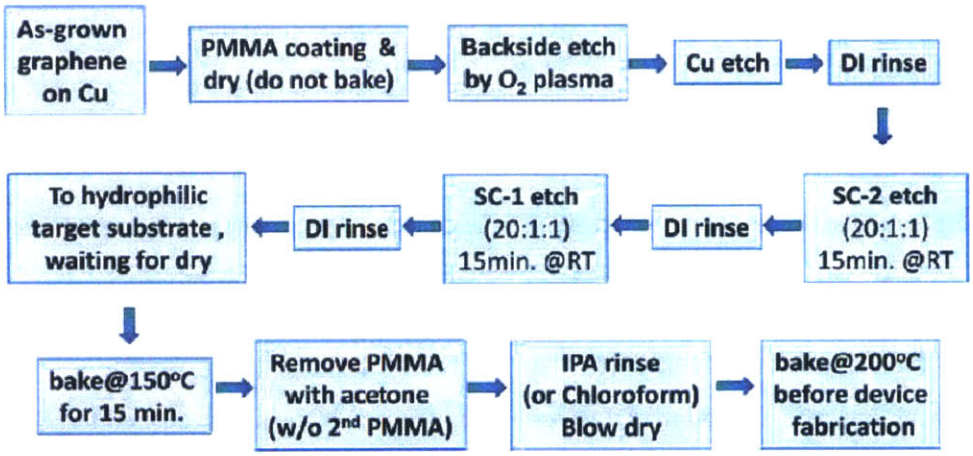

Figure 4.2 "Modified RCA (mRCA)" graphene transfer process flow. Reprinted with permission from [2].

On the other hand, for the other side of the graphene layer where it is in contact with PMMA, it has been a challenge to remove the PMMA completely without leaving residues, and considerable research has been carried out during the last few years to address this problem. For instance, it was reported that after the PMMA/graphene layer is transferred onto the target substrate, if an additional drop of PMMA solution was applied and coated on the PMMA/graphene/substrate stack, this additional drop of solution will help the original PMMA layer to be partially or fully redissolved, which will be helpful in obtaining a

more conformal adhesion of the graphene to the target substrate. In this way, it was found that there is a large reduction in cracks in the transferred graphene layer [4]. To remove the PMMA, since an acetone-only treatment fails to fully remove the PMMA, we found that annealing at an elevated temperature, higher than 360 °C [5], for a few hours under a H_2/Ar atmosphere has been used to follow the acetone treatment [1, 6-8]. This thermal treatment has also been widely used to yield a relatively clean graphene surface with minimal PMMA residues.

However, recent results also pointed out some issues regarding this post-annealing approach. When fabricating devices with exfoliated graphene on SiO_2/Si and investigating whether thermal annealing can effectively remove PMMA (e-beam lithography resist) residues, it was found that thermal treatment above 300 °C in vacuum was required to effectively remove resist residues on graphene surfaces; however, annealing at temperatures >300 °C will concomitantly bring graphene in close contact with SiO_2 substrates and induce increased coupling between them, which leads to heavy hole-doping and severe degradation of the carrier mobility in graphene devices [9].

The second issue is that this annealing treatment also cannot completely remove the PMMA layer. Through a TEM study with a suspended graphene sample placed on a TEM grid, it was found that the PMMA layer is decomposed in a two-step scheme [10]. The PMMA facing the ambient air is easily decomposed at a temperature as low as 160 °C, while the PMMA facing the graphene (within the same PMMA coating) appears to be much harder to decompose. Furthermore, a TEM examination reveals that annealing cannot completely remove the PMMA. Higher temperature annealing (> 250 °C) does not really yield a much cleaner surface compared with lower (200 °C) temperature annealing, but the higher temperature annealing increases the risk of graphene structural damage. It was found that the cleanliness of the graphene surface remains far from satisfactory even after annealing at up to 700 °C in a TEM vacuum chamber. It is suggested that although thermal annealing can help the graphene to have a clean surface by decomposing the PMMA layer, this treatment also adversely promotes the formation of local PMMA residues that have a strong bonding with graphene.

4.2.2 The effects of the PMMA-supported transfer process on the quality of CVD graphene

4.2.2.1 Motivation

When a graphene sample is transferred onto a target substrate, regardless of whether the graphene is CVD-G or Exf-G, two interfaces are formed with surrounding environments: bottom graphene surface/substrate surface and top graphene surface/ambient air atmosphere. Since all the carbon atoms in graphene are on its surface, how these atoms interact with the environments has an important effect on the properties of graphene. Particularly in the fabrication process of a graphene field effect transistor (GFET), these interactions affect the doping level of graphene, thereby shifting the Fermi level relative to the Dirac voltage, and generally reducing the carrier mobility of the graphene in the channel by increased scattering from charged impurities.

To mitigate the hole-doping in graphene, a lot of efforts have been made to either carry out a treatment or even change the substrate to minimize doping or to eliminating residues on the graphene surface. For example, h-BN has been proposed as a better substrate for graphene [11, 12]. Nevertheless, high quality h-BN is only available in the form of mechanically exfoliated flakes at present and furthermore the large scale fabrication of h-BN is still under development. As another example, the passivation of graphene by a hexamethyldisilazane (HMDS) treatment on a SiO_2/Si substrate was reported with an Exf-G sample that showed an improvement of in the graphene carrier mobility [13].

On the other hand, as well as the interaction of graphene with the underlying substrate, the adsorption of polar adsorbates in ambient air, such as oxygen or moisture [14, 15], also contributes to the hole-doping in graphene. These adsorbates are responsible for a discrepancy in the electrical properties of graphene, that are characterized either in air or in vacuum [16]. Furthermore, for CVD-G, PMMA residues can also act as a scattering center, thereby degrading the carrier mobility [17, 18].

Therefore, it can be inferred that the suppression of hole-doping is related to how well both of the graphene interfaces are controlled during the transfer: the bottom graphene surface/substrate surface, and the top graphene surface/ambient air. Additionally, having a clean surface after transfer should be

included for the requirement of a good CVD-G material. Up to now, most works have been developed with either Exf-G or CVD-G, exclusively. A comparison between the two would be highly desirable to confirm the effectiveness of the various approaches and to develop an optimal transfer process for CVD-G. In this work, we adopted the previously developed transfer technologies into our CVD-G and justified our work by applying the same or similar processes to Exf-G, from the transfer onto a target substrate to the fabrication of GFET devices. Furthermore, we also explored the passivation effect of the top graphene surface with HMDS and obtained improved transport properties.

4.2.2.2 Experimental

CVD-MLG samples were prepared by a LPCVD process. The synthesis process followed the established Cu foil-based LPCVD process [1, 19] by flowing H_2 and CH_4, where the growth temperature and pressure were maintained at 1035 °C and at 1.70 Torr, respectively. A 36 um-thick Cu foil (JX Nippon Mining & Metals, Japan) was used as a growth substrate. As a result, uniform MLG was synthesized over the foil. Before transfer, the graphene layer grown on the reverse side of the foil was removed using O_2/He plasma. The transfer process of this CVD-G followed the PMMA-supported wet transfer method, described in Fig. 4.1 [1].

Firstly, PMMA (with a molecular weight of 950,000, Microchem, 9% in Anisole (A9)), further diluted by 50% in anisole, was spun on as-grown graphene on a Cu foil. After baking this PMMA/graphene/Cu foil stack in 80 °C for 5 min, it was brought to a $FeCl_3$ based aqueous Cu etchant (CE-100, TRANSENE) bath for one hour until the Cu foil was completely etched. The resulting PMMA/graphene stack was carefully rinsed with DI water, and was subsequently dipped into 3M HCl solution to remove metallic salts on the graphene surface that were created in the Cu etching step. After 30 min of this treatment, the PMMA/graphene stack was carefully rinsed with DI water again. Such a cleaning method is referred to as "950K_HCl".

As an alternative to the 950K_HCl method, a PMMA/graphene stack cleaned by the mRCA [2]

process presented in Fig. 4.2 was also prepared in order to obtain a better morphology for the graphene. Here, PMMA with a lower molecular weight (495,000, Microchem, 8% in Anisole (A8)), further diluted by 50% in anisole, was used as a supporting layer for the graphene/Cu foil stack. Instead of the 3M HCl treatment in the "950K_HCl" process, a 20:1:1 $H_2O/H_2O_2/HCl$ treatment for 15 min, a careful rinsing with DI water, a subsequent 20:1:1 $H_2O/H_2O_2/NH_4OH$ treatment for 15 min, and a final rinsing with DI water were carried out in this cleaning process (this cleaning process will be referred as "495K_mRCA"). In particular, the PMMA/graphene stack was left on a DI water bath at least for one day before and after the mRCA cleaning in order to have the graphene surface as clean as possible.

As a substrate to transfer graphene, 300 nm-thick SiO_2/Si substrates were commonly used throughout this study and these were cleaned with acetone and isopropyl alcohol (IPA) at first. To investigate the effect of pre-treatment of the SiO_2/Si surface, two types of substrates were prepared: the type referred as "Pre_HMDS" that O_2/He plasma was applied for 5s to the SiO_2/Si surface cleaned by acetone/IPA and then HMDS was coated in an oven at 150 °C for 60s. This type is referred to "Solvents_only" and in this case a blank SiO_2/Si substrate just cleaned with acetone/IPA as a reference. The O_2/He plasma treatment for the "Pre_HMDS" was used to make the substrate surface highly hydrophilic by facilitating Si-OH group which helped the subsequent conformal deposition of HMDS. The previously prepared PMMA/graphene samples that had been floated on the DI water bath were transferred onto these two types of the SiO_2/Si substrates.

Afterwards, as the final step of transfer, the PMMA on graphene was removed using two methods: the type referred to "Post_acetone" dissolved the PMMA by soaking the samples in acetone overnight at RT, and the type referred to "Post_annealing" removed the PMMA by atmospheric annealing for two hours at 500 °C with H_2 and Ar. For a part of samples with "Post_acetone" process, another HMDS coating was implemented on top of the graphene surface, and as a result, this treatment is referred as "Post_HMDS". A highly crystalline Exf-G sample was also prepared by mechanically exfoliating HOPG

Table 4.1 Summary of transfer conditions for prepared CVD-G and Exf-G samples

Sample	Pre-treatment	Cleaning	Post_treatment
SS_CVD-G 950K	Solvents_only	950K_HCl	Post_acetone
HS_CVD-G	Pre_HMDS	950K_HCl	Post_acetone
SA_CVD-G	Solvents_only	950K_HCl	Post_annealing
SS_CVD-G 495K	Solvents_only	495K_mRCA	Post_acetone
SS_Exf-G	Solvents_only		Post_acetone
HS_Exf-G	Pre_HMDS		Post_acetone
SA_Exf-G	Solvents_only		Post_annealing

using an adhesive tape and the sample was then transferred onto a SiO_2/Si substrate. To understand the effect applied to the CVD-G, the same treatments were performed as the above on the SiO_2/Si substrates for Exf-G except for the cleaning process. The transfer conditions of prepared CVD-G and Exf-G samples are thus summarized in Table 4.1.

4.2.2.3 Improvement of the cleaning process

Table 4.2 shows the results of Raman spectroscopy (λ_{laser}=532 nm) characterization performed on the CVD-G and Exf-G samples under different transfer conditions. The average values of ω_G, ω_{2D}, I_{2D}/I_G, and I_D/I_G were calculated from Raman spectra taken 10 or more locations on each sample. Representative spectra obtained in the CVD-G samples and Exf-G samples are given in Figure 4.3(a) and (b), respectively.

First, the effect of the pre-surface treatment was studied. When the CVD-G was transferred onto a SiO_2 substrate treated with HMDS (referred as HS_CVD-G: here 'H' indicates HMDS pretreatment, and 'S' refers to 'solvents only' when removing PMMA on graphene.), a slight redshift of ω_G and ω_{2D}, and an increase of I_{2D}/I_G were observed, compared to the CVD-G on a SiO_2 substrate cleaned with solvents only (referred as SS_CVD-G 950K). This trend was commonly valid in the Exf-G samples as shown in the Table 4.2 and Fig. 4.3(b) through the comparison between the samples referred as HS_Exf-G and

SS_Exf-G. The overall positions of ω_G and ω_{2D} in both of these cases were lower than those of CVD-G. Hence, the mitigation of hole-doping in graphene by the HMDS treatment on a SiO_2 surface was confirmed in both the CVD-G and Exf-G samples.

Table 4.2 Results of ω_G, ω_{2D}, I_{2D}/I_G, and I_D/I_G from Raman spectra on each graphene sample

Sample	ω_G, [cm^{-1}]	ω_{2D}, [cm^{-1}]	I_{2D}/I_G	I_D/I_G
SS_CVD-G 950K	1587.6±1.3	2677.2±1.9	6.8±0.2	0.13±0.03
HS_CVD-G	1586.5±1.9	2676.4±3.9	7.4±0.2	0.13±0.07
SA_CVD-G	1602.1±2.0	2683.7±3.6	2.9±0.1	0.21±0.06
SS_CVD-G 495K	1587.7±0.7	2676.5±0.9	7.9±0.4	0.09±0.03
SS_Exf-G	1585.9±1.8	2677.1±3.0	8.0±0.5	0.09±0.04
HS_Exf-G	1584. 6±0.4	2674.2±0.9	9.1±0.2	0.12±0.04
SA_Exf-G	1607.8±0.8	2689.41.7	4.6±0.1	0.07±0.01

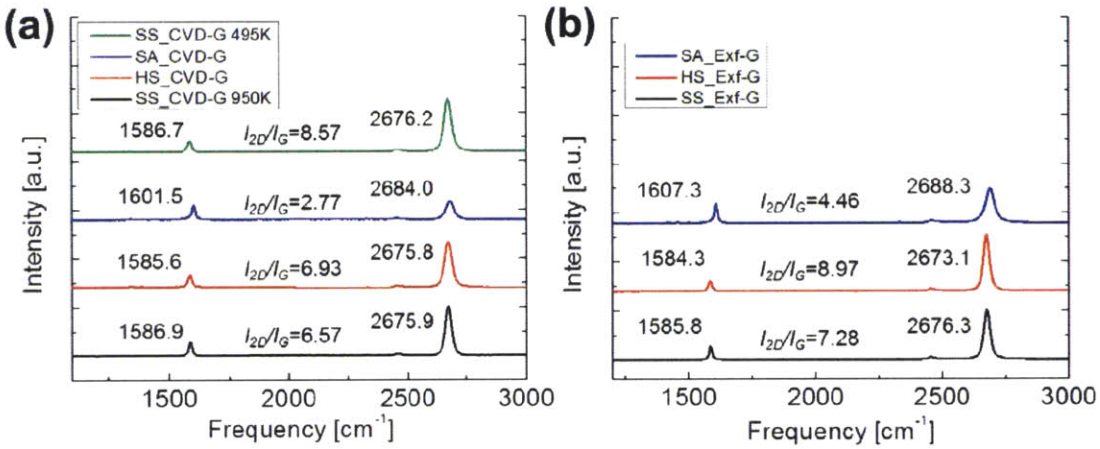

Figure 4.3 Representative Raman spectra of (a) CVD-G samples and (b) Exf-G samples with different transfer conditions provided in Table 4.1. The positions of ω_G and ω_{2D} of each sample are labeled together with I_{2D}/I_G, respectively.

It has been reported that Exf-G brought on a HMDS-treated SiO_2 substrate showed a higher carrier mobility, both by approaching the charge neutrality point all the way to 0 and by suppressing the hysteresis of field effect curves of the back gate voltage (V_{BG}) sweeps [13]. These two effects can account for the improvement in the graphene prepared by this HMDS treatment on the SiO_2 surface. From a chemical standpoint, HMDS can modify the SiO_2 surface with a following chemical reaction,

$$2\,\text{Si-OH} + \text{Me}_3\text{SiNHSiMe}_3 \longrightarrow 2\,\text{Si-O-SiMe}_3 + \text{NH}_3, \tag{4.1}$$

substituting the functional group of SiO_2 as three $-CH_3$ for –OH groups. This reaction is stable up to 500 °C where the –OH group starts to appear again. In contrast to the –OH group that is responsible for the hydrophilic feature of the SiO_2 surface, the three $-CH_3$ groups convert the surface to be hydrophobic. Therefore, the first advantage by the HMDS treatment is to eliminate the trapping of water at the graphene/SiO_2 interface in the transfer process because water molecules in contact with graphene are considered as one of the sources of charge doping in graphene, generally hole-doping [14, 20]. Particularly for CVD-G, water trapping between graphene and SiO_2 surface is more significantly involved than for Exf-G because most PMMA-supported transfers are carried out in water. A PMMA/graphene stack is usually brought wetly onto a SiO_2 surface from a DI water bath. Even if the water droplets are dried out by blowing compressed N_2, water molecules can still be trapped under the graphene layer to some extent, due to the hydrophilicity of the SiO_2 surface. This water together with other charged impurities adsorbed on the defective domain boundaries accounts for the higher degree of hole-doping in CVD-G than in Exf-G [20].

For these reasons, the HMDS coating can prevent the adsorption of these water molecules on the substrate surface. In addition, the weaker interaction of the non-polar $-CH_3$ group on the HDMS-treated surface with graphene than the highly polar –OH group can be expected, giving rise to the partial mitigation of the doping in graphene. Therefore, these hydrophobicity and passivation effects can contribute to the suppressed hole-doping in graphene. No remarkable difference in the I_D/I_G suggests that graphene does not undergo a structural change by the interaction with HMDS while the hole-doping was

mostly mitigated.

The investigation of the top surface of CVD-G was carried out toward two goals: a minimization of the PMMA residue at the end of the transfer and the isolation of the graphene surface from the ambient air which encourages hole-doping in graphene. It has been considered that the polymer residue adsorbed on graphene surface is also one of the sources to promote hole-doping of graphene, since the residue acts as a fixed charge scattering center [17, 18]. Figure 4.4(a) and (d) show the OM images and AFM height images of the samples, SS_CVD-G 950K, respectively. The observable PMMA residue indicated by macro-scale dark and micro-scale white spots in the images, respectively, implied that the use of acetone by itself could not completely eliminate this PMMA on the graphene cleaned by the 950K_HCl method. Instead of soaking in a static acetone bath, placing a PMMA/graphene sample in a stirring acetone bath was tried, but the resulting morphology of graphene showed a similar density of PMMA residue.

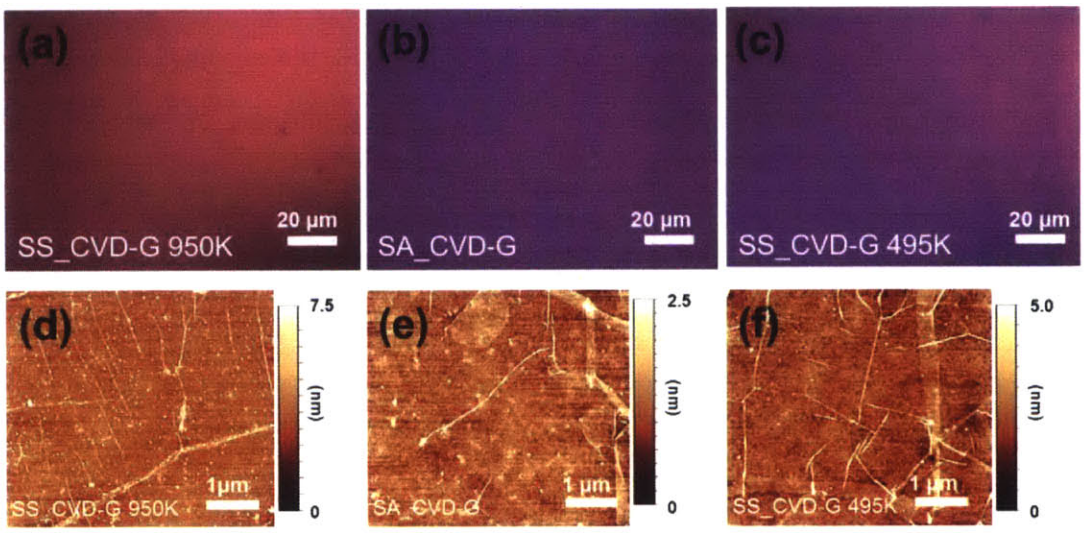

Figure 4.4 (a)-(c) are OM images of transferred CVD-G on a SiO_2/Si substrate with transfer conditions of SS_CVD-G 950K, SA_CVD-G, and SS_CVD-G 495K, respectively. (d)-(f) are the corresponding AFM height images, respectively.

Taking advantage of the weakening of the crosslinking of the PMMA by thermal stress [5], the "Post_annealing" treatment was implemented to effectively remove PMMA. As a result, a clean graphene surface in the sample referred as SA_CVD-G, was obtained, as illustrated in Fig. 4.4(b), although sporadically distributed PMMA residue was still observed along the graphene wrinkles on a small scale, as shown in Fig. 4.4(e). This annealing treatment was expected to alleviate the hole-doping of graphene, not only by excluding the PMMA on the graphene surface, but also by degassing the trapped water molecules and oxygen at the graphene/SiO_2 interface that was responsible for the hole-doping in graphene in the first place. The Raman spectra in Fig. 4.3(a) and Table 4.2, however, showed an opposite phenomenon occurring in the SA_CVD-G sample, as indicated by the remarkable blue shift of the ω_G and ω_{2D}, and the decrease of I_{2D}/I_G, which was consistent with the results observed by other researchers [9, 18, 21].

To explain these observations, we note that it has been known that graphene has a negative thermal expansion coefficient (TEC) of $-8.0\pm0.7\times10^{-6}$ K^{-1} [22] and consequently, both the G band and the 2D band can be red-shifted by a tensile strain [23]. However, over a given temperature range (RT to 500 °C), the TEC of SiO_2 is found to be $\sim7\times10^{-7}$ K^{-1}, much less than that of graphene. Assuming that graphene is pinned onto the SiO_2 surface during both annealing up to 500 °C and cooling down to RT, it was reasonable to exclude the strain effect to account for the blue shift of ω_G and ω_{2D} in the SA_CVD-G sample; consequently, we concluded that such a shift mainly arises from a significant heavy hole-doping in graphene.

The SA_CVD-G sample's ω_G is observed to be higher than 1600 cm^{-1} and I_{2D}/I_G is found to be smaller than 3 in Table 4.2 corresponding to a carrier concentration higher than 2×10^{13} cm^{-2}, which is observed in an electrochemically gated graphene [24]. As illustrated in Fig. 4.3(b) and Table 4.2, a heavy hole-doping was also observed in the Exf-G sample with "Post_annealing" treatment (referred as SA_Exf-G). This result can be attributed to a direct interaction of graphene with the Si-OH of SiO_2 at the interface [25], because water can block charge scattering from the substrate surface [26]. Otherwise, as

previously reported, although the annealing treatment contributed to mitigate hole-doping of graphene in a controlled atmosphere, for example in vacuum [27], when the annealed graphene was just exposed to ambient air, moisture and/or oxygen could become bound to the graphene surface [14, 15], conversely leading to hole-doping. This consequence was considered that the degree of hole-doping occurring in the ambient air exceeded the degree of hole-doping mitigation by the annealing in a reducing atmosphere. Furthermore, annealing at a higher temperature can result in a larger blue shift of ω_G under ambient air condition due to the increase of the susceptibility of the graphene surface, which is facilitated by the adsorption of polar adsorbates after annealing [27].

Therefore, the "Post_annealing" treatment could improve the cleanness of the graphene surface against the PMMA residue, but could also promote hole-doping in ambient air. Furthermore, reportedly annealing at an elevated temperature can strengthen the chemical interaction between PMMA and graphene [10]. In this respect, the notable increase of I_D/I_G in the SA_CVD-G sample in Fig. 4.3(a) and Table 4.2 can be understood by the distortion of sp^2-structure of graphene by the PMMA residue, while I_D/I_G of the SA_Exf-G sample, which was not involved with PMMA, did not show a significant difference in I_D/I_G, as shown in Fig. 4.3(b) and Table 4.2.

Considering these disadvantages of the "Post_annealing" treatment, modifications of PMMA and more careful cleaning of graphene were instead implemented to minimize the PMMA residue. In order to reduce the interaction of PMMA with graphene and to promote the dissolution of PMMA in acetone, a PMMA with a lower molecular weight of 495,000 (4% in anisole) was used instead of the PMMA (4.5% in anisole) used for SS_CVD-G 950K [28]. The thickness of the PMMA was also thinned from 300 nm to 200 nm. The baking step performed in the 950K_HCl method to enhance the adhesion between the PMMA and graphene was also skipped. To achieve a clean graphene surface, the PMMA/graphene stack was thoroughly treated with the mRCA cleaning procedure [2]. The resulting properties of the CVD-G sample prepared by this process are summarized in Table 4.1 and Table 4.2, referring to SS_CVD-G 495K. As shown in Fig. 4.4(c) and (f), this SS_CVD-G 495K sample showed an intact graphene layer on

a SiO_2/Si substrate with negligible PMMA residue. Nevertheless, the doping level in the graphene prepared by this transfer process was not significantly improved, as indicated by the Raman spectroscopy characterization. This contradicted a prior result which showed a modulation of the properties of graphene with respect to the PMMA concentration [28]. To account for this discrepancy, it was inferred that the adsorption of moisture and oxygen in the ambient air had a more dominant effect on the hole-doping of the graphene than came through the polymer residue.

4.2.2.4 HMDS capping on graphene

As a result of the experiments reported above, post treatment was used to protect the top graphene surface from ambient air. Two graphene samples, HS_Exf-G and SS_CVD-G, were exposed to HMDS by soaking each of them for 1 min and then spinning them dry. These samples, after the "Post_HMDS" treatment described above were referred to HH_Exf-G and SH_CVD-G, respectively. As a result of the treatment on these samples, a red shift of ω_G and ω_{2D}, and an increase of I_{2D}/I_G were observed in the Raman spectra as shown in Figure 4.5(a).

This Raman frequency shift by the "Post_HMDS" treatment turned out to be higher than the effect for the "Pre_HMDS" treatment sample. Particularly, when the both "Pre_HMDS" and "Post_HMDS" treatments were applied to the graphene, the lowest ω_G of 1580.9 cm^{-1} and 1585.4 cm^{-1} were observed in the Exf-G (HH_Exf-G) and the CVD-G (HH_CVD-G) samples, respectively. Moreover, no distinguishable change in I_D/I_G was observed after the treatment. The representative Raman spectra obtained in each HH_Exf-G and HH_CVD-G sample are illustrated in Fig. 4.5(b).

Considering the sensitivity of ω_G to the carrier concentration [24, 29], this result was noticeable in the sense that HH_Exf-G showed a nearly negligible carrier concentration in accordance with a ω_G of 1580 cm^{-1}. This approach toward avoiding increases in the carrier concentration of graphene can be understood in a similar manner to the deposition of a passivation layer like Al_2O_3 [30] to avoid the interaction of graphene with ambient moisture and oxygen during the field effect measurement. However, it should be

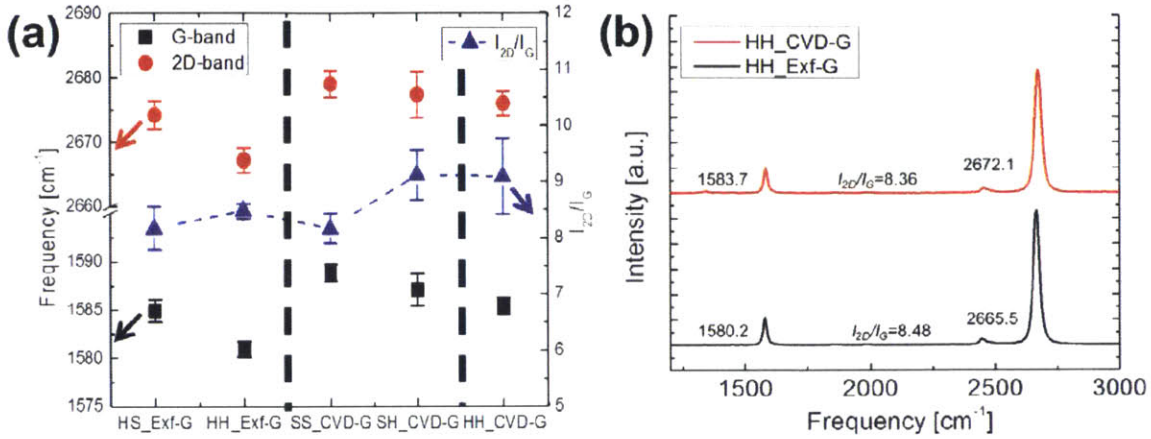

Figure 4.5 (a) The changes in ω_G, ω_{2D}, and I_{2D}/I_G of the Exf-G and CVD-G samples by the "Post_HMDS" treatment. The shifts between HS_Exf-G and HH_Exf-G and between SS_CVD-G and SH_CVD-G were obtained in the same sample, respectively, before and after the treatment. (b) The corresponding representative Raman spectra of an HH_Exf-G sample and an HH_CVD-G sample after the "Post_HMDS" treatment. The positions of ω_G and ω_{2D} of each sample are labeled together with I_{2D}/I_G, respectively.

noted that this treatment was not just used to preserve the graphene surface by capping it [31], but this treatment also gave rise to the mitigation of the doping level in graphene, as proven by the shift of ω_G and ω_{2D}, and the change of I_{2D}/I_G. Moreover, the I_D/I_G remained almost invariant so that no significant structural change was observed in graphene by the HMDS coating.

The mitigation of hole-doping was explained as an exchange of the graphene surface from adsorbed water and oxygen molecules by HMDS molecules. Since the adsorption of water and oxygen on graphene was known to occur as a physisorption with a reversible reaction [14, 15, 27], the higher binding energy of graphene with HMDS than water and oxygen can be expected when HMDS was deposited. Otherwise, the incorporation of the amine group (-NH-) in HMDS to graphene may give rise to a compensation of hole-doping in graphene, similar to the NH_2-terminated self-assembled monolayer (SAM) treatment on a SiO_2 substrate [32]. The treatment was effectively sustainable so that we could observe a remarkably low

ω_G in an HH_Exf-G sample in the Raman spectroscopy characterization carried out two weeks after the "Post_HMDS" treatment.

4.2.2.5 Scanning Kelvin probe microscopy (SKPM) characterization

The surface of CVD-G with respect to the HMDS treatments was analyzed through scanning Kelvin probe microscopy (SKPM) characterization, thereby providing the information on the work function of atomically thin layered materials [33, 34]. The measurement was carried out in ambient air at RT by using an interleave mode equipped in the AFM instrument. This mode allowed obtaining topographical information in the tapping mode and surface potential information in the non-contact mode at a given forward and backward line scan, respectively. A Pt-coated cantilever (AC240TM, Olympus) used in this study was lifted up to 10 nm from the surface for the backward scan while no external gate voltage was applied. A DC voltage was applied to the tip to compensate for the surface potential difference between the cantilever tip and the graphene surface. The contact potential difference (CPD) was defined by,

$$CPD(V) = (\Phi_{tip} - \Phi_{graphene}) / q, \qquad \text{(Eq. 4.1)}$$

where Φ_{tip} and $\Phi_{graphene}$ denote the work functions of the tip and graphene, respectively. Since the work function of the tip is a constant, the degree of doping in graphene can be determined by measuring the CPD [26, 35]. The SKPM measurements were carried out in four types of CVD-G samples, expressed to here as SS, SA, HS, and HH. After taking topography and surface potential images in a 10 μm by 10 μm area, the CPD of graphene was extracted in a 2 μm by 2 μm area in each sample. Figure 4.6(a) and (b) show the topography and surface potential images obtained in the SS_CVD-G sample, respectively.

Considering that the work function for the tip, Φ_{tip} is 4.93 ± 0.05 eV [36], the calculated graphene work function, $\Phi_{graphene}$ of this sample was in a reasonable range from a previously measured value of $\Phi_{graphene}$ ~4.6 eV [37]. However, because the measurement conditions and the tip's state can be susceptible to the measurement environment, the change of relative CPD of graphene in the four samples

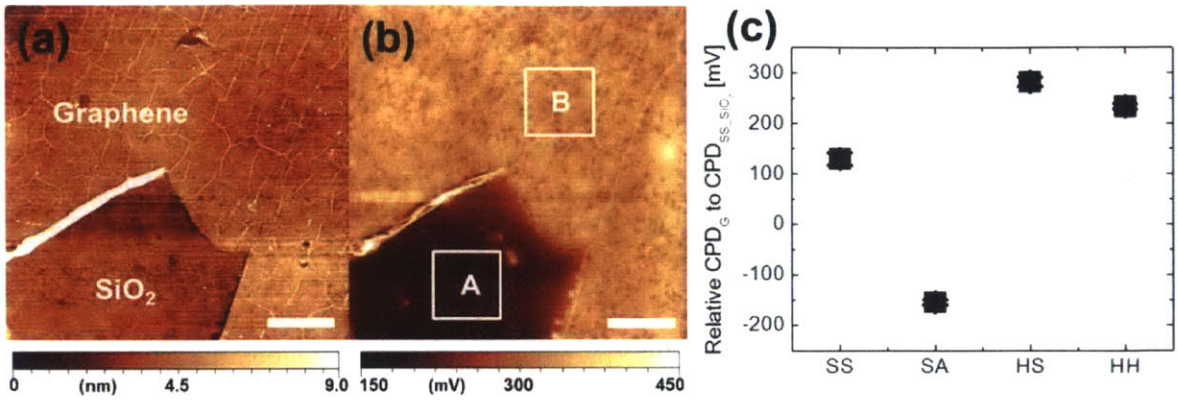

Figure 4.6 (a) AFM height images of a SS_CVD-G sample obtained by the tapping mode in forward scans. (b) The corresponding surface potential image by a non-contact mode in the backward scans. The scale bars in (a)-(b) are both 2 μm. (c) The CPD measured for CVD-G samples of SS, SA, HS, and HH relative to the CPD of SiO_2 in SS_CVD-G.

was monitored relative to the reference CPD of SiO_2 in the SS sample. The results are presented in Fig. 4.6(c). For example, the value of SS in the figure was extracted by subtracting the CPD of SiO_2 from the CPD of graphene here obtained, indicated as white squares A and B in Fig. 4.6(b), respectively.

First, to confirm the correlation between the doping in graphene and the surface potential, a SS sample with a mediocre doping level characterized by ω_G: ~1590.6 cm^{-1} and a SA sample with a heavy hole-doping level characterized by ω_G: ~1604.7 cm^{-1} were compared. Accordingly, a downshift of the relative CPD in ~280 mV was observed in the SA sample. This was understood in terms of the increase of $\Phi_{graphene}$ as ~0.28 eV arising from the decrease of the Fermi level of graphene, *i.e.*, promoting hole-doping in graphene. For the HS sample with a relatively lower hole-doping (ω_G: ~1588.7 cm^{-1}), the upshift of CPD by ~155 mV was observed. This clearly proves the presence of a suppression of hole-doping in graphene by the underlying HMDS layer as indicated in the Raman spectra in Fig. 4.3(a). Although the HH sample was expected to have the lowest hole-doping among the four samples as characterized by Raman spectroscopy (ω_G: ~1587.7 cm^{-1}), the CPD upshift was ~105 mV, and not higher than that of the

HS sample. Because the surface potential information in this HH sample was not just coming from graphene, the surface modification of graphene by the HMDS treatment should be considered for the magnitude of CPD upshift.

4.2.2.6 Device characteristics

The electrical performances of both CVD-G and Exf-G as treated by HMDS were demonstrated in this thesis by fabricating back-gated GFET devices. After transferring a graphene sample on a SiO_2/Si substrate, where the "Pre_HMDS" treatment was carried out, the metallization with Cr/Au layer was implemented on the graphene by evaporation and a subsequent lift-off process, after patterning was accomplished by using e-beam lithography (Raith 150). O_2/He plasma was used to pattern the graphene channels for both Exf-G and CVD-G samples. 5 Exf-GFET devices were thus fabricated where the channel length and width were 3 μm and 1 μm, respectively. For the CVD-GFET devices, 17 of the devices were made with channel widths of either 3.1 μm or 1.1 μm, while the channel length varied from 3 μm to 15 μm. All the measurements were carried out in ambient air at RT. Electrical characterizations on the same device were carried out before and after the "Post_HMDS" treatment for comparisons. Figure 4.7 shows the results obtained from one of the Exf-GFET devices.

It can be seen that the "Post_HMDS" treatment gave rise to the decrease of the voltage at the charge neutrality point (V_{CNP}), as shown in Fig. 4.7(a), while the hysteresis between the voltage sweep directions was almost same. The decrease of V_{CNP} was correlated with the obvious red shift of ω_G in the Raman spectra for this device obtained before and after the "Post_HMDS" treatment. Fig. 4.7(b) shows that the minimum conductance of the device increased after the "Post_HMDS" treatment. Since this implied the decrease of the charged impurity concentration in the graphene [38], the exclusion of polar adsorbates on graphene by the HMDS treatment could be justified in terms of device characteristics. As a result, about 20% of an increase in carrier mobility from 4608.0 $cm^2 V^{-1}s^{-1}$ to 5514.4 $cm^2 V^{-1}s^{-1}$ was observed by the "Post_HMDS" treatment in the lower carrier concentration region at $n[V_G^*]=1.25\times10^{12}$ cm^{-2}, while the

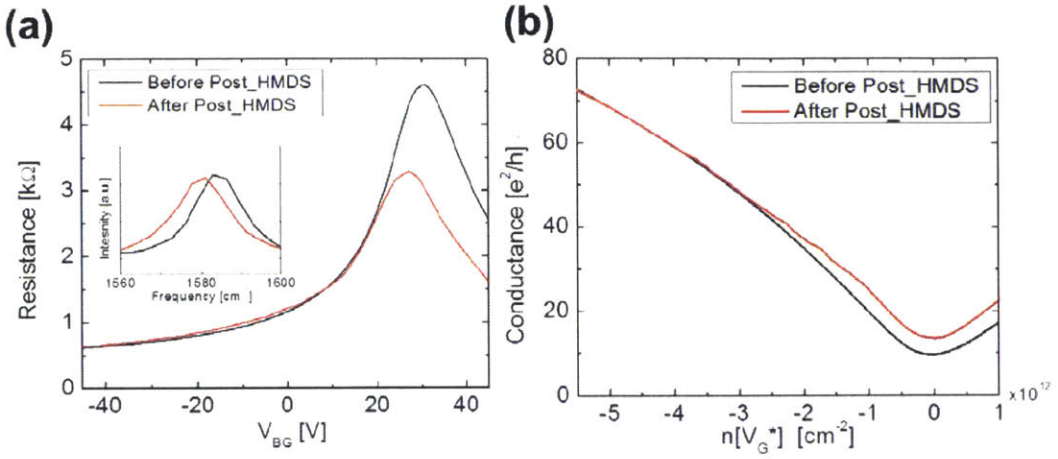

Figure 4.7 (a) Total resistance vs. V_{BG} sweeps from -50V to 50V before and after the "Post_HMDS" treatment on an HS_Exf-GFET device. The Raman spectra around G band obtained in the Exf-G of this device before and after the "Post_HMDS" treatment are shown in the inset. (b) Conductance vs. gate bias-induced carrier concentration curves before and after the "Post_HMDS" treatment.

carrier mobility in the high carrier concentration region at $n[V_G^*]=5.0\times10^{12}$ cm^{-2} was almost unvaried, changing only from 3312.9 $cm^2 V^{-1}s^{-1}$ to 3311.6 $cm^2 V^{-1}s^{-1}$. The mobility values were obtained by the relation:

$$n[V_G^*] = C_{ox}(V_{BG} - V_{CNP})/q\,, \qquad \text{(Eq. 4.2)}$$

$$\rho_{sh}^{-1} = n[V_G^*]q\mu\,, \qquad \text{(Eq. 4.3)}$$

where $n[V_G^*]$, C_{ox}, ρ_{sh}, and μ denote the carrier concentration induced by V_{BG} from the V_{CNP}, the capacitance of the gate oxide (here, 11.5 nF cm^{-2} for 300 nm-thick SiO_2), the sheet resistance of the graphene channel, and the mobility at a given carrier concentration. The carrier concentration of 1.25×10^{12} cm^{-2} for the μ was chosen for the purpose of comparing our results as given here with an earlier study using the HMDS treatment [13].

Based on this observation, the field effect measurements were carried out in the fabricated HH_Exf-G

devices where both the "Pre_ and Post_HMDS" treatments were implemented. The "Post_HMDS" treatment was performed at the final step after all the fabrication processes were completed. Figure 4.8(a) and (b) show a total resistance vs. V_{BG} results obtained in an HH_Exf-G and an HH_CVD-G device, respectively.

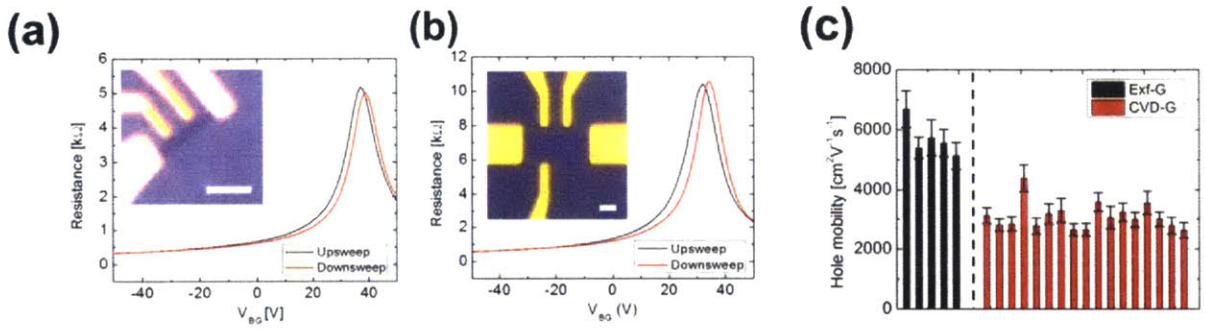

Figure 4.8 Total resistance vs. V_{BG} curves after sweeping from -50V to 50V (upsweep) and from 50V to -50V (downsweep) in (a) an HH_Exf-GFET and (b) an HH_CVD_GFET device, respectively. The corresponding OM images of the devices are shown in the inset, respectively. The scale bars are both 2 μm. (c) Extracted μ_{const} (hole) from the measurement results for the HH_Exf_GFET and HH_CVD_GFET devices.

The sweep of the back gate voltage from -50 V to 50V (upsweep) and in the reverse direction (downsweep) not only provided the information for V_{CNP}, but allowed us to extract the carrier mobility. Among the various carrier mobility models [39], together with the mobility at a given carrier concentration, μ, the carrier mobility independent of the carrier concentration, μ_{const}, was selected to characterize the device performances. The values were extracted from following equation based on the model,

$$R_{tot} = R_c + \frac{W/L}{\sqrt{n_0^2 + n\left[V_G^*\right]^2}\, q\mu_{const}} \text{ [28, 40],} \qquad \text{(Eq. 4.4)}$$

where R_{tot}, R_c, W, L, and n_0 denote the total resistance obtained from the field effect measurement, the contact resistance, the width and length of the graphene channel, the carrier concentration at V_{CNP}, respectively. The results of μ_{const} obtained for each device are given in Fig. 4.8(c) and the average value of V_{CNP}, the hysteresis between the voltage sweep directions (ΔV_{CNP}), μ_{cons}, n_o, and μ are presented in the following Table 4.3.

Table 4.3 Results of the device performances obtained in the HH-Exf-G devices and HH_CVD-G devices

	V_{CNP} [V]	ΔV_{CNP} [V]	μ_{cons} [$cm^2 V^{-1} s^{-1}$]	n_0 [$\times 10^{11} cm^{-2}$]	$\mu@n[V_G^*]=1.25\times10^{12} cm^{-2}$ [$cm^2 V^{-1} s^{-1}$]
HH_Exf-G	30.8±3.27	2.8±0.83	5700.1±597.5	6.72±1.98	6191.6±940.59
HH_CVD-G	30.5±6.94	4.5±3.02	3088.4±449.0	9.77±2.69	3973.1±535.31

Since no particular difference in the carrier mobility was observed in terms of the channel dimension, its effect will not be discussed further in this study. The HH_CVD-G devices showed electrical performances with similar V_{CNP} values to the HH_Exf-G devices but with a slightly higher hysteresis, lower carrier mobility, and higher intrinsic carrier concentration. The poorer properties in the HH_CVD-G devices relative to the HH_Exf-G devices were not surprising due to the carrier scattering centers created by the poly-crystalline structure of the CVD-G [41] and the introduction of extrinsic defects through the transfer process. Although the remarkably suppressed hole-doping in the HH_Exf-G was confirmed through the Raman spectra, the V_{CNP} was not remarkably improved. The relatively small differences in the performance between the HH_Exf-G and HH_CVD-G devices, however, still did shed light on the feasibility of the CVD-G fabrication process with this HMDS technique. In addition, As presented in Table 4.3, the mobility obtained at $n[V_G^*]=1.25\times10^{12}$ cm^{-2} showed a promising value, when it was compared to that for the Exf-G devices in the literature [13], even though the V_{CNP} was relatively high.

4.2.2.7 Conclusions

In summary, the effects from the PMMA-supported transfer process of CVD-G were studied by comparison with Exf-G in ambient air at RT. Throughout the control of the molecular weight of PMMA and a careful cleaning method was suggested for the transfer process to obtain a CVD-G sample with a highly clean surface. Furthermore, it was recognized that the interaction of the graphene surface with the surrounding environments served as a source to contribute hole-doping to graphene. A method for the passivation of graphene from such environments was attempted by using HMDS, and as a result, a highly mitigated hole-doping in graphene was observed when HMDS was treated on top of the graphene that had been transferred onto a HMDS-treated SiO_2/Si substrate. This effect was observed in both CVD-G and Exf-G. The electronic properties obtained in the GFET devices showed feasible carrier mobility and confirmed the suitability of the transfer process developed in this study.

4.3 Ethylene-vinyl acetate (EVA)-supported graphene transfer

4.3.1 Introduction

Although existing efforts have addressed many issues and challenges, there has not been much development in removing the wrinkles in the CVD graphene. Wrinkles have been observed ubiquitously in the CVD-G (and CVD h-BN) layers, likely due to the negative TEC of graphene [22] (and h-BN), while underlying metal substrates have a positive TEC value. Moreover, the wet transfer process carried out in a DI water bath also creates additional wrinkles on graphene when transferred onto a SiO_2/Si substrate. It has been shown that wrinkles cause scattering of carriers (which reduce the carrier mobility) [42] and the carbon atoms along the wrinkle are found to be less stable due to the curvature effect. It would be highly desirable to have wrinkle-free graphene for future applications.

From a practical point of view, on the other hand, one of the main requirements of the target substrates for graphene is the surface flatness. A graphene sheet (even with PMMA on top) is essentially delicate, so that it is challenging for the graphene to be conformal on an uneven substrate [43, 44].

Recalling the wet-transfer process described in Fig. 4.1, a graphene/PMMA sheet is placed on a target substrate by being scooped out of a DI water bath and then the sheet is dried by compressed N_2. Suppose there is a pre-patterned structure with a high aspect ratio on the substrate. While the graphene contacted on a horizontal side of the structure is dried, the side wall of the structure drains trapped water, making the PMMA/graphene sheet suspended. Aggressive N_2 blowing to push the suspended region onto the side walls of the substrate can result in ripping the graphene sheet. When the PMMA is removed, this suspended graphene eventually fails to sustain itself fully, leaving a torn region. This difficulty of the graphene transfer process limits the use of graphene, for example, for the back-end process of microelectronics.

For these reasons, a novel polymer, ethylene-vinyl acetate (EVA) was explored as a supporting layer for the graphene transfer. EVA consists of ethylene and vinylacetate, and is lighter, more flexible, ease-stretchable, and shows less deformation under pressure compared with PMMA. In addition, higher thermal conductivity with higher TEC, lower elastic modulus, and high elongation, all facilitated EVA as a good candidate of the transfer supporting material. Furthermore, the better solubility of EVA than PMMA in solvents was expected to leave a reduced residue for EVA on the graphene surface. In particular, taking advantage of its higher TEC and mechanical strength, two extreme cases were constructed to verify and validate the EVA-supported graphene transfer method: graphene transfer from textured Cu and graphene transfer onto an arbitrary substrate, a coin. The transfer process was found to be compatible with the established PMMA-supported transfer and the device properties of graphene using EVA as a supporting material were reasonably better than those using PMMA.

4.3.2 Graphene transfer from textured Cu

The overall procedures for transferring CVD-G from textured Cu are illustrated in Figure 4.9. To more clearly differentiate between the two approaches, trenches (or ripples) on a Cu foil were generated by pressing with a Fresnel lens. Conformal MLG was grown on a textured 25 μm thick-Cu foil (99.8%,

Alfa Aesar) with concentric circle patterns *via* a typical LPCVD process. After the growth process, graphene was transferred onto the final target substrate through a typical polymer-assisted wet transfer approach which comprises three essential steps; 1) spin-coating of the polymer support/carrier materials, 2) wet chemical etching of the Cu foil, and 3) transferring graphene/polymer onto a target substrate and removal of the polymer.

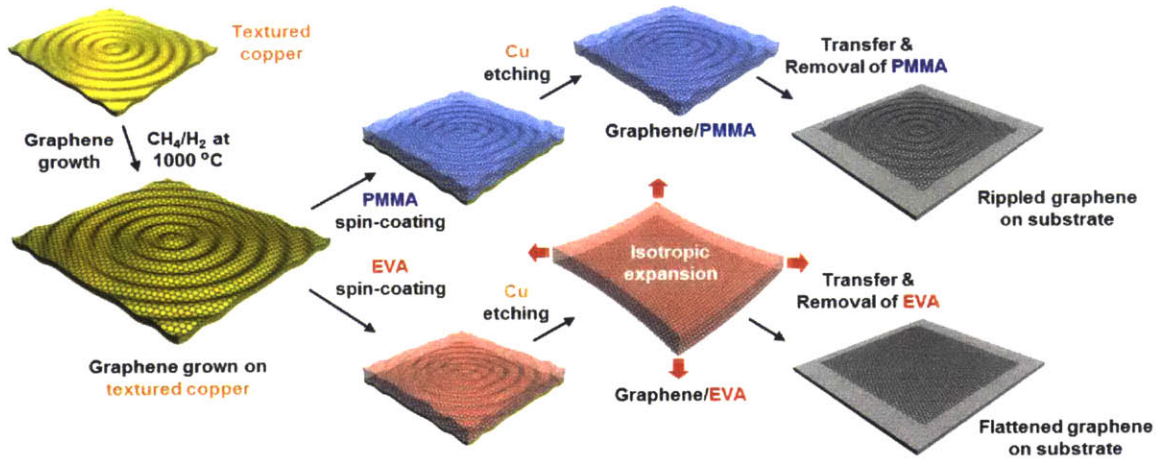

Figure 4.9 Schematic illustrations of transfer processes for a CVD-G grown on a textured Cu using both PMMA and EVA as a supporting material.

The only difference in the EVA-supported transfer of Fig. 4.9 was in the third step. In the typical PMMA-mediated graphene transfer, a PMMA/graphene stack was floated on a DI water bath at RT and the stack was later scooped out, and finally transferred onto a target substrate. In contrast, an EVA/graphene stack where EVA is spin-coated on the graphene was soaked in a moderately hot DI water bath maintained at 90 °C for 1 hour before scooping out (the remaining procedures are the same as that for the PMMA-supported transfer). During this period, the EVA film expanded was isotropically with applied thermal energy. The isotropic expansion allowed the EVA/graphene stack to become tightly attached to the final substrate, thereby reducing the amount of wrinkles of the textured Cu foil.

Consequently, it was expected that the graphene ripples which originated from the textured Cu could be lessened or eliminated during the transfer process through the isotropic expansion of EVA, whereas these ripples would have remained using the conventional PMMA-supported transfer.

Quantification of the graphene transfer by the two different techniques was evaluated and compared with results by OM and an α-step profilometer as shown in Figure 4.10. The OM image of the textured Cu exhibited well-defined concentric circle patterns, which led to a direct growth of graphene along these patterns of Cu. The height analysis also revealed that the wavelength and amplitude of the wrinkles were *ca.* 300 μm and 1.5 μm, respectively. These ripple (wavy) patterns were replicated and transferred to the final target substrate by using the PMMA-supported transfer method. Optical and topographical images show that the identical patterns of the textured Cu still remained on the PMMA/graphene stack. The EVA/graphene transferred onto flat substrates, on the other hand, had diminished/disappeared patterns. The uniform color contrast of the topographical image indicated that the EVA/graphene stack had a flattened surface with thickness uniformity, suggesting excellent transfer conformity of our new transfer

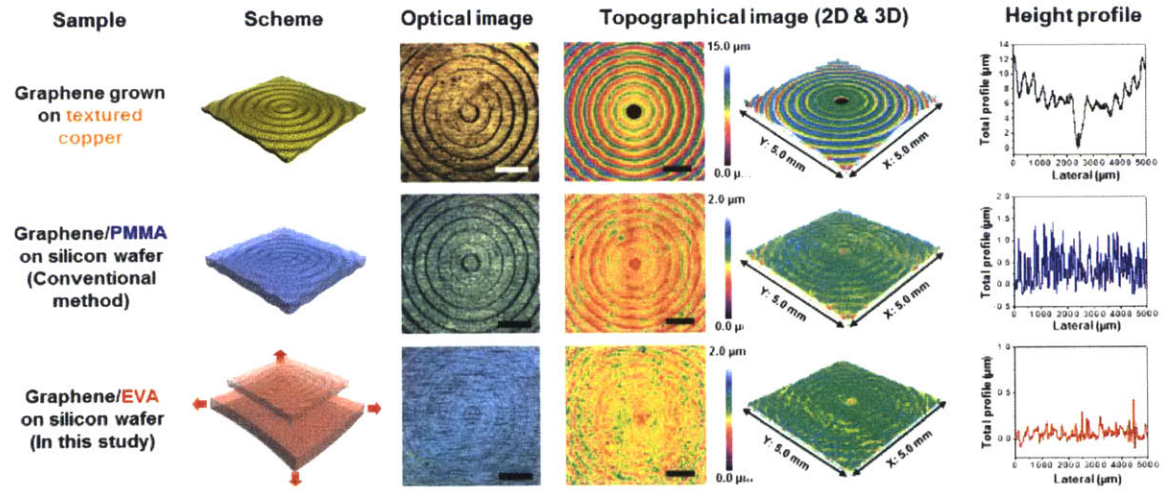

Figure 4.10 Transfer results of wavy graphene with EVA and PMMA as a supporting material. All graphic images and height analyses were taken before striping the supporting material. Scale bars are 1 mm.

technique. Topographic height profiles following the horizontal axis also revealed that the EVA/graphene stack had an excellent flatness. The difference in height between the high and low patterns ranged from 0.1 to 0.2 μm in the EVA/graphene stack, which in comparison was much smoother than that of the PMMA/graphene stack (ranging from 0.5 to 1.3 μm). Consequently, it was found that the macroscopic wrinkles from textured Cu could be reduced (even removed) by introducing the EVA polymer as a supporting material. Details of the mechanism and structural formation during transfer are discussed as follow.

As mentioned earlier, our new graphene transfer method with EVA exploits its thermal properties. In general, most solid materials expand upon heating and contract when cooled. The change in length with temperature may be expressed as,

$$l_f / l_0 = \alpha_l (T_f - T_0), \quad \textbf{or} \quad \Delta l / l_0 = \alpha_l \Delta T \qquad \text{(Eq. 4.5)}$$

where l_0 and l_f are the initial and final lengths as the temperature is changed from T_0 to T_f, respectively. The parameter α_l is the linear TEC. This TEC value is a material property that is indicative of its ability to increase its length as the result of applied thermal energy. The thermal conductivity (κ) is also an important factor in heat transfer. Under our experimental conditions, the α_l and κ values were estimated using the above equation and Fourier's law, and the results are summarized in Table 4.4.

Table 4.4 Material properties of PMMA and EVA

Sample	**Physical properties**			**Mechanical properties**		**Chemical properties**	
	Density ($mg\ cm^{-3}$)	Thermal conductivity ($W\ mK^{-1}$)	TCE ($\times 10^{-6}\ K^{-1}$)	Spring constant ($\mu N\ nm^{-1}$)	Elastic modulus (GPa)	Molecular formula	Solubility parameter ($MPa^{1/2}$)
PMMA	1.17	0.19	70	0.079	2.682	$(C_5O_2H_8)_n$	19/19.7 (PMMA/acetone)
EVA	0.96	0.34	180	0.026	0.258	$(C_2H_4)_n$ $(C_4H_6O_2)_m$	18.05/18.2 (EVA/xylene)

As mentioned earlier, the TEC of MLG is negative. At RT, graphene exhibits its lowest α_l value of *ca.* $-7 \times 10^{-6}\,K^{-1}$, and α_l decreases with increasing temperature. In this study, the shift of the MLG's TCE in the temperature range of interest was found to be negligible. It is worth noting that the α_l value for EVA is approximately 2.6 times higher than that of PMMA. Therefore, while the PMMA was dilated to l_0[45] at a given temperature (Figure 4.11(a), the EVA expanded to $l_0\{1+(180\times10^{-6}\ K^{-1})\Delta T\}$ at a given temperature (Figure 4.11(b)). It was also expected that the good thermal conductivity (0.34 Wm K^{-1}) and relatively high TCE value ($180\times10^{-6}\ K^{-1}$) of EVA would have a combined or synergistic effect on the isotropic expansion of EVA during the transfer process.

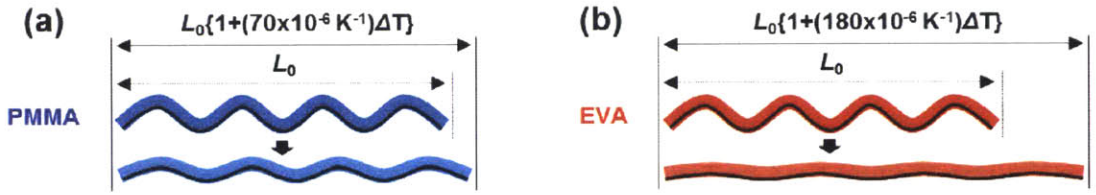

Figure 4.11 Schematically illustrated thermal expansion behavior between (a) PMMA and (b) EVA.

Figure 4.12 depicts the schematic explanation and the corresponding OM images of the comparison between PMMA and EVA upon thermal expansion. In the conventional PMMA-supported graphene transfer, the PMMA/graphene film did not make tight contact with the target substrate. The imbalance in the attachment gave rise to folded regions of the graphene and thus, transfer failures (graphene defects) were observed after the PMMA stripping. On the other hand, the EVA/graphene film expanded in response to the increased temperature, and the wavy patterned EVA/graphene film could be flattened and transferred without folding through an isotropic expansion of EVA.

Furthermore, the effectiveness of EVA as a supporting material was confirmed for a graphene grown on a crumpled Cu foil, as shown in Figure 4.13. Photographs and optical images showed excellent continuity over an mm-sized scale without observable cracks or tears in the graphene that had been transferred by EVA, while there were some cracks and tears in the PMMA-transferred sample.

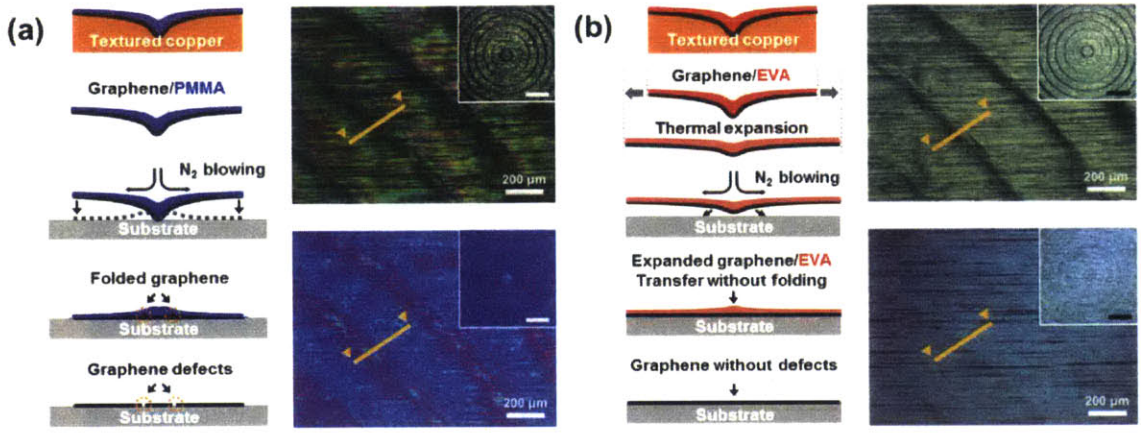

Figure 4.12 Comparison of the thermal expansion effects between (a) PMMA and (b) EVA during transfer. Schematic illustration represented the sequential steps of the graphene transfer from textured Cu. The illustration shows a cross-section through samples (yellow lines in the OM). These OM images depict spin-coated polymer on the textured Cu (upper) and the effect of attaching the polymer/graphene film on a SiO_2/Si substrate (lower). Low magnification OM images are shown in the inset, respectively. Scale bar is 1 mm.

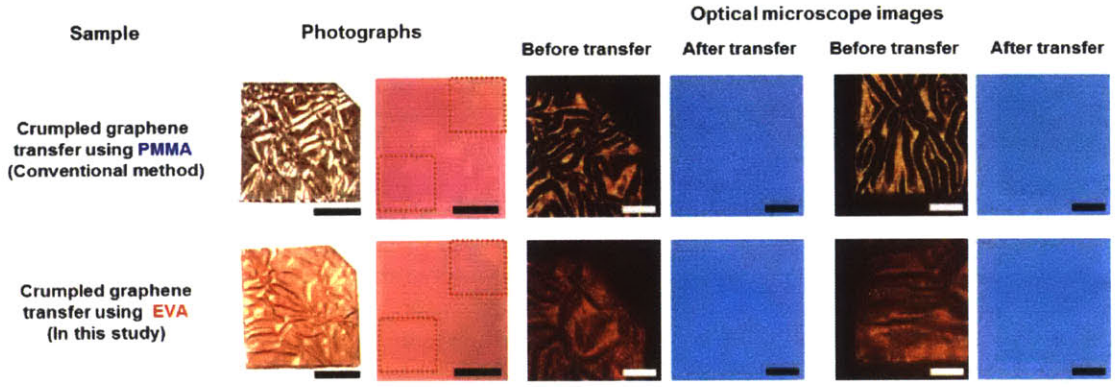

Figure 4.13 Photographs of graphene grown on a crumpled Cu (scale bar is 3.5 mm), and OM images of transferred graphene (scale bar is 1 mm). Two sets of graphene samples transferred on a SiO_2/Si substrate are shown comparatively using PMMA (upper) and EVA (lower) as a supporting material, respectively.

4.3.3 Graphene transfer onto arbitrary substrates

The mechanical properties of the EVA are another important contributing factor to the effective graphene transfer. The influence of the mechanical properties of the supporting materials on the graphene transfer was investigated by using the back side of one-cent Cu coin as an arbitrary substrate, as illustrated in Figure 4.14. Interestingly, both PMMA/graphene and EVA/graphene films exhibited quite a different behavior when transferred to this coin. It has been known that amorphous polymers (*i.e.*, PMMA) are usually hard and brittle below their glass transition temperatures because of the low mobility of their molecules, whereas the semi-crystalline polymers (*i.e.*, EVA) with relatively strong intermolecular forces behave more like rubber-like materials, providing elasticity and impact resistance [46-48].

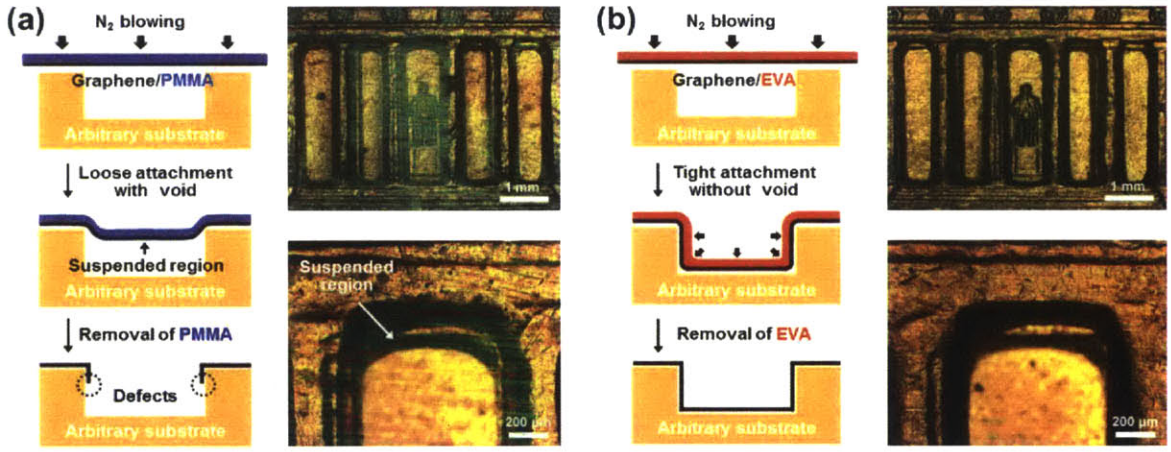

Figure 4.14 Different behaviors in the graphene transfer process with between (a) PMMA and (b) EVA during the transfer process onto an arbitrary substrate. The reverse side of the coin (1 cent) was chosen as the arbitrary substrate. A schematic illustration represents the sequential steps for transferring graphene to the substrate. The corresponding OM images with different magnifications are provided.

Accordingly, graphene defects (cracks and tears) may have formed during the conventional PMMA-supported transfer process due to the weaker flexibility of the PMMA layer. As shown in the schematic

explanation and the corresponding OM images in Fig. 4.14, there was always an unattached/suspended region between the PMMA/graphene film and the uneven substrate. The PMMA/graphene film did not make a conformal contact on an arbitrary substrate and the unattached/suspended regions tended to break easily and cracks formed after PMMA stripping. Different from the PMMA/graphene film, the EVA/graphene film tended to cover the surface of the side wall and this film made a tight contact without any unattached/suspended region. This made up for the drawback of thee weak flexibility PMMA. Figure 4.15 shows two magnified OM images captured at different focal planes. These confirmed that the EVA/graphene film was completely covered over the arbitrary substrate with a good coverage over the whole surface.

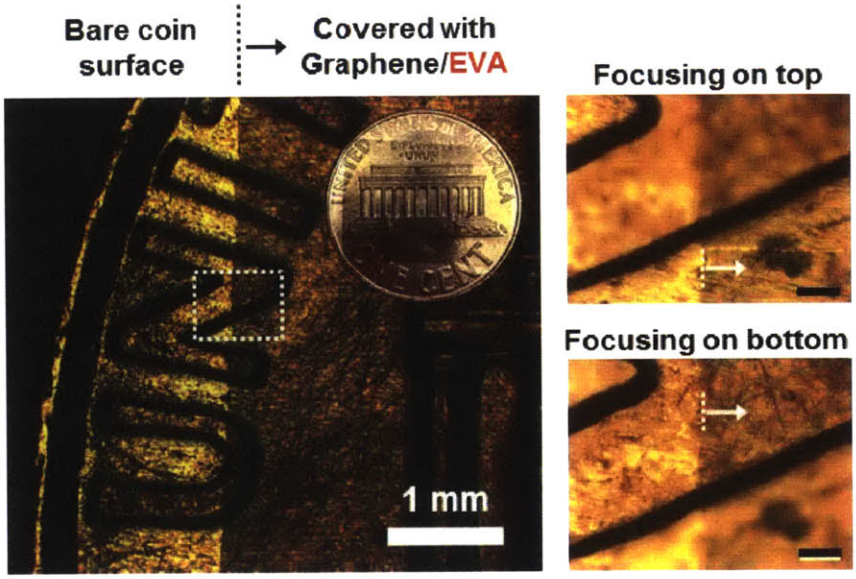

Figure 4.15 OM images of coin partially covered with EVA/graphene film. Enlarged optical images were taken at different focal distances (scale bar indicates 200 μm).

In order to achieve an in-depth insight into the transferring mechanism, the elastic mechanical properties of the PMMA/graphene and EVA/graphene films were investigated by indenting an AFM tip at the center of the suspended area [49, 50]. Figure 4.16 presents curves of force (F) vs. deformation (η),

measured for PMMA/graphene and EVA/graphene films, not only by pushing the films but also by pulling them. When the tip and sample are in contact (Fig. 4.16 inset), the elastic deformation of the polymer/graphene film (η), the deflection of the AFM cantilever (ΔZ_c), and the displacement of the scanning piezotube of the AFM (ΔZ_{piezo}) are related by the following equation,

$$\eta = \Delta Z_{piezo} - \Delta Z_c \qquad \text{(Eq. 4.6)}$$

In addition, the applied F can be estimated from the following equation,

$$F = K_c \Delta Z_c, \qquad \text{(Eq. 4.7)}$$

where K_c is the spring constant of the cantilever. A tip with a K_c of 80 N m^{-1} was used in this study. For the elastic deformation regime, there is a linear relationship between F and η, and the slope of the $F(\eta)$

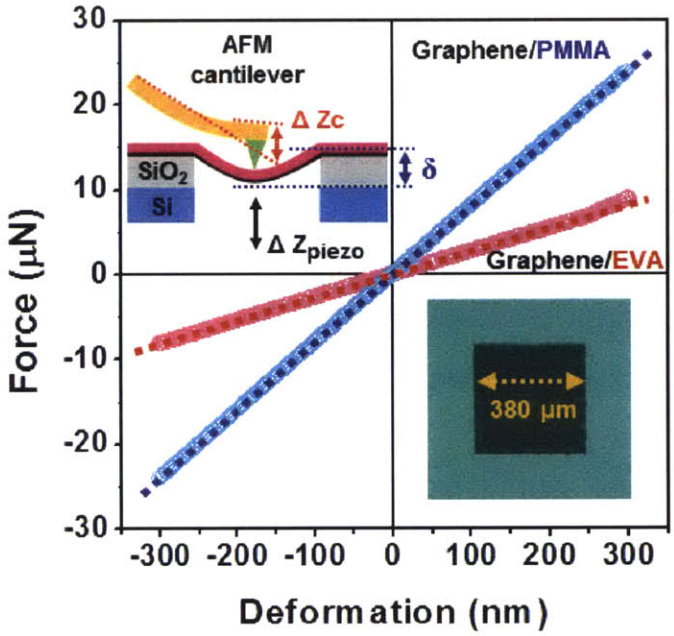

Figure 4.16 Force vs. deformation traces measured by pushing and pulling at the center of the suspended PMMA/graphene and EVA/graphene films. The slope of the traces around zero deformation is marked by a dotted line. Schematic diagram (top-left) and OM (bottom-right) of a suspended graphene sample prepared for the bending test are inset.

curves does not change after repeated deformations, proving the absence of permanent damage. This slope of the curves provides access to the effective spring constant (K_{eff}) of the polymer/graphene films through Hooke's law [45, 51]. Importantly, the effective spring constant of the EVA/graphene film was 0.026 μN nm^{-1} in the linear elastic regime, which is much smaller than that of the PMMA/graphene film (0.079 μN nm^{-1}). Considering that the relatively low K_{eff} value of the EVA/graphene film is indicative of the weak restoring force against the deformation, the EVA/graphene film possesses increased flexibility, softness, and conformability.

In addition to the low K_{eff} value, the EVA/graphene film revealed a substantial decrease in the elastic modulus (E). The elastic modulus of the polymer/graphene films was obtained from the initial unloading contact stiffness, S, which is defined as,

$$S = dP / dh, \qquad \text{(Eq. 4.8)}$$

which is the slope of the initial portion of the unloading curve [52, 53]. Based on Sneddon's theory, the initial unloading contact stiffness can be derived as follows,

$$S = 2\beta[(A/\pi)E_r]^{1/2}, \qquad \text{(Eq. 4.9)}$$

where A is the contact area, β is a constant related to the geometry of the indenter (for a Berkovich indenter, β = 1.034), and E_r is the reduced elastic modulus. The quantity E_r can be calculated from the following equation,

$$E_r = [(1-\nu)/E] + [(1-\nu_i)/E_i], \qquad \text{(Eq. 4.10)}$$

where E and ν are the elastic modulus and Poisson's ratio of the polymer/graphene films, respectively, and E_i and ν_i are the same quantities for the nanoindenter (E_i = 0.4098 GPa, ν_i = 0.278). Under our experimental condition, the E values of the PMMA/graphene and EVA/graphene films were measured as 2.682 and 0.258 GPa, respectively. It is also worth noting that the approximately one-tenth lower E value of the EVA/graphene film implies higher elasticity and lower stiffness in comparison with the PMMA/graphene film. As demonstrated by the enhanced mechanical strength of the EVA/graphene film, the

suitable K_{eff} and E values of the support/carrier materials are essential for a successful graphene transfer onto arbitrary substrates.

With the flexibility, robustness, and high elongation properties of the EVA layer, the EVA/graphene film tends to follow the surface of the underlying substrate and can be tightly attached at the surface of the arbitrary substrate without any structural defects.

4.3.4 Electrical properties of polymer-mediated graphene samples

The residues of the supporting material, especially the polymer residues of PMMA, inevitably remained on the graphene surface and adversely affected the graphene's intrinsic electrical properties. In this study, the ideal graphene transfer without polymer residues was further examined by means of the chemical properties of the supporting materials. The chemical parameters of the polymer in the solvent, including the intermolecular interaction, chain conformation, and solubility, are strongly affected by the inherent properties of the polymer as well as by the environmental conditions. In particular, the solubility parameter (δ) could be considered as an important factor in determining the dissolution efficiency of the supporting materials [54, 55].

The Hildebrand-Scatchard equation is an equation for calculating the enthalpy change (ΔH_m) for the polymer-solvent mixing system, and can be expressed as,

$$\Delta H_m = V_m(\delta_p - \delta_s)^2 \phi_p \phi_s, \qquad \text{(Eq. 4.11)}$$

where V_m is the volume of the mixture, δ_p and δ_s are the solubility parameters, and ϕ_p and ϕ_s are the volume fraction of the polymer and solvent, respectively. For a polymer to be soluble in a solvent, the change in the Gibbs free energy of mixing (ΔG_m) must be negative (favorable), in accordance with the following basic thermodynamic equation,

$$\Delta G_m = \Delta H_m - T\Delta S_m, \qquad \text{(Eq. 4.12)}$$

where, T is the temperature and the ΔS_m is the entropy of mixture. The ΔS_m term is usually positive, and thus, ΔH_m is the determining factor. Since $\Delta H_m \approx (\delta_p - \delta_s)^2$, the highest solubility is achieved when the δ_p

and δ_s values are equal due to the negative entropy term. Namely, mixtures of materials with similar δ values are likely to be miscible and thermodynamically compatible.

Acetone is the most widely used solvent for the dissolving/removing of PMMA. From Table 4.4, the PMMA has a solubility parameter of about 19 $MPa^{1/2}$, and the solubility parameter difference ($|\delta_{PMMA} - \delta_{acetone}|$) is 0.7. In the case of EVA (δ_p value of 18.05 $MPa^{1/2}$), however, the acetone is not suitable due to the solubility parameter mismatch. It has been known that an aromatic hydrocarbon, such as xylene, is more suitable solvent for dissolving/removing EVA. For this study, the xylene with a δ_s value of 18.2 $MPa^{1/2}$ was chosen to afford the effective removal of EVA residues from the graphene surface. The xylene is best matched with EVA, and the $|\delta_{EVA}-\delta_{xylene}|$ value is revealed to be 0.15, indicating that xylene is 'good solvent' for EVA (Table 4.4). Importantly, the interactions between the EVA polymer and the xylene solvent are energetically favorable to swell the EVA polymer chains and completely dissolve away the EVA layer from the graphene surface.

Figures 4.17 present the OM images of graphene samples transferred onto a SiO_2/Si substrate where PMMA and EVA were used as a supporting material and were removed by acetone and xylene, respectively. As expected from the lower solubility parameter difference between EVA and xylene than the one between PMMA and acetone, the EVA-supported transfer resulted in a highly clean graphene surface. The consistency of the color contrast in the Fig. 4.17(b) suggests that the transferred graphene using an EVA polymer has an excellent uniformity of thickness. Furthermore, while the surface of the graphene sample that used PMMA as a supporting layer showed wrinkles and polymer residues, as indicated by a white arrow and a black arrow in Fig. 4.17(a), respectively, the graphene surface after stripped off EVA exhibited dimmed wrinkles and insignificant residues, as shown in Fig. 4.17(b).

To evaluate the quality of the transferred graphenes, Raman spectroscopy characterization was firstly performed before electrical characterization, as shown in Figure 4.18(a). In terms of the ω_G and I_{2D}/I_G indicating that those are a monolayer of graphene, respectively, there is no significant difference in values between two samples. Nonetheless, the I_D/I_G of the EVA-transferred graphene was negligible below the

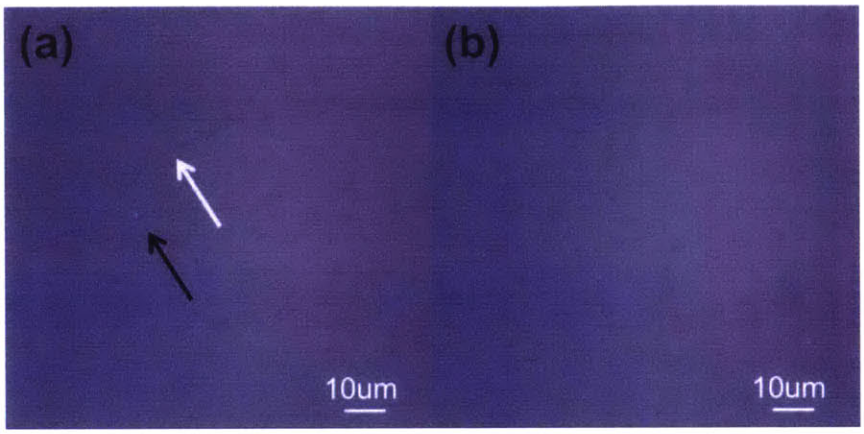

Figure 4.17 OM images of graphene transferred onto SiO_2/Si with (a) PMMA and (b) EVA as a supporting material. While the graphene transferred by PMMA showed distinct wrinkles (white arrow) and residues (black arrow), a nicely clean surface was observed in the graphene transferred by EVA (see (b)).

Raman detection limit, while that of the PMMA-supported graphene was substantionally high at around 0.13. This characterization suggested the EVA-supported transfer method is relatively beneficial to minimize the creation of defects in the graphene the during the transfer.

In the following, the electricl properties of both the samples were investigated by fabrigating back-gate FET devices with the same process introduced in sec. **2.3.2**. The characterization results performed in an ambient air at RT are shown in Fig. 4.18 (b)-(c). Since poly-crystalline grpahene samples grownt by the Cu-mediated LPCVD process were used for the fabrication, the carrier mobility values themselves were not so high as the ones obtained in the previous chapters. Nonetheless, compared with the GFET based on graphene transferred by PMMA, the graphene transferred by EVA exhibits slightly higher carrier mobility (μ_{Hall}), as summarized in Fig. 4.18(c). These enhanced electrical performance in graphene transferred with EVA supporting layer (slightly decreased carrier density (n_s) **and increased** μ_{Hall} values) can be explained by decreased carrier scattering centers in graphene, resulting from reduced wrinkles and

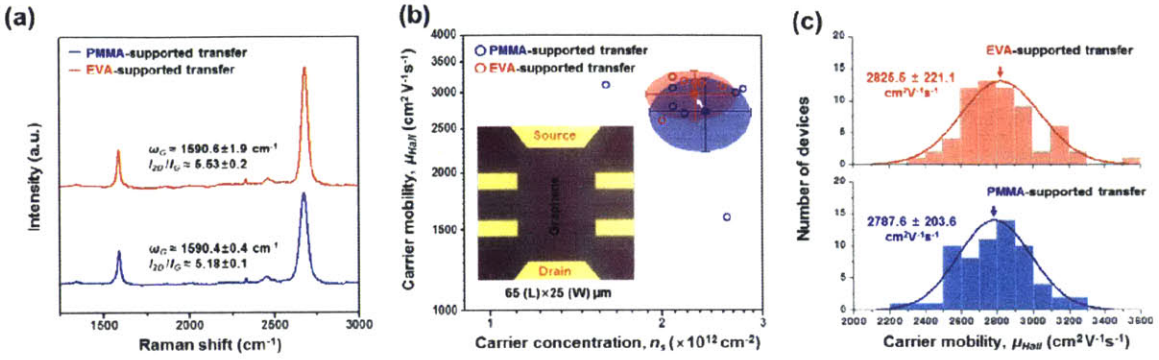

Figure 4.18 (a) Representative Raman spectra of graphene samples transferred using PMMA (blue) and EVA (red) as a supporting material. The positions of ω_G and I_{2D}/I_G of each sample are labeled together, respectively. (b-c) The electrical characterization results of the GFET devices fabricated with both the graphene samples in (a). (b) Carrier concentration at the Dirac point and the corresponding μ_{Hall} of 10 devices of the each graphene sample. The OM image of one device is in the inset. (c) Entire μ_{Hall} of the devices of each graphene sample. The corresponding average values of μ_{Hall} are included, respectively.

EVA residues. As demonstrated previously, the EVA supporting layer with good thermal conductivity and high TCE value resulted in the reduced graphene wrinkles during isotropic expansion step. The substantially suppressed wrinkles were maintained even after transfer process, implying reduction in charge carrier scattering. Furthermore, the decrease in n_s is associated with the well-matched solubility parameters between EVA and xylene. The interactions between EVA and xylene are energetically favorable and thus, the EVA layer could be completely dissolved away from graphene surface, yielding the enhanced electrical performances without charged impurities.

4.3.5 Conclusions

As a new supporting material for graphene transfer, EVA was explored to tackle the challenging issues in the established PMMA-supported transfer. Its excellent materials properties including a high

TEC and mechanical strength were expected to reduce the density of graphene wrinkles and to enable a conformal transfer onto an uneven substrate without voids. Two extreme processes, transfer of wavy graphene grown a textured Cu foil and transfer of graphene onto a pre-patterned target substrate, were designed. As a result, the EVA-supported transfer showed much a nicer graphene morphology on the target substrate than the PMMA-supported transfer by showing a diminished wavy pattern and by agreeably accommodating the substrate topography. Furthermore, the good match of EVA with xylene as a removing agent gave rise to a highly clean graphene surface with negligible residue; accordingly, the electrical properties of graphene were also obtained to be slightly better. We believe that the use of EVA as a supporting material paves the way for the technological development of graphene transfer for better quality of the graphene after transfer.

References

[1] Bhaviripudi S, Jia X, Dresselhaus MS, Kong J. Role of Kinetic Factors in Chemical Vapor Deposition Synthesis of Uniform Large Area Graphene Using Copper Catalyst. Nano Letters. 2010;10(10):4128-33.

[2] Liang X, Sperling BA, Calizo I, Cheng G, Hacker CA, Zhang Q, et al. Toward Clean and Crackless Transfer of Graphene. Acs Nano. 2011;5(11):9144-53.

[3] Kern W. Handbook of Semiconductor Wafer Cleaning Technology: Science, Technology, and Applications: Noyes Publications; 1993.

[4] Li X, Zhu Y, Cai W, Borysiak M, Han B, Chen D, et al. Transfer of Large-Area Graphene Films for High-Performance Transparent Conductive Electrodes. Nano Letters. 2009;9(12):4359-63.

[5] Kashiwagi T, Inaba A, Brown JE, Hatada K, Kitayama T, Masuda E. EFFECTS OF WEAK LINKAGES ON THE THERMAL AND OXIDATIVE-DEGRADATION OF POLY(METHYL METHACRYLATES). Macromolecules. 1986;19(8):2160-8.

[6] Kedzierski J, Hsu P-L, Reina A, Kong J, Healey P, Wyatt P, et al. Graphene-on-Insulator Transistors Made Using C on Ni Chemical-Vapor Deposition. Ieee Electron Device Letters. 2009;30(7):745-7.

[7] Lin Y-C, Jin C, Lee J-C, Jen S-F, Suenaga K, Chiu P-W. Clean Transfer of Graphene for Isolation and Suspension. Acs Nano. 2011;5(3):2362-8.

[8] He KT, Wood JD, Doidge GP, Pop E, Lyding JW. Scanning Tunneling Microscopy Study and Nanomanipulation of Graphene-Coated Water on Mica. Nano Letters. 2012;12(6):2665-72.

[9] Cheng Z, Zhou Q, Wang C, Li Q, Wang C, Fang Y. Toward Intrinsic Graphene Surfaces: A Systematic Study on Thermal Annealing and Wet-Chemical Treatment of SiO2-Supported Graphene Devices. Nano Letters. 2011;11(2):767-71.

[10] Lin Y-C, Lu C-C, Yeh C-H, Jin C, Suenaga K, Chiu P-W. Graphene Annealing: How Clean Can It Be? Nano Letters. 2012;12(1):414-9.

[11] Dean CR, Young AF, Meric I, Lee C, Wang L, Sorgenfrei S, et al. Boron nitride substrates for high-quality graphene electronics. Nature Nanotechnology. 2010;5(10):722-6.

[12] Petrone N, Dean CR, Meric I, van der Zande AM, Huang PY, Wang L, et al. Chemical Vapor Deposition-Derived Graphene with Electrical Performance of Exfoliated Graphene. Nano Letters. 2012;12(6):2751-6.

[13] Lafkioti M, Krauss B, Lohmann T, Zschieschang U, Klauk H, v Klitzing K, et al. Graphene on a Hydrophobic Substrate: Doping Reduction and Hysteresis Suppression under Ambient Conditions. Nano Letters. 2010;10(4):1149-53.

[14] Yang YX, Murali R. Binding mechanisms of molecular oxygen and moisture to graphene. Applied Physics Letters. 2011;98(9).

[15] Ryu S, Liu L, Berciaud S, Yu Y-J, Liu H, Kim P, et al. Atmospheric Oxygen Binding and Hole Doping in Deformed Graphene on a SiO2 Substrate. Nano Letters. 2010;10(12):4944-51.

[16] Wood JD, Schmucker SW, Lyons AS, Pop E, Lyding JW. Effects of Polycrystalline Cu Substrate on Graphene Growth by Chemical Vapor Deposition. Nano Letters. 2011;11(11):4547-54.

[17] Farmer DB, Golizadeh-Mojarad R, Perebeinos V, Lin Y-M, Tulevski GS, Tsang JC, et al. Chemical Doping and Electron-Hole Conduction Asymmetry in Graphene Devices. Nano Letters. 2009;9(1):388-92.

[18] Pirkle A, Chan J, Venugopal A, Hinojos D, Magnuson CW, McDonnell S, et al. The effect of chemical residues on the physical and electrical properties of chemical vapor deposited graphene transferred to SiO2. Applied Physics Letters. 2011;99(12).

[19] Li X, Cai W, An J, Kim S, Nah J, Yang D, et al. Large-Area Synthesis of High-Quality and Uniform Graphene Films on Copper Foils. Science. 2009;324(5932):1312-4.

[20] Chan J, Venugopal A, Pirkle A, McDonnell S, Hinojos D, Magnuson CW, et al. Reducing Extrinsic Performance-Limiting Factors in Graphene Grown by Chemical Vapor Deposition. Acs Nano. 2012;6(4):3224-9.
[21] Ahn Y, Kim H, Kim Y-H, Yi Y, Kim S-I. Procedure of removing polymer residues and its influences on electronic and structural characteristics of graphene. Applied Physics Letters. 2013;102(9).
[22] Yoon D, Son Y-W, Cheong H. Negative Thermal Expansion Coefficient of Graphene Measured by Raman Spectroscopy. Nano Letters. 2011;11(8):3227-31.
[23] Mohiuddin TMG, Lombardo A, Nair RR, Bonetti A, Savini G, Jalil R, et al. Uniaxial strain in graphene by Raman spectroscopy: G peak splitting, Gruneisen parameters, and sample orientation. Physical Review B. 2009;79(20).
[24] Das A, Pisana S, Chakraborty B, Piscanec S, Saha SK, Waghmare UV, et al. Monitoring dopants by Raman scattering in an electrochemically top-gated graphene transistor. Nature Nanotechnology. 2008;3(4):210-5.
[25] Nagashio K, Yamashita T, Nishimura T, Kita K, Toriumi A. Electrical transport properties of graphene on SiO2 with specific surface structures. J Appl Phys. 2011;110(2).
[26] Shim J, Lui CH, Ko TY, Yu Y-J, Kim P, Heinz TF, et al. Water-Gated Charge Doping of Graphene Induced by Mica Substrates. Nano Letters. 2012;12(2):648-54.
[27] Ni ZH, Wang HM, Luo ZQ, Wang YY, Yu T, Wu YH, et al. The effect of vacuum annealing on graphene. Journal of Raman Spectroscopy. 2010;41(5):479-83.
[28] Suk JW, Lee WH, Lee J, Chou H, Piner RD, Hao Y, et al. Enhancement of the Electrical Properties of Graphene Grown by Chemical Vapor Deposition via Controlling the Effects of Polymer Residue. Nano Letters. 2013;13(4):1462-7.
[29] Ni ZH, Yu T, Luo ZQ, Wang YY, Liu L, Wong CP, et al. Probing Charged Impurities in Suspended Graphene Using Raman Spectroscopy. Acs Nano. 2009;3(3):569-74.
[30] Kang CG, Lee YG, Lee SK, Park E, Cho C, Lim SK, et al. Mechanism of the effects of low temperature Al2O3 passivation on graphene field effect transistors. Carbon. 2013;53:182-7.
[31] Ni ZH, Wang HM, Ma Y, Kasim J, Wu YH, Shen ZX. Tunable stress and controlled thickness modification in graphene by annealing. Acs Nano. 2008;2(5):1033-9.
[32] Park J, Lee WH, Huh S, Sim SH, Kim SB, Cho K, et al. Work-Function Engineering of Graphene Electrodes by Self-Assembled Monolayers for High-Performance Organic Field-Effect Transistors. Journal of Physical Chemistry Letters. 2011;2(8):841-5.
[33] Lee NJ, Yoo JW, Choi YJ, Kang CJ, Jeon DY, Kim DC, et al. The interlayer screening effect of graphene sheets investigated by Kelvin probe force microscopy. Applied Physics Letters. 2009;95(22).
[34] Kim SM, Hsu A, Araujo PT, Lee Y-H, Palacios T, Dresselhaus M, et al. Synthesis of Patched or Stacked Graphene and hBN Flakes: A Route to Hybrid Structure Discovery. Nano Lett. 2013;13(3):933-41.
[35] Shi Y, Kim KK, Reina A, Hofmann M, Li L-J, Kong J. Work Function Engineering of Graphene Electrode via Chemical Doping. Acs Nano. 2010;4(5):2689-94.
[36] Lorenzoni M, Giugni A, Torre B. Oxidative and carbonaceous patterning of Si surface in an organic media by scanning probe lithography. Nanoscale Research Letters. 2013;8.
[37] Yu Y-J, Zhao Y, Ryu S, Brus LE, Kim KS, Kim P. Tuning the Graphene Work Function by Electric Field Effect. Nano Lett. 2009;9(10):3430-4.
[38] Adam S, Hwang EH, Galitski VM, Das Sarma S. A self-consistent theory for graphene transport. Proceedings of the National Academy of Sciences of the United States of America. 2007;104(47):18392-7.
[39] Venugopal A, Chan J, Li X, Magnuson CW, Kirk WP, Colombo L, et al. Effective mobility of single-layer graphene transistors as a function of channel dimensions. J Appl Phys. 2011;109(10).
[40] Kim S, Nah J, Jo I, Shahrjerdi D, Colombo L, Yao Z, et al. Realization of a high mobility dual-gated graphene field-effect transistor with Al2O3 dielectric. Applied Physics Letters. 2009;94(6).

[41] Yu Q, Jauregui LA, Wu W, Colby R, Tian J, Su Z, et al. Control and characterization of individual grains and grain boundaries in graphene grown by chemical vapour deposition. Nature Materials. 2011;10(6):443-9.
[42] Li X, Magnuson CW, Venugopal A, An J, Suk JW, Han B, et al. Graphene Films with Large Domain Size by a Two-Step Chemical Vapor Deposition Process. Nano Letters. 2010;10(11):4328-34.
[43] Caldwell JD, Anderson TJ, Culbertson JC, Jernigan GG, Hobart KD, Kub FJ, et al. Technique for the Dry Transfer of Epitaxial Graphene onto Arbitrary Substrates. Acs Nano. 2010;4(2):1108-14.
[44] Suk JW, Kitt A, Magnuson CW, Hao Y, Ahmed S, An J, et al. Transfer of CVD-Grown Monolayer Graphene onto Arbitrary Substrates. Acs Nano. 2011;5(9):6916-24.
[45] Castellanos-Gomez A, Poot M, Steele GA, van der Zant HSJ, Agrait N, Rubio-Bollinger G. Elastic Properties of Freely Suspended MoS2 Nanosheets. Advanced Materials. 2012;24(6):772-+.
[46] Schrauwen BAG, Janssen RPM, Govaert LE, Meijer HEH. Intrinsic deformation behavior of semicrystalline polymers. Macromolecules. 2004;37(16):6069-78.
[47] Bedoui F, Diani J, Regnier G. Micromechanical modeling of elastic properties in polyolefins. Polymer. 2004;45(7):2433-42.
[48] Arnoult M, Dargent E, Mano JF. Mobile amorphous phase fragility in semi-crystalline polymers: Comparison of PET and PLLA. Polymer. 2007;48(4):1012-9.
[49] Gomez-Navarro C, Burghard M, Kern K. Elastic properties of chemically derived single graphene sheets. Nano Letters. 2008;8(7):2045-9.
[50] Lee C, Wei X, Kysar JW, Hone J. Measurement of the elastic properties and intrinsic strength of monolayer graphene. Science. 2008;321(5887):385-8.
[51] Frank IW, Tanenbaum DM, Van der Zande AM, McEuen PL. Mechanical properties of suspended graphene sheets. Journal of Vacuum Science & Technology B. 2007;25(6):2558-61.
[52] Yan W, Pun CL, Simon GP. Conditions of applying Oliver-Pharr method to the nanoindentation of particles in composites. Composites Science and Technology. 2012;72(10):1147-52.
[53] Li XD, Bhushan B. A review of nanoindentation continuous stiffness measurement technique and its applications. Materials Characterization. 2002;48(1):11-36.
[54] Ueno K, Fukai T, Nagatsuka T, Yasuda T, Watanabe M. Solubility of Poly(methyl methacrylate) in Ionic Liquids in Relation to Solvent Parameters. Langmuir. 2014;30(11):3228-35.
[55] Lee JN, Park C, Whitesides GM. Solvent compatibility of poly(dimethylsiloxane)-based microfluidic devices. Analytical Chemistry. 2003;75(23):6544-54.

Chapter 5. Conclusions and future works

5.1 Summary

In this thesis, the preparation of 2-D materials by CVD which comprises the synthesis of both graphene and h-BN and their transfer was discussed. The thesis covered the discussions ranging from in-depth understanding of the process to the technological developments. In 2-D materials, the CVD process is regarded as the most promising synthesis method for scale up toward manufacturing as the synthesized materials present superb quality closer to their mechanically exfoliated counterparts. Nevertheless, the CVD-grown 2-D materials-based applications often show a great variety of properties depending on the lab settings. In most cases, the preparation process determines the baseline device properties of 2-D materials.

In this respect, I tried to make efforts to establish concrete criteria that could be used to obtain the highest quality of 2-D materials on a target substrate where device fabrication would be carried out later. I separated the preparation process into two parts, synthesis and transfer. Firstly, I started by probing the most well-developed process in each part, the Cu-mediated graphene synthesis and the PMMA-supported wet transfer, respectively. Through this investigation, currently pending issues yet to be resolved to improve the graphene quality were enlightened. Accordingly, I attempted to develop processes to tackle the issues both in the Cu-mediated graphene synthesis and in the PMMA-supported wet transfer process. These efforts served as a platform to explore another type of 2-D material, h-BN. Furthermore, the effects sought to replace the growth substrate and the supporting material in each part by Pt and EVA, respectively. The 2-D materials prepared by exploiting these materials were found to have better quality in terms of properties and morphologies on a target substrate. Finally, it is worth noting that the preparation conditions that provided the highest carrier mobility for graphene field effect devices were the directly transferred sub-mm sized single crystalline monolayer graphene flakes onto monolayer h-BN grown by the Pt foil method. The corresponding mobility value was *ca.* 10,000 $cm^2\ V^{-1}s^{-1}$, which was exceptionally high for CVD-graphene under the measurement condition: ambient air at room temperature.

5.1.1 Synthesis of graphene by CVD

The Cu-mediated graphene synthesis process was mainly studied. By considering the synthesis of graphene on a Cu foil as a thin film deposition process, the effects of various process parameters on the graphene morphology were analyzed. We recognized the domain boundaries of graphene as a defect that impairs the graphene quality, and sought to increase the domain size by adjusting the process parameters. Accordingly, sub-mm sized domains could be obtained with a Cu enclosure system, which was sizable enough to process without involving domain boundaries. In fact, such big domains were observed inside the enclosure with a dissimilar growth manner to the outside. This was understood as arising from an extremely low CH_4 concentration inside, that suppressed the nucleation density and impeded the growth. The carrier mobility in a single big domain was found to be remarkably higher than that in a continuous graphene sheet that would involve domain boundaries. This result proved that the scattering effect of domain boundaries was important in carrier transport.

In the following, we described a novel APCVD process that we developed to achieve a monolayer graphene material. The APCVD process has been known to be challenging because the dominant kinetics does not favor a self-limiting growth. I remarked how hydrogen could be used as one of the parameters to determine the growth kinetics in the APCVD growth process. Accordingly, the graphene morphology with respect to the introduction of hydrogen in each growth step was examined; as a result, a pristine monolayer graphene was obtained when hydrogen was excluded overall the entire growth steps. Here, the lack of hydrogen allowed for converting the growth kinetics to the surface-reaction limited, resulting in a self-limiting growth. This was advocated by the change of the domain shape.

Apart from the synthesis, a characterization method to estimate a graphene domain size was developed. As it is challenging to directly locate the domain boundaries under microscopes, another approach to figure out the domain size was explored. I assumed that the nucleation sites would be relatively defective, thereby being susceptible to a chemical reaction. When graphene samples were moderately annealed in air, I found morphological changes in each domain center, namely, nucleation

sites. As the distance between these nucleation sites was consistent with the domain size, the effectiveness of this method could be validated by comparing two graphene samples with a different domain size, and thereby obtained agreement with Raman spectroscopy characterization results.

We also attempted to growth graphene on a different metal substrate, a Pt foil. By exploiting a bubble transfer method, the Pt substrate could be used over and over again without generating environmentally hazardous materials containing etchants. The growth of MLG has been challenging on Pt due to the significant carbon solubility like Ni. This allows forming multilayer by precipitating carbons during the cooling step. In this study, by lowering the growth temperature, we could suppress the carbon precipitations and obtain a pristine MLG over the Pt substrate. The followed electrical characterizations through the fabrication of graphene FET devices confirmed a superior quality of the graphene sample grown by a Pt foil over one grown by a Cu foil.

5.1.2 Synthesis of h-BN by CVD

Based on the synthesis of graphene by CVD processes, the synthesis of h-BN was explored. The growth system was almost the same as the graphene CVD set up, but with an additional chamber which activated an h-BN precursor. Accordingly, the same graphene growth substrates, both a Cu foil and a Pt foil, could be exploited to synthesize h-BN. Furthermore, a simple modification of the growth system allowed for demonstrating the synthesis of h-BN/graphene hybrid structures in a single process flow.

Like the earlier graphene synthesis, a Cu-mediated process was firstly investigated. The h-BN morphologies with respect to the process parameters, such as the growth temperature, the source activation temperature, hydrogen flow rate, etc. proved that this Cu-mediated h-BN growth was not so suitable for obtaining a high quality monolayer h-BN sample. Nevertheless, a continuous monolayer could be produced over a narrow process window.

Alternatively, monolayer h-BN with a far better quality was obtained over a Pt-mediated process. Different from the growth by Cu, a continuous monolayer was simply obtained with a wide process

window, namely, a self-limiting growth process. This growth feature was understood by the high catalytic activity of Pt to decompose borazine. Various characterizations confirmed the decent quality of the resulting h-BN material. In particular, as mentioned earlier, graphene devices fabricated on the h-BN exhibited remarkably high carrier mobility. This result manifested the h-BN grown by Pt had acceptable quality as s device component in graphene-based applications.

5.1.3 Transfer process

As another important process determining the quality of 2-D materials, a polymer-supported wet graphene transfer process was carefully investigated. Through this study, I aimed for preserving the original quality of 2-D materials on a target substrate.

Firstly, in the PMMA-supported transfer, after understating the effect of various parameters involved in each transfer step, I proposed an optimized transfer process to obtain a clean graphene surface and to suppress hole-doping in graphene. In particular, by adopting HMDS for the passivation of the graphene surface with respect to surrounding environments, the mitigation of hole-doping was confirmed. This investigation provided for obtaining feasible carrier mobility values in the graphene devices that utilized this transfer process.

Next, I attempted to use a new polymer, EVA, as a supporting material to be used for the purpose of resolving challenges of the PMMA-supported transfer process. In this regard, two extreme processes, the transfer of wavy graphene grown on a textured Cu foil and the transfer of graphene onto a pre-patterned substrate (a 1 cent copper coin), were designed to justify the effectiveness of EVA over PMMA. The high thermal expansion coefficient and flexibility of the EVA polymer were expected to be beneficial in those cases. As a result, the graphene transferred with EVA exhibited a diminished wavy pattern and an agreeably conformal coating on the coin, respectively, which the PMMA-supported transfer failed to accomplish. These results suggest the suitability of EVA over PMMA as a supporting layer for practical uses.

5.2 Future works

As mentioned in the introduction of this thesis, the value of graphene is not just the use of its unique properties. As a pioneering material in the 2-D materials family, the research and development in graphene have served as providing groundwork and foundation for other types of 2-D materials. In this regard, I expect that this thesis can provide a platform upon which to build preparation processes that could be useful for various other 2-D materials. Therefore, as a future work, it is reasonable to expand the category of 2-D materials from graphene and h-BN to other types of 2-D materials. This also multiplies the numbers of combinations among the 2-D materials for preparing hybrid structures. The best candidate material right now seems to be MoS_2. While graphene and h-BN are electrically semi-metallic and insulating, respectively, monolayer MoS_2 is semiconducting with 1.8 eV for its direct band gap. This feature allows MoS_2 for being applied as a switching element in the electronic and optoelectronic devices. There are prior studies on the preparation of MoS_2 [1-4] and on the corresponding applications [5, 6]. Like the role of graphene in the 2-D materials family, I expect the advance of my investigation into MoS_2 will provide criteria for the study of few-layered transitional metal dichalcogenide (TMDC) materials.

Regarding the contents discussed in this thesis, there are future works to complement my own study. First, in the synthesis part, I learned about the carrier scattering effect on the grain boundaries by observing the great improvement of the carrier mobility of single crystalline graphene. In this regard, the Cu enclosure system that produced such a big graphene domain needs to be adapted in a way to be compatible with manufacturing. I expect that someone will eventually find a route to develop a closed system surrounded by Cu walls, analogous to the Cu enclosure.

Regarding the Pt-mediated growths of both graphene and h-BN, it was challenging to estimate how the domain size depends on their high growth rate. In this regard, the domain structure of both materials should be verified. This confirmation provides further understanding of the growth mechanism that appeared to be different from that for the Cu-mediated growths. As well as the method that was found in this thesis for exposing nucleation sites, the liquid crystal (LC)-assisted polarizing optical microscopy

(POM) approach [7, 8] can be attempted as a characterization method. This LC-assisted POM method takes advantage of the subordinated LC alignment by the underling domains.

In the transfer section, the use of EVA in the bubble transfer process will be expected to give a better morphology for 2-D materials generally. Recalling the transfer process, generation of H_2 bubbles lift up a polymer/2-D material stack from the Pt surface. PMMA is a comparatively delicate polymer, so that it can be deformed or torn by excessively generated bubbles. I expect that the EVA-supported bubble transfer method will be able to give mechanical robustness with a reduced density of wrinkles for the transfer of 2-D materials from one substrate to another.

Furthermore, one drawback of the wet transfer process of 2-D materials is the incompatibility with a target substrate that should avoid involving water. For example, quantum dot materials like PbS can be degraded by the contact with water. Accordingly, dry transfer with a thermal release tape [9] can be an alternative, but this particular approach requires a highly flat substrate. In this regard, either a PMMA-supported or an EVA-supported dry transfer process can be considered by modifying the established wet transfer process [10].

References

[1] Shi Y, Zhou W, Lu A-Y, Fang W, Lee Y-H, Hsu AL, et al. van der Waals Epitaxy of MoS2 Layers Using Graphene As Growth Templates. Nano Letters. 2012;12(6):2784-91.

[2] Lee Y-H, Yu L, Wang H, Fang W, Ling X, Shi Y, et al. Synthesis and Transfer of Single-Layer Transition Metal Disulfides on Diverse Surfaces. Nano Letters. 2013;13(4):1852-7.

[3] van der Zande AM, Huang PY, Chenet DA, Berkelbach TC, You Y, Lee G-H, et al. Grains and grain boundaries in highly crystalline monolayer molybdenum disulphide. Nature Materials. 2013;12(6):554-61.

[4] Ling X, Lee Y-H, Lin Y, Fang W, Yu L, Dresselhaus MS, et al. Role of the Seeding Promoter in MoS2 Growth by Chemical Vapor Deposition. Nano Letters. 2014;14(2):464-72.

[5] Wang H, Yu L, Lee Y-H, Shi Y, Hsu A, Chin ML, et al. Integrated Circuits Based on Bilayer MoS2 Transistors. Nano Letters. 2012;12(9):4674-80.

[6] Yu L, Lee Y-H, Ling X, Santos EJG, Shin YC, Lin Y, et al. Graphene/MoS2 Hybrid Technology for Large-Scale Two-Dimensional Electronics. Nano Letters. 2014;14(6):3055-63.

[7] Son J-H, Baeck S-J, Park M-H, Lee J-B, Yang C-W, Song J-K, et al. Detection of graphene domains and defects using liquid crystals. Nature Communications. 2014;5.

[8] Park J-H, Park JC, Yun SJ, Kim H, Luong DH, Kim SM, et al. Large-Area Monolayer Hexagonal Boron Nitride on Pt Foil. Acs Nano. 2014;8(8):8520-8.

[9] Caldwell JD, Anderson TJ, Culbertson JC, Jernigan GG, Hobart KD, Kub FJ, et al. Technique for the Dry Transfer of Epitaxial Graphene onto Arbitrary Substrates. Acs Nano. 2010;4(2):1108-14.

[10] Petrone N, Dean CR, Meric I, van der Zande AM, Huang PY, Wang L, et al. Chemical Vapor Deposition-Derived Graphene with Electrical Performance of Exfoliated Graphene. Nano Letters. 2012;12(6):2751-6.